Development of Dielectric Composites for Dielectric and Energy Storage Applications

by

Yang Tong

A dissertation submitted to the Graduate Faculty of
Auburn University
in partial fulfillment of the
requirements for the Degree of
Doctor of Philosophy

Auburn, Alabama
December 16, 2017

Keywords: Permittivity, dielectric loss, composite,
ferroelectric polymer, percolation theory, glass-ceramic

Approved by

Zhongyang Cheng, Chair, Professor of Materials Engineering
Majid Beidaghi, Assistant Professor of Materials Engineering
Pengyu Chen, Assistant Professor of Materials Engineering
Xinyu Zhang, Associate Professor of Chemical Engineering

Abstract

Dielectrics, which are materials responding to an external electric field with a polarization, have been widely used in industries. Dielectrics with high permittivity and high breakdown strength are required for the applications including high charge capacitors and energy storage devices, where the dielectric composites could found their position as the potential candidates. As the commonly used matrix for dielectric composite, glasses and polymers exhibit high breakdown strength, but small permittivity. To increase the permittivity and energy storage density, a great deal of effort has gone into developing the high breakdown strength matrix filled with high permittivity ceramics or conductive materials to create new types of dielectrics that is easier to process while maintaining useful dielectric properties.

For the purpose of getting the optimized composites for dielectric and energy storage applications, both polymer based and glass based composites were fabricated and studied in the research. By the using of different matrix and fillers and optimization of fabrication process, the dielectric composites with excellent performances were obtained. According to the analysis of the data from testing, these composites were proved to be the potential candidates for the applications including high charge capacitors, energy storage device and even wearable electronics.

As the first part of research, for the purpose of effectively increase dielectric constant, conductor-polymer was considered to be the next part of research for making potential dielectric composites. The 2-D conductor $Ti_3C_2T_X$ was selected as the filler due to its high conductivity

and P(VDF-TrFE) was used as the polymer matrix because of the relatively good permittivity and high breakdown strength to create the polymer based composite by solution casting. The hot pressing and silicon coupling agent was used to modify the morphology of the polymer composites. It was found that the percolation threshold is dependent on the testing frequency and is about 11.9 wt% at 100Hz, which is smaller than the composites using spherical conductive particle fillers. At room temperature, the dielectric constant of 10% composite is about 1570 at low frequency range, which is more than 100 times of the matrix material.

Although the increase of dielectric constant by combining 2-D conductive fillers and polymer matrix was proved by previous studies, the application of the composites is still limited by the high loss and low breakdown strength. Therefore, ceramic-polymer dielectric composites with different concentrations (0-30 vol%) were studied to create a composite with high energy and low loss. $CaCu_3Ti_4O_{12}$ ceramic was selected to be the fillers due to its extremely high permittivity and P(VDF-CTFE) was used as the polymer matrix because of the relatively good permittivity and high breakdown strength. The silicon coupling agent was used to improve the uniformity of the polymer composites. It was observed that as the amount of silicon coupling agent increases, there is a obviously increase in the breakdown strength and simultaneously a slightly decrease in permittivity, which lead to a overall increasing energy storage density. Overall, the best energy density was found to be 4.61 J/cm^3 from the composite film with 15 vol% $CaCu_3Ti_4O_{12}$ concentration.

Finally, the research focus was turned to the detailed studies glass based dielectric composites due to the fact that the type of materials have the ability to keep the balance between

high permittivity and energy storage density. The ceramic-glass with different glass concentrations (0-20 wt%) was prepared using nano-sized $BaTiO_3$ as the ferroelectric ceramic fillers and SiO_2 as the glass matrix by both randomly mixing and chemical coating methods. The variety of nanopowders were used to make composite pellets by conventional sintering under different conditions, such as molding pressure, sintering temperature, and ceramic powder size. In addition, the vacancies were introduced to $BaTiO_3$ nanopowders by the methods of vacuum pretreatment and hydrogen pretreatment. By summarize the results, several conclusions about processing effects were obtained. Firstly, compare with the powders obtained other mixing method, the samples produced from core-shell particles by Stöber process exhibit the better performance including higher permittivity, lower loss and higher breakdown strength; Secondly, the permittivity of composites decreases while the breakdown strength increases with the increasing concentration of glass; Thirdly, compare with other sizes of particles, the composites made by 200 nm ceramic powders are showing highest breakdown simultaneously keep the high permittivity; finally, the dielectric properties are strongly depended on the the vacancies introduced by pretreatment, the same pretreat temperatures will lead to different results for different size of particles. From the analysis of all summarized data, the highest permittivity was found to be higher than 3100 while the highest energy density was reached to be 1.6 J/cm^3 for the composite with the 2.5 wt% glass, 200 nm particle size by a 950°C pretreat temperature, which makes them attractive for both high charge capacitors and energy storage devices. More than that, by changing the method of sintering to SPS, another type of dielectric with extremely high dielectric constant, relatively high loss and low breakdown strength have also be created. At

1k Hz, a maximum dielectric constant of 811,895 and a loss of 0.457 were detected from the composites made by SiO_2 atomic layer deposited 140 nm $BaTiO_3$ nanopowders. Due to the layered structure of these SPS composites, some samples with ordinary dielectric constants and low loss which is close to the properties of insulators were also produced simultaneously with the same condition. Most of SPS composites have shown a very low breakdown strength below 0.1 MV/m; by the adding of ZrO_2, the breakdown strength of composites can be increased to 1.622 MV/m with a polarization of 19 $\mu C/cm^2$. Furthermore, $Ba_{0.5}Sr_{0.5}TiO_3$-SiO_2 composites were fabricated by the same process with SiO_2 coating layers and solid state sintering. The $BaTiSiO_5$ phase were also found due to the reaction of SiO_2 and BST which lead to the change in XRD patterns, decrease of T_c and lower dielectric constant of the composites. With 1 wt% SiO_2 additive, the maximum polarization, breakdown strength are about 20.28 $\mu C/cm^2$ and 260 kV/cm, which suggests an energy storage density about 2.56 J/cm^3 with a efficiency as high as 79%. Tunability of the BSTS composites was reduced by introduction of SiO_2, but the breakdown strength of the composites was improved remarkably, which is much advantageous for high power tunable applications.

Acknowledgments

I would like to give my gratitude to my advisor, Dr. Zhongyang Cheng, who has guided my thinking to reach my full potential through the completion of my research and dissertation during my graduate studies at Auburn University. I would like to emphasize that his influence on me was not only with regards to scientific knowledge but also as a person.

I would like to give my sincere thanks to my committee members, Dr. Majid Beidaghi, Dr. Pengyu Chen, and Dr. Xinyu Zhang, for their kind support and insightful suggestions. Special thanks to Mr. Steven Moore for his general technical support.

Special thanks also go to all my friends, especially group members: Dr. Lin Zhang, Dr. Xu Lu, Dr. Patrick Bass, Dr. Zhizhi Sheng, Dr. Lidong Ma, Ms. Wenya Du, Mr. Hossein Talebinezhad, Ms. Liangxi Li, Mr. Farrukh Najmi, Mr. Jiachen Liu, Mr. Yancen Cai and Mr. Baisheng Ma. I also would like to thank Mr. Armin Vahid for preparation of the 2-D conducting materials, and Ms. Julia Zhao for the help on preparation of the ceramic-glass composites. Best regards to all of my friends: Dr. Jing Dai, Dr. Yating Chai, Dr. Honglong Wang, Dr. Naved Siddiqui, Dr. Victor Agubra, Dr. Yuanyuan Zhang, Dr. Jinglie Zhou, Ms. Fuling Yang, Mr. Songtao Du, Mr. Yan Chen, and Ms. Anqi Zhang. My time in this PhD program has been more fun and interesting with them together.

Most importantly, I wish to express my love and gratitude to my parents, for their great love, emotional support, and encouragement which inspire me all the time during my studies and also throughout my life. Finally, I would like to acknowledge the financial support of this work

by NASA through Grant #G00007275. I also appreciated their support on the providing of facilities and helping of research work.

Table of Contents

List of Tables

List of Illustrations

Chapter 1

Introduction and Research Objectives

Dielectric materials with high capacity to store electric power, are one of the most active academic research areas in advanced functional materials for applications such as embedded capacitors and energy storage[1,2].

From the need of increasing the energy or charge stored in the capacitor with certain volume, dielectrics with high permittivity, low loss and high breakdown strength highly required for applications; From manufacture and device reliability point of view, materials which are flexible, easy to process, and can stand with high mechanical impact, are highly desirable[3-5].

Traditionally, the high capacitors made by a single material such as ceramic, polymer, and glass are commonly used in the industrial applications. However, The applications of ceramics are greatly impeded since their low breakdown fields and poor flexibility, while for polymers and glasses, the low permittivity values. Therefore, developing of the composites which combine the advantages of each composition has attracted a great deal of attention, including ceramic-polymer, ceramic-glass and conductor-polymer composites[6-8].

1.1 Theory of Dielectric Materials

1.1.1 Permittivity

In a dielectric material, charges cannot flow freely. The presence of an electric field E causes the bound charges in the material to be slightly separated or oriented. Permittivity

measures how the electric field effects, and is affected by, a dielectric medium. Under a DC electric field, the permittivity of a material was defined as[1,9]:

$$\vec{D} = \varepsilon_0 \vec{E} + \vec{P} \tag{1-1}$$

$$\vec{D} = \varepsilon \vec{E} = \varepsilon_0 \varepsilon_r \vec{E} \tag{1-2}$$

where D is the electric displacement field, ε is permittivity of the material between the plates, ε_0 is the permittivity of vacuum ($8.8541878176 \times 10^{-12}$ $C^2/J \cdot m$), ε_r is the relative permittivity of a material.

As a part included in the electric displacement, the polarization P in a dielectric material can be originated from different mechanisms. In general, there are four mechanisms including the electronic polarization caused by the displacement of outer electron cloud from the inner positive nucleus, ionic polarization due to the ionic responds with a change in the relative distance in between them, orientational polarization from the aligned dipoles along electric field direction, and space charge polarization when the space charge appears and caused the separation of positive and negative charges[1,9]. The influence of the polarization of different mechanisms with changing frequency was shown in **Figure 1-1**. The responded polarization P which reflects the induced dipole moments p was defined as[10,11]:

$$\vec{P} = \frac{\sum_{i=1}^{N} \vec{p}_i}{dV} \tag{1-3}$$

Based on the equation 1-1 and 1-2, the material polarization P under the electric field E can be expressed as:

$$\vec{P} = (\varepsilon_r - 1)\varepsilon_0 \vec{E} = \chi \varepsilon_0 \vec{E} \tag{1-4}$$

where $\chi=\varepsilon_r-1$ is the dielectric susceptibility of the material.

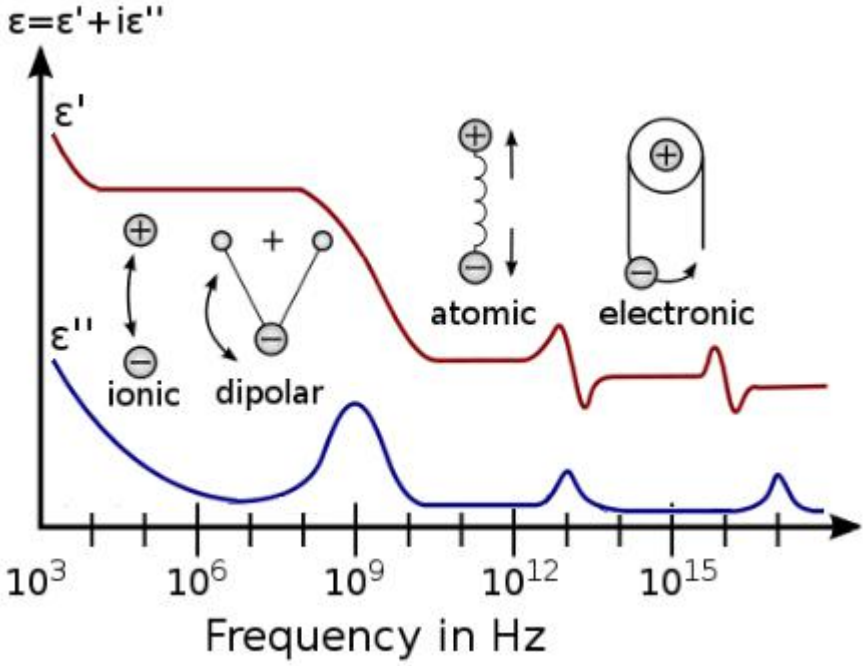

Figure 1-1 The frequency dependency of real and the imaginary part of the permittivity spectrum for various mechanisms of polarization

When an AC electric field is applied onto a dielectric, there is a displacement current going through the dielectric. The electric displacement D and polarization P under AC electric field became complex and was defined as:

$$\vec{D}^* = \varepsilon_0 \vec{E} + \vec{P}^* \tag{1-5}$$

$$\vec{P}^* = (\varepsilon^*_r - 1)\varepsilon_0 \vec{E} \tag{1-6}$$

where ε^*_r is the complex permittivity which reflects the complex nature of D and P.

1.1.2 Dielectric Loss

As opposed to the response of a vacuum, the response of normal materials to external fields generally depends on the frequency of the field. When the time-varying electric field (AC) is applied to a dielectric material, the complex permittivity with frequency and can be expressed as:

$$\varepsilon^*_r = \varepsilon'_r - j\varepsilon''_r \tag{1-7}$$

in which j is the imaginary unit, ε'_r is the real part of the permittivity, which is related to the stored energy within the medium; ε''_r is the imaginary part of the permittivity, which is related to the dissipation (or loss) of energy within the medium. For the quantification the lost electric energy, the dielectric loss has been defined.

The dielectric loss of a material indicates the inherent dissipation of electromagnetic energy (e.g. heat). It can be parameterized in terms of either the loss angle δ which was defined as:

$$\tan\delta = \frac{\varepsilon''_r}{\varepsilon'_r} \tag{1-8}$$

where tanδ is also named as loss factor.

The relationship between ε'_r and ε''_r can be described by Kramers-Krong relations[9]:

$$\varepsilon'_r(\omega) = \varepsilon_{r\infty} + \frac{2}{\pi}\int_0^\infty \frac{u\varepsilon''(u)}{u^2-\omega^2}du \tag{1-9}$$

$$\varepsilon''_r(\omega) = \frac{2}{\pi}\int_0^\infty [\varepsilon'(u)-\varepsilon_{r\infty}]\frac{\omega}{u^2-\omega^2}du \tag{1-10}$$

where $\varepsilon_{r\infty}$ is the permittivity at high-frequency limit and ω is the angular frequency. If let $\omega=0$, the equation 1-7 becomes:

$$\int_0^{\infty} \varepsilon''_r(\omega)\, d(\ln\omega) = \frac{\pi}{2}(\varepsilon_{rs} - \varepsilon''_{r\infty}) \tag{1-11}$$

where ε_{rs} is also named as the static permittivity. Equation 1-9 implies that in order to obtain a higher ε_{rs}-$\varepsilon_{r\infty}$, then a higher ε''_r is required.

1.1.3 Relaxation

Dielectric relaxation refers to the relaxation response of a dielectric material to an external electric field, which exhibits a momentary delay in the dielectric response of a material. Dielectric theories for relaxation were developed and virtually have been applied in different systems. In classical physics, the dielectric relaxation is often described with the assumptions that for the dielectric relaxation of an ideal, non-interacting population of dipoles to an alternating external electric field, using a simple Debye equation[9]:

$$\varepsilon^*_r(\omega) = \varepsilon_{r\infty} + \frac{\varepsilon_{rs} - \varepsilon_{r\infty}}{1 + j\omega\tau_0} \tag{1-12}$$

Or

$$\varepsilon'_r = \varepsilon_{r\infty} + \frac{\varepsilon_{rs} - \varepsilon_{r\infty}}{1 + \omega^2\tau_0^{\,2}} \tag{1-13}$$

$$\varepsilon''_r = \frac{(\varepsilon_{rs} - \varepsilon_{r\infty})\omega\tau_0}{1 + \omega^2\tau_0^{\,2}} \tag{1-14}$$

$$\tan\delta = \frac{\varepsilon''_r}{\varepsilon'_r} = \frac{(\varepsilon_{rs} - \varepsilon_{r\infty})\omega\tau_0}{\varepsilon_{rs} + \varepsilon_{r\infty}\omega^2{\tau_0}^2} \tag{1-15}$$

where τ_0 is the characteristic relaxation time of the relaxation process (which relaxation frequency $f_0=\omega_0/2\pi = 1/2\pi\tau_0$. The ε_{rs}-$\varepsilon_{r\infty}$ reflects the contribution of the relaxation process to the static dielectric constant and is also called as the permittivity strength of the relaxation process. By combing the Equation 1-11 and 1-12, the equation can be written as:

$$(\varepsilon'_r - \frac{\varepsilon_{rs} + \varepsilon_{r\infty}}{2})^2 + {\varepsilon''_r}^2 = (\frac{\varepsilon_{rs} + \varepsilon_{r\infty}}{2})^2 \tag{1-16}$$

In this relationship, the maximum value of ε"r occurs at ω0 and tanδ reaches its maximum at ω_δ:

$$\omega_0\tau_0 = 1 \tag{1-17}$$

$$\tan\delta_{\omega=\omega_\delta} = \frac{\varepsilon_{rs} - \varepsilon_{r\infty}}{2(\varepsilon_{rs}\varepsilon_{r\infty})^{1/2}} \tag{1-18}$$

The schematic of ε'_r-ε''_r relation is shown in **Figure 1-2** and **Figure 1-3**.

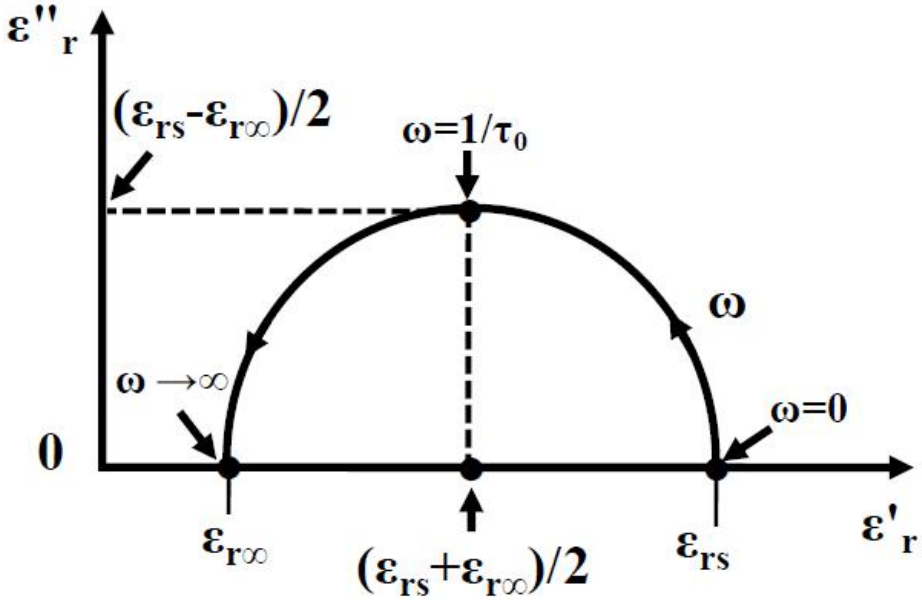

Figure 1-2 The schematic for dielectric material with only one relaxation time based on Debye equation

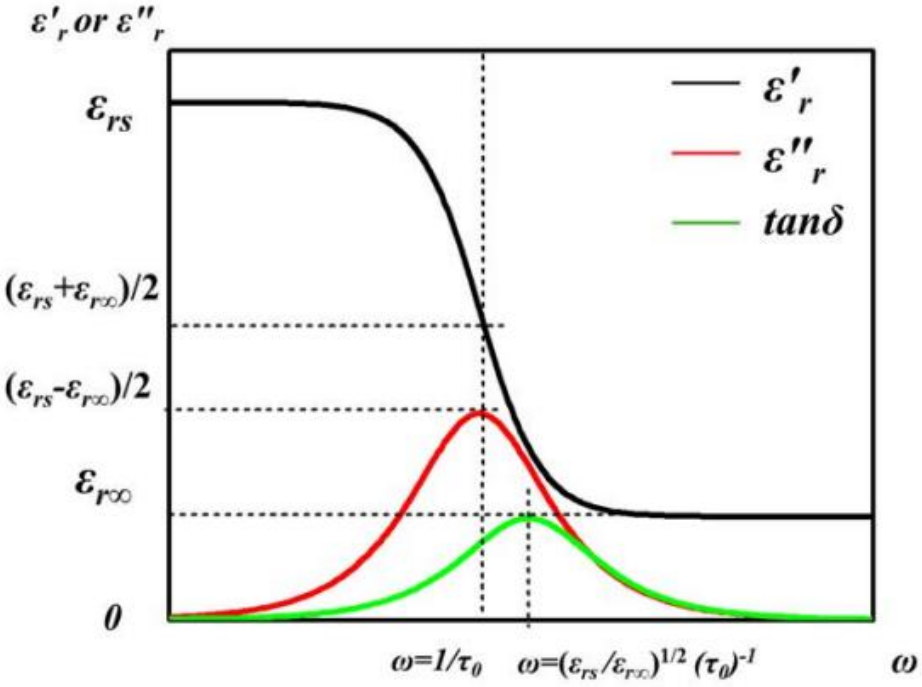

Figure 1-3 The schematic of ε'_r, ε''_r and tanδ as the functions of ω based on Debye equation

It should be noticed that the Debye equation only describes the dielectric response of the simplest one relaxation process, which does not fit the experimental results for most dielectric materials that have a set of relaxation time. For real materials, the frequency dependence of the permittivity is more complicated, many empirical relaxation equations that have been introduced to describe the relaxation phenomena. For example, Cole-Cole equation is shown as[9,12]:

$$\varepsilon^*_r(\omega) = \varepsilon_{r\infty} + \frac{\varepsilon_{rs} - \varepsilon_{r\infty}}{1 + (j\omega\tau_0)^{1-\alpha}} \tag{1-19}$$

where $0<\alpha<1$ and the maximum loss occurs at $\omega\tau_0=1$. Some of the experimental results agree well with Cole-Cole equation that $\alpha>0$. Also, there are varies of modifications were put forward for Cole-Cole equation for better fitting the experimental results. It has been found that several materials obey these equations, however, it has yet to find a formula can be summed up to fit in all of the cases.

1.2 Classification of Dielectric Materials

Dielectric materials including gases, liquids, and solids, are widely used in the current industry for different applications based on their different and unique dielectric properties[18-21]. With regard to the solid dielectrics as the priorities in current research, it is important to figure out the category a material belongs to before the starting.

All dielectric materials can be classified either by the compositions or the structures. By the composition the dielectrics can be classified into inorganic and organic materials, the classification by this method contains some information about the difference in industrial

performance including flexibility and processing temperatures; Compare with it, the classification according to the material structure is more clearly in distinguishing the differences in their dielectric properties, by this method all the dielectrics can be classified into two categories: nonpolar materials and polar materials[1].

1.2.1 Non Polar Materials

As introduced above, dielectrics can be classified into two major categories by their structures: nonpolar materials and polar materials. A nonpolar material is a material whose molecule or unit cell does not have a permanent dipole moment; A polar material is a material possessing a permanent dipole moment which is associated with its molecule or unit cell[13].

For the nonpolar inorganic materials, they are usually showing the low permittivity. For example, ε(silicon)≈3.7, ε(diamond)≈5.5~10, ε(paraffin)≈1.9~2.5, ε(carbon tetrachloride)≈2.0 and ε(quartz) ≈4.4[1]. As the highest dielectric constant found to date in a nonpolar material, dielectric $(Ta_2O_5)_{0.92}$-$(TiO_2)_{0.08}$ has shown a relative higher permittivity up to 126 at room temperature[14]. Therefore, the application of a single nonpolar material in high permittivity applications is limited.

1.2.2 Polar Materials

By definition, the polar material is a material exhibiting a permanent dipole moment which is associated with their molecules or unit cells. For a part of the polar materials, the interaction among the dipoles is strong enough to make them align with the same direction,

which leads to a polarization without the electric field applied to the material. These materials are named as pyroelectric materials, the polarization without electric field is named as spontaneous polarization. The spontaneous polarization in some of the pyroelectric materials can be switched by the external electric field, this material was named as ferroelectrics[13,15]. Since the spontaneous polarization changes with applied electric field, ferroelectric materials usually exhibit a very high permittivity, it makes the ferroelectrics have attracted a lot of attention in dielectric applications. The Polarization-Electric Field relation of a ferroelectric material was shown in **Figure 1-4**, which also displayed the basic feature of this material[16,17].

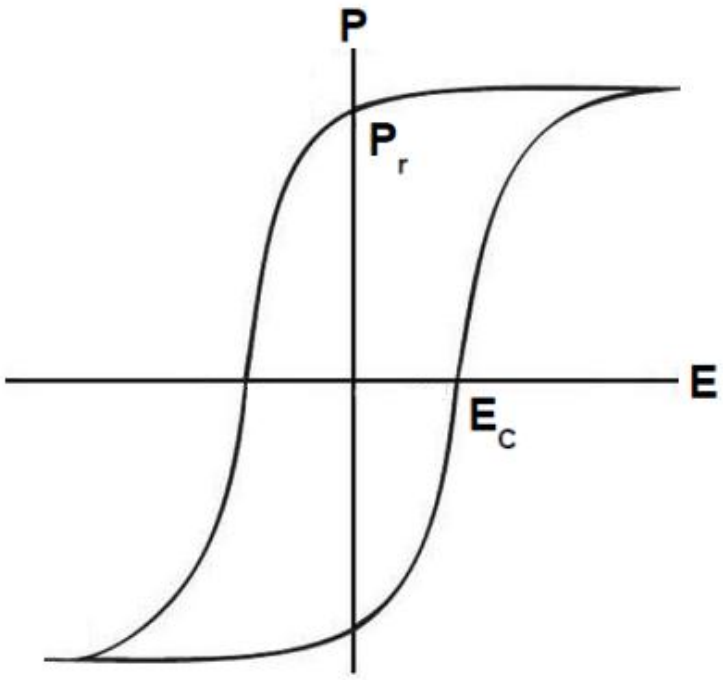

Figure 1-4 The P-E loop of a ferroelectric material

Although these ferroelectrics exhibited a high dielectric constant, their dielectric constant is strongly dependent on temperature, especially when it is around the phase transition

temperature between ferroelectricity and paraelectricity. This can be considered as a critical temperature for ferroelectric material, which is also named as Curie Temperature. As an example, the temperature dependence of permittivity for $BaTiO_3$ ceramics was shown in **Figure 1-5**. At a temperature higher than this phase transition temperature, the dielectric constant is dependent on the temperature by the Curie-Weiss law as[13]:

$$\varepsilon'_r = \frac{C}{T - T_c} \tag{1-20}$$

where T_c is the Curie temperature, and C is the Curie constant.

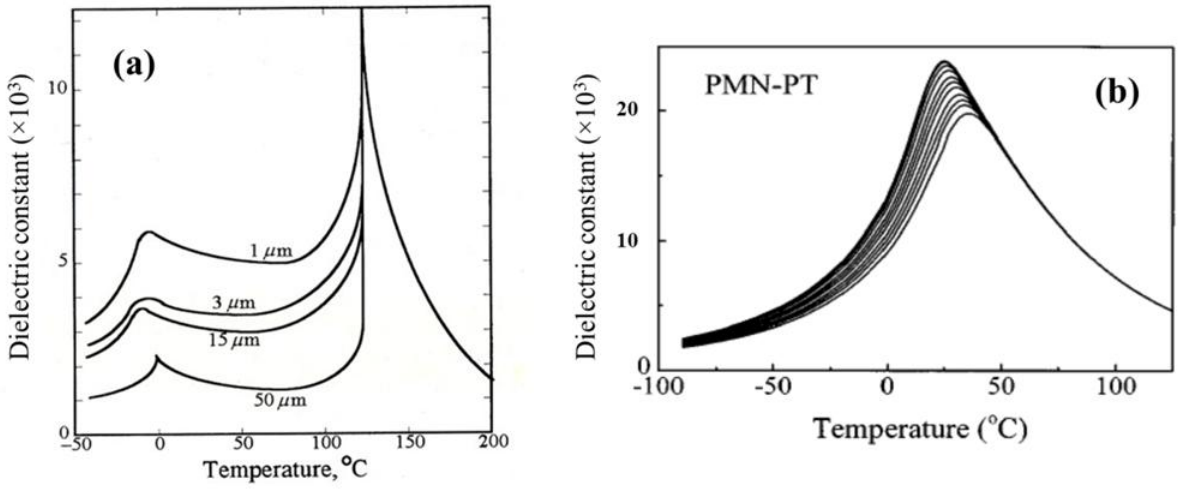

Figure 1-5 Dielectric constant versus temperature of (a) $BaTiO_3$ FE ceramics with different grain sizes at frequency of 1 kHz[13]; (b) 0.9PMN-0.1PT Relaxor FE ceramics different frequencies from 100 Hz to 100 kHz[18]

Some ferroelectric based solid solution ceramics/crystals, exhibit a so-called relaxor ferroelectric behavior, which indicates the ferroelectric materials that exhibit high electrostriction.

From some of the research, the random electric fields were believed to play a central role in establishing the relaxor phase, in part because the B sites of perovskite relaxors are occupied by random mixtures of heterovalent cations. To date, any material for which the real part of the dielectric permittivity Graphic exhibits a broad peak at a temperature graphic that depends on the measuring frequency is classified as a relaxor[18].

1.3 Application of Dielectrics

Nowadays, dielectric materials were widely used in a variety of applications, such as capacitors, electronic package, and dielectric resonators. In the real electronic systems, their primary functions are including energy storage, pulsed power generation, capacitive coupling in the electrical circuit, and enclose and protect an electronic device in order to reduce the overall noise between operating supplies. Based on the application, the dielectrics have been categorized into three classes by the Electronic Industries Association (EIA)[1]:

Class I: Dielectric materials with a relatively low permittivity 15~500 and small dielectric loss ≤ 0.003;

Class II: Dielectric materials with high permittivity based on ferroelectric ceramics or crystals (500~20,000);

Class III: Dielectric materials based on conductive phase with high capacitances and very low breakdown field.

1.3.1 High/low Permittivity

High permittivity composites are promising the wide range of applications in microelectronics, electrical engineering, biomedical engineering, etc. Groups of large, specially constructed, low-inductance high-voltage capacitors are used to supply huge pulses of current for many pulsed power applications. These include electromagnetic forming, Marx generators, pulsed lasers, pulse forming networks, radar, fusion research, and particle accelerators. Reservoir capacitors are used in power supplies where they smooth the output of a full or half wave rectifier. They can also be used in charge pump circuits as the energy storage element in the generation of higher voltages than the input voltage[19].

Capacitors are connected in parallel with the power circuits of most electronic devices and larger systems to shunt away and conceal current fluctuations from the primary power source to provide a clean power supply for signal or control circuits. Audio equipment, for example, uses several capacitors in this way, to shunt away power line hum before it gets into the signal circuitry. The capacitors act as a local reserve for the DC power source and bypass AC currents from the power supply. This is used in car audio applications when a stiffening capacitor compensates for the inductance and resistance of the leads to the lead-acid car battery.

1.3.2 Energy Storage

A capacitor can store electric energy when disconnected from its charging circuit, so it can be used as a temporary battery, or like other types of rechargeable energy storage system. Capacitors are commonly used in electronic devices to maintain power supply while batteries are being changed to prevents loss of information in volatile memory.

Additionally, in electric power distribution, capacitors are used for power factor correction. Such capacitors often come as three capacitors connected as a three phase load. Usually, the values of these capacitors are given not in farads but rather as a reactive power in volt-amperes reactive. The purpose is to counteract inductive loading from devices like electric motors and transmission lines to make the load appear to be mostly resistive. Individual motor or lamp loads may have capacitors for power factor correction, or larger sets of capacitors may be installed at a load center within a building or in a large utility substation.

The energy stored in a dielectric material under an electric field E can be expressed by the relationships between E and D presented[20,21]:

$$W_E = \int \vec{E} \cdot d\vec{D} \tag{1-21}$$

where W_E are energy storage density defined as the energy stored in the unit volume.

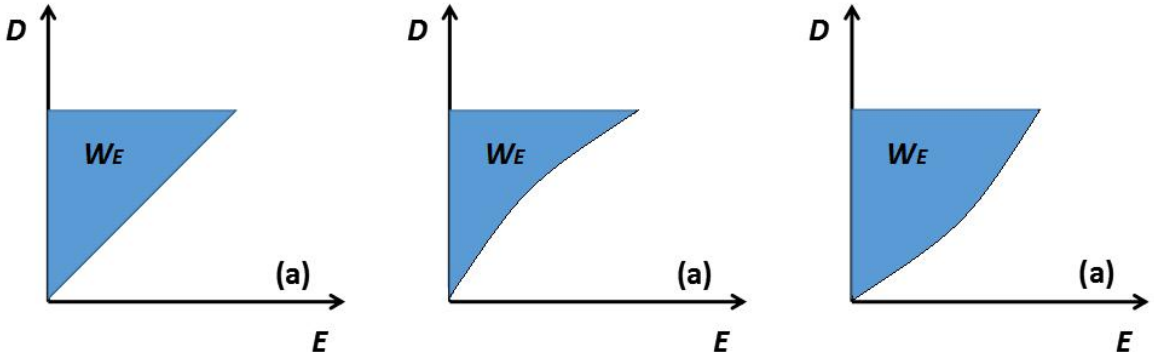

Figure 1-6 Energy stored in the material by displacement D under the electric field E: (a) linear; (b) positive curvature; (c) negative curvature

As shown in **Figure 1-6**, the curvature of D vs. E is critical to the energy density W_E. For linear dielectrics, the following relation is valid:

$$\vec{D} = \varepsilon * \vec{E} \tag{1-22}$$

From Equation 1-20 and 1-21, for linear dielectrics, the energy density can be simplified as[20]:

$$W_E = \frac{1}{2} \varepsilon'_r \, \varepsilon_0 \vec{E}^2 \tag{1-23}$$

According to the equations of energy calculation, to design a proper dielectric material with high recoverable energy-storage density and high efficiency, the requirements including high electric breakdown field, largely saturated polarization, and small remnant polarization, are highly desirable for the dielectrics in energy storage applications. As shown in **Figure 1-7**, there are four kinds of dielectrics with different amount of energy stored. Usually, linear dielectrics possess a high breakdown field and lower energy loss, but their low permittivity is not suitable for energy-storage application; Ferroelectrics have larger permittivity, but their larger remnant polarization leads to a small energy-storage density and high loss; Comparatively, relaxor ferroelectrics with nanosized domains and zero net remnant polarization antiferroelectrics are more fitted for energy storage because of their large saturated polarization and small remnant polarization[8].

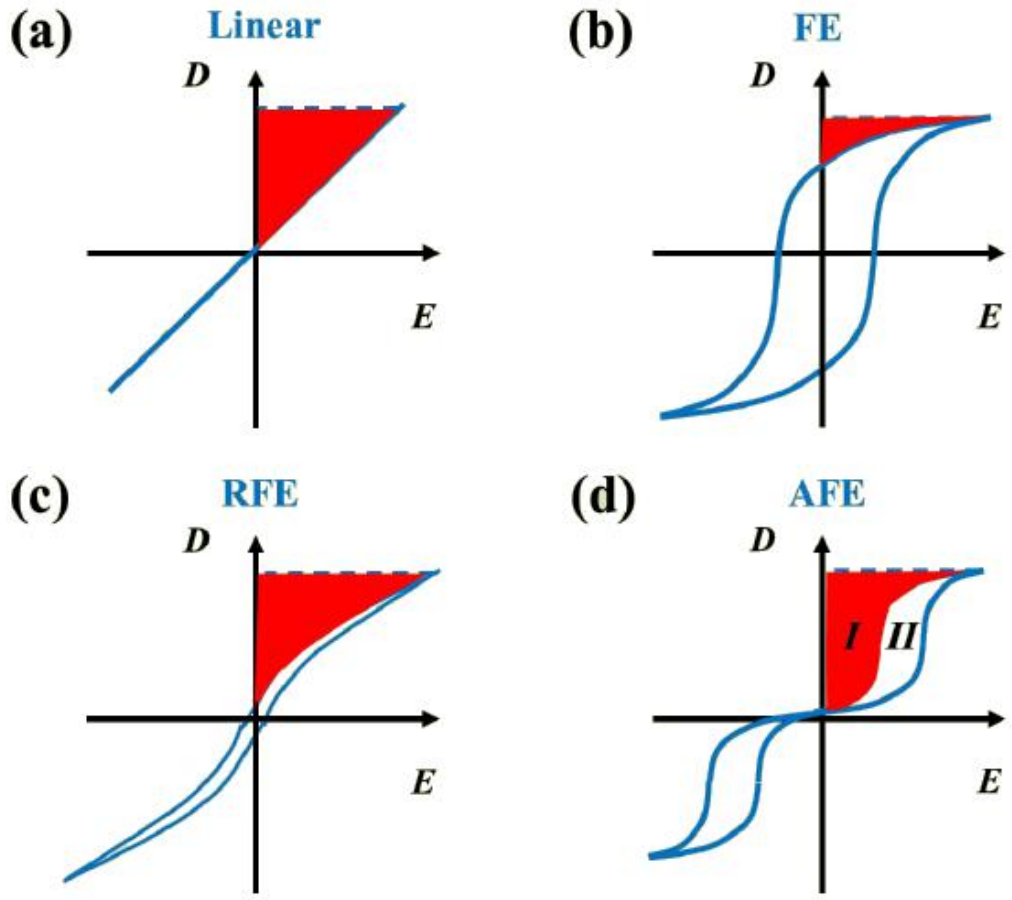

Figure 1-7 Diagram of hysteresis and energy storage density for (a) linear dielectrics, (b) ferroelectrics, (c) relaxor ferroelectrics, and (d) antiferroelectrics[8]

The different parameters which are required for high energy density are quite difficult to have the high value simultaneously on a single material. Some of the inorganic materials can exhibit high permittivity, however, their dielectric strengths E_b are very low[22]; Organic materials usually have very high dielectric strengths E_b but don't exhibit high permittivity[13]. Due to this reason, there is a great need to combine the advantages of different materials to increase the overall energy stored by making them into the form of composites. Meanwhile, with

the development of new manufacturing processes composite materials, glass-ceramic and polymer-based ferroelectrics, are found to be the potential for application in this area, which combines with the higher breakdown field of linear dielectric and larger polarization of ferroelectrics[8].

In car audio systems, large capacitors store energy for the amplifier to use on demand. Also, for the flash tubes, capacitors are used to hold the high voltage. Large capacitor banks are used as energy sources for the exploding-bridge wire detonators or slapper detonators in nuclear weapons and other specialty weapons. Experimental work is underway using banks of capacitors as power sources for electromagnetic armor and electromagnetic railguns and coilguns.

Conventional capacitors provide less than 360 J/kg of specific energy, whereas a conventional alkaline battery has a density of 590 kJ/kg[24]. There is an intermediate solution: Supercapacitors, which can accept and deliver charge much faster than batteries, and tolerate many more charge and discharge cycles than rechargeable batteries. They are however 10 times larger than conventional batteries for a given charge[24].

1.3.3 Wearable Electronics

Beyond the energy storage and pulse power applications mentioned previously, high permittivity composites especially conductor-dielectrics composites are also considered to be the novel functional materials have a great potential application in wearable electronics. For example, high elastic rubber-matrix composites with high dielectric permittivity are attracting great attention due to their easy, low-temperature processing and flexibility, especially in electrical engineering application such as potential cable accessories. This is because they could balance

the distribution of electric field of cable termination to prevent the cable from failure. In this field, one has to explore flexible rubber–matrix composites with high dielectric permittivity and low dielectric loss. Up to now, it is difficult to obtain flexible two-component rubber-matrix composites that meet all properties mentioned above when a single functional filler is employed. For example, one has to increase the concentration of ceramics in order to improve the dielectric permittivity of two-component rubber-matrix composites. This results in a concomitant decrease in their elasticity. However, conducting fillers, such as metal, carbon black, carbon fiber, and carbon nanotube are used, the dielectric permittivity of the composites increases remarkably when the concentration of conducting fillers is close to the percolation threshold. In this case, the dielectric loss of the composites always increases dramatically and their resistivity decreases sharply. Therefore, the resolution of the problems above is essential if flexible rubber–matrix composites are applied as electric cable accessories[25].

1.4 Dielectric Composites

By definition, a composite material is a material made from two or more constituent materials with significantly different physical or chemical properties that, when combined, produce a material with characteristics different from the individual components. The physical properties of a composite can be the sum, combination, or product of the properties of its constituents based on their physical properties and connectivity[26].

Composite materials were widely studied in materials science attempt to obtain the advanced properties. For the field of dielectrics, in order to combine superior properties from a

different class of materials to obtain better performance than the constituent dielectrics, composites including ceramic-polymer, conductor-polymer, and ceramic-glass have been studied.

1.4.1 General Concepts of Composites

For the composites with two constituents, based on their connectivity and morphology of each phase, can be defined as 0-0, 1-0, 2-0, 3-0, 1-1, 2-1, 3-1, 2-2, 3-2, and 3-3 as shown in **Figure 1-8**, where 0/1/2/3 represent the number of dimensions for each component in the composite[27-31]. For example, for 0-3 composite it is defined as 0-dimension isolated nanoparticles embedded inside 3-dimensions continuous matrix[31,32].

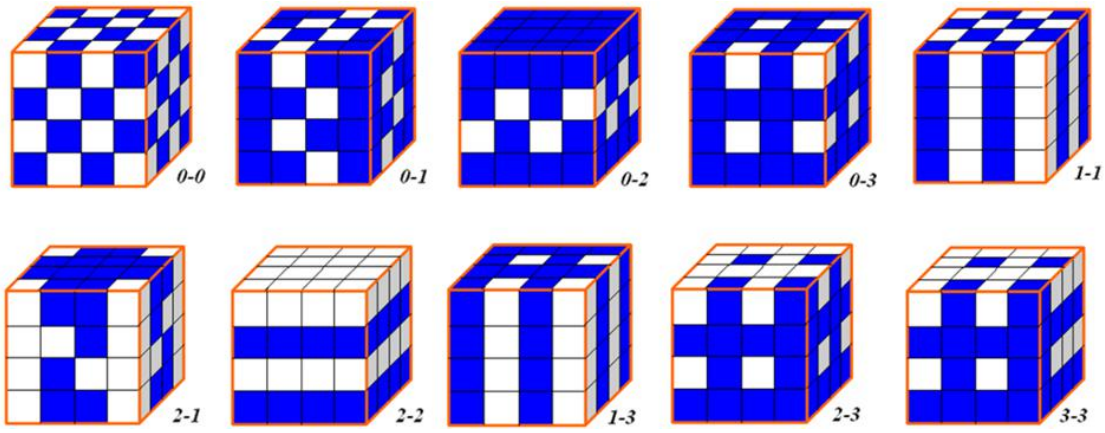

Figure 1-8 The connectivity patterns in diphasic composite[26]

The dielectric property of the composite was known to be a function of many factors including the size and shape of filler particles, the permittivity of filler and matrix respectively, the morphology and distribution of fillers in matrix, volume fraction of the filler in the composite,

and the appearance of interfacial layer between filler and matrix. Take the 2-phase composites with parallel or series connectivity to be an example, the effective dielectric constant ε′ of the composite is[18]:

$$\varepsilon'^{n} = v_1 \varepsilon_1'^{n} + v_2 \varepsilon_2'^{n} \tag{1-24}$$

where ε'_1 and ε'_2 are the dielectric constants of the ceramic particles and polymer matrix respectively, v_1 and v_2 are the volume fraction of the ceramic particles and polymer matrix respectively. $v_1=A_1/A$ and $v_2=A_2/A$ in parallel case; $v_1=d_1/d$ and $v_2=d_2/d$ in series case; n is +1 and -1 for parallel and series connection, respectively. The schematic of both connections was shown in **Figure 1-9**.

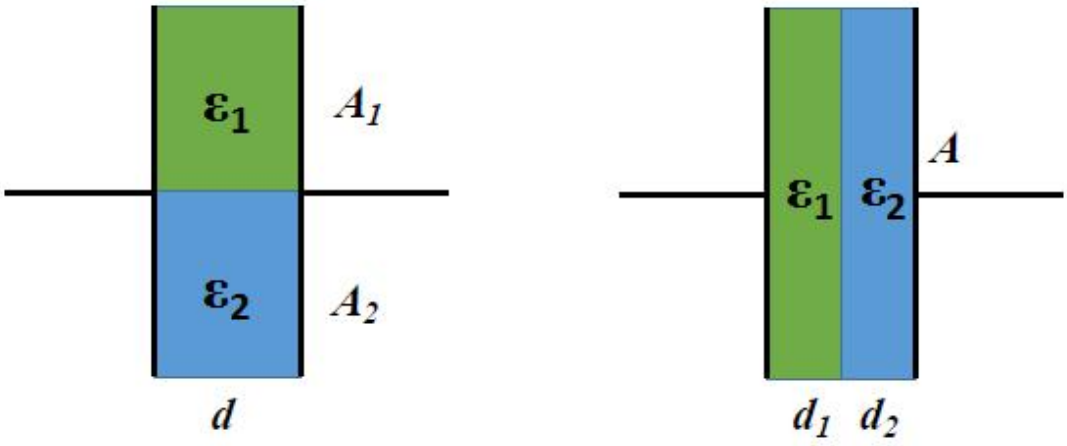

Figure 1-9 The schematic of parallel and series connections

In most cases, the effective permittivity of the 2-phase composites should lie between the values determined by Equation 1-24 for parallel and series cases because the real composites are the statistical mixtures of its components. The schematic of the permittivity of the 2-phase composite was shown in **Figure 1-10**.

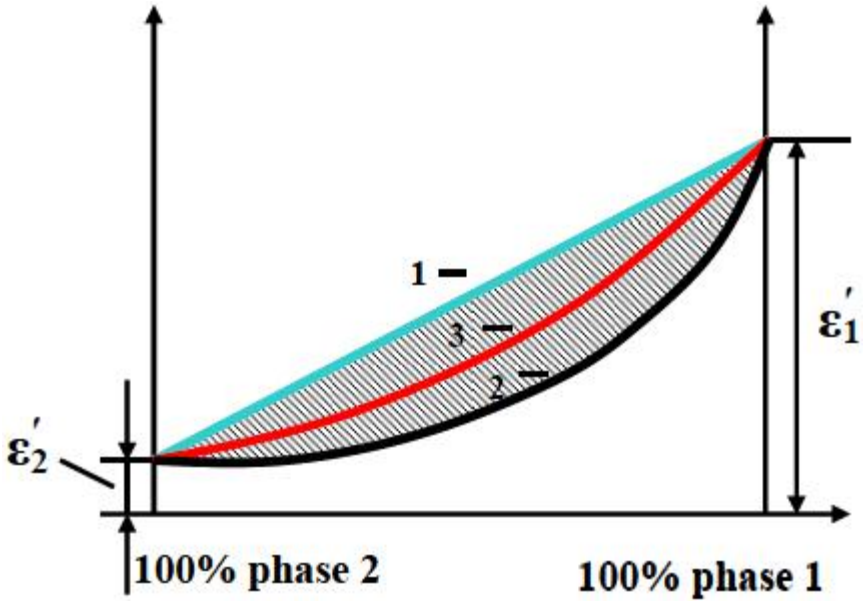

Figure 1-10 The schematic of permittivity of 2-phases composite for 1-parallel connection, 2-series connection and 3-real composite[23]

1.4.2 Flexible Polymer-Based Dielectric Composites

Dielectric materials which are flexible with a low processing temperature, exhibit a high dielectric constant, and have a high breakdown field, are required for many applications. To meet these different needs for dielectrics, polymer-based composites have been widely studied in last three decades.

Based on the fillers used, the polymer-based composites can be classified into two types: one is dielectric-dielectric composites in which the fillers are dielectric materials; the other is conductor-dielectric composites where the fillers are conducting materials as shown in **Figure 1-11**[33,34].

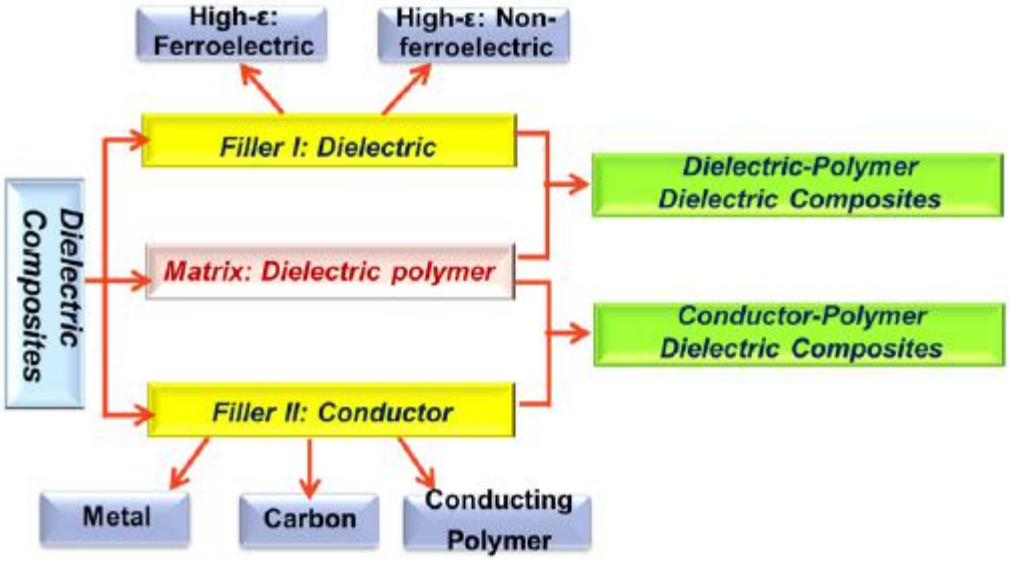

Figure 1-11 The schematic of classifications of polymer-based composites[35]

In both types of composites, the polymer matrix plays a key role in the dielectric performance of the composites. Especially, the breakdown field of a composite is mainly dependent on the polymer matrix. Therefore, various polymers have been used based on their processibility, flexibility, dielectric response, dielectric strength, melting temperature, and glass transition temperature, such as PMMA, PVC, PU, PVDF. Among all the polymers, PVDF and its co/terpolymers have been widely used as polymer matrix due to the high permittivity exhibited (>10)[36-41].

Understanding the dielectric response of a polymer-based composite has also been a topic of interest in fundamental research and applications. Various models have been introduced simulating the permittivity of a composite using the dielectric property of its constituents. Based upon mathematical analogy, results are deemed valid for permittivity, electric conductivity, heat conductivity, and diffusivity of such materials.

1.4.2.1 Conductor-Polymer Dielectric Composites

The conductive-polymer composites are another approach towards high dielectric constant materials, which belong to the field of conductor-dielectric composites. The dielectric property of a conductor-dielectric composite can be determined by the percolation theory. When the filler content is smaller than a certain value named as percolation threshold, the composite can be treated as a dielectric and its permittivity increases with increasing filler content rapidly, a very high permittivity may be obtained in the composites when the filler content is close to percolation threshold. As the filler content approaches and then exceed the percolation threshold, the composite will be transformed into a conductor. Therefore, the percolation threshold is very critical for the conductor-dielectric composites. The percolation threshold is dependent on the geometry, shape, size, and distribution of the conducting fillers, therefore conductors with various shapes ranging in size have been studied as fillers in this type of composites. In addition, it has been experimentally found that the percolation threshold is also strongly dependent on the process of preparation, which is mainly due to the distribution changes of the fillers[42-46].

The effective dielectric constant of a conductor-dielectric composite is dependent on the volume content of conductor filler as shown in **Figure 1-12**. When the filler of concentration is low, conductive particles are randomly distributed and separated from each other in the matrix, the properties of the composites are mainly dominated by the matrix. As the concentration increases, local clusters of particles begin to form which lead to the permittivity increases. When the filler content approaches a certain value, at the so-called percolation threshold, the pattern of conductive particles creates the conductive cluster and a network of channels connected by the conductive fillers. When the content of the filler is lower than the percolation threshold, the

dielectric constant of composites increases with a content of conducting filler, which is expressed as[47]:

$$\varepsilon_r \propto (\varphi_c - \varphi)^{-s} \quad (\varphi < \varphi_c) \tag{1-25}$$

where ε_r is the effective dielectric constant of the composite, φ is the content of filler, φ_c is the percolation threshold, s is the critical exponent. Importantly, Equation 1-25 indicates that the content should be close to the threshold for the composite to exhibits a giant dielectric constant; it is experimentally founded that as the filler content approaches the percolation threshold, the dielectric constant can be increased to the value of more than 1000[33]. Therefore, the percolation threshold can be considered to be the concentration of composition at which the conductor particles form channels through the composite. For a real conductor-dielectric composite, the percolation is strongly dependent on the microstructure of the composite[48,49].

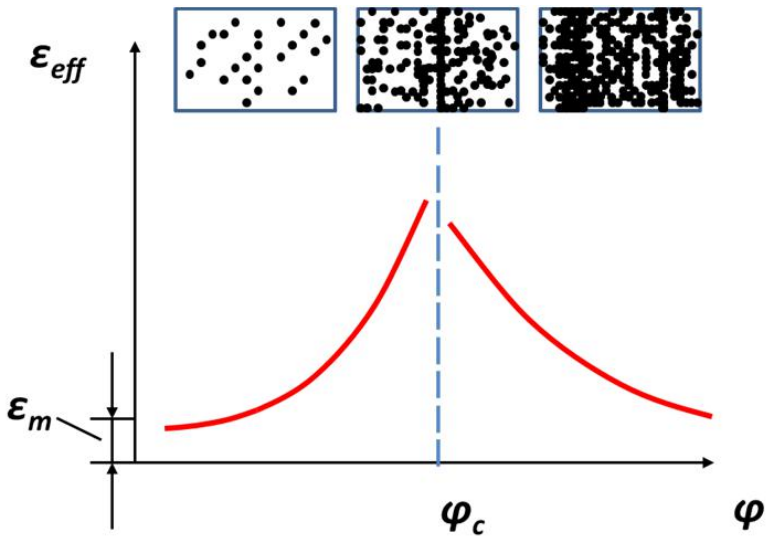

Figure 1-12 Effective permittivity of a 0-3 conductor-dielectric composite versus the volumetric content of conducting filler[34]

For a real conductor-dielectric composite, the research was focused on the percolation threshold and the composition dependence of the conductivity and permittivity. Based on random resistance network model, it was obtained that the effective permittivity at low frequency can be approximately expressed as[50]:

$$\varepsilon_{eff} = \varepsilon_m [A(\varphi_c - \varphi)^{\alpha} + B(\varphi_c - \varphi)^{\beta}]^{-1} \tag{1-26}$$

where the ε_{eff} is the effective permittivity, ε_m is the permittivity of matrix, φ_c is the percolation threshold, $\varphi < \varphi_c$, $A > 0$, $B > 0$, $\alpha > 0$, and $\beta > 0$.

For a random binary system, it was derived as[51]:

$$\varepsilon_{eff} = \varepsilon_m \left(\frac{\varphi_c - \varphi}{\varphi_c}\right)^{-s} \tag{1-27}$$

where s is a critical/power constant. Equation 1-27 became much simpler, therefore it is widely used in the literature to fit the experimental results. Based on above equations, one would find that a high permittivity can be achieved in a conductor-dielectric composite when the concentration of the filler is approaching the percolation threshold from low concentration side. This approach has been widely studied for the development of high permittivity composites since the 1980s[49,51]. The equations also indicate that the dielectric constant of the matrix has a direct influence on the ε_{eff} of a composite.

Table 1-1 Dielectric properties of conductor-polymer composites

Filler	Matrix	Filler size	Dielectric properties			Parameters		Freq	Ref.
			φ_m	ε_r max	tanδ	φ_c	s		
Ni	PVDF	20-30nm	28%	1273	2.04	27.80%	0.82	1k	[52]
Ag	PVDF	100nm×20μm	2%	379	0.25	20.00%	0.89	1k	[53]
Ag	PI	0.5μm	12.50%	400	--	12%	0.27	1k	[54]
Steel	PVDF	30μm×500μm	10%	427	800	9.40%	0.36	50	[55]
CF	PE	8μm×100μm	30%	35	<0.2	30%	1	200k	[56]
CF	PVDF	8μm×101μm	7%	80	<0.1	6.60%	0.86	1k	[57]
Carbon	PU	130nm	10%	2000	1000	10.00%	1.78	129	[58]
MWCNT	PVDF	-	2%	300	<0.8	1.60%	0.31	1k	[59]
MWCNT	PVDF	20nm×30μm	6%	1500	<2	3.80%	1.05	1k	[60]
MWCNT	PVDF	30nm×10μm	15%	5000	<2	8%	1.63	1k	[61]
MWCNT	PVDF	40nm×15μm	12%	2000	1	10.40%	1.06	1k	[62]
Graphite	PVDF	25μm×60μm	2.34%	$>10^7$	>200	1.01%	0.76	100	[63]
Graphite	HDPE	10-20μm	10%	4000	>800	4%	0.76	50k	[64]
PANI	PVDF	100nm	5%	400	<1	4.20%	0.3	1k	[65]

For the various of conductor-dielectric composites, the study has focused on the dependence of the dielectric behavior on the type of filler, the filler concentration, and the microstructure of the composite system. Especially, it was experimentally confirmed that the percolation threshold is strongly dependent on the conductivity, geometry, shape, size, and distribution of the conducting fillers[66]. Therefore, except for conventional spherical fillers, 1-D and 2-D fillers including carbon fibers, carbon nanotubes, and graphene have been used in the fabrication of polymer-based composites. The high dielectric constant of these composites have been reported with low percolation threshold φ_c; However, the very high dielectric loss was observed in all of these composites[67-70]. The dielectric properties of some representative conductor-polymer composites using 1-D and 2-D fillers were listed in **Table 1-2**, in which the

obvious increase in both dielectric constant and loss can be found compared with conventional composites. Due to their outstanding properties discussed above, 2-D materials have become a kind of important filler in the field of the dielectric composite.

Table 1-2 Dielectric Properties of 1-D and 2-D Conductor-Polymer Composites

Filler	Polymers	Composite Properties				Filler Size	Ref.
		φ_c	ε_r max	tanδ	f (Hz)		
PPY Clips	PVDF-TrFE	8 wt.%	2000	4	1,000	200nm×0.5μm	[71]
Ag Fiber	PVDF	20 vol.%	379	0.15	1,000	100nm×20μm	[72]
Steel Fiber	PVDF	9.4 vol.%	427	0.3	50	30μm×500μm	[73]
Carbon Fiber	PP	5 wt.%	400	>1	1,000	20-200nm	[74]
Graphite Plate	PVDF	1.01 vol.%	$>10^7$	>200	100	0.5-25μm	[75]
MWCNT	PVDF	10.4 vol.%	2000	>1	1	40nm×15μm	[76]
TFP-MWCNT	PVDF	8 vol.%	5000	2	1,000	30nm×10μm	[77]
Graphene	PS	10.9 vol.%	1741	1	100	30nm×3nm	[78]
Graphene Oxide	Epoxy	0.15 vol.%	5000	--	1,000	--	[79]

1.4.2.2 Ceramic-Polymer Dielectric Composites

For dielectric-dielectric composites, it is extremely important to find fillers with a high permittivity. Compare that most of the inorganic materials exhibit a permittivity ranging from a few to hundreds, the polar ceramics exhibit a higher permittivity up to 10^4 even 10^5. Therefore, various of ferroelectric and relaxor ceramics have been widely used in the development of dielectric-dielectric composites. As previous introduced, however, that the permittivity of these polar ceramic is very temperature dependent and most of them exhibit a strong electromechanical effect, both of which are not desirable for many dielectric applications. The

ceramics have a weak electromechanical effect and exhibit weak temperature dependence on their permittivity, are urgently necessary for the development of advanced dielectric composites[83-88].

A great deal of research on the development of polymer-based composites including nanocomposites has been done and some great progress has been made in the area to enhance the permittivity of the composite or reduce dielectric losses. Ferroelectric filler based composite materials such as $BaTiO_3$ (BT), $PbZrO_3$ (PZT), $BaSrTiO_3$ (BST) and $Pb(Mg_{1/3}Nb_{2/3})O_3$ (PMN), have been detailing studied by researchers; Moreover, ceramics with a giant permittivity such as $CaCu_3Ti_4O_{12}$ (CCTO), which are developed during last decade, were studied as the filler in composites lead to relatively high permittivity[89,90]. Also, many preparations and methods were studied to improve the quality of polymer itself or improve the uniformity of composites, such as annealing and other heat treatment at different temperature environment, hot pressing, stretching, coupling agent, ultraviolet radiation, etc.

To determine the dielectric constant of a real composite, various models have been introduced to simulate the composites and many formulas have been proposed to describe the composition dependence of the dielectric constant for 0-3 composites. For all of these models, the dielectric property of the composite is expressed as the function of composite's composition, the permittivity of the matrix, and the permittivity of filler materials. In some of the models, there is one more parameter contained, which is related to the shape and orientation of filler particles[91]. Some of the excellent composites for the purpose of energy storage were listed in **Table 1-3**.

Table 1-3 Dielectric properties of ceramic-polymer composites

Polymer Matrix	Ceramic filler	Size of filler	Vol%	k	tanδ	W_E (J/cm^3)	E_b (MV/m)	Ref.
PC	$BaTiO_3$	30-50 nm	50%	20	<0.01	3.9	210	[92]
P(VDF-HFP)	$BaTiO_3$	30-50 nm	50%	37	<0.07	6.1	210	[92]
P(VDF-CTFE) 91/9	$BaTiO_3$	50-70 nm	23%	25	<0.05	3.7	150	[93]
P(VDF-TrFE-CTFE) 78.8/5.4/15.8	$BaTiO_3$	50-70 nm	30%	65	<0.07	7.0	150	[93]
P(VDF-HFP)	$BaTiO_3$	30-50 nm	50%	32	<0.05	3.2	164	[94]
P(VDF-TrFE)70/30	$BaTiO_3$	<100 nm	20%	24	<0.05	1.8	130	[95]
PVDF	$BaTiO_3$	100 nm	20%	20	<0.03	3.54	200	[96]
PVDF	$BaTiO_3$	100nm	3%	11	<0.05	16.2	410	[97]
PS	$BaTiO_3$	63 nm	33%	45	0.06	9.7	222	[98]
P(VDF-TrFE-CTFE) 63/29/8	BST nanowire	--	17.5%	70	0.09	10.48	300	[99]
PVDF	BFN	--	5%	18	0.05	1.45	60	[100]
P(VDF-CTFE)94/6	BST	50 nm	10wt%	45	<0.05	6.5	250	[101]
PVDF	BST nanofiber	250 nm × 10μm	4.4%	13	<0.05	5.24	405	[102]
PVDF	PZT nanowire	160 nm × 2200 nm	50%	43	<0.05	1.16	15	[103]
P(VDF-HFP)	kaolinite	1500 nm		12	<0.05	19	750	[104]
P(VDF-TrFE) 50/50	PMN-PT	500 nm	50%	250	<0.05	15	120	[105]
PVDF	BCTS	500 nm	0.59%	13	<0.03	4	20	[106]

1.4.3 Ceramic-Glass Dielectric Composites

In general, due to their high permittivity, ferroelectric ceramics are attractive for high charge capacitors and electric energy storage devices. However, their applications are still very

limited due to the large loss and the relatively low dielectric strength. Therefore, there is a great need to find the method for improving the performance of ferroelectric ceramics for high permittivity and energy storage applications. As one of the potential methods to obtain better composites, glass-ceramic composites have been studied because of their lower porosity, higher breakdown field, and other unique attributes. Compare with the polymer-based composites, glass-ceramics possess a better thermal stability and electromechanical stability which is good for a variety of applications. Different glass composites have been detailed studied to achieve the improvement of energy density due to that the arisen breakdown strength by the decreased porosity, the reduced grain/pore size, and the decreased remnant polarization[106]. Among many methods for forming ceramic-glass, coating with low-melting-point glass is an effective method which can be operated at ambient temperature. A core-shell structure will result in the removal of porosity, and possibly forming new solid solutions to reduce the polarization loss. The properties of the core component such as reactivity and dielectric stability may be modified. Some of the ceramic-glass composites for the purpose of energy storage were listed in **Table 1-4**.

Table 1-4 Dielectric properties of ceramic-glass composites

Glass Composition	Ceramic	Glass Content	k	tanδ	W_E (J/cm^3)	E_b (MV/m)	Ref.
PbO-SiO_2	$NaNbO_3$	16 mol.%	160	--	1.87	56.5	[107]
Al_2O_3-SiO_2	BST 50/50	40 mol.%	1000	<0.01	0.9	80.0	[108]
BaO-SiO_2-B_2O_3	BST 40/60	5 vol.%	750	--	0.89	20.0	[109]
$SrCO_3$-TiO_2-SiO_2-Al_2O_3-BaF_2	$BaTiO_3$	7 wt.%	4000	0.02	0.32	7.5	[110]
BaO-Al_2O_3-B_2O_3-SiO_2	BST 30/70	4 wt.%	440	<0.01	0.52	16.4	[111]
SiO_2	$BaTiO_3$	2 wt.%	2500	0.01	1.2	20	[112]
BaO-B_2O_3-Al_2O_3-SiO_2	Mn doped TiO_2	15 wt.%	110	<0.01	1.15	50.2	[113]
$BaCO_3$-$SrCO_3$-TiO_2-Al_2O_3-SiO_2	BST 40/60	60 wt.%	229	<0.01	2.81	52.6	[114]
BaO-B_2O_3-Al_2O_3-SiO_2	BST 70/30	45 wt.%	180	<0.02	3.1	46.8	[115]
B_2O_3-Al_2O_3-SiO_2	$KSr_2Nb_5O_{15}$, $SrNb_2O_6$	50 wt. %	130	0.02	5.67	99	[116]

1.4.4 Interface Effect in Composites

In the most modeling studied on ceramic-polymer composites, the effective dielectric constant was only dependent on the permittivity of the ceramic particles and the polymer matrix. However, accurately predicting the effective dielectric constant has proven to be difficult due to other factors introduced. More recently, many researchers working on dielectric behavior have been focusing on the interface effect at the atomic or molecular level of materials[117-119].

For dielectric composites, there are interactions between those atoms and its surroundings on the interface between two uniform phases. The interactions lead to forces change over atomic

distances and fluctuate with thermal activity, which produced the properties difference compare with the bulk phases. As approaching the interface of phases, the forces will become increasingly modified. It is clear that interfaces have played an important role in controlling both electron and ion transportation in composites. For example, for the case of 0-3 composites, as the fillers are surrounded by the matrix, the interface between two phases will exhibit significant dominance as the particle size decreases. The relation between particle size and interface region (volume ratio of the interlayer and integral filler material) was shown in **Figure 1-13**, in which three thicknesses are assumed for the interfacial layer and the filler particles are treated as spheres with the same diameter. In addition, the interfacial properties may become variable when the particles are small enough thus bulk phase disappeared[35,118]. For example, with atomic doping of a semiconductor crystal, even though the dopant has a small influence on the structure, it can cause a remarkable change of the electrical properties of the material in total. Due to the reasons discussed here, the dielectric properties will also be increasingly dominated by their interfacial interactions, usually in the form of a degree of polarization and charge separation. The interfaces in dielectric composites can have either passive or active influence.

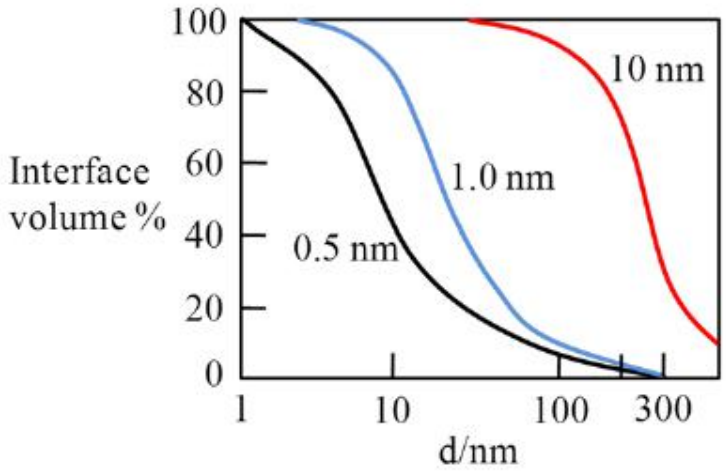

Figure 1-13 Volume fraction of interfacial layer as the function of the diameter of filler particles, where the thickness of the interfacial layers is assumed as 0.5, 1.0, and 10 nm respectively[35,118]

1.5 Objectives of Research

In this work, dielectric composites including ceramic-polymer, conductor-polymer, and ceramic-glass composites were studied. By connecting all the results and discussion obtained from these composites, an overall objective of developing composite for both high permittivity and energy density applications was pushed forward. For the conductor-polymer composite research, a 2-D high conductivity material $Ti_3C_2T_X$ was introduced to be the filler in P(VDF-TrFE) 70/30 mol% polymer matrix; In the part of ceramic-polymer composite study, CCTO was used as ceramic filler and P(VDF-CTFE) 88/12 mol% was used as polymer matrix; Finally, the $BaTiO_3$-SiO_2 composites were fabricated and tested in order to study the ceramic-glass in dielectric composite. By the series of experiments, following goals were reached:

1. Study and create different types of composites with excellent performance, to provide a series of new dielectric as potential candidates in high permittivity and energy storage applications;

2. For ceramic-polymer composites, combine the advantages of ceramic filler and polymer matrix to achieve the improvement of energy storage density, and study the influence of processing conditions;

3. For conductor-polymer composites, create a new material with high dielectric constant, calculate the important parameters according to the percolation theory, then discuss the difference and advantages achieved by using 2-D MXene filler with high conductivity;

4. For ceramic-glass composites, increase the dielectric strength and simultaneously keep high dielectric constant, to achieve the purposes of increasing overall energy density and obtain a relative balance between dielectric strength and dielectric constant, then study the detailed influence of processing conditions such as vacancies introduction;

5. Provide detailed analysis results of dielectric behavior and microstructure of composites to contribute to the theoretical knowledge of dielectric composites. According to all of the results and discussion, find the position of composites in the research field of dielectric materials and then make recommendations for the future development of dielectric composites in a wide variety of applications.

Chapter 2

Preparation and Characterization Methods

In this chapter, all of the preparation and characterization methods used in experiments will be discussed in details. The information for raw materials used for composites preparation including both filler and matrix will be presented firstly from the view of materials feature; Then, the methods of composites fabrication will be introduced in details, including both of synthesis procedure and optimization process, for ceramic-polymer, conductor-polymer, and ceramic-glass composites, respectively; Finally, the characterization methods including properties measuring, structures observation, data analysis, and calculation will be discussed and explained.

2.1 Raw Materials Used

2.1.1 MXene 2-D Material $Ti_3C_2T_X$

After the discovery of outstanding properties in graphene, two-dimensional (2-D) materials became a hot research interest in materials science. A new family of 2-D materials, MXenes have emerged recently which consisting of transition metal carbides, nitrides, and carbonitrides[1]. MXenes are discovered by selectively etching layers of elements from their corresponding 3-D structure, the so-called MAX phases. In addition, the outer surfaces of the exfoliated layers are always terminated with F, OH, and O groups during the etching process[2,3]. More than 70 MAX phases have been discovered, but till date, the reported MXene family only

includes Ti_3C_2, Ti_2C, Ti_3CN, $(Ti_{0.5}Nb_{0.5})_2C$, $(V_{0.5}Cr_{0.5})_3C_2$, Ta_4C_3, Nb_2C, V_2C, and Nb_4C_3, thus more MXene materials are expected to be found[4].

Since their discovery, MXenes have been reported to possess fascinating properties. For example, calculation from density functional theory have shown that MXene exhibits an in-plane elastic constant exceeding 500 GPa[5]; Semiconducting MXenes give a very large Seebeck Coefficients at low temperatures[6]; More importantly, the conductivity of MXenes is comparable to that of multilayered graphene[7]. These exceptional properties may be used for a variety of applications and have attracted much attention from researchers in various fields. As reported, MXenes are considered to be strong candidates for electrode materials in energy storage applications; They are also tested as supporting materials for platinum nanoparticles which achieving an extraordinarily stable catalyst for fuel-cell applications; Moreover, MXenes exhibited excellent enzyme immobilization abilities with biocompatibility for redox proteins, which shows promise for applications in electrochemical biosensors[8-10].

For the studies of the conductor-polymer composites, due to the excellent properties of MXenes materials including high conductivity and 2-D structure, a high permittivity, and low percolation threshold were expected in MXenes-polymer composites. For this purpose, one of the members of MXenes family, $Ti_3C_2T_X$ nanosheets were used as the 2-D fillers for the fabrication of polymer composites based on P(VDF-TrFE) copolymer. Both of the water and DMF based $Ti_3C_2T_X$ suspension was received as the ready-prepared 2-D fillers for this research. The high permittivity and relatively low loss were obtained as a result of characterization from the composites.

2.1.2 Calcium Copper Titanate $CaCu_3Ti_4O_{12}$

Due to the giant permittivity and unique dielectric behaviors, the material $CaCu_3Ti_4O_{12}$ with perovskite-related structure and belong to the $ACu_3Ti_4O_{12}$ family of the compound has got a lot of attention, for one of the potential high dielectric material[11,12]. After the optimization by trying different calcining temperatures, the permittivity as high as 20,000 for ceramics and 300,000 for single crystals at 1 kHz and room temperature have been reported and remains almost constant at the temperature between 100 and 600 K[13,14]. However, no detectable crystallographic structure change compare with the other member of its family of the compound has been found[14].

By the neutron diffraction, $CaCu_3Ti_4O_{12}$ was indicated to the cubic-perovskite structure with Im3 group symmetry[14], which was shown in **Figure 2-1**. Consider its similarities with ferroelectrics, the Ti^{4+} within TiO_6 octahedra contributes to part of its giant permittivity. However, the $CaCu_3Ti_4O_{12}$ exhibits more constraint than ferroelectrics because the octahedron formed a square planar around Cu^{2+}, which lead to a tension on Ti-O bonds to increase the polarization of the TiO_6 octahedra[15,16]. Current experimental results are likely to show the large permittivity is related to extrinsic reasons, including the creation of internal barrier layer capacitances at twin boundaries, the disorder-induced lattice discontinuity or displacement, the Maxwell-Wagner-type contribution of depletion layers at the interface between sample and contacts, the inhomogeneity of local dielectric boundaries, the limited reoxidation lead to the formation of semiconducting grains and insulating grain boundaries, the electrode/sample effects and the doping effect[12-14,17,18].

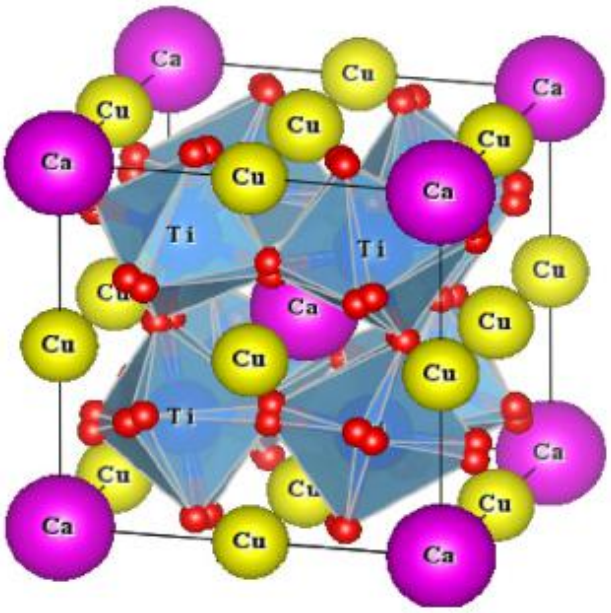

Figure 2-1 The structure of $CaCu_3Ti_4O_{12}$[19]

In the studies of the dielectrics properties for ceramic-polymer composites, $CaCu_3Ti_4O_{12}$ prepared by the solid-state reaction was received from the previous Ph.D. student and used as the ceramic fillers. High purity powders of $CaCO_3$, CuO, and TiO_2 were ground in a polyethylene bottle with zirconia grinding pellets and following with a 1075 °C sintering to obtain the polycrystalline $CaCu_3Ti_4O_{12}$, then they were ball milled to nanoparticles with an average size of 500nm. The ready-prepared pure ceramics exhibit a high permittivity up to 160,000[20].

2.1.3 Barium Titanate $BaTiO_3$

In electronic industry, ferroelectric ceramics are important as they have a high permittivity and offer wide applications such as capacitors, sensors, actuators, power transmission and high energy storage devices[21]. As one of the important ferroelectric ceramic

have been widely studied, although $BaTiO_3$ ceramic exhibit a high permittivity, the applications are limited due to the large loss and the relatively low dielectric breakdown strength. In recent years, the use of lead-containing materials have been controlled, the $BaTiO_3$-based ceramic material becomes the focus of dielectric research once again. Therefore, there is a great need to find the method for improving the performance of $BaTiO_3$-based dielectric for a variety of applications[22].

As well studied, lead-free ferroelectric ceramic $BaTiO_3$ has a perovskite structure and can be used for capacitors, positive temperature coefficient of resistivity (PTCR) thermistor, piezoelectric devices, optoelectronic elements and semiconductors[23]. The doping in $BaTiO_3$ ceramics was also studied for many years to improve the electrical and dielectric properties[24]. The solid-state $BaTiO_3$ can exist in five phases, from high temperature to low temperature are hexagonal, cubic, tetragonal, orthorhombic and rhombohedral crystal structure, all of them exhibit the ferroelectric effect except cubic. Take the cubic phase as an example, $BaTiO_3$ consisting of octahedral TiO_6 centers, Ba^{2+} is located at the center of the cube with a nominal coordination number of 12. Lower symmetry phases are stabilized at lower temperatures, associated with the movement of the Ba^{2+} to the off-center position. The atomic structure of $BaTiO_3$ was shown in **Figure 2-2**.

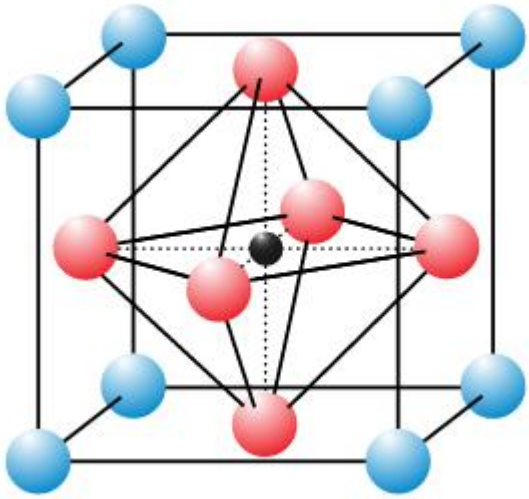

Figure 2-2 The structure of $BaTiO_3$ (Ba-blue, Ti-black, O-pink)[25]

In the preparation of glass-ceramic composite for dielectric energy storage study, 99% $BaTiO_3$ purchased from nanopowders US Research Nanomaterials. A silica shell was coated on ceramic nanopowders by the Stöber process, then the high-temperature sintering was used to obtain the uniform glass-ceramic pills. Both 100 nm particles with cubic phase and 200 nm particles with tetragonal phase were studied for the purpose of optimization.

Beside sintering temperature, the size of nanopowder also plays an important role in the ceramic sintering. With the size change, the main ceramic filler $BaTiO_3$ used in the research will exhibit different crystal structures. For the study of particle size effect, 100 nm and 200 nm powders were used to make $BaTiO_3$-SiO_2 composites. Both of the nanopowders were coated with SiO_2 and then high temperature sintered to make ceramic pellets; The structure difference between them was also studied by SEM observation. The picture of 100 nm and 200 nm nanopowders were shown in **Figure 2-3**.

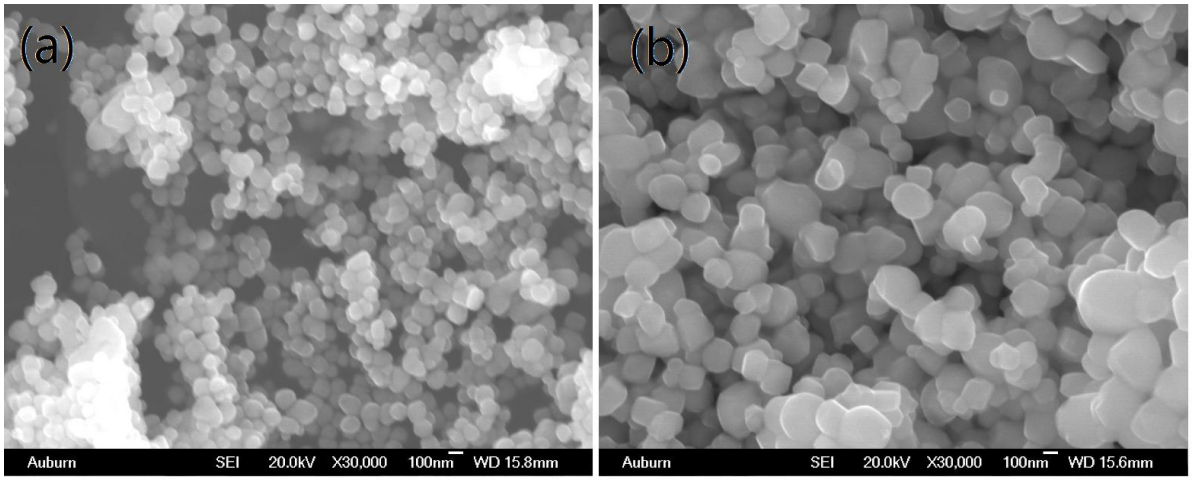

Figure 2-3 The SEM picture of (a) 100 nm and (b) 200 nm $BaTiO_3$ nanopowders

It has been proved by a number of observations that, the electrical properties of perovskite crystal materials including $BaTiO_3$ based composites are also closely related to its oxygen vacancies, which can be controlled by heating in low oxygen partial pressure conditions. For the purpose of increasing permittivity of $BaTiO_3$ fillers, the $BaTiO_3$-SiO_2 glass-ceramic composite was prepared after a pretreatment on $BaTiO_3$ nanopowders to introduce vacancies. The effects of vacancies on the microstructure and electrical properties of coated BaTiO3 ceramics were investigated, the influence of vacuum pretreatment condition such as temperature and atmosphere environment was studied to further optimize the material properties.

For the study on the influence of different pretreatment temperatures, $BaTiO_3$ with both 100 nm and 200 nm particle size were pretreated to introduce vacancies at 850 °C, 900 °C, 950 °C and 1000 °C with either the vacuum environment (low pressure $\leq 5\times10^{-3}$ torr) or H2 forming gas environment. environment before coating. 2.5, 5, 10, 15 and 20 wt% SiO_2-$BaTiO_3$ composites were prepared for both vacuum pretreated and H_2 gas pretreated samples.

2.1.4 Barium Strontium Titanate $Ba_{0.5}Sr_{0.5}TiO_3$

Strontium Titanate is an oxide of strontium and titanium with the chemical formula $SrTiO_3$. At room temperature, it is a centrosymmetric paraelectric material with a perovskite structure and has a dielectric constant around 300 at low electric field. At low temperatures, it approaches a ferroelectric phase transition with a very large dielectric constant but remains paraelectric down to the lowest temperatures measured as a result of quantum fluctuations, making it a quantum paraelectric[26].

Among numerous ferroelectric materials, the solid solution quaternary $(Ba_XSr_{1-X})TiO_3$ system which takes advantage of the high dielectric constant of $BaTiO_3$ and the structural stability of $SrTiO_3$, is a promising candidate for thin film capacitors due to its paraelectric phase at room temperature and a resulting lack of aging and fatigue effects. BST is widely used as lead-free dielectric materials due to their high dielectric constant, low dielectric loss, high tunability of dielectric properties and controllable Curie temperature[27]. However, the conventional applications of BST ceramics are usually limited by their low breakdown strength. Recently, a lot of attention has been attracted to a variety of BST based glass–ceramics composites, which is considered as one of the best potential candidates for high energy storage devices due to their high dielectric constant and breakdown strength. Numerous works have been carried out to reduce the dielectric constant of BST to a suitable value. Moreover, lower dielectric loss and larger tunability are also expected for some of the applications. It is known that for perovskite structures ceramics, small amounts of doping could greatly affect the dielectric properties. The effects of various elements, such as Mn, Co, Fe, Mg, etc. have been investigated to modify the electrical properties of BST[28-30]. In comparison with conventional ceramics, composites are

considered much more promising due to their novel properties that colligate the advantages of different materials. Dielectric materials with a low loss such as Al_2O_3, $MgWO_4$, $ZnNb_2O_6$, Mg_2TiO_4, $BaWO_4$, and $MgAl_2O_4$ were added into BST to fabricate new composites, which keep relatively low dielectric constant and loss compared with pure BST[31-33].

2.2 Conductor-Polymer Composite Fabrication

2.2.1 Experimental Procedure

In the preparation of composites, P(VDF-TrFE) 70/30 mol.% copolymer from Solvey was utilized as the polymer matrix; The different weight concentrations (2,4,6,8,10 wt. %) of $Ti_3C_2T_X$ were added into P(VDF-TrFE) matrix as fillers. Firstly, the P(VDF-TrFE) copolymer was dissolved in N, N-dimethylformamide (DMF) with magnetic stirring for 12 hours at room temperature. Simultaneously, the certain amount of $Ti_3C_2T_X$-water suspension was mixed with DMF and heated to 60 °C in an oven for the evaporation of the water from to obtain the $Ti_3C_2T_X$-DMF suspension. Then the prepared P(VDF-TrFE) solutions were added into $Ti_3C_2T_X$-DMF suspension to form the uniform the well-mixed solution by sonicating the mixture 30 minutes and magnetic stirring 12 hours. After that, the mixture was cast on the glass substrate and dried at 70 °C for 8 hours to make films. The as-cast films were released from glass plates carefully and stacked in four layers then hot-pressed at 200 °C to improve the uniformity of composites. Finally, the composite samples were annealed at 140 °C for 12 hours to obtain the samples for the following testing. The final composite films prepared by solution casting was shown in **Figure 2-4**.

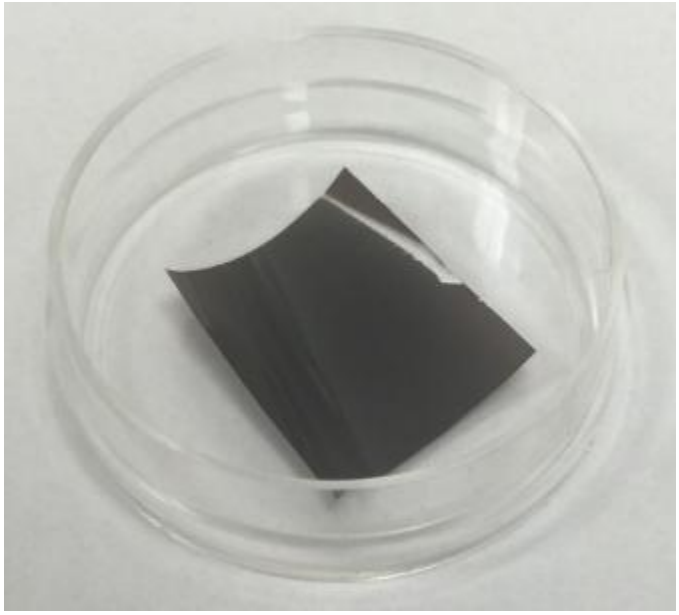

Figure 2-4 The final product thin film by solution casting

2.2.2 Optimization

As introduced, the $Ti_3C_2T_X$-P(VDF-TrFE) composite thin films with different concentrations 2, 4, 6, 8, 10, 12 and 14 wt% of ceramic fillers were prepared by solution casting for dielectric study. The as-cast films are relatively brittle and not uniform due to the random distribution of the 2-D filler. Therefore, to obtain better dielectric properties optimization including annealing, hot pressing, silicon coupling agent and improve dispersion of solute by change solvent the was used for the modification of the performance of composite thin films.

2.2.2.1 Dispersion Improvement

As the filler used in the composite preparation, $Ti_3C_2T_X$ 2-D sheets were provided in the form of water-based suspension. Due to the insoluble of P(VDF-TrFE) in water, it is impossible to make a uniform mixture by directly mixing the P(VDF-TrFE) solution and $Ti_3C_2T_X$-water suspension. The solvent of $Ti_3C_2T_X$ suspension has been changed to an organic solvent. Firstly, the certain amount of $Ti_3C_2T_X$-water suspension was mixed with DMF by stirring and sonication. Then, the mixture was heated to 90 °C in an oven to evaporation the water. Due to the lower boiling temperature and higher evaporation rate of water, the uniform DMF-based suspension can be obtained. After the solvent change, the P(VDF-TrFE) solutions were added to the $Ti_3C_2T_X$-DMF suspension to form the well-mixed solution by sonicating the mixture 30 minutes and magnetic stirring 12 hours. Finally, the solution was used for solution casting process to make films. The above-discussed process was shown in **Figure 2-5**.

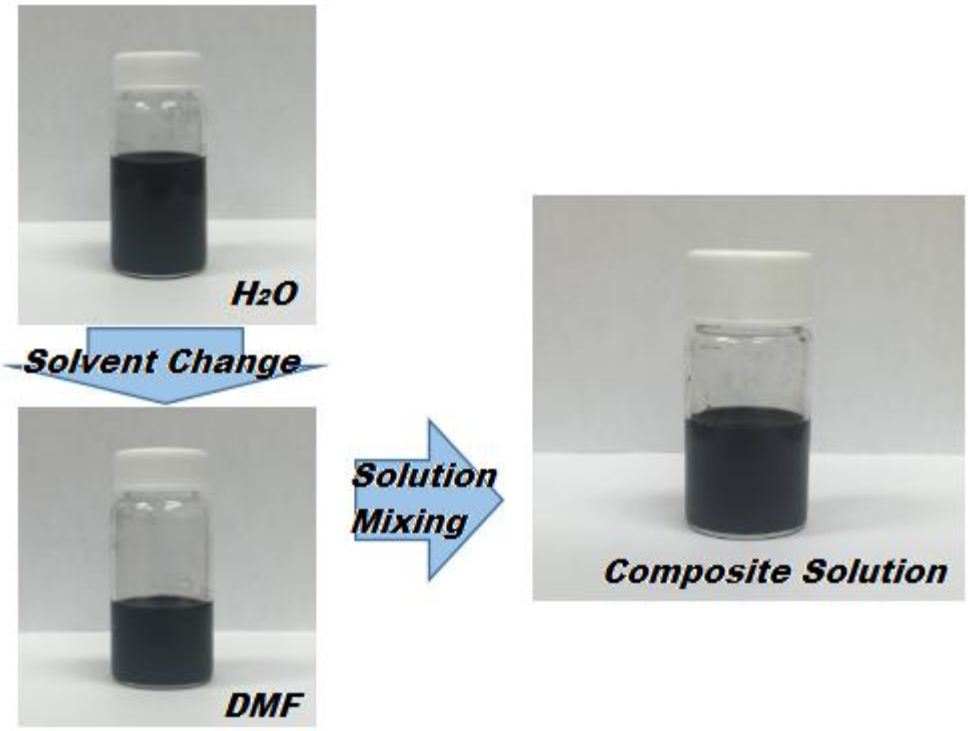

Figure 2-5 The solvent changing and mixing process of composite solution

2.2.2.2 Hot Pressing Process

The hot pressing was also used to improve the performance of conductor-polymer composite to improve the uniformity of filler distribution in the polymer matrix. Due to the similarity in physical properties of the polymer matrix, the same condition of high temperature (200 °C) and high force (10 tons) was applied in this process. The flexible polymer film obtained by hot pressing was shown in **Figure 2-6**.

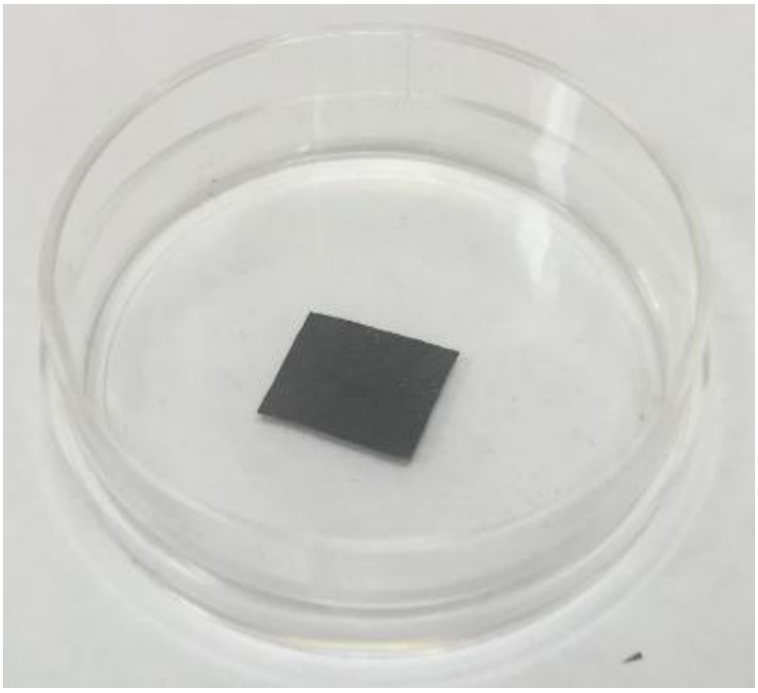

Figure 2-6 The conductor-polymer composite after hot pressing

2.2.2.3 Silicon Coupling Agent

The effect of silane coupling agent adding was also studied for conductor-polymer composites. The coupling effect between filler and polymer matrix was expected to be achieved similarly with ceramic-polymer composites. The $Ti_3C_2T_X$-P(VDF-CTFE) composites were modified with 0.5, 1, 2 and 5wt% silane coupling agent to find the best-using conditions. The testing results proved that the bridge-linked action of silane coupling agent can improve the uniformity of the composites, which lead to a lower percolation threshold. The physical and chemical properties of silane coupling agent were listed in **Table 2-1**.

Table 2-1 The physical and chemical properties of silane coupling agent

Product name	1 H, 1H, 2H, 2H-Perfluorooctyltrichlorosilane
Company	Alfa Aeasr
Molecular Formula	$C_8H_4Cl_3F_{13}Si$
Synonyms	Trichloro-1 H, 1H, 2H, 2H-Perfluorooctylsilane
CAS#	78560-45-9
Flash Point	54 °C
Boiling Point	84-85 °C
Solubility in water	Reacts
Density (g/ml)	1.638
Molar Mass (g/mol)	481.55

2.3 Ceramic-Polymer Composite Fabrication

2.3.1 Experimental Procedure

The $CaCu_3Ti_4O_{12}$-P(VDF-CTFE) 0-3 composite thin films were prepared by traditional solution casting method. P(VDF-CTFE) 70/30 mol% copolymer was used as the polymer matrix and dissolved in N, N-Dimethylformamide (DMF) under magnetic stirring for 12 hours. The 1075 °C sintered polycrystalline $CaCu_3Ti_4O_{12}$ ceramics were ball milled to nanoparticles with an average size of 500nm was used as the ceramics and added into the solutions. After the $CaCu_3Ti_4O_{12}$ powder had been added, the mixture was stirred for 12 hours and then sonicated for 30 minutes, then the $CaCu_3Ti_4O_{12}$-P(VDF-CTFE) solution was cast on the glass plates at 70 ºC for 8 hours following an annealing process. In the following experiments, the surface

modification was added in the process by using silicon coupling agent before casting. The overall process flowchart for $CaCu_3Ti_4O_{12}$-P(VDF-CTFE) 0-3 composite fabrication was shown in **Figure 2-7**.

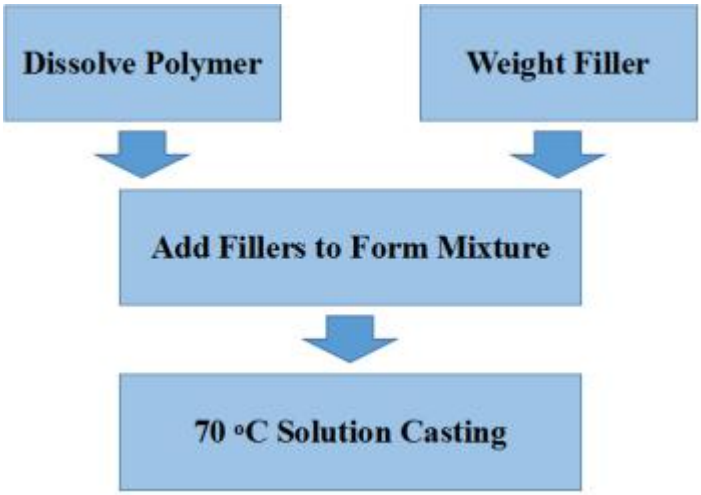

Figure 2-7 The preliminary flowchart of ceramic-polymer composite preparation

2.3.2 Optimization

As introduced, the $CaCu_3Ti_4O_{12}$-P(VDF-CTFE) nanocomposite thin films with different concentrations 5, 10, 15, 20, 25 and 30 wt% of ceramic fillers were prepared by solution casting. It was found that the porosity of as-cast films is relatively high due to the evaporation of the solvent. Therefore, to obtain better dielectric properties optimization including annealing, hot pressing, and silicon coupling agent were used for the modification of the performance of composite thin films such as the uniformity and crystallinity.

2.3.2.1 Annealing Process

The removal of DMF solvent and the improvement in crystallinity of polymer matrix plays an important role in the overall electric properties of the ceramic-polymer composites. Therefore, the annealing process is necessary for both solution casting and hot pressing samples, the annealing temperature is an important factor that improving the performance of composites. The process was carried out after the obtain of composite thin films with different temperatures for the study of temperature influence. Due to the fact that the crystallization temperature of P(VDF-CTFE) 88/12 is around 160 ºC, the as-casted composite films were put on the glass plates in an oven and then annealing process was kept at 150 °C, 160 °C and 170 °C respectively for 12 hours.

2.3.2.2 Silicon Coupling Agent

Besides the optimization by annealing and hot pressing, the effect of silane coupling agent adding was studied. In order to achieve the expected coupling effect, a conclusion of theoretical calculation about the minimum amount 1 wt% was obtained before experiments, then $CaCu_3Ti_4O_{12}$-P(VDF-CTFE) composites modified with 0.5, 1, 2 and 5wt% silane coupling agent were prepared to verify the calculation. The testing results proved that the bridge-linked action of silane coupling agent can improve the uniformity thus optimize the dielectric response of the ceramic-polymer composites. The schematic of silane coupling agent reaction process is shown in **Figure 2-8**.

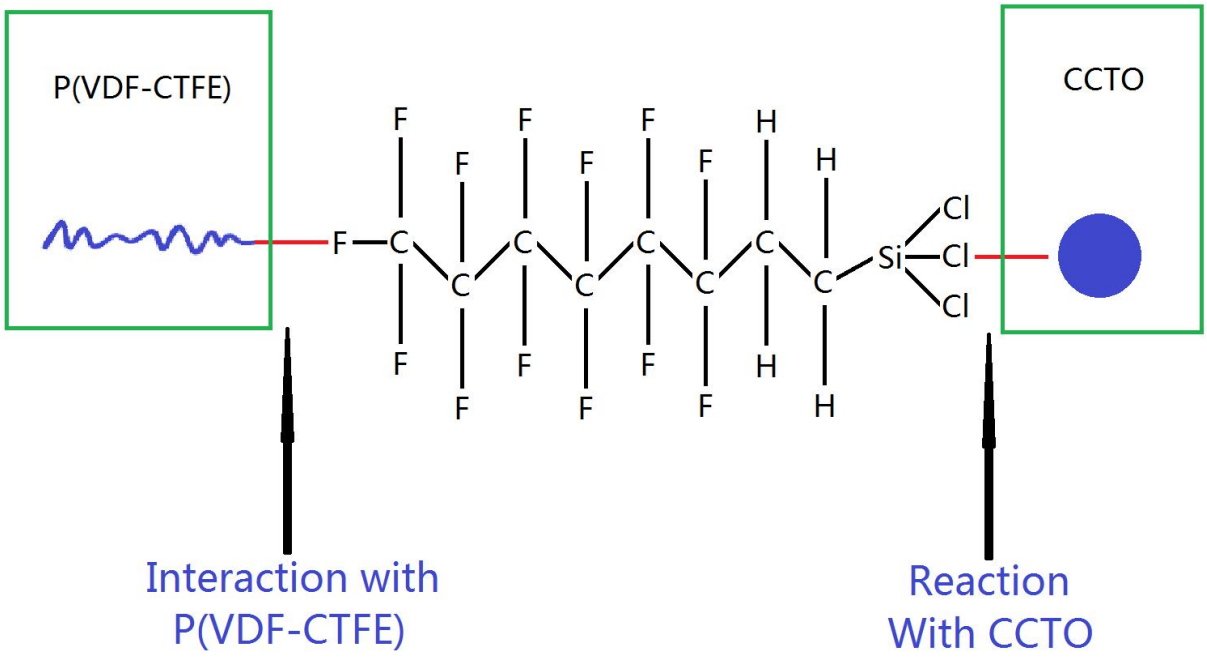

Figure 2-8 The schematic of silane coupling agent reaction process

2.4 Ceramic-Glass Composite Fabrication

2.4.1 Experimental Procedure

2.4.1.1 Preparation of $BaTiO_3$-SiO_2 Composites

In the preparation of glass-ceramic composite for dielectric energy storage study, a SiO_2 layer was coated on $BaTiO_3$ nanopowder by the Stöber process. The silica shell was obtained by utilizing the chemical reaction between tetraethylorthosilicate (TEOS, $SiO_4C_8H_{20}$) and H_2O in suspension environment, thus the thickness of shells on each $BaTiO_3$ particles can be adjusted by the addition of TEOS. The reaction between TEOS and H_2O was shown in **Figure 2-9**. 99% $BaTiO_3$ purchased from nanopowders US Research Nanomaterials, 28-30% Ammonia solution purchased from VWR International, 99.0% Tetraethyl orthosilicate, and 99.5% Acetic acid

purchased from Sigma-Aldrich were used as the raw material in the Stöber process. Following the chemical coating, hand granulation method was used to make the ceramic green body. For the thickness calculation of SiO_2 layer, $BaTiO_3$ nanopowders were assumed to be perfect sphere then react products attached to the surface of the powder.

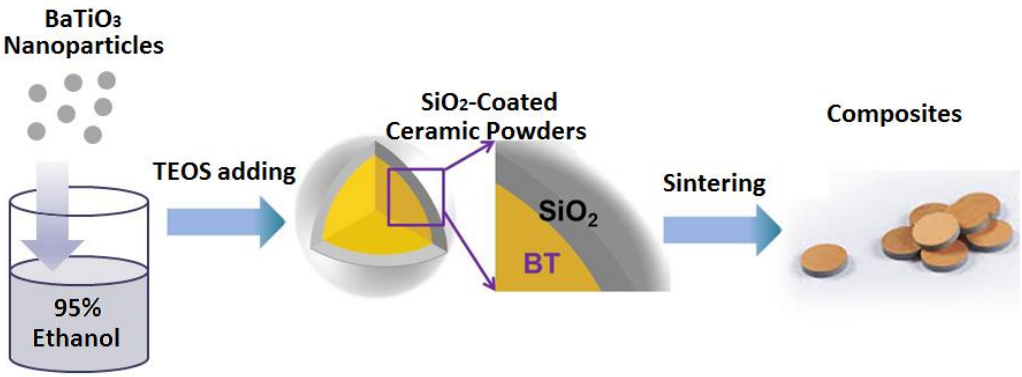

Figure 2-9 Schematic of the preparation of $BaTiO_3$-SiO_2 composites

After the SiO_2 layer coating and hand granulation, the ceramic sintering process was taken at high temperature. The temperature increasing rate was set up at a low level of 2 °C/min in this process. The as-prepared ceramic green bodies were put in a crucible, firstly heated up to 600°C and hold for 1 hour to remove PVA. The samples were further heated up to sintering temperatures 1170°C, 1200°C, and 1230°C and kept for 5 hours, then slowly cooled down to obtain the ceramics in the form of pellets. The 46100 Barnstead Thermolyne furnace used for sintering was shown in **Figure 2-10**, The final ceramic pellet is shown in **Figure 2-11**.

Figure 2-10 Image of 46100 Barnstead Thermolyne furnace

Figure 2-11 The final product SiO_2-$BaTiO_3$ composite pellet

2.4.1.2 CuO additive in SiO_2 Coated $BaTiO_3$ Composites

$BaTiO_3$ powders coated with 2.5 wt% SiO_2 without pretreatment were used to study the influence of CuO additive. Firstly, the $BaTiO_3$ powder was activated by acetic acid treatment and stabilized by magnetic stirring for 30 minutes and ultrasonic for 30 minutes at room temperature. Secondly, Tetraethylorthosilicate (TEOS) was added with magnetic stirring for 30 minutes and ultrasonic for 30 minutes. Thirdly, ammonia water was added drop by drop and PH of the suspension was controlled at about 9.5 by the amount of ammonia. After that, the suspension was heated to 40 °C and the reaction last for 5 hours to allow the hydrolysis and condensation of TEOS to form a SiO_2 coating layer on $BaTiO_3$ powders. The obtained powders were washed with ethanol and then dried at 120 °C overnight. Different content of CuO (0, 0.5, 1.0, 1.5, 2.0 ,2.5, 3.0 mol%) was added to the prepared composite powders by ball milling. Finally, the ceramic powders were mixed with 5% PVA binder and pressed to pills, then sintered by a conventional sintering method at 1230 °C.

2.4.1.3 Preparation of $Ba_{0.5}Sr_{0.5}TiO_3$-SiO_2 Composites

The $Ba_{0.5}Sr_{0.5}TiO_3$ coated with different contents of SiO_2 (0, 1, 2, 3, 4, 5 wt.%) composites were prepared by Stöber Method and conventional solid-state reaction process. Commercially available $Ba_{0.5}Sr_{0.5}TiO_3$ powders from nGimat Co. was used as the ceramic fillers. Firstly, the original BST powders were fully suspended in a mixed solution of ethanol and acetic by magnetic stirring and ultrasonic for 30 minutes. Tetraethylorthosilicate (TEOS) was added in

the suspension and the amount of TEOS was controlled to modify the SiO_2 weight ratio in the prepared powders. The pH value was adjusted to about 9.5 by adding ammonia water drop by drop. After that, the mixtures were heated to 40 °C and the reactions last for 5 hours under stirring. Finally, the coated powders were washed with ethanol and dried at 120 °C in the air overnight. The obtained powders were mixed with 5 wt.% polyvinyl alcohol (PVA) solution and pressed into pills. A conventional sintering process was used to fabricate composites. The pills were burned at 600 °C in air for 4 hours to remove the PVA binder and then sintered at 1230 °C.

2.4.2 Optimization

As introduced, the SiO_2-$BaTiO_3$ composite pellets with different concentrations 2.5, 5, 10, 15, and 20 wt% of SiO_2 glass composition were prepared by chemical coating and hand granulation for dielectric study. To obtain better dielectric properties, process effects including mixing method, sintering temperature, powder size, glass composition, and vacancies were studied for the improvement of the composite performance.

2.4.2.1 Pretreatment of $BaTiO_3$ Nanopowders

For the study on the influence of pretreatment conditions, the $BaTiO_3$ nanopowders with 99% purity and 200 nm average particle size from US Research Nanomaterials were pretreated under vacuum and reducing atmosphere respectively at different temperatures (850°C, 900°C, 950°C and 1000°C). For the vacuum pretreatment, the air pressure was controlled below 5×10^{-3} torr; for the reducing pretreatment, the 25% hydrogen forming atmosphere was used. The

pretreatment under low oxygen pressure or reduction environment leads to the formation of oxygen vacancies in varying degrees. Accordingly, the interaction between $BaTiO_3$ and oxygen in the gas phase can be described by the following formulas[34,35]:

$$O_o \leftrightarrow \frac{1}{2}O_2 + V_o^{\bullet} + e' \tag{2-1}$$

$$O_o \leftrightarrow \frac{1}{2}O_2 + V_o^{\bullet\bullet} + 2e' \tag{2-2}$$

After pretreatment, the vacancies introduced powders were used as the raw materials for the preparation of glass-ceramic composites.

2.4.2.2 Sintering Temperature

The ceramic green bodies were prepared by the chemical coating and hand granulation method. In the process of sintering, the temperature is the most important factor that determines the performance of the final product. Therefore, during the sintering process, different temperatures were used to find the influence. The as-prepared ceramic green bodies were put in a crucible, firstly heated up to 600 °C and hold for 1 hour to remove PVA. The samples were further heated up to sintering temperatures 1170 °C, 1200 °C, and 1230 °C and kept for 5 hours, then slowly cooled down to obtain the ceramics in the form of pellets. For obtaining the dense ceramic-glass composite, temperature increasing was set up with a slow rate of 2 °C/min, then slowly cooled down. The temperature vs. time of the sintering process was shown in **Figure 2-12**.

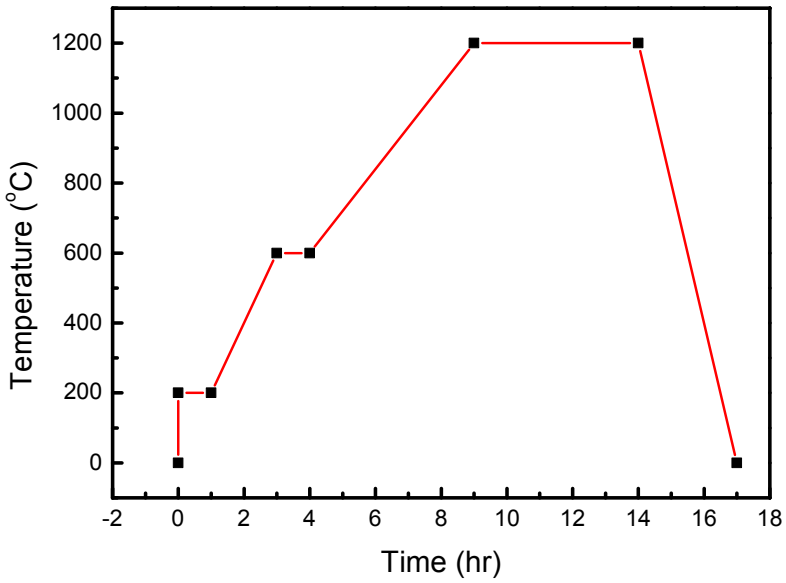

Figure 2-12 The sintering steps of composite samples

2.4.2.3 Spark Plasma Sintering

Spark plasma sintering (SPS) is a sintering technique with a pulsed DC current directly passes through the graphite die as well as the powder compacts[36]. In SPS, the heat generation is internal with a very high heating or cooling rate (up to 1000 K/min), which provides the power to densification of powder compacts and results in a near theoretical density at lower sintering temperature[37]. For the study of the influence by different sintering method on ceramic-glass composites, the $BaTiO_3$-SiO_2, $BaTiO_3$-ZrO_2, and $BaTiO_3$-Al_2O_3 composites were created by spark plasma sintering (SPS) from NASA. The glass-coated $BaTiO_3$ nanopowders with different particle size, glass content and preparing methods were jointly prepared by Auburn University and NASA; The resulting composite pellets were obtained by SPS with different sintering and

annealing temperatures then sent to Auburn University. Due to the large thicknesses, all of the samples were cut from the cross sections to get 2 or 3 pieces and polished for further processing. As an example, the three different layers obtained from one of the samples were shown in **Figure 2-13**.

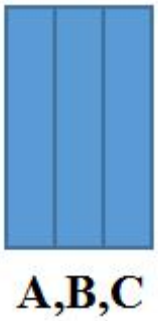

Figure 2-13 Small pieces of ceramic from the part of original sample

Due to the reason of protecting ceramic sample, the samples have been mounted in the polymer (PMMA) firstly. The sample and polymer matrix have been cut from the cross-section to obtain thinner pieces of ceramics suitable for impedance measurements. After cutting, good pieces of each sample have been chosen to be polished to get smooth surfaces. For the characterization of the dielectric properties of the sample, the small pieces of samples were sputtered with gold on top and bottom surfaces as electrodes. To obtain a uniform coating of gold for the electrode, four times of 30-second coating of each side is necessary, which resulted in a gold layer with a thickness of 40-60 nm.

2.5 Characterization Methods

2.5.1 Crystalline Structure Determination

X-ray diffraction (XRD) method has been widely used to characterize the structures of different materials including ceramics and polymers. The results of XRD can provide important information such as phases, crystallinity, orientation, etc. Therefore, the prepared composites were characterized by XRD. The X-ray diffraction was scanned at 40 kV and 20 mA and diffracted X-ray was measured between 10 to 80°. A scanning speed of 5°/min and a sampling interval of 0.05° were set up for this work. The obtained diffraction pattern was compared to confirm the presence of the phase in the materials by matching their unique peaks, then the d-spacing can be calculated by Bragg's law.

2.5.2 Microstructure Analysis

As a type of electron microscope that images the sample surface with a high-energy beam of electrons, Scanning Electron Microscopy (SEM) was used for the structures analysis for composites. By interacting with the atoms, the information such as the surface morphology and composition distribution could be recorded. Signals including secondary electrons, backscattered electrons, characteristic X-ray, cathodoluminescence, and transmitted electrons have been collected in this process. According to those signals, high-resolution images of the sample surface can be obtained; other important information including grain size and phase distribution can also be obtained.

For SEM observation, samples obtained from the fabrication process were stuck on conductive tape and then gold coating by using a Pelco SC-6 sputter coater, which was shown in **Figure 2-14**. JEOL JSM 7000F FE-SEM was operated at 20 kV to take the secondary electron images at high magnifications, and compositional analysis was completed using the Oxford

Instruments Electron Dispersive X-ray Spectroscopy (EDS) system. The SEM and EDS system was shown in **Figure 2-15**.

Figure 2-14 The Pelco SC-6 sputter used for gold coating

Figure 2-15 The JEOL JSM 7000F FE-SEM Scanning Electron Microscopy (SEM) used in the microstructure determination of composites

2.5.3 Dielectric Properties Analysis

For the characterization of the dielectric properties of the composites, the samples were abraded to reduce the thickness and polished to obtain smooth surfaces, then sputtered with gold on both surfaces as electrodes. The dielectric properties of the samples were characterized by Agilent 4294A impedance analyzer from 100 Hz to 1 MHz using the Cp~D function. The image of 4294A impedance analyzer was shown in **Figure 2-16**. The permittivity of the composites was calculated from the capacitance using the parallel plate mode. This experiment was calibrated each time to eliminate any background noise. In order to characterize the temperature

dependence of the dielectric response, samples were held with a home-made measurement probe and were then heated using a Fisher Isotemp 800 Series Programmable oven.

Figure 2-16 The image of Agilent 4294A impedance analyzer

2.5.4 Energy Density Calculation

For the measurement and calculation of energy density for dielectric materials, the Precision-LC100 system with H.V. Supply Amplifier/Controller was used to test the breakdown field and P-E loop of composite samples. In the testing, the composite thin film was put into the holder and soaked in silicone oil then the drive voltage was increased continuously until sample breakdown with a test frequency of 10 Hz. During the process, the P-E loop and breakdown field

for each drive voltage was obtained, which was used in the energy density calculation[25-28]. The energy density of a dielectric is defined as:

$$W_E = \int_0^{D_{max}} EdD \tag{2-3}$$

where W_E are energy storage density (J/m^3), E and D are the electric field and electric displacement, respectively. For the dielectrics with high permittivity, D can be replaced by the polarization P, the above equation can be changed as follows:

$$W_E = \int_0^{P_{max}} EdP \tag{2-4}$$

Based on Equation 2-4, the integral method was used to calculate the energy density from P-E loop obtained from different composites.

Chapter 3

Conductor-Polymer Composite Using 2-D Conductive Fillers

In this chapter, the conductor-polymer nanocomposites with a high dielectric constant and a low percolation threshold was prepared by using the MXenes 2-D material $Ti_3C_2T_X$ nanosheets as the 2-D conductive filler and P(VDF-TrFE) 70/30 as the polymer matrix by a unique process developed recently by combining the solution casting and hot pressing. The highest dielectric constant of these nanocomposites was found to be up to more than 2100 and a high dielectric loss of 10, simultaneously shown a low percolation threshold which is smaller than 12 wt%. Therefore, the composites are showing the attraction in the applications including pulse power generation, high permittivity capacitors, wearable electronics and other electric systems.

3.1 Introduction

Compare with the dielectric-dielectric composites, conductor-dielectric composites were proved to be the unique materials which can exhibit high dielectric constant by a relatively small amount of conductor fillers[1-4]. According to the discussion in Chapter 1, for the various of conductor-dielectric composites, the study has focused on the dependence of the dielectric behavior on the geometry, shape, size, and distribution of the conducting fillers[1]. Therefore, except for conventional spherical fillers, 2-D fillers have been used in the fabrication of polymer-based composites. Among them, a family of 2-D materials consisting of transition metal carbides,

nitrides, and carbonitrides, were produced by selectively etching layers from their corresponding 3-D MAX phases, known as MXenes[5]. The electrodes made up of the conductive carbide flakes produced by sonicating the MXenes nanosheets exhibit gravimetric capacitances and show exceptional promise in energy storage systems as flexible electrode materials[6,7]. Considering the excellent properties of MXenes materials including high conductivity and 2-D structure which were introduced in Chapter 2, a high dielectric constant and low percolation threshold were expected in MXenes-polymer composites. For this purpose, one of the members of MXenes family, $Ti_3C_2T_X$ nanosheets were used as the 2-D fillers for the fabrication of polymer composites based on P(VDF-TrFE) copolymer.

3.2 Samples

In the preparation of composites, P(VDF-TrFE) 70/30 mol.% copolymer from Solvey was utilized as the polymer matrix; The different weight concentrations (2, 4, 6, 8, 10, 12, 14 wt%) of $Ti_3C_2T_X$ were added into P(VDF-TrFE) matrix as fillers. The composites were obtained by the solution casting and hot pressing process as introduced in Chapter 2. In the hot pressing, regarding the configuration of the stack, the as-cast composite films were labeled as “P” for the bottom side with a thin polymer layer and “C” for the top side. The as-cast films were released from glass plates carefully and stacked in four layers then hot-pressed with a configuration of PCCP, in which the “P” side of one as-cast film is in contact with the “P” side of the next as-cast film, to obtain the uniform and denser microstructure of composites[8]. The summarized process

of composite films preparation was shown in **Figure 3-1**. The conditions of sample preparation and experiments are summarized in **Table 3-1**.

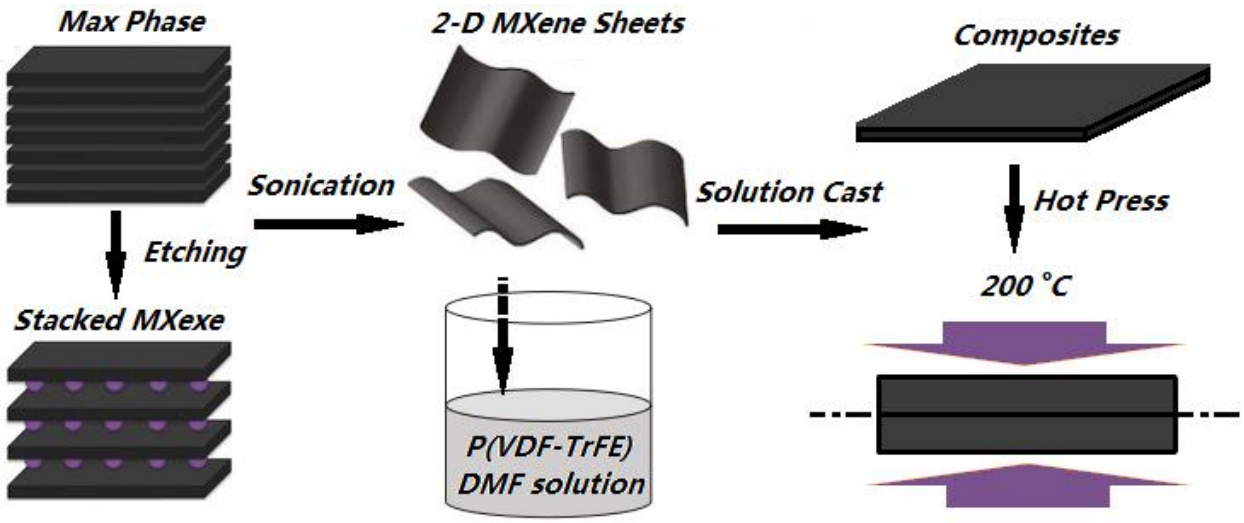

Figure 3-1 Schematic of the preparation of $Ti_3C_2T_X$-P(VDF-TrFE) films

Table 3-1 Conditions of the preparation and experiments

Conditions	Value
Filler Contents	0, 0.25, 0.5, 1, 1.5, 2, 4, 6, 8, 10, 12, and 14 wt.%
Coupling Agent Contents	0, 0.5, 1, 1.5, and 2 wt.%
Type of Coupling Agents	2
Casting Temperature	70 °C
Annealing Temperature	140 °C
Hot Pressing Temperature	200 °C
Temperature Dependency	-50 ~ 130 °C
Testing Frequency	100 Hz ~ 1 MHz

3.3 Structure and Morphology Characterization

3.3.1 X-ray Diffraction

The thicknesses of composite thin films were about 40-80 μm depending on the $Ti_3C_2T_X$ filler concentration. For the characterization of the crystal structure, the X-ray diffraction patterns of composite thin films with different filler contents were recorded and shown in **Figure 3-2**. From the XRD patterns of pure polymers films as well nanocomposites with 0.25, 0.5, 1, 1.5, 2, 4, 8 and 12 wt% $Ti_3C_2T_X$ filler contents in **Figure 3-2 (a)**, P(VDF-TrFE) polymer without fillers are partially crystallized to show the clear peaks after the annealing process with a suitable temperature (140 °C), the prominent peak in XRD pattern of the fabricated $Ti_3C_2T_X$-P(VDF-TrFE) composites is from the (200)/(110) of the crystalline phase, which shows that the copolymer is mostly in its ferroelectric β phases[9]. With $Ti_3C_2T_X$ fillers added, the obvious intensity increase was found on the main peak of polymer crystal, which shown the crystallinity increase by mixing. It is clear that no new peaks appeared due to the new compound, which shows the good state of 2-D filler random dispersion. Interestingly, it has been observed that with the increasing $Ti_3C_2T_X$ filler content up to 1.5 wt%, these peaks are becoming sharper and stronger, suggesting the higher crystallinity of the copolymer in the composite films. However, the crystallinity decreases at higher filler contents as the peak's intensity decreases for the composites with 1.5 to 12 wt% of the $Ti_3C_2T_X$ content. In contrast, The 2θ of (200)/(110) peak are firstly decreasing in the filler content range of 0 to 8 wt% and then increases from 8 to 12 wt%. The trend of intensity and peak location as the functions of $Ti_3C_2T_X$ filler content was shown in **Figure 3-2 (b)**.

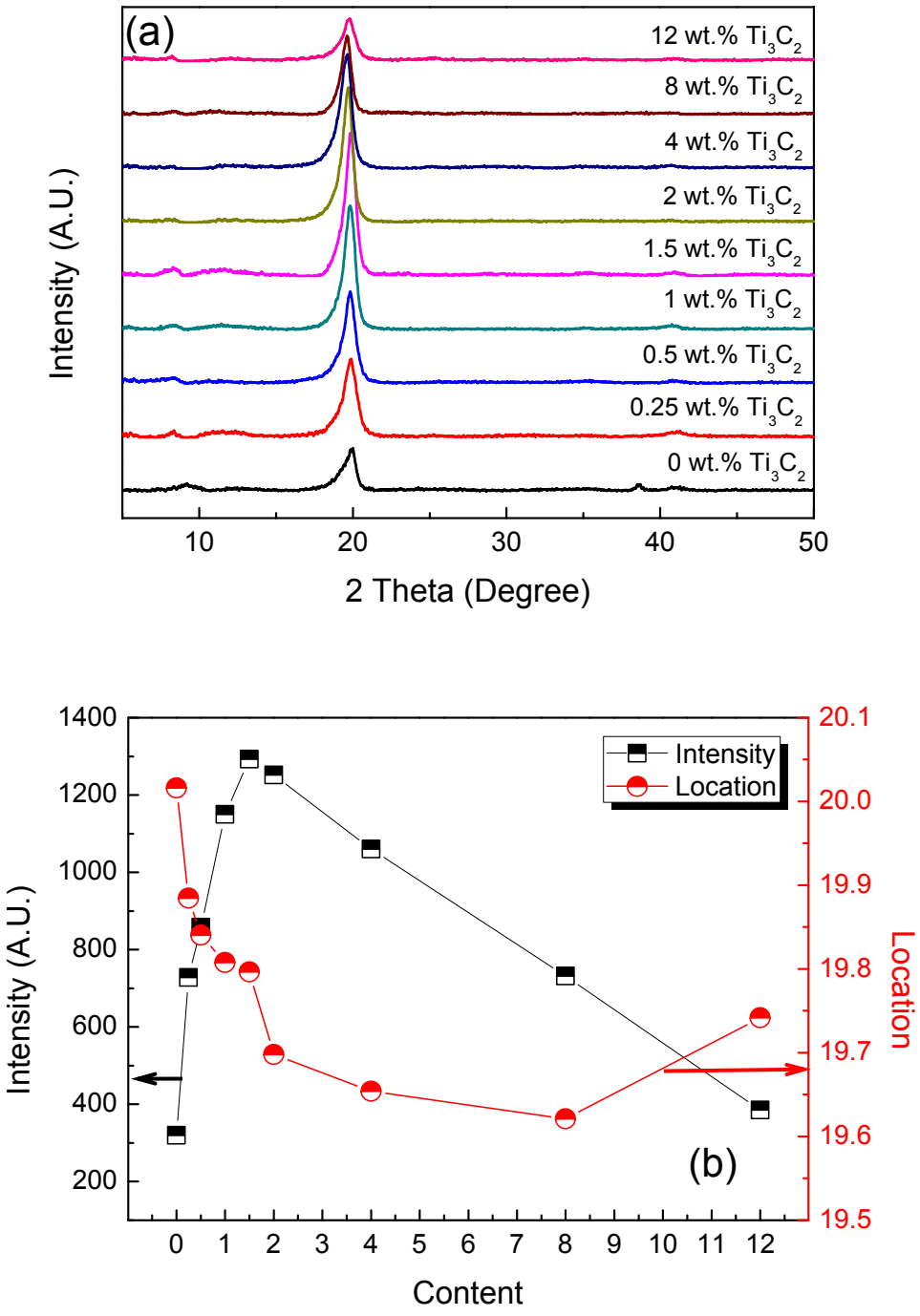

Figure 3-2 (a) The XRD patterns of $Ti_3C_2T_X$-P(VDF-TrFE) composite films with different filler contents and (b) The intensity and peak location as the functions of filler content

3.3.2 Differential Scanning Calorimetry

The change of crystallinity in composites was also confirmed by differential scanning calorimetry (DSC) and shown in **Figure 3-3**, in which two peaks were found on the curve are correspond to phase transition and melting. The obvious changes of peak shape and position are reflecting the difference in crystallinity and melting temperatures. For comparison, the peak area and temperature of both peaks were shown in **Figure 3-4 (a)** and **(b)**, respectively. By considering both of the results, it can be concluded that the addition of $Ti_3C_2T_X$ fillers will influence both crystallinity and melting temperature; among them, the calculated crystallinity increasing may partly due to the sharply amplified increase of XRD peak intensity, which was possibly from the titanium in fillers.

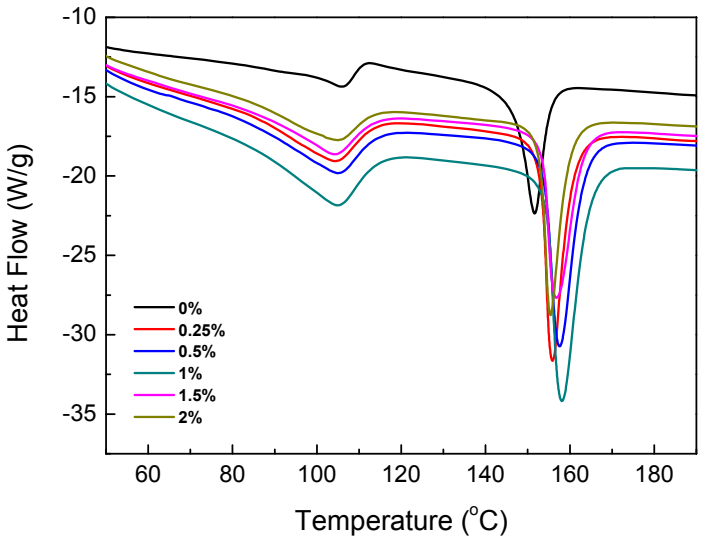

Figure 3-3 The DSC patterns of $Ti_3C_2T_X$-P(VDF-TrFE) films with selected filler contents (0, 0.25, 0.5, 1, 1.5 and 2 wt.%)

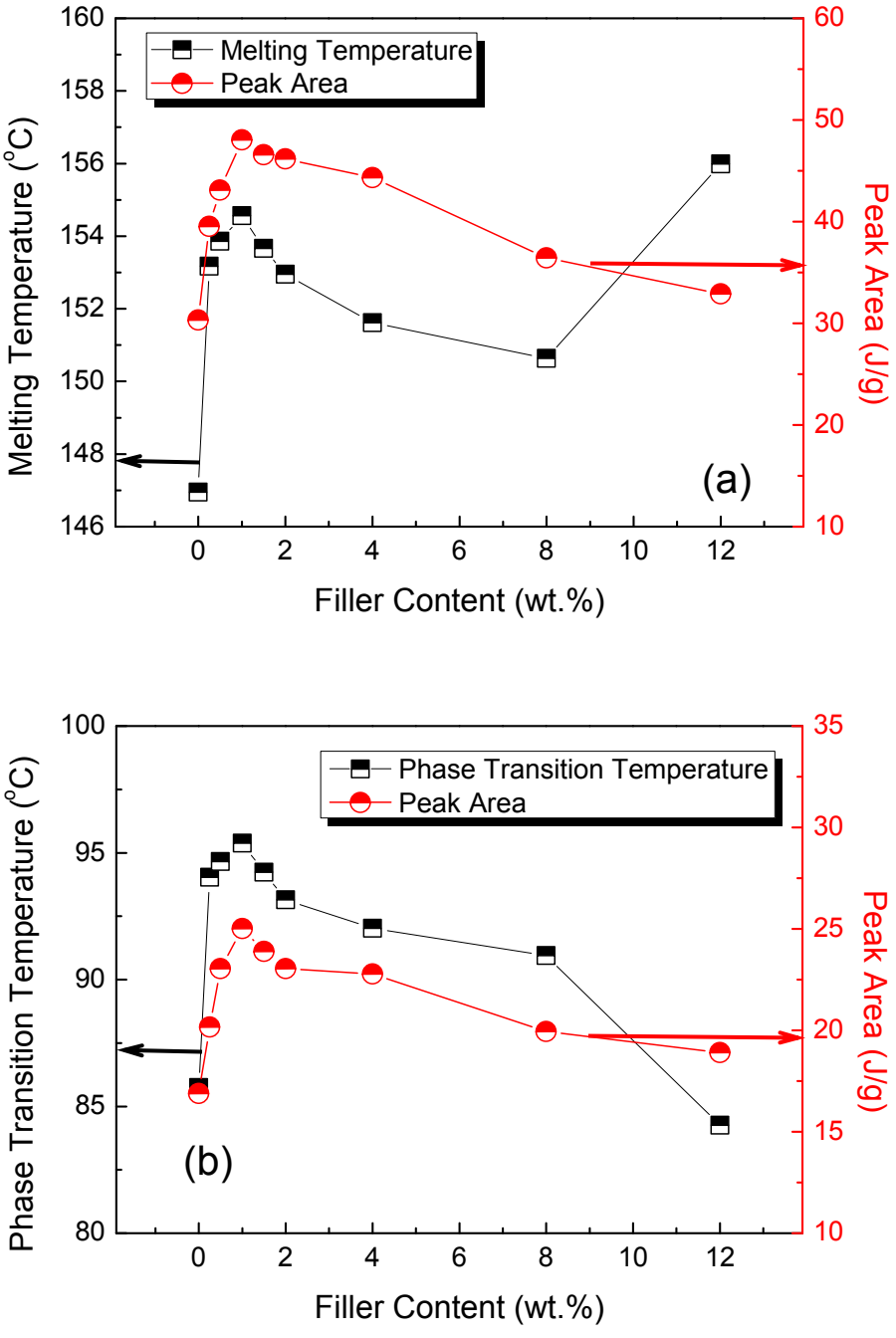

Figure 3-4 The peak area and temperature of and (a) melting peaks and (b) phase transition peaks recorded from the DSC patterns as a function of the filler contents

3.3.3 Scanning Electron Microscopy

By the scanning electron microscopy (SEM) observation, the distribution and morphology of composites were recorded and the results are given in **Figure 3-5**. As shown in **Figure 3-5 (a)**, the $Ti_3C_2T_X$ 2-D sheets with a large width and very small thickness are loosely stacked in parallel, which shown the well-separated state of the 2-D material. When the 2-D material was added in a relatively dense polymer matrix which shown in **Figure 3-5 (b)**, with the two-step process of solution casting and hot pressing, the samples were expected to show a uniform microstructure. As a result of verification, the images of 10 wt% $Ti_3C_2T_X$-P(VDF-TrFE) composites after hot pressing are presented. It can be seen from the top of the composite thin film in **Figure 3-5 (c)** and **(d)**, the surface of the composite is dense and smooth, fillers were clearly random distributed and no obvious defect could be found. From the cross-section in **Figure 3-5 (e)** and **(f)**, the good distribution of fillers can be proved according to the good uniformity in the whole range of the sample.

Figure 3-5 (a), The SEM images $Ti_3C_2T_X$ 2-D sheets; (b), the SEM images of PVDF-TrFE top surface; (c) and (d), The top surface of 10 wt.% composite film; (e) and (f), The uniform microstructure from cross section of 10 wt.% composite film

3.3.4 Fourier Transform Infrared Spectroscopy

For the study of further insights into chemical and physical interactions that dictate the formation of the composites, the composition of various samples was studied by Fourier transform infrared spectroscopy (FTIR) and the results were shown in **Figure 3-6**. The pure P(VDF-TrFE) polymer and composites have shown similar peaks of FTIR spectra. As an example, the comparison of FTIR spectra for pure P(VDF-TrFE) and composite film with 1 wt% $Ti_3C_2T_X$ fillers were shown in **Figure 3-6 (a)**, for both of samples the β-phase peaks at 1275 and 840 cm^{-1}[10] can be clearly distinguished, which is an evidence of the existence of β-phase that consistent with XRD patterns. Compare the results between pure polymer and composites, the position of peaks of them are almost identical, which indicates there is no obvious chemical reaction between filler and polymer matrix. From the contradistinction of composites with $Ti_3C_2T_X$ and mixture solution in a broader range as shown in **Figure 3-6 (b)**, the spectra of mixture solution have contained all the peaks of 2D material, which is different with the polymer-based composite. Due to the polymers were dissolved, the β-phase peaks at 1275 and 840 cm^{-1} were disappeared from the spectra of the mixture; the peaks of CH_3 at 1456 and 2853 cm^{-1} cannot be found from the spectra of composite because of the evaporation of DMF[11]. Consider the reasonable peak location from both P(VDF-TrFE) and $Ti_3C_2T_X$ in the mixture solution, there is no obvious evidence that interactions exist between polymer matrix and fillers.

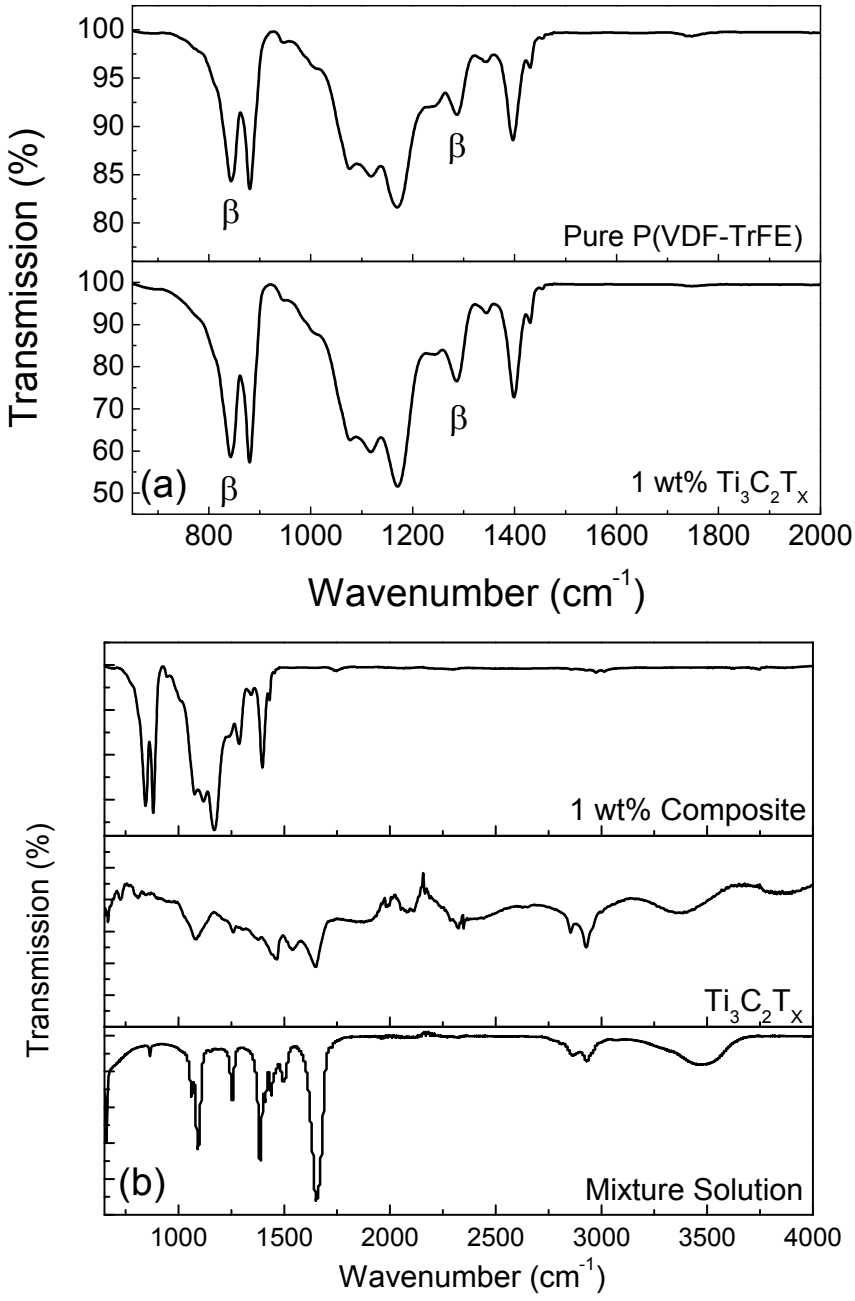

Figure 3-6 Fourier transform infrared spectra (FTIR) of (a) Pure P(VDF-TrFE) polymer and composite film with 1 wt.% 2D fillers; (b) The comparison of composite film with 1 wt% $Ti_3C_2T_X$ fillers, pure $Ti_3C_2T_X$ in solid state, and mixture solution of polymer and fillers

For the convenience of comparison between the pure polymer and the composite, the position and transmission value of all peaks were identified and shown in **Figure 3-7**. For all of the peaks, the transmission decreased when 1 wt.% of $Ti_3C_2T_X$ filler was added due to the feature of the filling material. Regarding the position of peaks, most of the peaks observed from the FTIR for P(VDF-TrFE) didn't change after the adding of fillers. An only changed peak was found at 1231 cm^{-1} of the FTIR for P(VDF-TrFE) and moved to 1243 cm^{-1} for composites with 1 wt.% of $Ti_3C_2T_X$. This peak does not come from any functioning group of P(VDF-TrFE) polymer. Therefore, a weak bond exists in this polymer matrix, and the shift of peak position may due to the modification of the bond by the filler addition[11].

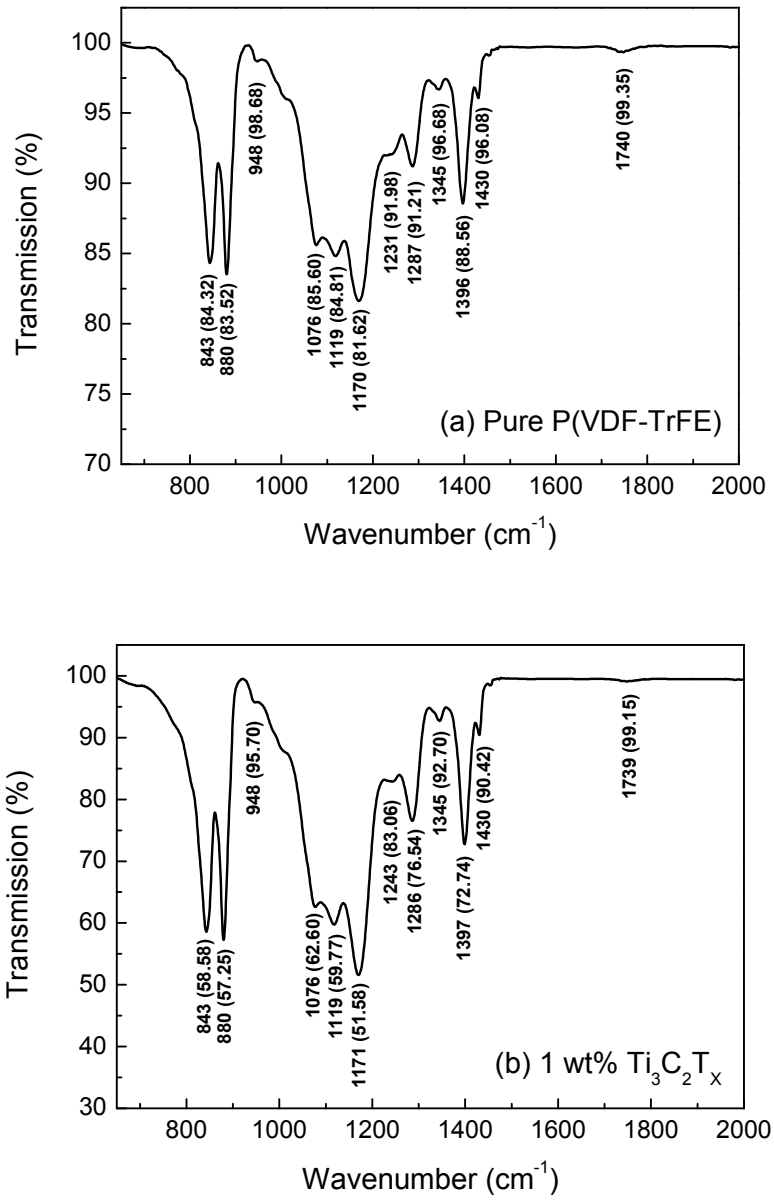

Figure 3-7 The detailed peak position and transmission value of Fourier transform infrared spectra (FTIR) of (a) Pure P(VDF-TrFE) polymer and (b) composite film with 1 wt.% 2D fillers

3.4 Dielectric Properties

3.4.1 Frequency Dependency of Dielectric Properties at Room Temperature

The frequency dependence of the dielectric constant, loss and electrical conductivity of $Ti_3C_2T_X$-P(VDF-TrFE) composites at room temperature are shown in **Figure 3-8**. In the whole range of frequency, an obvious increase of dielectric constant was detected with the increasing content of $Ti_3C_2T_X$ fillers before 10 wt%; With the content of filler further increases, the dielectric constant at low frequency start to decrease for the percolation phenomenon. A high dielectric constant (1573 at 100 Hz and 730 at 1 kHz) and a loss (0.8 at 100 Hz and 0.4 at 1 kHz) were found in the composites with 10 wt% of $Ti_3C_2T_X$ sheets. The dielectric constant of composites with a low filler content (<10 wt%) shown a similar frequency dependence with the pure polymer, which is an evidence for the frequency dependence of the dielectric constant is mainly dominated by the polymer matrix. However, as the filler content increased to a higher content of 12 wt%, the dielectric behavior starts to change by increasing the dielectric constant in the high-frequency range of 100k-1M Hz. When $Ti_3C_2T_X$ content reaches 14 wt%, the dielectric behavior became more smooth and showing a weak frequency dependence.

Based on the data shown in **Figure 3-8**, the inclusion of conductive fillers not only leads to a high dielectric constant but also results in a high dielectric loss and conductivity increase. From **Figure 3-8 (c)**, it can be seen that the conductivity of composites rapidly increases in low frequency with the whole $Ti_3C_2T_X$ content range. In the low content range, the conductivity induced by $Ti_3C_2T_X$ fillers are considered as main part of the loss in the composites and makes the loss increase; As the content of conductive particles is close to the percolation threshold the particles are considered very close to each other, a higher conductivity will be obtained

simultaneously. When the polymer layers between neighboring particles are too thin to withstand the local electric field, the leakage current became the main reason for high dielectric loss.

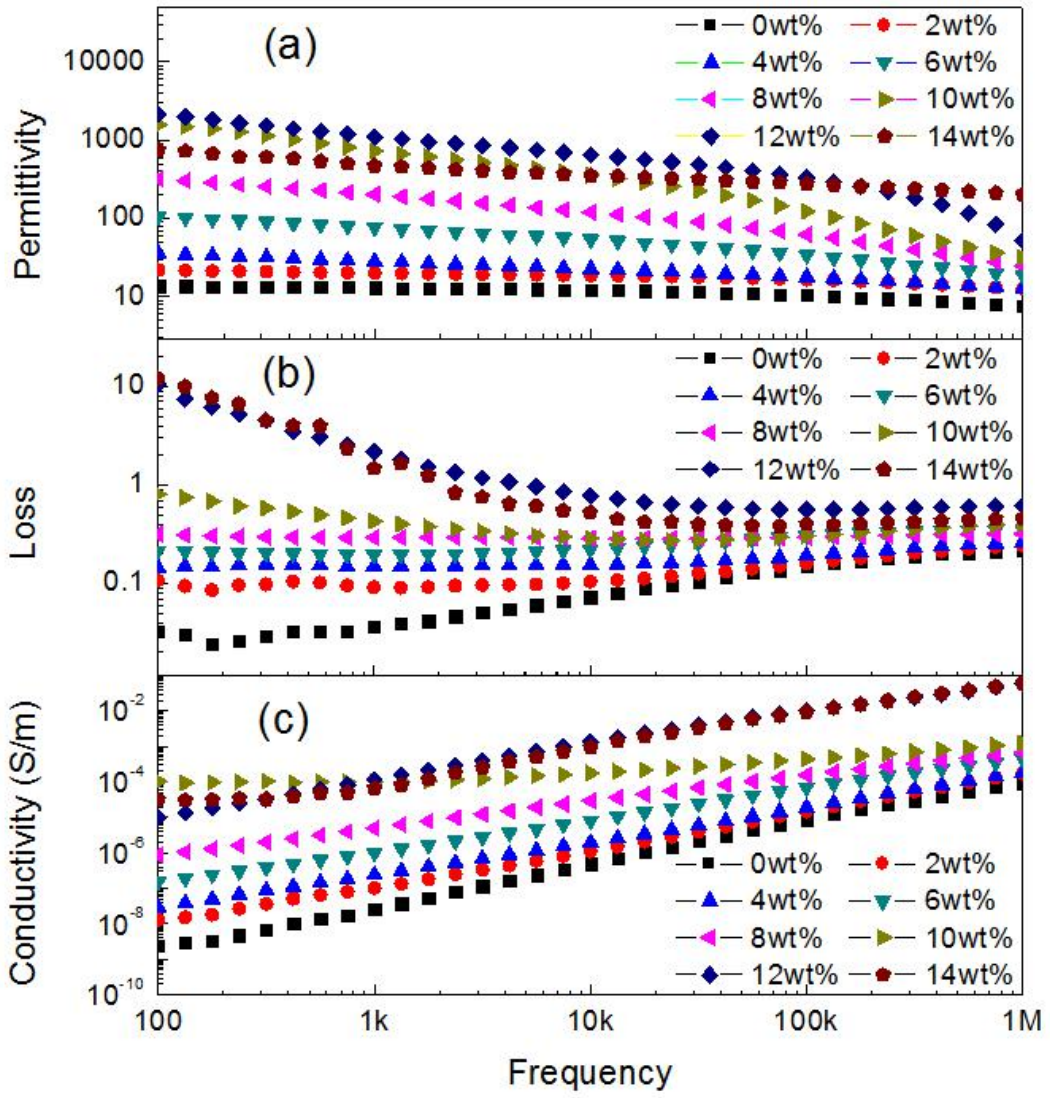

Figure 3-8 The dielectric/electric properties including (a) dielectric constant, (b) dielectric loss, and (c) conductivity against different filler contents

3.4.2 Temperature Dependency of Dielectric Properties

The temperature dependence of the dielectric properties of composites with different filler contents at 1 kHz, 10 kHz, 100 kHz and 1 MHz are characterized in the range from -50 °C to 130 °C and the results were given in **Figure 3-9**. Obviously, the dielectric constant increase with the increasing filler concentration in the whole temperature range. For the composites with 12 wt% $Ti_3C_2T_X$, a dielectric constant of more than 2200 with a loss as low as 2.07 was recorded at 1000 Hz when the temperature reaches 130 °C.

For the pure matrix polymer, there are two characteristic temperatures as the glass transition temperature T_g and the ferroelectric phase transition temperature T_f. As shown in **Figure 3-9 (a)**, the glass transition introduced relaxation process at -20 °C to 20 °C, at which there is a step of dielectric constant associated with loss peak; The T_f was found near 110 °C, at which there are sharp peaks on both dielectric constant and loss. Due to the dominance of polymer matrix on the dielectric properties, the composites with the low filler contents (<8 wt%) exhibit a similar typical relaxation process around T_g, as well as the peaks around T_f. However, not only similarities but obvious differences were also found between them. With the filler content increasing, the peaks around T_g are becoming weaker; ferroelectric phase transition peaks around T_f are becoming wider and relocate at higher temperatures; for the composites with high contents (>10 wt%), the glass transition-related peaks no longer exist. From the change of trend for dielectric-temperatures relationship for different filler content, it can be concluded that: 1. With the increase of $Ti_3C_2T_X$ 2-D filler concentration, the main mechanism of dielectric is changing from the relaxation-dominated to percolation-dominated; and 2. The weaker ferroelectric phase transition peaks will be obtained by the adding of $Ti_3C_2T_X$ 2-D fillers, which

is possibly due to the lower crystallinity and smaller crystals in the composites[12]. Overall, by adding the $Ti_3C_2T_X$ 2-D fillers to P(VDF-TrFE) matrix with a content close to percolation threshold, the dielectric stability with changing temperature can be improved.

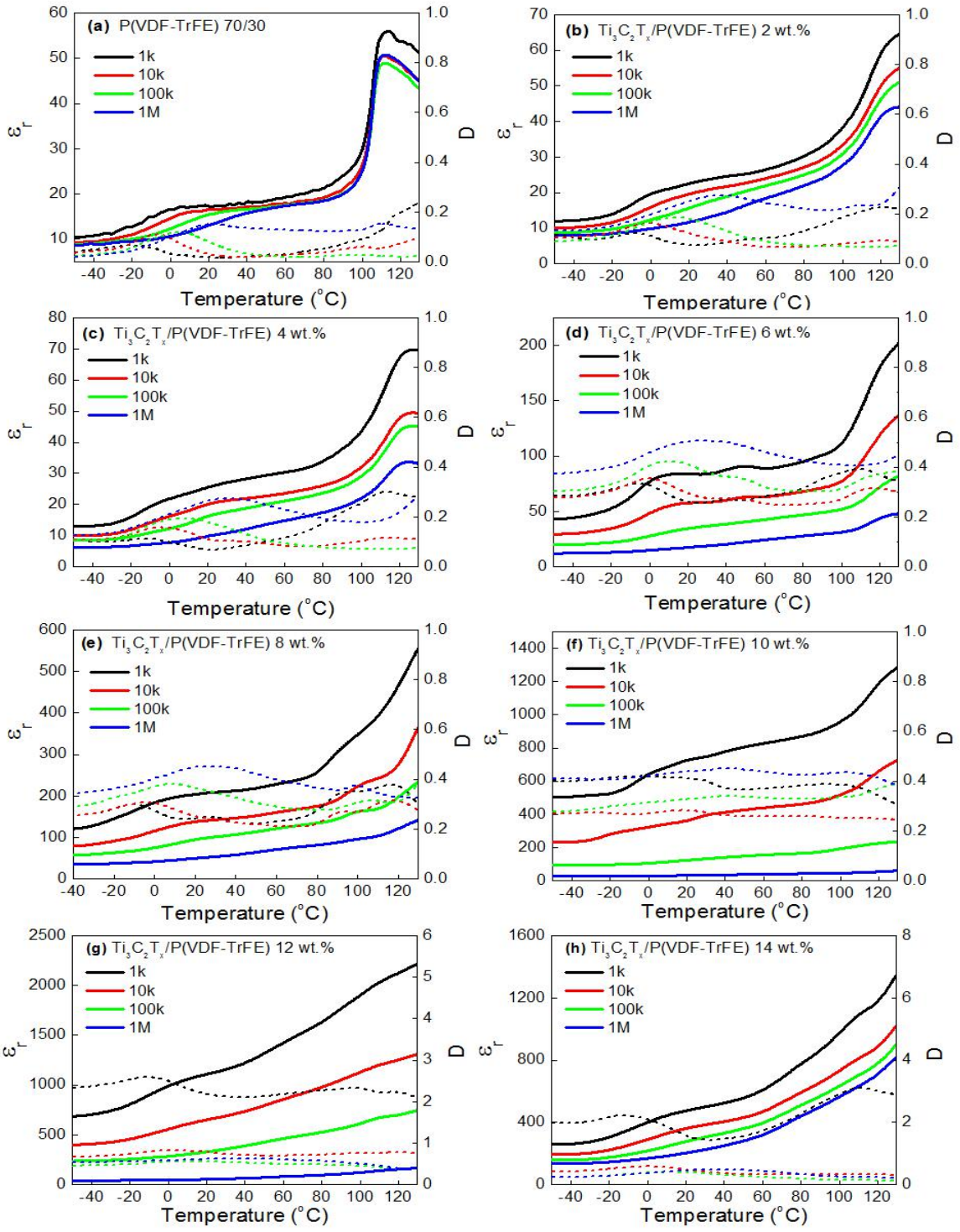

Figure 3-9 The temperature dependence of dielectric constant which was plotted by solid lines and dielectric loss which were plotted by dotted lines with 0, 2, 4, 6, 8, 10, 12 and 14 wt% filler

3.4.3 Dielectric Properties at High Electric Fields

Although the dielectric constants of composites are sharply increasing with the adding of 2D conductive fillers, their high conductivity lead to a very low breakdown strength. For the samples with the filler contents equal or above 4 wt%, the large leakage currents under DC were detected. Therefore, the composites with high filler contents have very low energy storage densities. Compare with the properties of these samples, the breakdown strength of composites with low content of fillers are close to the one of pure polymer, which leads to the much higher energy storage density. For the calculation of energy density, the P-E loops of composites with low filler contents (0.25, 0.5, 1, 1.5 and 2 wt%) were recorded. From the P-E loops of composites with different filler contents, as shown in **Figure 3-10 (a)**, the sample with 1.5 wt% $Ti_3C_2T_X$ have shown a maximum polarization of 13.8 $\mu C/cm^2$ under the electric field of 2800 kV/cm. From the P-E loops, the maximum energy storage density calculated by P-E loop is 5.66 J/cm^3 from the composite with 1.5 wt% $Ti_3C_2T_X$ filler. The P-E loops of the sample which have largest energy storage density (1.5 wt%) were shown in **Figure 3-10 (b)**. As the summary, the properties of composites with low filler contents (0.25, 0.5, 1, 1.5 and 2 wt%) were shown in **Table 3-2**, the trend of saturation polarization, remaining polarization, breakdown strength and energy density of composites with changing filler contents were plotted in **Figure 3-11**.

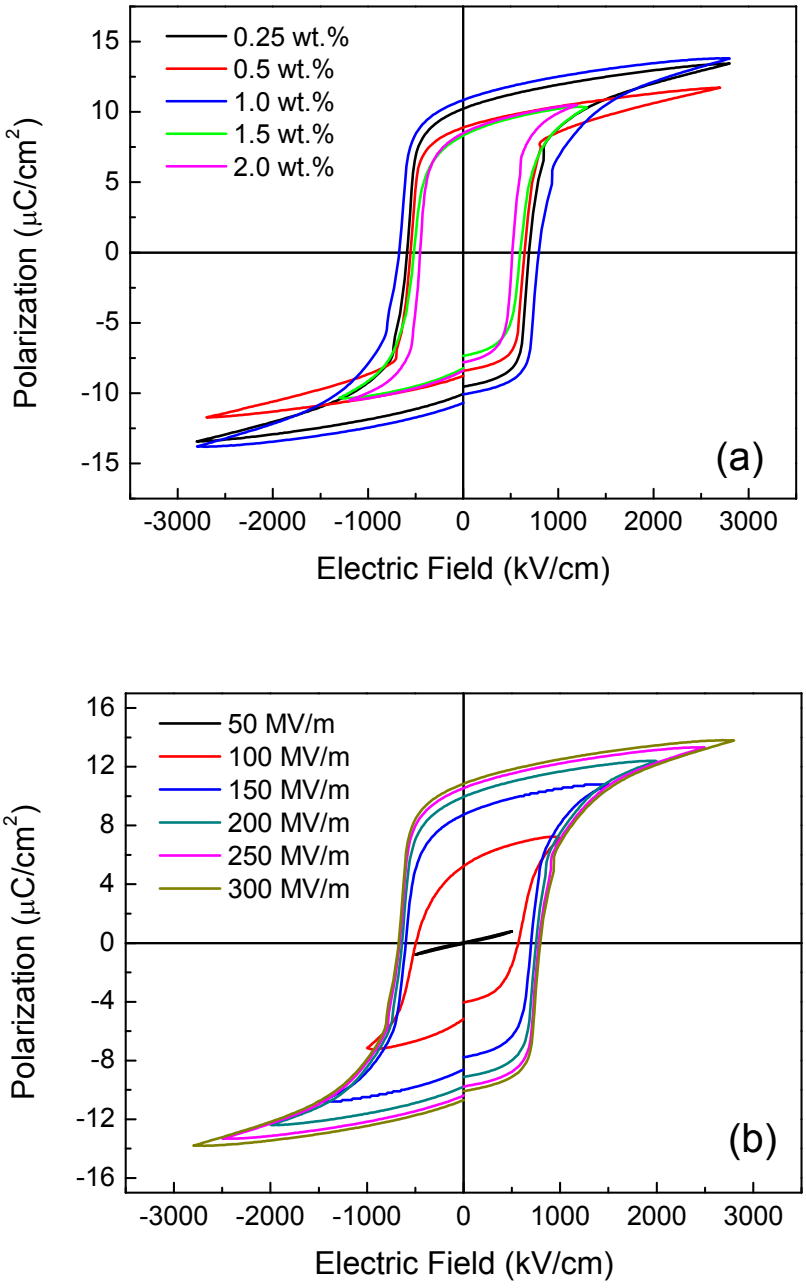

Figure 3-10 (a) The P-E loops of composites with different filler contents at the maximum electric applied and (b) The P-E loops of the sample with 1.0 wt% $Ti_3C_2T_X$ filler under different electric fields until breakdown

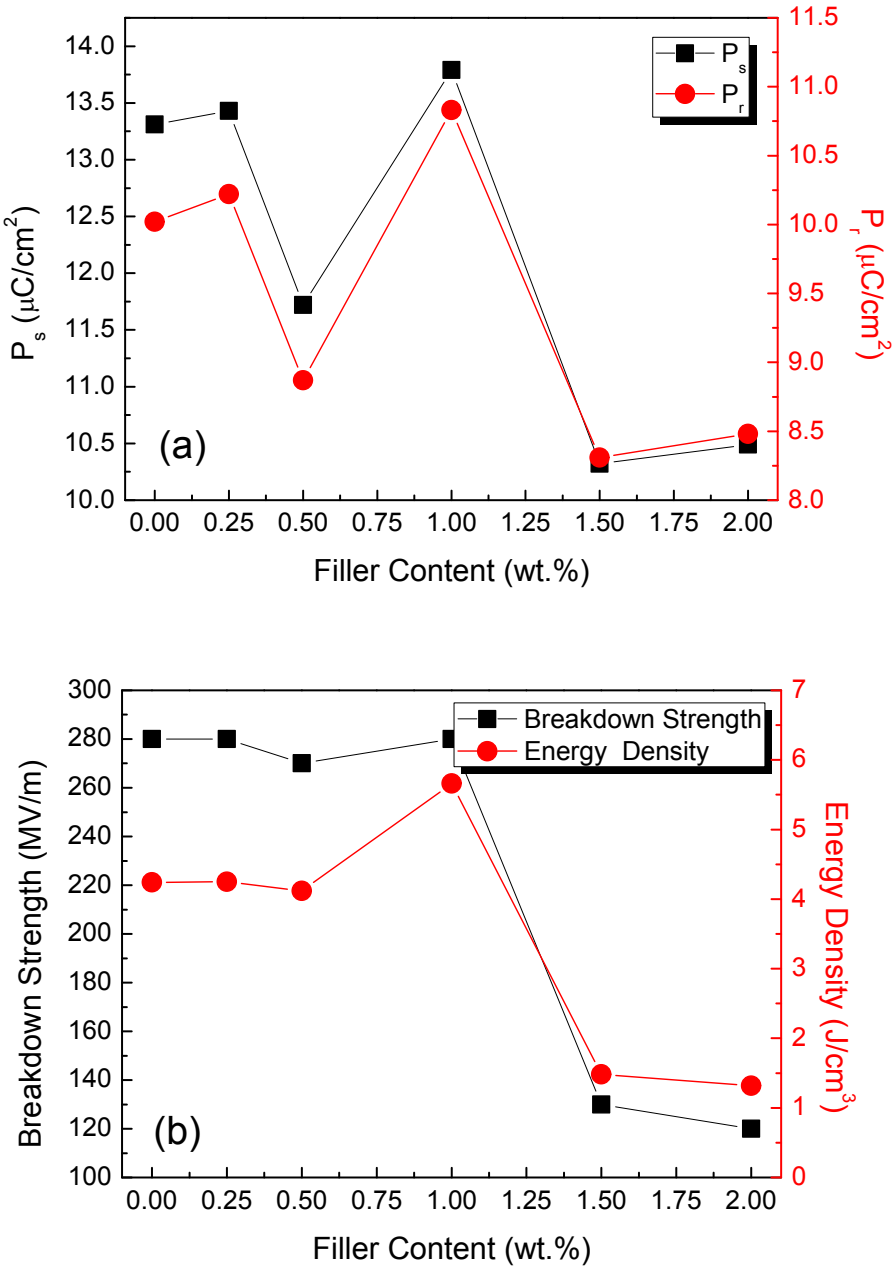

Figure 3-11 (a) The saturation polarization (Ps) and remaining polarization (Pr) of composites with different filler contents at the maximum electric applied and (b) The breakdown strength and energy density of the composites

Table 3-2 The summarized properties of composites with low filler contents

Filler Content	ε_r	tanδ	E_b (MV/m)	E_c (MV/m)	P_s (μC/cm^2)	P_r (μC/cm^2)	Effectiveness	W_E (J/cm^3)
0.00%	13	0.03243	280	59	13.31	10.02	22.76%	4.24
0.25%	14	0.03577	280	60	13.43	10.22	22.60%	4.25
0.50%	14	0.03675	270	56	11.72	8.87	26.02%	4.12
1.00%	14	0.03875	280	61	13.79	10.83	29.31%	5.66
1.50%	15	0.03988	130	50	10.32	8.31	22.08%	1.48
2.00%	22	0.10829	120	45	10.49	8.48	21.03%	1.32

3.5 Discussion

3.5.1 Percolation Threshold

For the further study of composition dependence of dielectric behaviors, the dielectric constant at different frequencies was used to find the percolation threshold. As shown in **Figure 3-12**, the dielectric constant ratio of the composite to the matrix was plotted against $Ti_3C_2T_X$ filler contents. By the trend of dielectric constant changing, the percolation threshold of $Ti_3C_2T_X$-P(VDF-TrFE) composite at low-frequency range are very likely to be located near the composition of 12 wt%; The reduced increase amount of dielectric constant may suggest a percolation threshold smaller than 12 wt% at low frequencies, and the smooth increasing curve of dielectric constant at high frequency is the evidence that the φ_c was increased to a value higher than 0.12. Based on the above discussion, the percolation threshold of the composites at low frequencies should between 10 wt% and 12 wt%, therefore the samples before 10 wt% can be considered as the dielectric by the percolation theory. To find the percolation threshold, the

dielectric constant plotted in **Figure 3-8** were used in the fitting, by changing the form of Equation 1-27 as[1,2]:

$$\frac{\varepsilon_r}{\varepsilon_m} = \left(\frac{\varphi_c}{\varphi_c - \varphi}\right)^s \quad (\varphi < \varphi_c) \tag{3-1}$$

where ε_m is the dielectric constant of the matrix polymer. The fitting results of dielectric constants at 100 Hz with different $Ti_3C_2T_X$ filler contents are shown as the red lines in **Figure 3-12 (a)**. It can be obtained that the percolation threshold φ_c as 11.96 wt% and critical exponent s as 2.63 at 100 Hz. Although the theoretical value of φ_c is approximately 0.16 for homogeneous composite containing randomly oriented spherical shape fillers by calculation, the fillers in polymer matrix are always clusters formed by the randomly distributed fillers with a complex shape, will lead to the φ_c are lower than the theoretical value. It also can be seen that the dielectric constant of $Ti_3C_2T_X$-P(VDF-TrFE) composites is higher than the composites using spherical shape fillers, this could be attributed that the 2-D particles are aligned with their surfaces close to each other but separated by the polymer matrix. Compare with the values of the constants in suggested simulation ($s \approx 0.7$) and reported experimental results (0.167 to 2.4), the composites obtained a considerable higher critical exponent s. Another possible reason of the large difference between theoretical value and experimental results is due to the contribution of relaxation from the fillers: with the content of filler increases to the concentration close to φ_c, the leakage becomes much stronger, which lead to the fitting error when the filler contents are relatively higher. In addition, the value of both φ_c and s were found to dependent on the testing frequency in above discussion. Therefore, the φ_c and s with different filler contents were shown

in **Figure 3-12 (b)**. From 100 Hz to 1 MHz, the φ_c varied from 11.96 wt% to 13.12 wt%, while s decreases from 2.63 to 0.80.

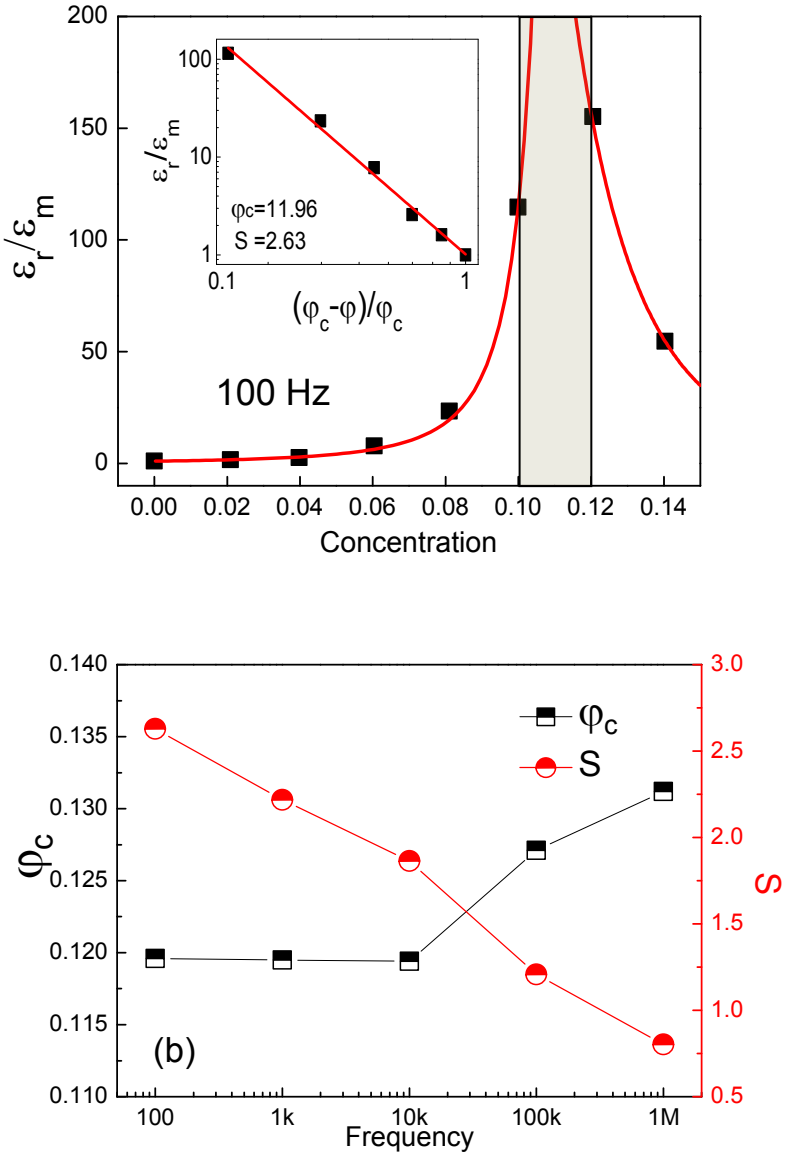

Figure 3-12 (a) The $\varepsilon_r/\varepsilon_m$ and fitting by percolation theory at 100 Hz, (b) The percolation threshold φ_c and critical exponent s obtained by fitting

From the fitting results with different frequency, as shown in **Figure 3-12(b)**, the value of φ_c and s were found to depend on the testing frequency in above discussion. For the composites, the σ at low frequency is almost independent of the frequency. According to the previously reported results, it is known that the CDCs exhibit a strong dependence on the dielectric constant on the frequency when φ is close to φ_c[13]. Therefore, it is expected that the fitting constant φ_c should increase with increasing frequency for this case. For the study of percolation threshold fitting with the reduced impact of frequency, the conductivity of composites was used in the following equation:

$$\sigma = \sigma_0 + A\omega^n \tag{3-2}$$

where A and n are constants, ω is angular frequency, σ_0 is the composites original conductivity which is independent of the frequency. To find the σ_0, the frequency dependence of conductivity σ were used in the fitting, by changing the form of Equation 3-2 as:

$$\ln(\sigma - \sigma_0) = \ln A + n \ln \omega \tag{3-3}$$

Based on Equation 3-3, the σ_0, A, and n can be then obtained by the fitting using the frequency dependence of σ for different composites. Therefore, the σ_0 of all composites with different testing temperatures were collected. As an example, the result of 2 wt.% composite with 20 ^oC testing temperature is plotted and shown in **Figure 3-13**. From the fitting, a negative σ_0 can be calculated from some of the composites, therefore the σ_0 cannot be used to find the percolation threshold.

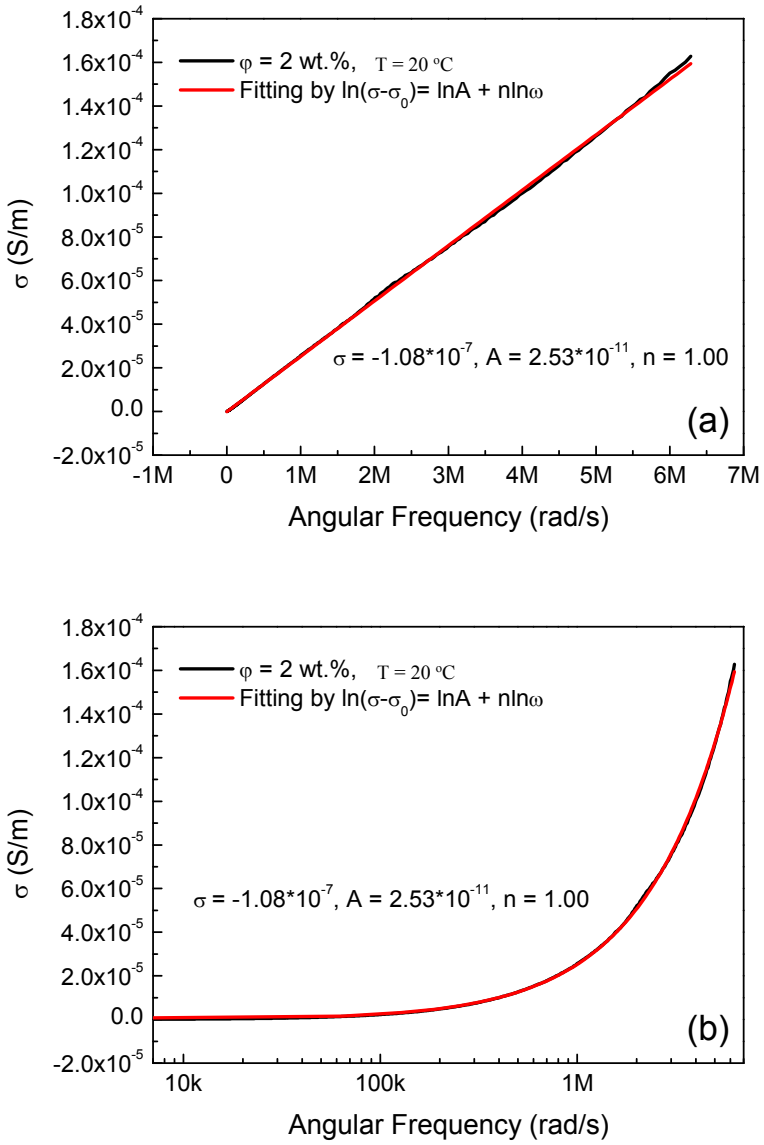

Figure 3-13 The σ and fitting result for the composites with 2 wt.% filler content at 20 °C vs. (a) angular frequency and (b) logarithmic angular frequency

The negative σ_0 got from fitting shows the problem of this method. For the further study of the fitting method of the percolation threshold, the frequency dependency of the conductivity

composite system was plotted and observed. As an example, the σ vs. frequency of composites with 2 wt.% $Ti_3C_2T_X$ with different testing temperatures were plotted in **Figure 3-14**, in which the obvious two frequency regimes can be found, especially for the results from low temperatures. When Equation 3-2 is used to analyze the conductivity of the composite system, it is found that the two frequency regimes exist for the experimental results of all composites with different filler content. Therefore, the conductivity of composites in the low-frequency range is suitable for fitting. In order to maintain the consistency of fitting, the conductivity in the frequency range of 100 to 100k Hz for all composites were used in the fitting. As an example, the fitting based on the σ of composites with 2 wt.% $Ti_3C_2T_X$ at 20 °C were plotted in **Figure 3-15**. Compare with the previous results, fitting results with low-frequency range are perfectly matched with the original data and provides positive σ_0.

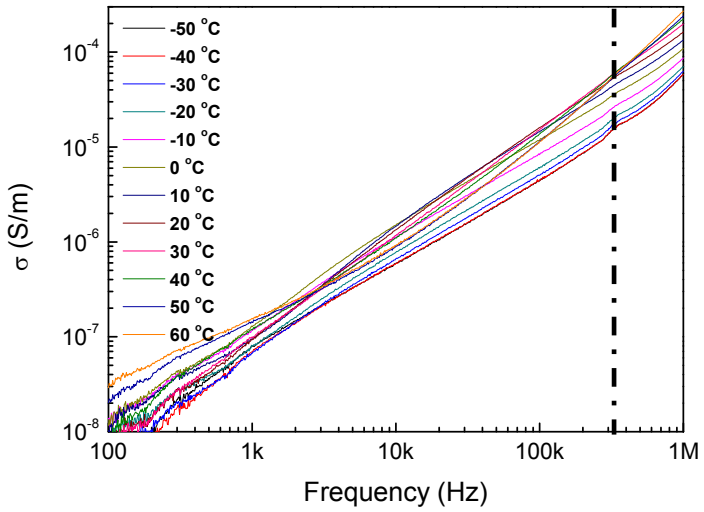

Figure 3-14 The frequency dependence of conductivity for the composites with 2 wt.% $Ti_3C_2T_X$ with different testing temperatures

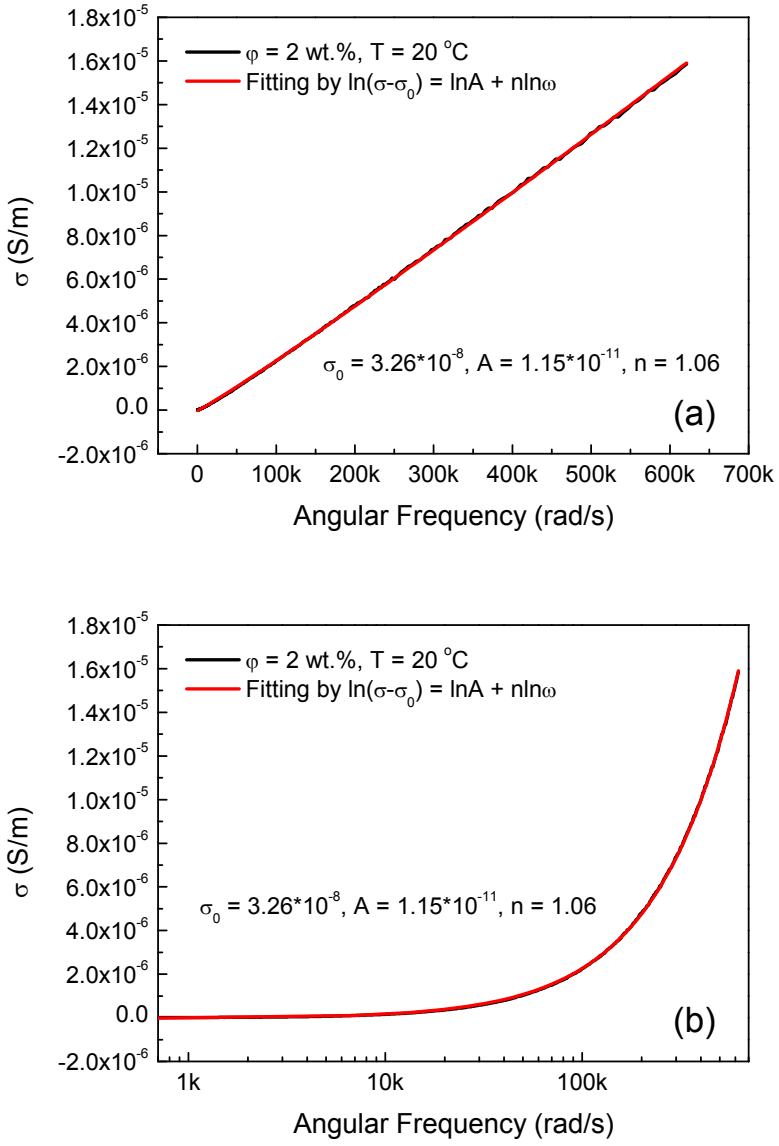

Figure 3-15 The σ and fitting result for the composites with 2 wt.% filler content from 100 Hz to 100k Hz vs. (a) angular frequency and (b) logarithmic angular frequency

The σ_0 of composites with different testing temperatures were obtained by fitting discussed previously. Therefore, the σ_0 in the frequency range of 100 to 100k Hz was used in the fitting based on the following equation:

$$\frac{\sigma_0}{\sigma_m} = \left(\frac{\varphi_c}{\varphi_c - \varphi}\right)^s \tag{3-4}$$

where σ_m is the original conductivity of the matrix polymer which is not dependent on frequency. The φ_c of composites under different temperatures were obtained. As an example, the fitting results of σ_0/σ_m at 20 °C with different $Ti_3C_2T_X$ filler contents are shown as the red lines in **Figure 3-16**. A φ_c of 11.6 wt.% were obtained by fitting, which is close to the fitting result by Equation 3-1. By using the data from different testing temperatures, the φ_c and s with different testing temperature were collected and listed in **Table 3-3**.

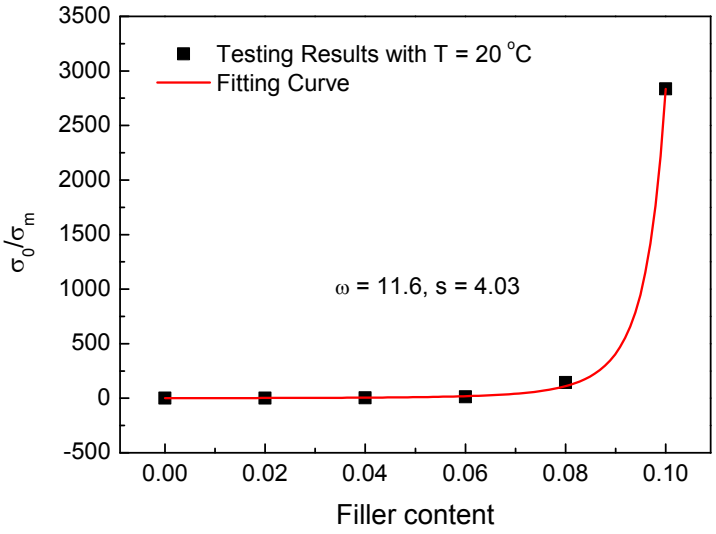

Figure 3-16 The σ_0/σ_m and fitting by percolation theory using the data from 20°C testing, where the ω represents percolation threshold

Table 3-3 The φ_c and s of composites with different testing temperatures

Temperature	φ_c	s
-50 °C	11.9 wt.%	5.03
-40 °C	10.5 wt.%	2.41
-30 °C	10.3 wt.%	1.75
-20 °C	10.2 wt.%	1.69
-10 °C	10.1 wt.%	1.20
0 °C	10.6 wt.%	2.52
10 °C	10.0 wt.%	0.68
20 °C	11.6 wt.%	4.03
30 °C	11.7 wt.%	3.43
40 °C	10.6 wt.%	1.85
50 °C	10.3 wt.%	1.37
60 °C	10.5 wt.%	1.57
70 °C	10.7 wt.%	1.71
80 °C	10.8 wt.%	1.74
90 °C	12.4 wt.%	2.70
100 °C	11.0 wt.%	1.80
110 °C	10.0 wt.%	0.56
120 °C	12.2 wt.%	2.12
130 °C	10.6 wt.%	1.06

The φ_c of composites as listed in **Table 3-3** was then plotted and shown in **Figure 3-17**. No obvious trend was found from the temperature dependence of φ_c. From the curve, the percolation threshold of the composite system is mostly located between 10 to 12 wt.%. In another word, the fitting result of φ_c is independent of testing temperature. Therefore, by the analysis, as discussed above, a new method for the calculation of percolation threshold was developed, which can effectively reduce the impact of ambient temperature.

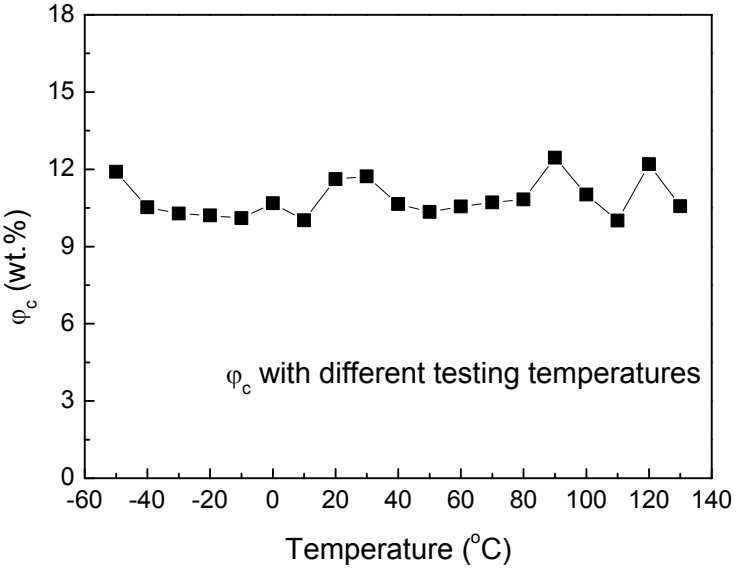

Figure 3-17 The φ_c of composite system by fitting using the σ with different testing temperatures

3.5.2 Effect of Silicon Coupling Agent

Due to the fact that the dielectric properties may be modified by the change of connection between conductive filler and polymer matrix, the composite films with fixed $Ti_3C_2T_X$ concentration were prepared with different amount of silicon coupling agent. Two different silicon coupling agents, 1H, 1H, 2H, 2H Perfluorooctyltrichlorosilane (Agent #1) and 3 Aminopropyltriethoxysilane (Agent #2) were selected according to their react capability with the $Ti_3C_2T_X$ compound. Due to the fact that 4 wt% sample has a relatively high permittivity (69 at 100 Hz) and low loss (0.16) among all samples with different concentration, the effect of two coupling agents were studied respectively. Based on calculation, certain amount of Ti3C2TX-water suspension was injected in beakers to fix the filler content at 4 wt%. Then the two silicon

coupling agents were added to the suspension respectively with different concentrations (0, 1, and 2 wt%), following with 15 minutes sonication to make sure the reaction complete. The ready-prepared suspensions were used for the solution casting and hot pressing, with the identical condition for the preparation of composite films without coupling agent as discussed previously. The permittivity, loss, and conductivity of 4 wt% composite films with 1 wt% coupling agent #1 and #2 were shown in **Figure 3-18** respectively. From the curves, silicon coupling agents effectively improved the dielectric constant, and simultaneously the loss was also increased. The results showed that for a fixed amount of agent used, coupling agent #2 is more effective in improving the dielectric constant.

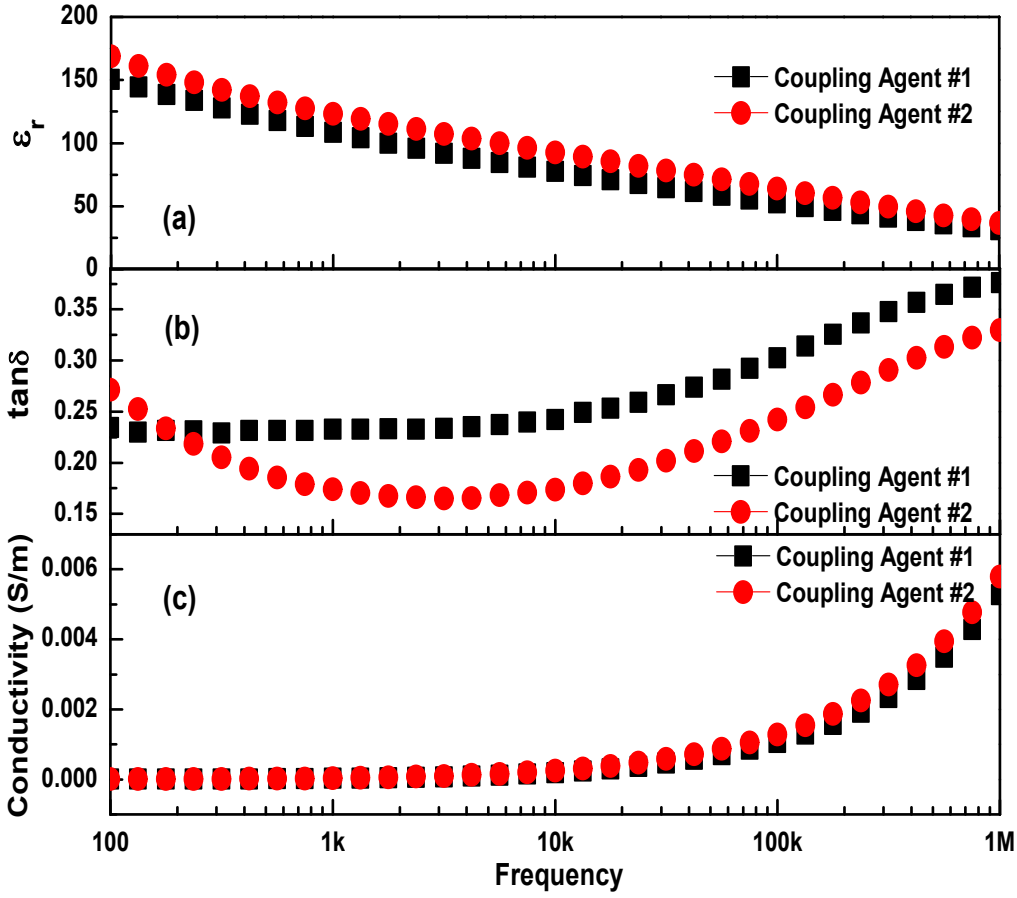

Figure 3-18 The frequency dependency of (a) permittivity, (b) loss and (c) conductivity of 4wt% composite films with 1% of coupling agent #1 and #2 respectively

Due to the high effectiveness of silicon coupling agent #2, the composite samples with different amount of agent #2 were prepared to find the suitable amount. The properties of samples were shown in **Figure 3-19**, which reflects the adjustability of the dielectric properties by changing the concentration of coupling agent. The dielectric constant get a maximum value of 196 and simultaneously result in an increased loss of 0.37 at 100 Hz when 0.5 wt% of agent #2

was added; compare with this result, a concentration of 1 wt% lead to an increased dielectric constant at the higher frequency range with a lower loss. The trend of dielectric properties was shown in **Figure 3-20**. From the trend, a clear trend that for both coupling agents, 1% concentration give the highest permittivity, medium loss, and lowest resistivity. As a conclusion, silicon coupling agents can increase the permittivity and loss of composite films; added hot pressing can increase the breakdown field and decrease the permittivity and loss.

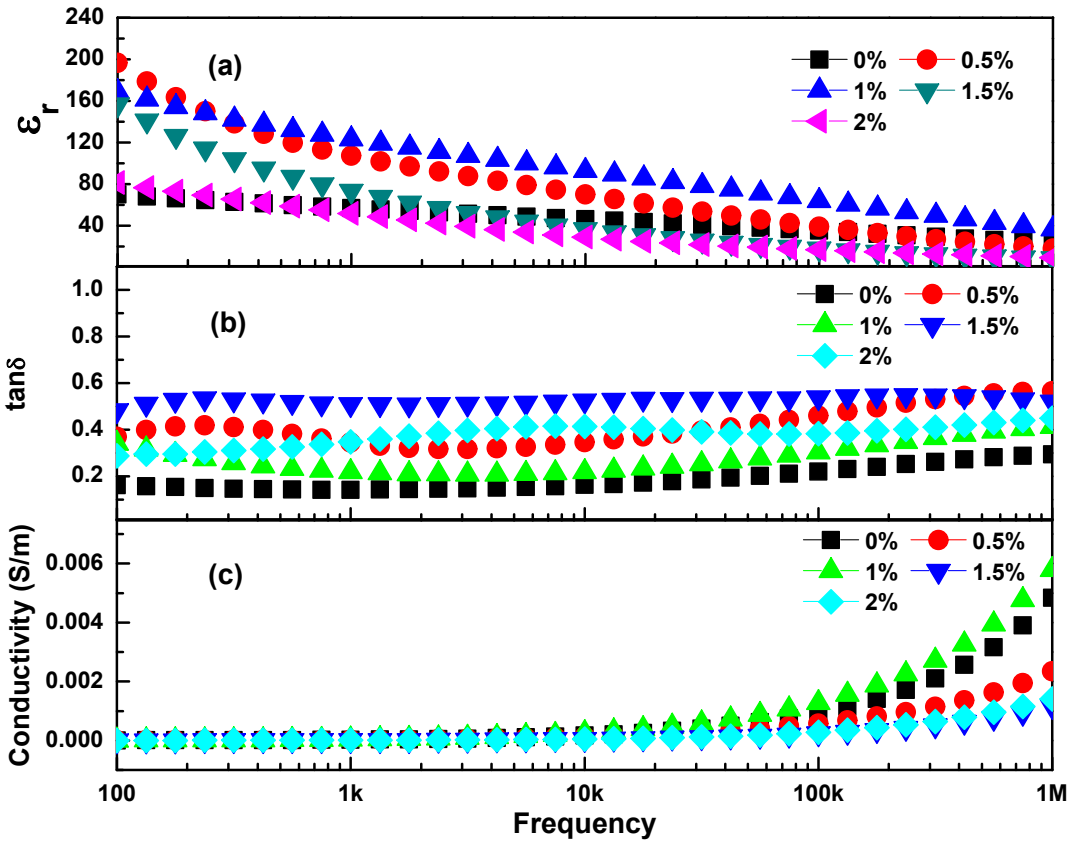

Figure 3-19 The frequency dependency of (a) permittivity, (b) loss and (c) conductivity of 4 wt% composite films with 0-2% coupling agent #2

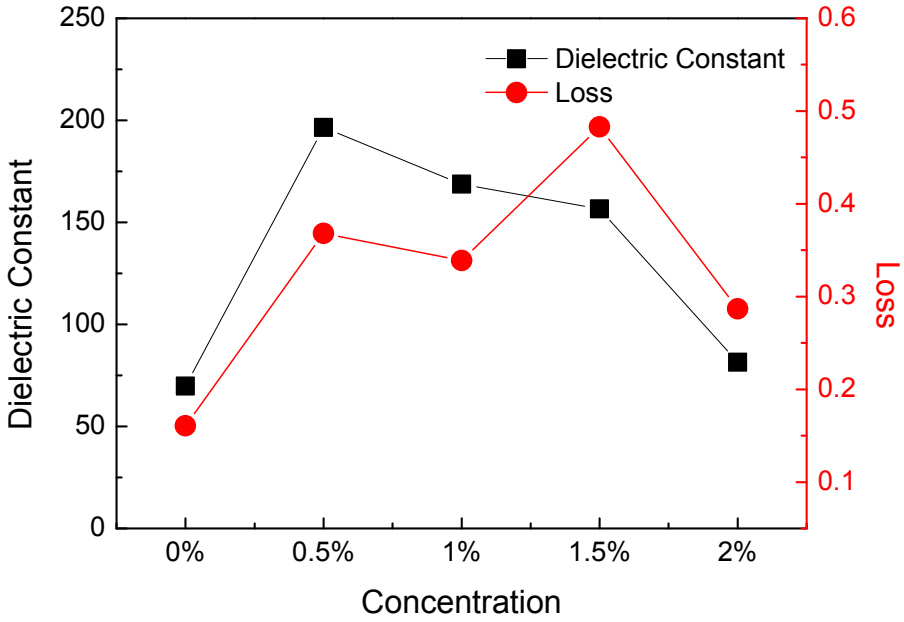

Figure 3-20 The permittivity and loss of 4 wt% composite films as the function of the amount of coupling agent #2 at 100 Hz

3.5.3 Crystallinity Increase Due to Filler Addition

As shown previously, the P(VDF-TrFE) polymer added by different contents of filler got the clear (200)/(110) peaks in XRD pattern with obvious different intensities. For the calculation of crystallinity from XRD patterns, the data for $Ti_3C_2T_X$-P(VDF-TrFE) composite films zoomed near the sharp peak is presented in **Figure 3-21 (a)**. In addition to the peak of (200)/(110) near 20°, the broad peak near 18° with a much lower intensity which is due to the amorphous phase was also found by fitting and illustrated as the insert in **Figure 3-21 (a)**[9]. The crystallinity was then estimated by comparing the area from the crystalline diffraction peak with the total diffraction area of the following equation:

$$C = 100\% \times \frac{I_{cr}}{I_{cr} + I_{non}} \tag{3-5}$$

where C expresses the apparent crystallinity, I_{cr} represents the intensity of diffraction of the crystalline peak, and I_{non} represents the intensity of diffraction of the non-crystalline material. The result of calculated crystallinity is shown in **Figure 3-21 (b)**. Clearly, a sharp increase on crystallinity (from 50.3 to 87.7 %) was observed with the addition of small amount of filler (<1 wt%); with the increase of amount adding to polymer matrix, the drop of crystallinity suggesting that the crystallization process will be hindered by too much doping. Two different colors were used in **Figure 3-21 (b)** to decompose the two divided stages in the trend of crystallinity as a function of filler contents. For the convenience of comparison, the peak intensity/area and crystallinity of both crystal and non-crystal phases in the composites with different filler contents obtained from fitting were listed in **Table 3-4**.

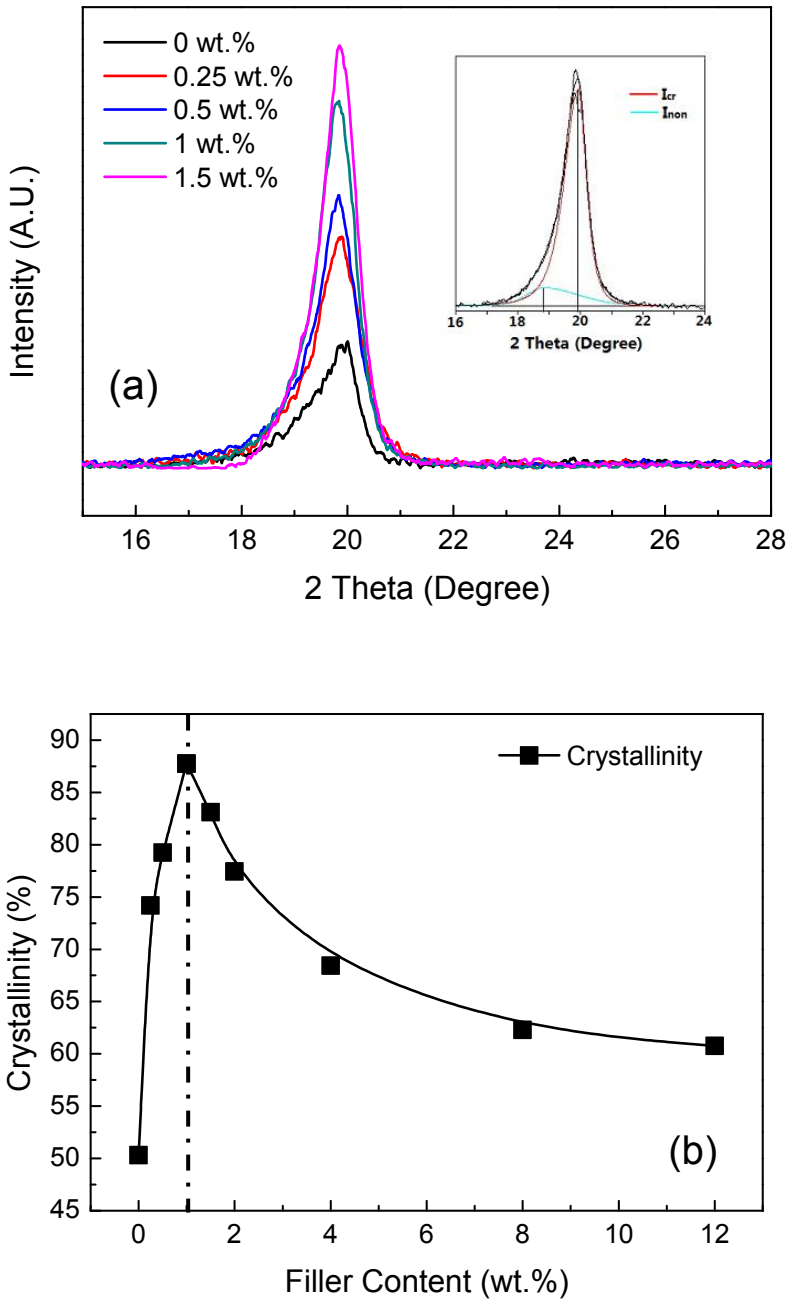

Figure 3-21 (a) The stacked XRD patterns of $Ti_3C_2T_X$-P(VDF-TrFE) films with selected filler contents (0, 0.25, 0.5, 1 and 1.5 wt.%) and (b) The crystallinity calculated from XRD as a function of the filler contents

Table 3-4 The peak intensity, peak area (represent by I_{cr} and I_{non} respectively) and calculated crystallinity of crystal and non-crystal phases from the fitting of XRD

Filler Content (wt.%)	Peak Height of Crystal (A.U.)	Peak Height of Non-Crystal (A.U.)	I_{cr}	I_{non}	Crystallinity ($C=100\%\times I_{cr}/[I_{cr}+I_{non}]$)
0	320	14	20466	20422	50.3
0.25	728	182	49115	17096	74.18
0.5	858	152	52609	13784	79.24
1	1150	132	89980	12574	87.74
1.5	1293	101	95225	19367	83.1
2	1252	44	89262	26020	77.43
4	1060	38	76338	38944	68.42
8	732	22	36956	22383	62.28
12	385	18	30208	19518	60.75

For comparison, the crystallinity calculated from the DSC melting peaks of composites as the functions of filler contents were shown in **Figure 3-22**. The trend of crystallinity found by DSC is consistent with that were found by XRD peaks, the differential rate between of samples are quite close. By using the crystallinity of pure polymer calculated from XRD as a standard, the crystallinity of the composites with different filler content was calculated from DSC results. As shown, the maximum crystallinity of samples is 79.8 % from the composite with 1 wt.% $Ti_3C_2T_X$, which is about 1.6 times of the crystallinity of pure P(VDF-TrFE); from **Figure 3-21 (b)**, the crystallinity calculated from the XRD is in the range of 50.3 ~ 88.7 %, where the maximum value is about 1.7 times of minimum value, therefore the very close results were obtained by two different methods.

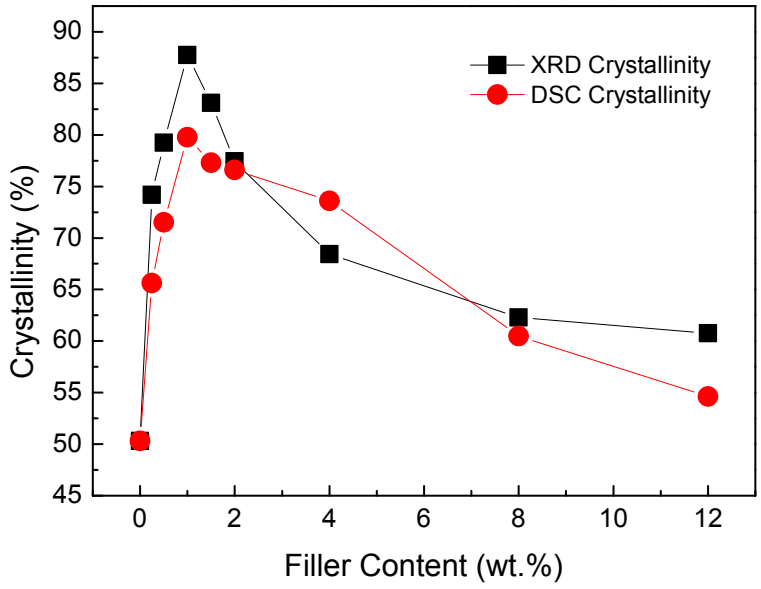

Figure 3-22 Crystallinity calculated from the DSC melting peaks as a function of filler content

3.6 Summary

In summary, the nanocomposite with a high dielectric constant and low percolation threshold was developed by dispersing novel 2-D nanoscale particles $Ti_3C_2T_X$ into P(VDF-TrFE) matrix. The composites shown uniform microstructure due to the two steps process consisted of solution casting and hot-pressing. The percolation threshold is dependent on the testing frequency and is about 11.96 wt% at 100Hz, which is smaller than the composites using spherical conductive particle fillers. At room temperature, the 12 wt% composite exhibits a high dielectric constant higher than 2100 at 100 Hz; In addition, the 10 wt% composite exhibit the high dielectric constant of more than 1500 associated with a loss of 0.8 at 100 Hz which is much smaller then other reported high-dielectric constant 2-D filler based composites. It indicates that

the new relaxation processes are induced in composites due to the adding of 2-D shape fillers, which is the dominating mechanism of stability improvement in changing temperatures. It was found that the crystallinity of P(VDF-TrFE) matrix was sharply increased due to the induced 2-D fillers, the maximum crystallinity can reach to 87.74 % when the filler content is 1 wt%. Due to the flexibility and excellent dielectric properties of the new composite material created, a bright future has been shown that the material may become a strong candidate of applications such as soft/wearable electrics, high permittivity capacitors, sensors, and energy storage devices.

Chapter 4

Ceramic-Polymer Composite with Coupling Agent

In this chapter, the Calcium Copper Titanate $CaCu_3Ti_4O_{12}$ ceramic filler and P(VDF-CTFE) 88/12 polymer matrix was combined by a process of solution casting with silicon coupling agent pretreatment as an example system of the ceramic-polymer composite with relatively high energy storage density and high breakdown strength. The preparing conditions including annealing temperature, filler content and coupling agent amount were studied in details. By combining all of the optimized conditions, the highest energy density up to more than 4 J/cm^3 was found in the composite thin films with 15 wt% ceramic fillers with a substantially increased breakdown strength of 230 MV/m.

4.1 Introduction

As shown previously, the conductor-polymer composites with high dielectric constant have been prepared by combining the solution casting and hot pressing processes. Although the dielectrics created shown a high dielectric constant, the hot pressing is difficult to apply on the cases when having a relatively high shape accuracy requirements, especially for the application in microelectromechanical systems. In addition, the breakdown strength of conductor-polymer composites is very limited due to the leakage current. Therefore, this type of dielectric it is not good for electrical energy storage applications, such as mobile electronic devices, stationary power systems, and hybrid electric vehicles[1-5]. According to the introduction in Chapter 1,

ceramic-polymer are suitable for conventional capacitors to compare with other composites because of their high breakdown strength; it is also interesting to have the dielectric with a low processing temperature and being highly flexible[6-10]. Among the ceramic-polymer composites, the ones using $CaCu_3Ti_4O_{12}$ (CCTO) as filler have shown a relatively high dielectric constant[11-15]. However, the energy storage density was not studied in previous reports due to the fact that these composites may have a low electric breakdown field. Therefore, for the purpose of enhancing the uniform distribution of ceramic filler to increase the breakdown strength, the influence of processes such as annealing and coupling agent in solution casting was studied to optimize the material properties.

4.2 Samples

In the preparation of composites, P(VDF-CTFE) 88/12 mol% copolymer from Solvey was utilized as the polymer matrix; The different volume concentrations (5, 10, 15, 20, 25, and 30 vol.%) of CCTO were added into P(VDF-CTFE) matrix as fillers. The composites were obtained by the solution casting with the coupling agent as introduced in Chapter 2. In the coupling agent effect study, in order to achieve the expected coupling effect, the different amount (0.5, 1, 1.5, 2 and 3wt.%) was carried out. The 1 H, 1H, 2H, 2H-Perfluorooctyltrichlorosilane was added to the mixture of CCTO and 95% ethanol solution and then stirred to pretreat the filler particles. Right after the stirring process, both suspensions with and without pretreatment are initially uniform, but in different colors. This indicates that the coupling is indeed attached to the surface of CCTO particles. By standing the solution for 48

hours right after mixing, the stability of CCTO-P(VDF-CTFE) in DMF solution with silicon coupling agent was confirmed and shown as the comparison in **Figure 4-1 (a)** and **(b)**. The conditions of sample preparation and experiments are summarized in **Table 4-1**.

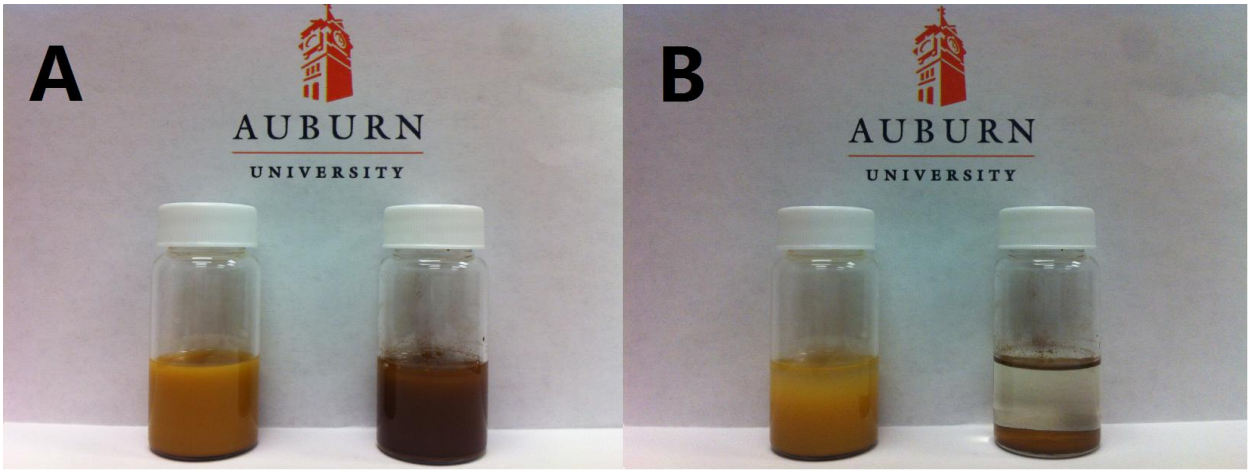

Figure 4-1 (a) Freshly prepared and (b) 48 hours later images of the CCTO-P(VDF-CTFE) mixture in DMF solution with/without silicon coupling agent

Table 4-1 Conditions of the preparation and experiments

Conditions	Value
Filler Contents	5, 10, 15, 20, 25, and 30 wt.%
Coupling Agent Contents	0, 0.5, 1, 2, and 3 wt.%
Casting Temperature	70 °C
Annealing Temperature	160 °C
Hot Pressing Temperature	200 °C
Temperature Dependency	-50 ~ 130 °C
Testing Frequency	100 Hz ~ 1 MHz

4.3 Structure and Morphology Characterization

For the confirmation of the composite microstructure with different processing conditions, the SEM picture of the cross-section of composite films was taken and shown as follows. The pictures of composites without coupling agent were shown in **Figure 4-2**, the pictures of composites modified by different silicon coupling agent amount with a fixed filler content of 15% were shown in **Figure 4-3**.

As shown in **Figure 4-2**, the composite samples without coupling agent are consists of clearly separated ceramic particles and the polymer matrix. The loose polymer fibers and detached ceramic fillers show the low density; the gathering fillers with little polymer around have shown the nonuniform structure due to the bad surface connection. From the image of the cross section shown in **Figure 4-3**, a dense structure of the samples with silicon coupling agent was found. Compare with the loose fibers and detached fillers found in the cross-section pictures from the composites without the coupling agent, the ceramic fillers in composite thin films with coupling agent are tightly wrapped by the polymer matrix, which proved the effect of coupling agent obviously. When the amount of coupling agent is fixed, the structure of composite films is changing mainly due to the different filler content. For the samples with higher content of fillers (>25 wt%), the gathering of CCTO particles was observed clearly. However, when increasing the amount of coupling agent with a fixed filler content, the contour of fillers are getting blurred, which indicates the effective surface modification by the coupling agent.

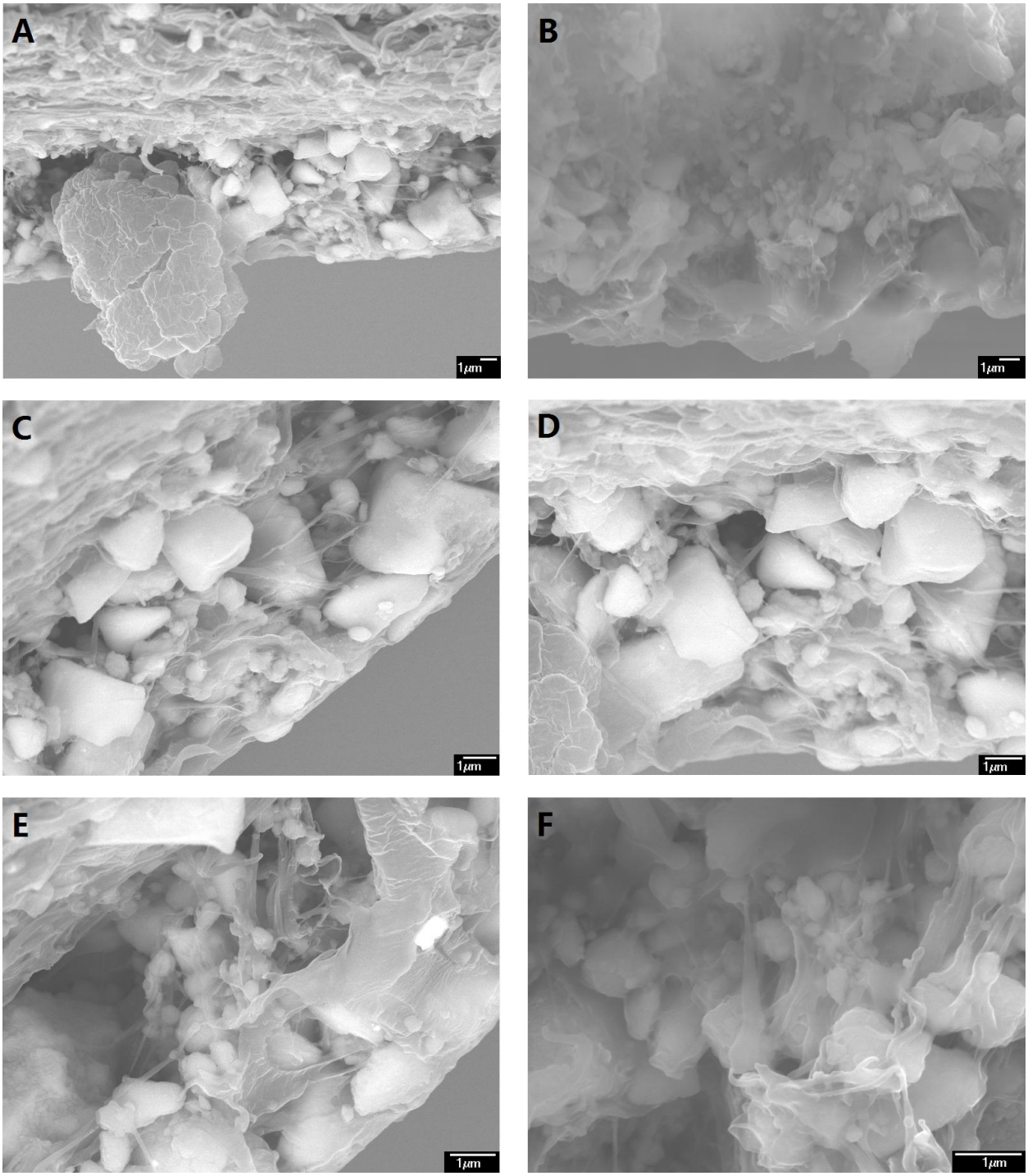

Figure 4-2 The pictures of composite cross section with 15 vol% ceramic fillers (a)5000, (b)6000, (c)7000, (d)8000, (e)10000, and (f)15000 times magnified by SEM

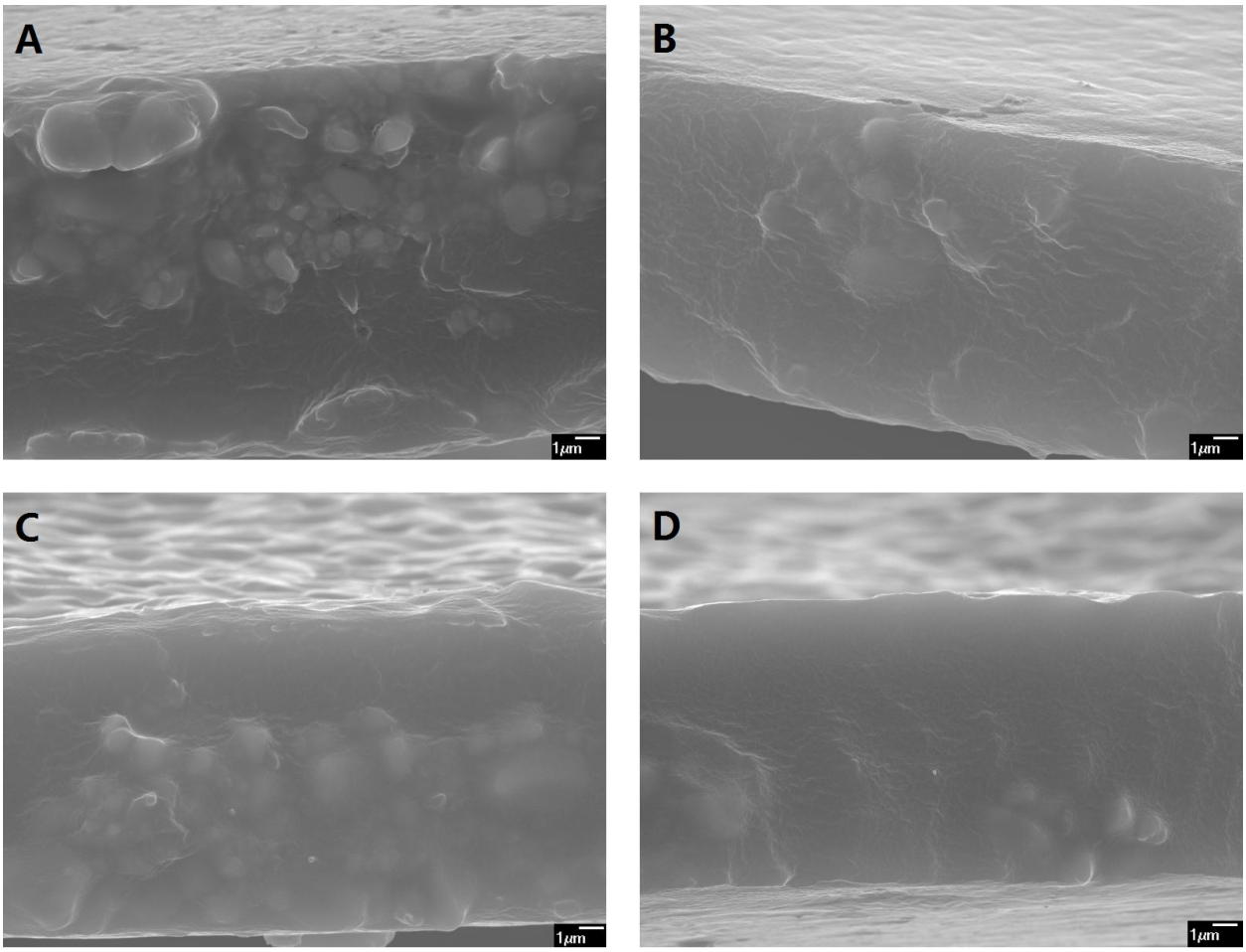

Figure 4-3 The pictures of composite cross section with 15 vol% ceramic fillers and (a)0.5 wt%, (b)1 wt%, (c)2 wt%, and (d)3 wt% silicon coupling agent

4.4 Dielectric Properties

4.4.1 Dielectric Properties with Different Filler Contents

The dielectric constant and loss of CCTO-P(VDF-CTFE) composite with different filler contents (5-30 vol%) and a fixed amount of silicon coupling agent (1 wt%) in the range of

100Hz to 1MHz was recorded as a function of frequency and shown in **Figure 4-4**. All of the composite samples have shown the higher dielectric constant compared with P(VDF-CTFE), but much lower than the dielectric constant of CCTO ceramic. It is clear that with the increasing filler content, the dielectric constant of composite films is also increasing; for each one of the samples, in the range of 100Hz to 1MHz, the dielectric constant is decreasing as the frequency increases. The dielectric loss of all the composite films are close in values and are increasing with the increasing frequency. The concentration dependence of dielectric permittivity and loss for different frequency are shown in **Figure 4-5**.

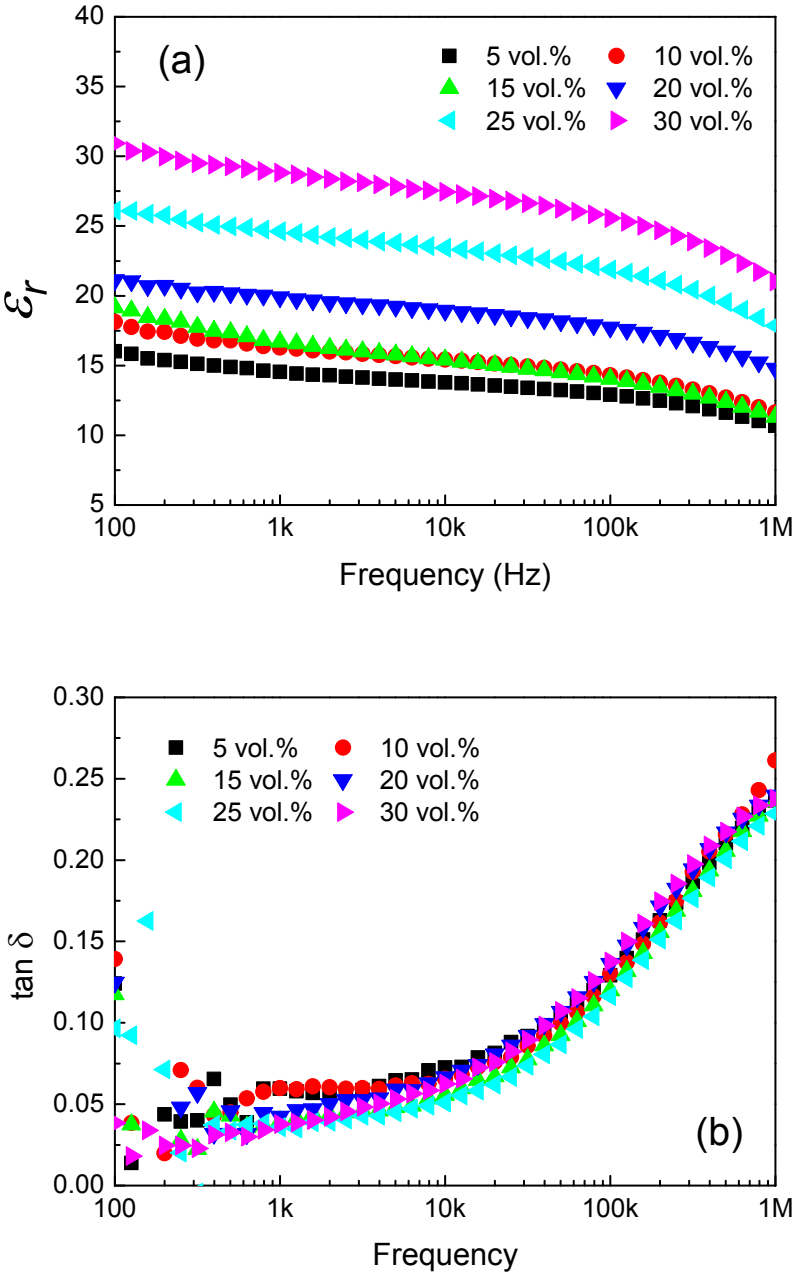

Figure 4-4 Frequency dependence of (a) dielectric permittivity and (b) dielectric loss as a function of CCTO percentage at room temperature

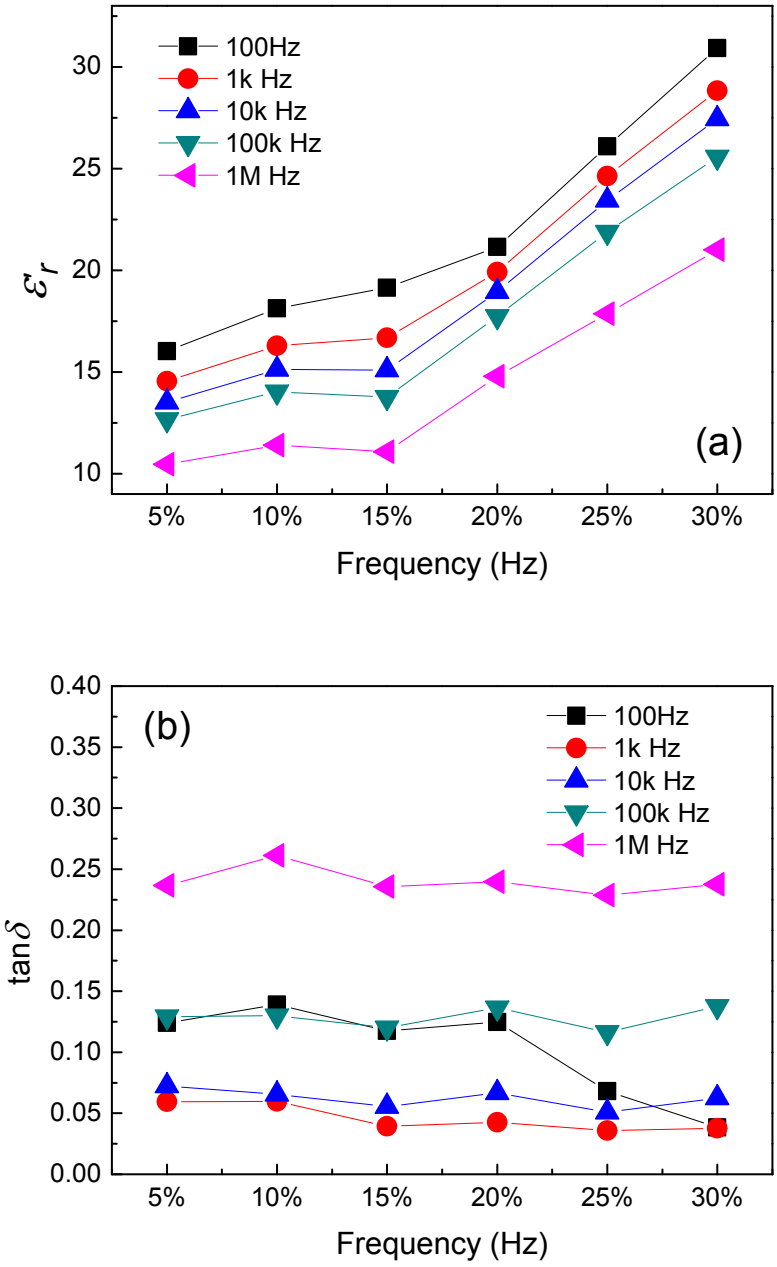

Figure 4-5 Concentration dependence of dielectric constant and loss

Except for dielectric constant and loss, the P-E loops and breakdown strength of the composites were also tested in the silicone oil and shown in **Figure 4-6**. With the increase of filler content, the breakdown strength of composites was obviously decreased. According to the calculation from P-E loops, by adding 1 wt% silicon coupling agent, the samples with different filler contents were shown the relatively large breakdown strength which leads to the high energy storage densities. As an example, The P-E loops of composites with 15 vol% of CCTO under different breakdown field are shown in **Figure 4-6**. The breakdown field of 15 vol% composite thin film reaches 230 MV/m, while the polarization at the electric field has arrived 4 μC/cm^2. Calculated by Equation 1-19, the energy density can be as high as 4.42 J/cm^3.

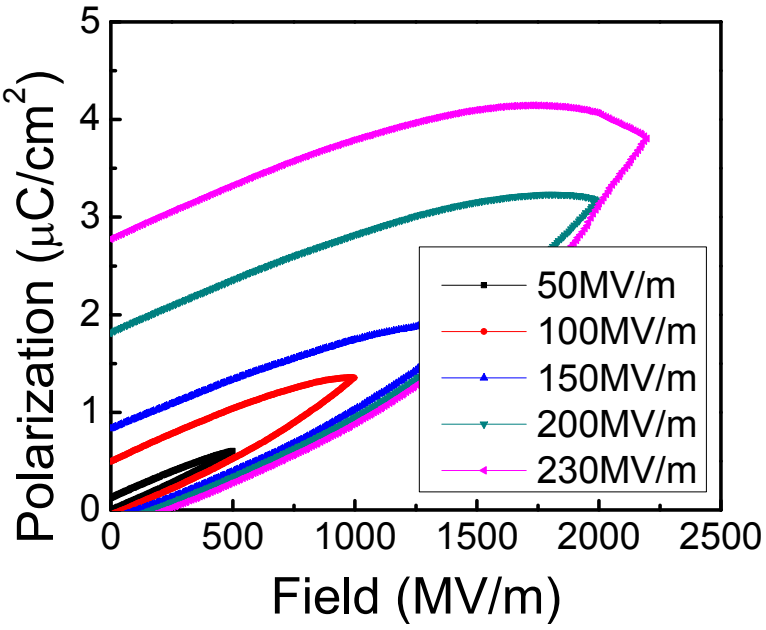

Figure 4-6 The P-E loop of composites with 15 vol% of CCTO under different breakdown field

The E_b of the composites is shown in **Figure 4-7**, where the E_b obtained in the composites using uncoated CCTO is also presented for comparison. For the composites using uncoated CCTO, the E_b decreases with increasing filler content. Clearly, the composites using Cl_3-silane coated CCTO have a much higher E_b than the composites using uncoated CCTO, which is a direct result of the improvement in the connection or interface between the polymer matrix and filler particles. For example, for the composites with 15 vol.% of CCTO, the E_b of the composites using Cl_3-silane coated CCTO is more than 3 times higher than that of the composites using uncoated CCTO. More interestingly, the E_b of these composites increases initially with increasing CCTO content. The highest E_b (>240 MV/m) is observed in the composites with 15 vol.% CCTO.

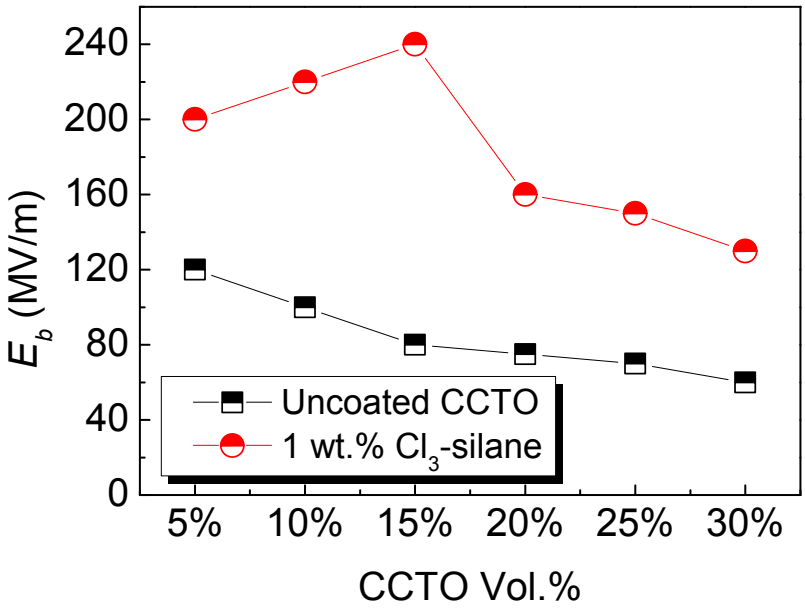

Figure 4-7 Electric breakdown field (E_b) versus CCTO content for the composites using: 1) CCTO coated with 1 wt.% Cl_3-silane and 2) uncoated CCTO

4.4.2 Temperature Dependency of Dielectric Properties

The temperature dependence of dielectric properties of CCTO-P(VDF-CTFE) composites was studied. The gold coated thin films have been sandwiched between two electrodes holder covered by a shell in the oven, and then connected with the testing system. Low down the temperature to -50 °C, wait for equilibrium, and then slowly increase the temperature to 140 °C, wait for thermodynamic equilibrium for each 5 °C and save the data for each equilibrium state. The temperature dependence of dielectric properties of CCTO-P(VDF-CTFE) 10%, 20%, and 30% composites were studied and illustrated in **Figure 4-8**; For comparison, the concentration dependence of permittivity and loss at 1000 Hz for different temperatures were shown in **Figure 4-9**. The dielectric permittivity for all samples increases with increasing temperature and decreases as the frequency increases, dielectric loss increase with temperature and decreases with CCTO percentage increasing. This sudden increase in dielectric permittivity that is observed at 100Hz at high temperature may be assigned to the space charge or interfacial polarization effects. The higher the frequency is, the higher the peak temperature is and the higher the peak value is. The dielectric constant increases with increasing temperature before the glass transition temperature. From 20 °C to 100 °C, the value of dielectric constant is almost independent of temperature. At high temperatures, the dielectric loss increased with increasing temperature due to the conductivity of polymer itself. The dielectric constant and loss of composites with another volume of CCTO (< 30 vol%) show the similar trend with increasing temperature.

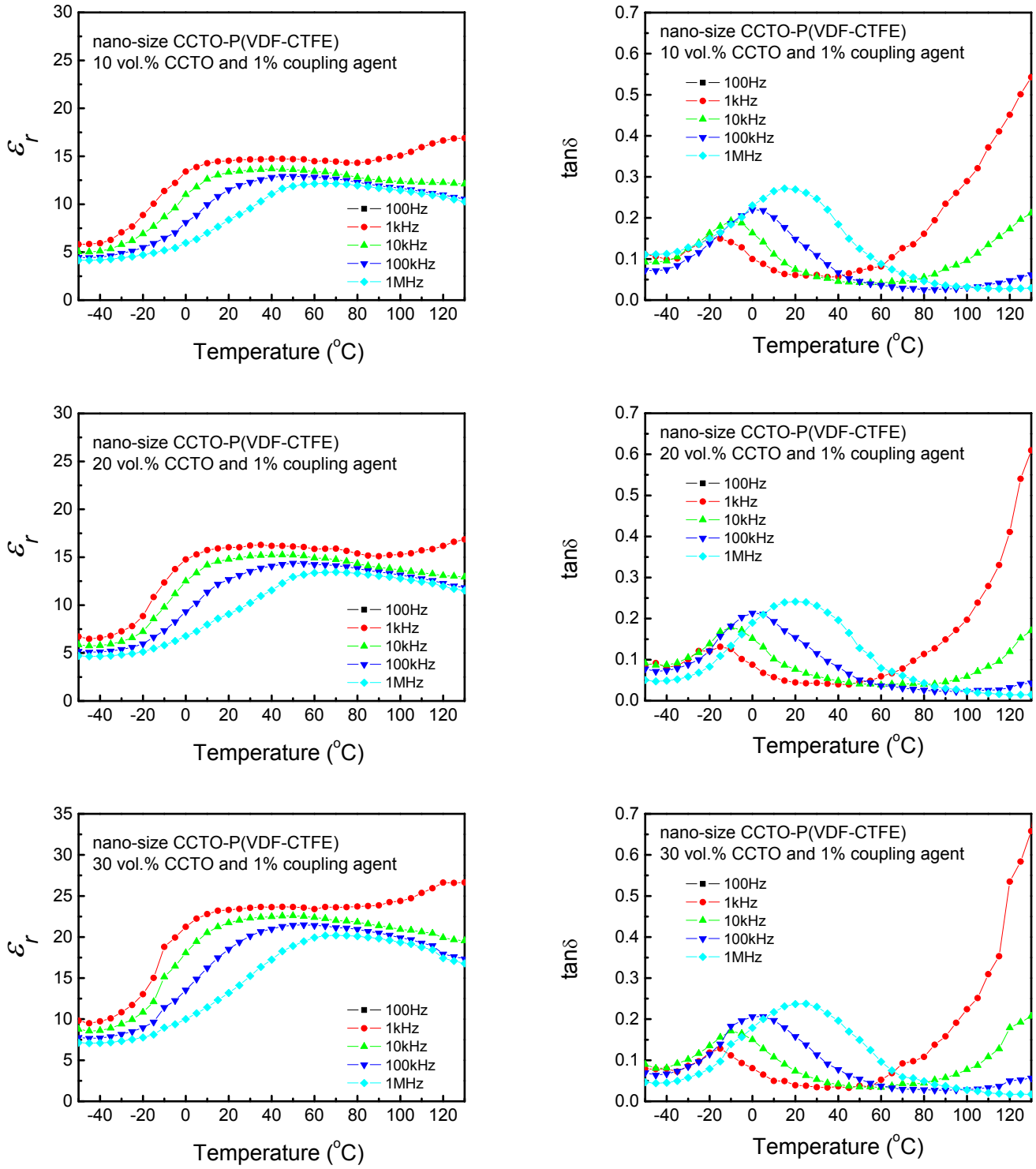

Figure 4-8 Temperature dependence of dielectric behavior

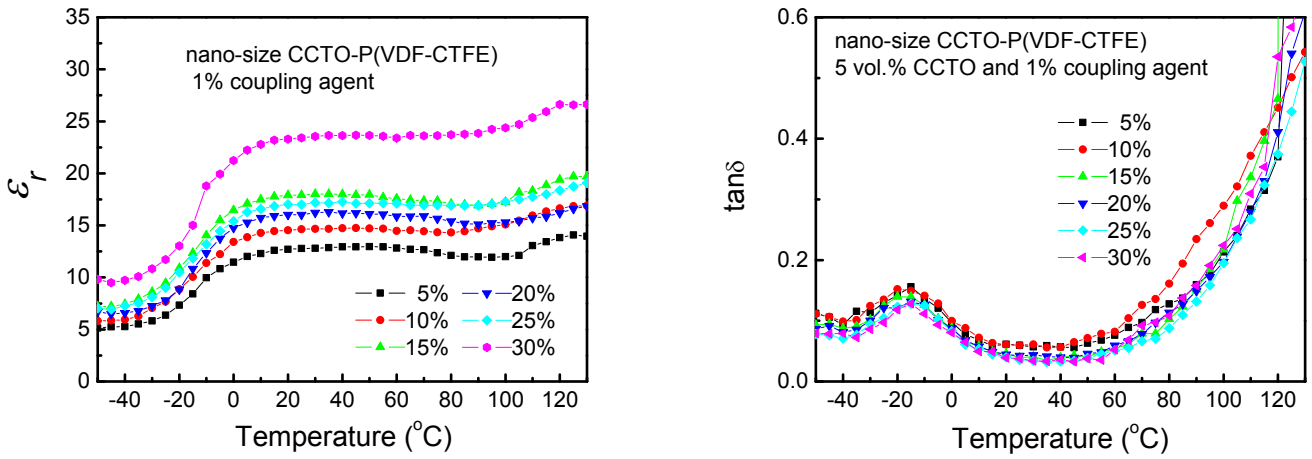

Figure 4-9 The concentration dependence with temperatures change at 1000 Hz

4.5 Discussion

4.5.1 Coverage of Silicon Coupling Agent

The effectiveness of Cl_3-silane coating on the CCTO was examined by the stability of the CCTO suspension in the solution of P(VDF-CTFE) in DMF. From the suspension of CCTO in P(VDF-CTFE) solution, two suspensions have different colors, which indicate the existence of Cl_3-silane in the suspension. In other words, the Cl_3-silane was not lost during the process of drying the mixture at 80 °C. After stored at room temperature for 48 hours, the suspension of Cl_3-silane coated CCTO particles shows a much better stability than the suspension of uncoated CCTO. The results indicate that the process reported here indeed results in a chemical attachment of Cl_3-silane molecules onto the surface of CCTO. Also, from the SEM observation, the Cl_3-silane coated CCTO particles have a better/stronger connection with the polymer matrix.

The surface of uncoated CCTO in the composites is clear, while the surface of Cl_3-silane coated CCTO in the composites is becoming blurry. For the CCTO with 0.5 wt.% Cl_3-silane, the CCTO surface is not clear but can be recognized. For the CCTO with higher Cl_3-silane content, it is hard to recognize the CCTO surface. That is, there is a good wettability between the Cl_3-silane and P(VDF-CTFE). The results also confirm that the Cl_3-silane molecules are attached to CCTO surface.

As a brief summary of above results, schematic pictures are presented in **Figure 4-10** for the relationship/microstructure among Cl_3-silane, CCTO, and P(VDF-CTFE) in the composites. For the composites using uncoated CCTO, a clear interface between CCTO and matrix exists as shown in **Figure 4-10 (a)**. However, for the composites using Cl_3-silane coated CCTO, both the stability observation of the CCTO suspension in P(VDF-CTFE) solution and the SEM observation of CCTO surface in the composites indicate: 1) the process reported here can chemically attach the Cl_3-silane molecules onto CCTO surface, and 2) the Cl_3-silane molecules have a good wettability with P(VDF-CTFE). Additionally, the ratio of Cl_3-silane to CCTO used in the process is important. It is expected there is a critical ratio for this. Below this critical ratio, the surface of CCTO is partially coated with Cl_3-silane as shown in **Figure 4-10 (b)**. At this critical ratio, the coverage of CCTO surface reaches its maximum, at which a layer of Cl_3-silane is formed on the surface of CCTO as shown in **Figure 4-10 (c)**. Above this critical ratio, the surface coverage of CCTO with Cl_3-silane does not change. Thus, the further increase in the ratio only results in non-attached Cl_3-silane molecules in the system as shown in **Figure 4-10 (d)**. It should be mentioned that even the ratio of Cl_3-silane to CCTO is below the critical ratio the individual Cl_3-silane may exist in the composites as shown in **Figure 4-10 (b)** and **(c)**. Due to the

good wettability between Cl_3-silane and P(VDF-CTFE), one would expect the formation of a polymer blend of P(VDF-CTFE) and Cl_3-silane, which would change the nature of the polymer matrix in the 0-3 composites.

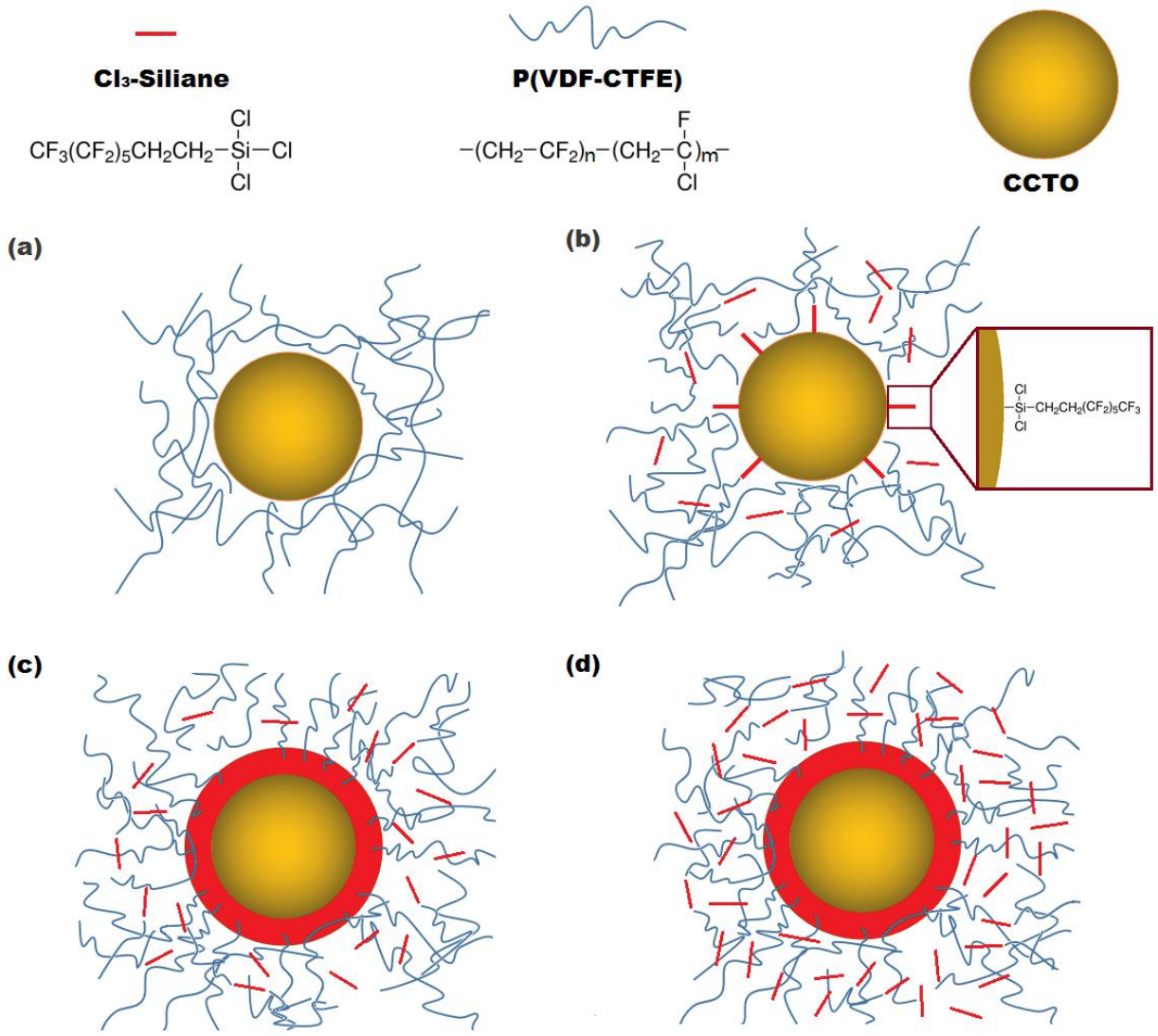

Figure 4-10 Schematic microstructure of the composites of CCTO, P(VDF-CTFE), and Cl_3-silane: a) no Cl_3-silane; b) the ratio of Cl_3-silane to CCTO is lower than the critical ratio; c) the ratio of Cl_3-silane to CCTO is the critical ratio; d) the ratio of Cl_3-silane to CCTO is high

4.5.2 Effect of Silicon Coupling Agent on Dielectric Properties

For the ceramic pretreatment, the 95% ethanol + 5% water solution of silicon coupling agent has been added to the mixture with calculated amounts. 0.5%, 1%, 1.5%, 2% and 3% silane coupling agent pretreated CCTO added into solutions respectively and fully mix with the polymer solution by 12 hours stir. Solution casting at 70 °C for 8 hours to evaporate the solvent and then anneal at 160 °C for 12 hours. It was found when the coupling agent amount is small (<1 wt%), the dielectric constant are almost independent with the agent amount; when the coupling agent amount are larger (>1 wt%), dielectric constant decreases with increasing agent amount linearly. As an example, the normalized dielectric constant and loss of the composite film with 15 vol% filler content as the function of coupling agent amount were plotted in **Figure 4-11**, the normalized dielectric constant and loss of the composite film with 20 vol% filler content as the function of coupling agent amount were plotted in **Figure 4-12**.

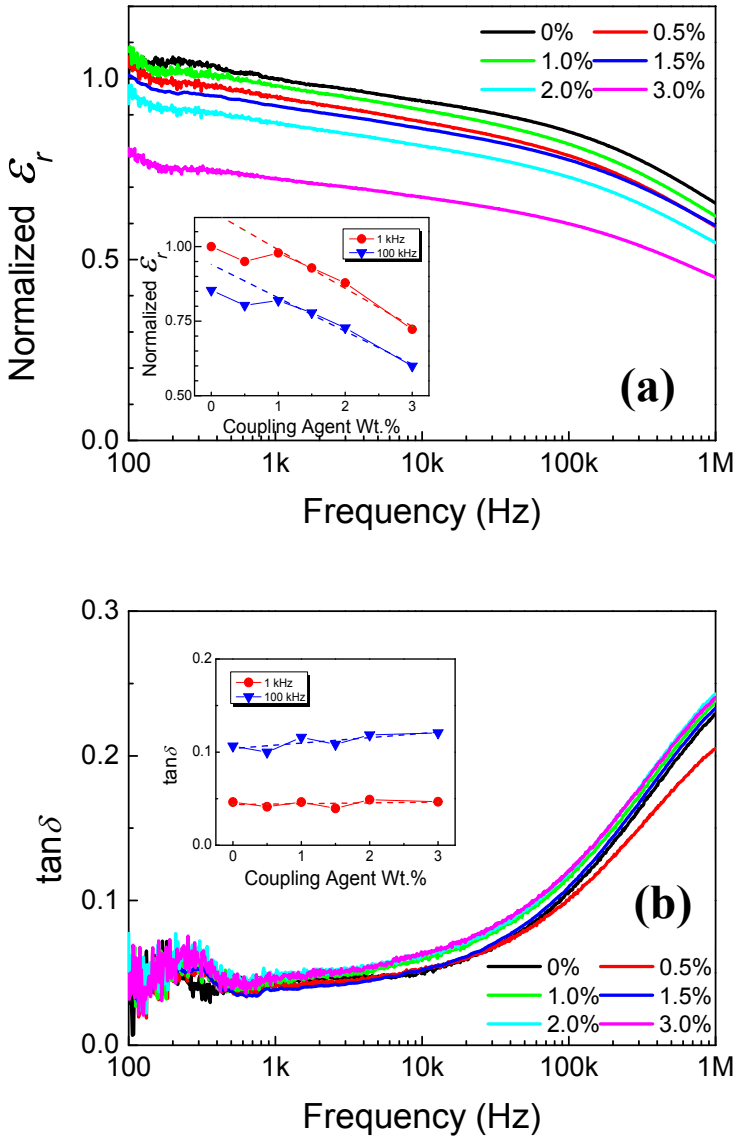

Figure 4-11 The normalized dielectric constant and dielectric loss of the composites using 15 vol.% Cl_3-silane coated CCTO with different ratios

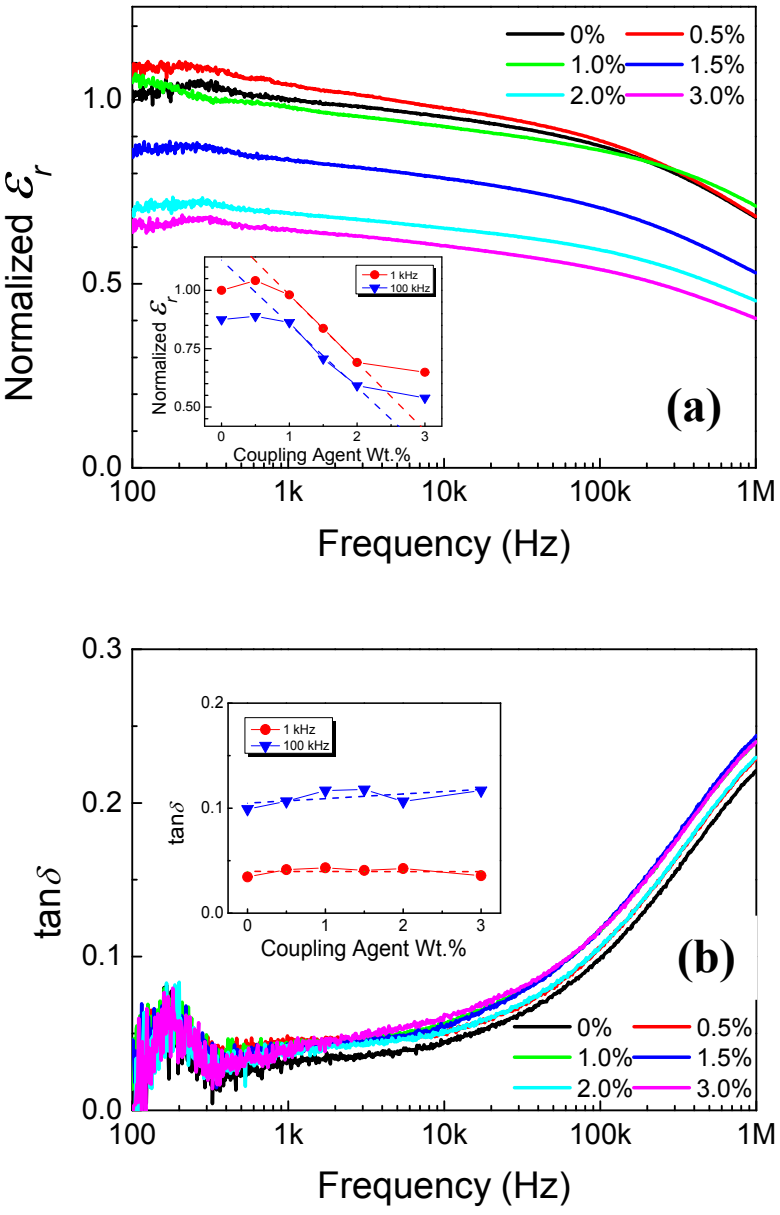

Figure 4-12 The normalized dielectric constant and dielectric loss of the composites using 20 vol.% Cl_3-silane coated CCTO with different ratios

Following above results and discussion, the composites with different CCTO contents are studied using CCTO particles coated with 1.0 wt.% Cl_3-silane. The ε_r of these composites at room temperature is shown in **Figure 4-13 (a)**. As expected, the ε_r increases with increasing CCTO content. For the composites with 20 vol.% of CCTO, a dielectric constant of more than 20 is obtained at 100 Hz. Besides the dielectric constant and loss, the breakdown strength of composites has been studied by place thin films between two electrodes of the holder and soaked in silicone oil, constantly increase the drive voltage until sample breakdown. With the increasing coupling agent amount, the breakdown strength continues increasing with a decreasing growth rate. As an example, the trend of breakdown strength of 20 vol% composites with different coupling agent amount was shown in **Figure 4-13 (b)**, in which the relatively high values for both dielectric constant and breakdown strength of samples with 1 wt% coupling agent have been confirmed.

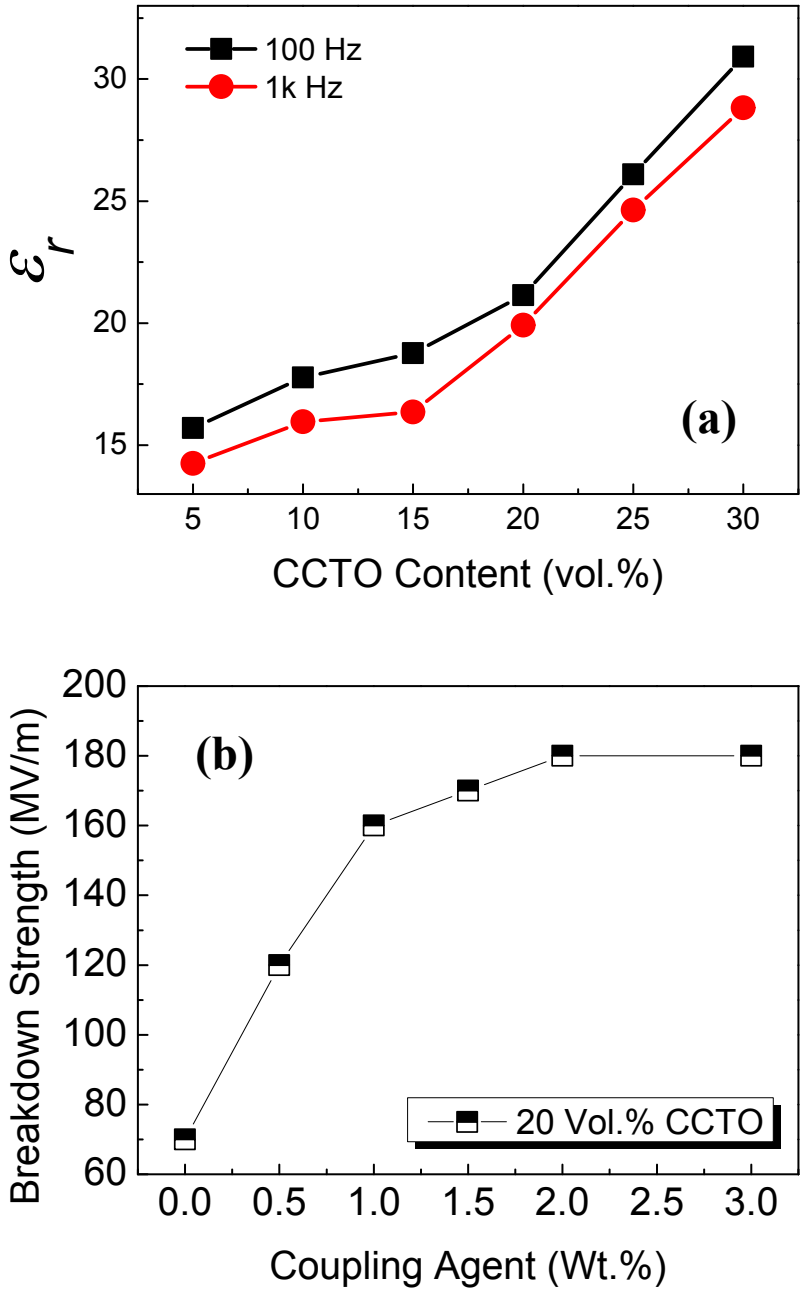

Figure 4-13 (a) The dielectric constant versus CCTO content for the composites using CCTO coated with 1 wt.% of Cl_3-silane and (b) The breakdown strength of 20 vol% composites with different coupling agent amount

4.6 Summary

The $CaCu_3Ti_4O_{12}$(CCTO)-P(VDF-CTFE) 88/12 mol.% composite films (10~20μm) with relatively high dielectric constant were prepared by the solution casting. To enhance the uniform distribution of ceramic filler, the coupling agent 1H, 1H, 2H, 2H Perfluorooctyltrichlorosilane were used. The dielectric constant and dielectric strength of the composites were studied using Impedance Analyzer and H.V. Supply Amplifier/Controller respectively for the energy density calculation. The annealing effect, amount of coupling agent and temperature dependence of dielectric properties were studied for these composite films; The dielectric properties and energy storage of CCTO-P(VDF-CTFE) composites with silane coupling agent were systematically studied. The dielectric constant (ε_r) of the composite increased with increasing volume fraction of CCTO at the frequencies from 100 Hz to 1MHz. The energy density of these nanocomposites can reach 4.61 J/cm^3 when CCTO volume fraction around 15 vol.% with 1 wt% silicon coupling agent and annealing under 160 °C environment. For the fixed CCTO percentage samples, the dielectric permittivity decreases as the frequency increases, the dielectric loss is increasing with the increasing frequency. The dielectric permittivity for all samples increases with increasing temperature, the dielectric loss also increase with temperature.

Chapter 5

Ceramic-Glass Composite

In this chapter, the ceramic-glass composites with potential properties for dielectric applications were prepared by the different methods and raw materials. The Barium Titanate $BaTiO_3$ and Barium Strontium Titanate $Ba_{0.5}Sr_{0.5}TiO_3$ were used as the ceramic fillers; the Silicon Dioxide SiO_2 was used as the glass composition. The processes of wet chemical coating, ball milling, solid/liquid phase sintering and spark plasma sintering were used to create composite pellets with different features. In the series of experiments, dielectric constant, dielectric loss, tunability, breakdown field and SEM images were recorded; preparing conditions including sintering temperature, particle size, SiO_2 content and introduction of vacancies were studied in details. By summarizing the results and analysis, the potential properties of high dielectric constant, high energy density, good tunability and low loss was achieved from the various of ceramic-glass composites.

5.1 Introduction

In previous chapters, the polymer-based composites with both conductor and dielectric ceramic fillers have been prepared by the processes including solution casting, hot pressing, annealing and silicon coupling agents. Although the two types of dielectrics created shown a good potential in some dielectric related applications, both of them are limited to a variety of other systems. The $Ti_3C_2T_X$-P(VDF-TrFE) composite thin films exhibited a high dielectric

constant, but their loss is also high due to the percolation between fillers; In addition, the breakdown strength of conductor-polymer composites with high filler content is very small therefore they can not meet the requirements of high voltage devices. For the other created composite, CCTO-P(VDF-CTFE) have a high dielectric strength up to 230 MV/m, but they are simultaneously shown a low dielectric constant of 18. Therefore the ceramic-polymer composites created are still limited in the applications requiring a high dielectric constant. As mentioned in Chapter 1 for introduction, ceramic-glasses combined the high dielectric constant and high dielectric strength due to their low porosity and high relative density. Additionally, by creating new glass-ceramic composites, the improved stability and reduced dielectric loss also can be achieved[1-3]. It has been proved by a number of observations that, for a ferroelectric perovskite ceramic such as Barium Titanate ($BaTiO_3$) and its related solid solution Barium Strontium Titanate ($Ba_XSr_{1-X})TiO_3$ system, a core-shell structure formed by nanoparticle and glass coat will result in the removal of porosity, and possibly forming new phases to reduce the polarization loss[4-8]. The properties of the core component such as reactivity and dielectric stability may be modified[9]. However, the effect of processing methods on the coated particles was not systematically in previous reports. For the purpose of providing diversified candidates of ceramic-glass composites for dielectric applications, processing methods including pretreatment, sintering, and activation, were studied on perovskite ceramic-based composites ($BaTiO_3$ and $Ba_{0.5}Sr_{0.5}TiO_3$).

5.2 Sample and Systems

In the preparation of ceramic-glass composites, $BaTiO_3$ and $Ba_{0.5}Sr_{0.5}TiO_3$ nanopowders with 99% purity from US Research Nanomaterials were utilized as the ferroelectric core; The different weight concentrations (2.5, 5, 10, 15, and 20 wt.%) of SiO_2 shell were coated by the chemical reaction between tetraethylorthosilicate (TEOS) and H_2O in suspension environment according to stöber process[10,11]. The composites were obtained by the process of press and sintering as introduced in Chapter 2. For the study on the influence of vacancies, a part of the $BaTiO_3$ nanopowders was pretreated under vacuum (pressure was controlled below 5×10^{-3} torr) and reducing atmosphere (25% hydrogen forming gas) respectively at different temperatures (850, 900, 950 and 1000 °C). The coated nanopowders were then sintered under different conditions. The parameters including particle size (100 and 200 nm), sintering temperature (1170, 1200 and 1230 °C) and sintering method (conventional sinter and SPS), were tried to learn the processing and microstructure effect on dielectric properties. The conditions of sample preparation and experiments are summarized in **Table 5-1**.

Table 5-1 Conditions of the preparation and experiments

Conditions	Value
Glass Contents	2.5, 5, 10, 15, and 20 wt.%
CuO Additivation	0, 1.0, 1.5, 2.0, 2.5, and 3.0 mol.%
Ceramic Fillers	$BaTiO_3$ and $Ba_{0.5}Sr_{0.5}TiO_3$
Sintering Temperature	1170, 1200 and 1230 °C
Pretreat Temperature	850, 900, 950 and 1000 °C
Sintering Methods	Conventional sinter and SPS
Vacuum Pretreatment	Below 5×10^{-3} torr
Atmosphere Pretreatment	25% hydrogen forming gas
Particle Size	100 and 200 nm
Testing Frequency	100 Hz ~ 1 MHz

5.3 $BaTiO_3$-SiO_2 Composites Prepared by Conventional Sintering

5.3.1 Structure and Morphology Characterization

5.3.1.1 X-ray Diffraction

For the analysis of coated $BaTiO_3$ ceramics sintered at 1230 °C, room temperature X-ray diffraction patterns of the samples with different preparation conditions were taken. In the **Figure 5-1**, **(a)** shows the patterns of the composites with different SiO_2 concentrations; **(b)** shows the patterns of $BaTiO_3$ coated with 2.5 wt.% SiO_2 and different pretreat temperatures; **(c)** shows the patterns of $BaTiO_3$ powders with different pretreat temperatures. The information can be obtained that the second phase for coated ceramic appeared after sintering. The appearance of secondary phase is due to the interface reactions between the original two phases $BaTiO_3$ and SiO_2 to form the Ba-Ti-Si-O compounds, the diffraction peaks of this phase are consistent with $Ba_2TiSi_2O_8$. Obviously, the intensity of diffraction peaks for secondary phase increases with the concentration of silica coated on $BaTiO_3$ particles; the diffraction peaks of $BaTiO_3$ phases decreases due to the consuming during the reactions. However, the samples with different pretreat temperatures shown the similar diffraction peaks, which indicates when the vacancies were introduced into $BaTiO_3$ ceramic by pretreatment, the crystal structure will maintain tetragonal symmetry. Moreover, it was evidenced in XRD that for all of the samples, the diffraction peaks of SiO_2 are difficult to be found, which was also indicated it is difficult to control the diffusion and reactions between SiO_2 and $BaTiO_3$ phases under high temperature.

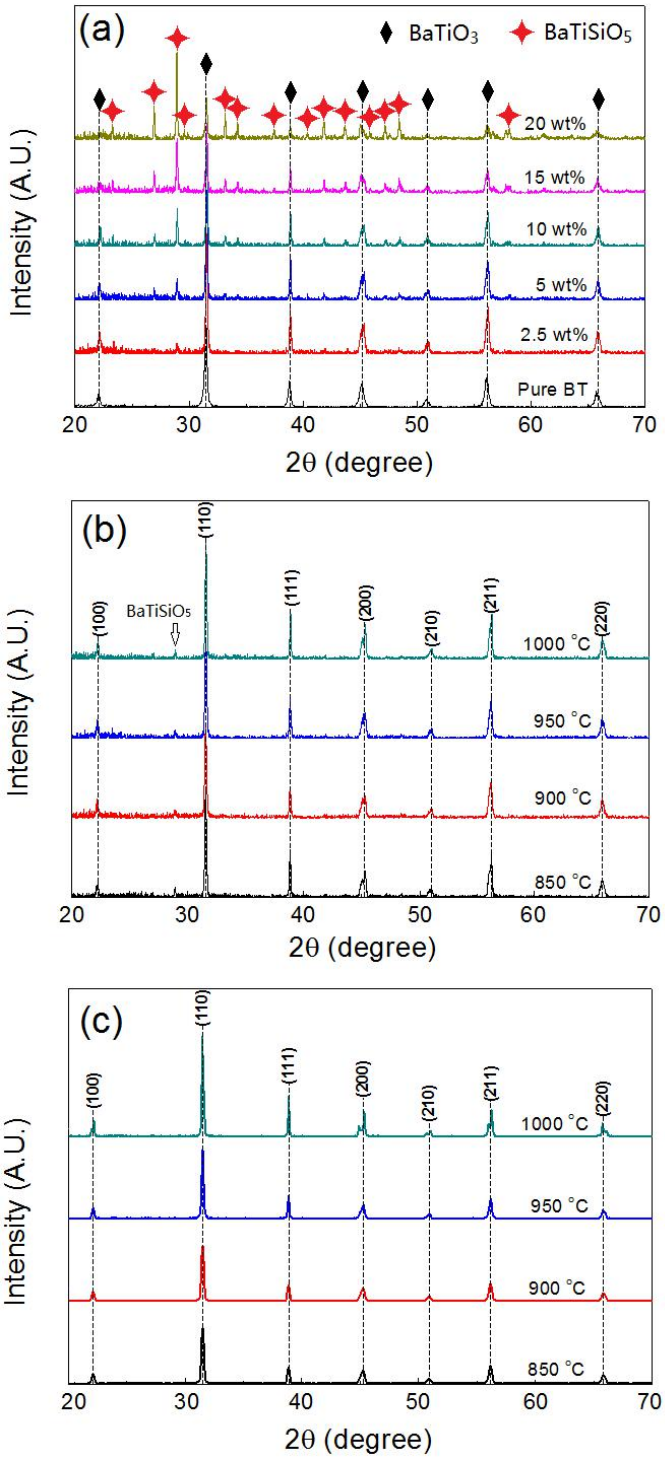

Figure 5-1 XRD patterns of coated $BaTiO_3$ (a) composites with different SiO_2 concentrations, (b) composites with different pretreat temperatures and (c) pretreated powders

5.3.1.2 Thickness of Glass Coating Layer

By the microscopes observation, the distribution and morphology of composites were recorded and the results are given. Firstly, the good uniformity of coating layers was verified by the TEM as shown in **Figure 5-2**. 100 nm and 200 nm $BaTiO_3$ particles coated with 2.5, 10 and 20 wt% SiO_2 were observed and shown from **Figure 5-2 (a)** to **(f)**. From the figures, the SiO_2 coated particles produced by stöber process got a tight connection between ceramic cores and uniform coating layers. The thickness of coating layer is increasing the percentage of SiO_2 for the size-fixed particles; the layer of 200 nm particles are thicker than that of 100 nm particles.

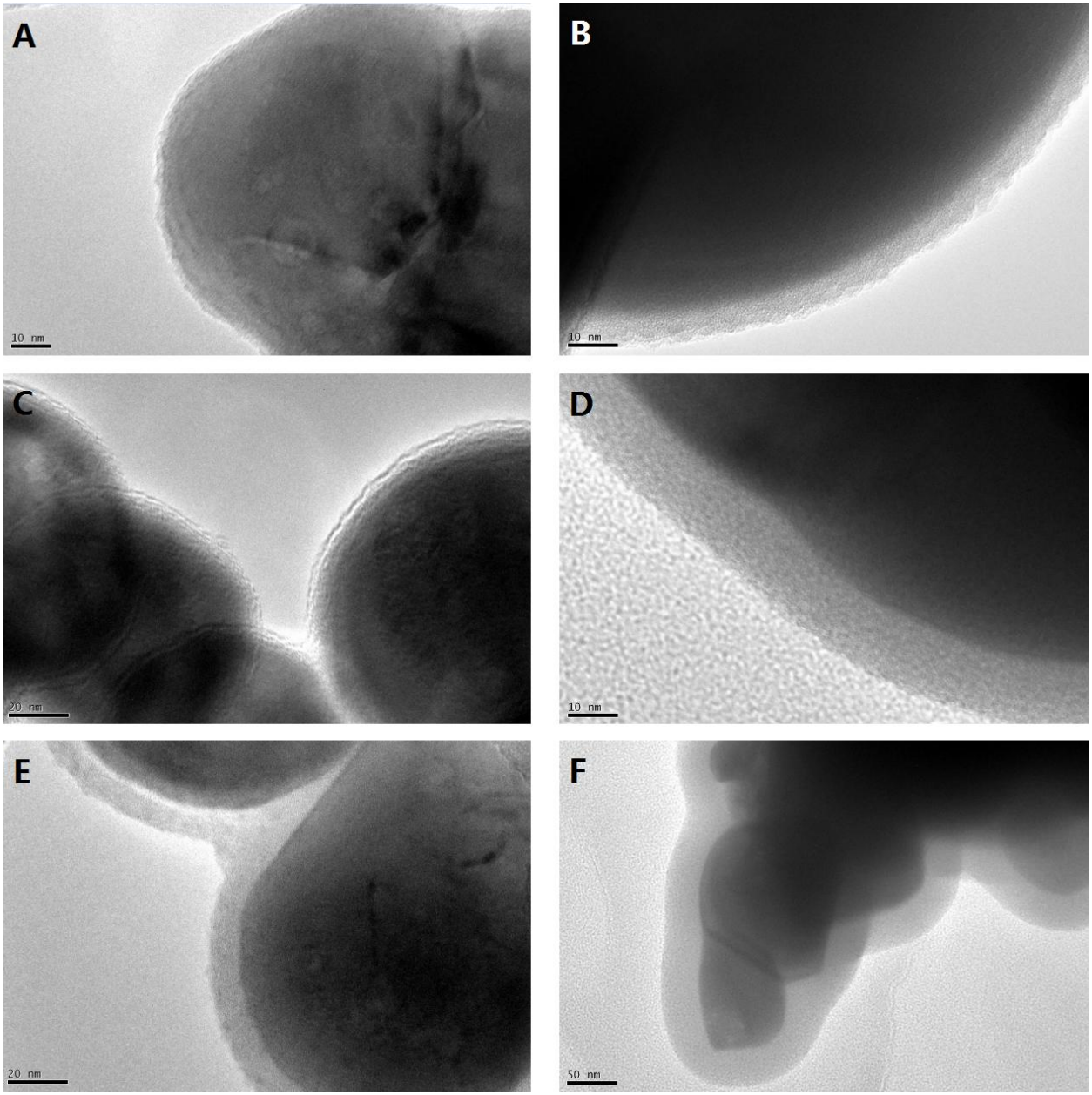

Figure 5-2 The transmission electron microscope (TEM) image of (a) and (b) 2.5% SiO_2 coated 100 nm and 200 nm $BaTiO_3$ particles, respectively; (c) and (d) 10% SiO_2 coated 100 nm and 200 nm $BaTiO_3$ particles, respectively; (e) and (f) 20% SiO_2 coated 100 nm and 200 nm $BaTiO_3$ particles, respectively

5.3.1.3 Scanning Electron Microscopy

For the confirmation of the composite microstructure with different processing conditions, the SEM picture of cross section of composite films was taken and shown as follows. The pictures of 20 wt% SiO_2 composites with different sintering temperatures and particle size were shown in **Figure 5-3**. The cross-section of low temperature (1170 °C) sintered pills have been shown in **Figure 5-3 (a)** and **(b)**, in which the loose structure of composites and weakly connected particles have been found. By the increase of sintering temperature, the composites obtained by 1200 and 1230 °C are showing much higher density. As shown in **Figure 5-3 (c)** and **(d)**, the 1200 °C sintered composites have shown the ceramic cores are separately distributed in the densely formed glass phase. With a higher sintering temperature up to 1230 °C which are shown in **Figure 5-3 (e)** and **(f)**, the densely connected grains were obtained, which is usually results in a high dielectric constant and low dielectric loss.

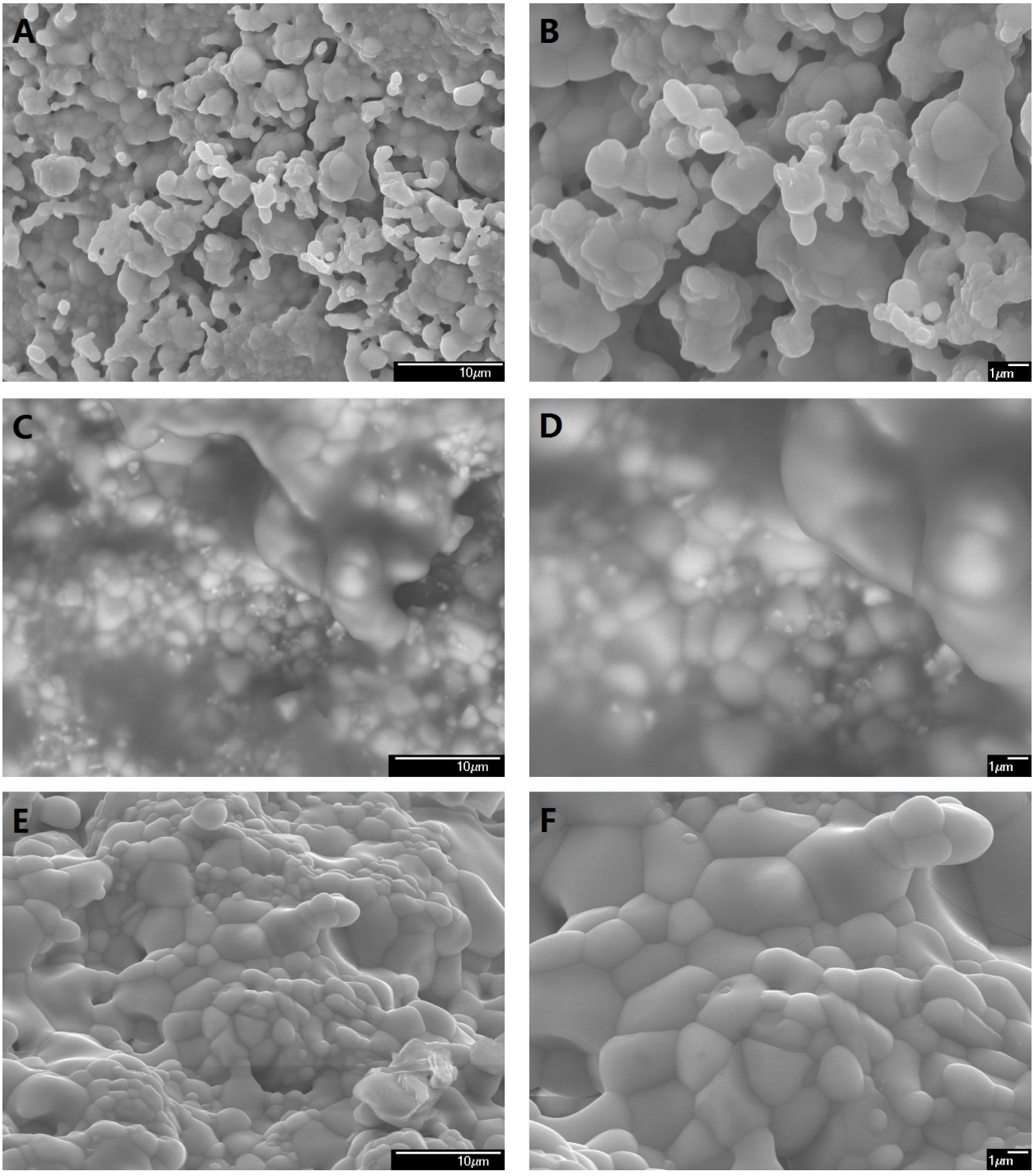

Figure 5-3 The scanning electron microscope (SEM) image of composites with different sintering temperatures of (a) and (b) 1170 °C; (c) and (d) 1200 °C; (e) and (f) 1230 °C

Then, the pictures of composites made by 200 nm nanopowders with fixed sintering temperature of 1230 °C and different SiO_2 contents were shown in **Figure 5-4**. It can be seen from that the structure of the composite pellet is relatively dense; The grains formed by sintering were uniformly distributed with the relatively consistent and small grain sizes. From the picture of the cross-section of the composite pellet with high content of SiO_2 up to 20 wt%, the increase of SiO_2 content the $BaTiO_3$ cores are homogeneously dispersed in a covered glass layer can be treated as an evidence of the liquid phase sintering in a favorable environment. Therefore, with the increasing of SiO_2 content, coating layers on nanoparticles can be treated as an inhibitor. The contact between $BaTiO_3$ cores was broken by SiO_2 coating layer, retains the original small grain size thus it can undertake the high-temperature sintering.

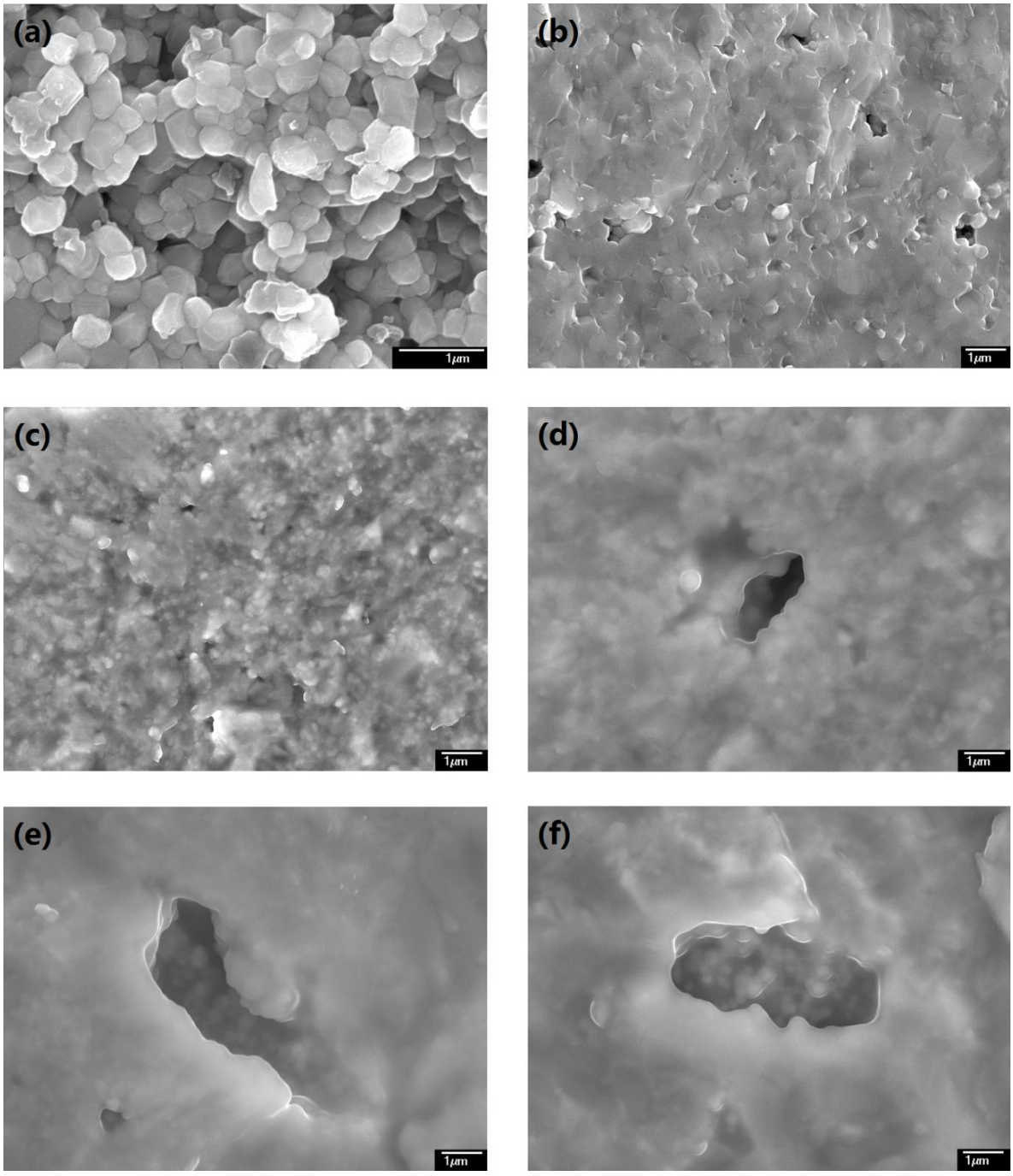

Figure 5-4 The scanning electron microscope (SEM) image of 200 nm composites with SiO_2 contents of (a) 0 wt%, (b) 2.5 wt%, (c) 5 wt%, (d) 10 wt%, (e) 15 wt%, and (f) 20 wt%

5.3.1.4 Microstructure of $BaTiO_3$-SiO_2 Composites with CuO Additivation

For the confirmation of the phase composition with different processing conditions, the phase structure of 2.5 wt% SiO_2 coated $BaTiO_3$ powder and sintered glass-ceramics with different contents of CuO (0, 1.0, 1.5, 2.0, 2.5, and 3.0 mol.%) were characterized by X-ray diffraction patterns are shown in **Figure 5-5**. As shown in the X-ray diffraction patterns, it can be seen that the SiO_2 coated powder have a pure perovskite structure without impurity, which indicates that the SiO_2 coating layer was in the form of amorphous. Similar to the powders, the patterns of sintered ceramics exhibit a perovskite structure without any peak of CuO, which indicates that Cu^{2+} have diffused into the ceramics in the form of a solid solution. However, as the content of CuO increased, the trace of $BaTiSiO_5$ phase was detected from the XRD patterns. Therefore, the interface reaction between $BaTiO_3$ and SiO_2 also happened without any effect from the doping. In addition, the gradually splitting peaks around 45o with an increase of CuO could be attributed to the crystal structure undergoes the mixed phases of pseudocubic and tetragonal to tetragonal phase transition[12].

Figure 5-5 XRD patterns of 2.5 wt% SiO_2 coated $BaTiO_3$ glass-ceramics with different contents of CuO

For the confirmation of the composite microstructure with different CuO contents, the SEM picture of the cross-section of composite films was taken and shown as follows. The pictures of 2.5 wt% SiO_2 coated $BaTiO_3$ glass-ceramics with different contents of CuO (0, 1.0, 1.5, 2.0, 2.5, 3.0 mol%) were shown in **Figure 5-6**. As previously reported, that coated SiO_2 layer could indicate a reaction between $BaTiO_3$ cores, which inhabits the grain growth of $BaTiO_3$ during sintering[13,14]. As a reflection, the grains sizes of glass-ceramics are about 200-300 nm, which is a little bigger than the powders due to the thin SiO_2 coating layer with inhibits the grain growth effectively. Compare with the glass-ceramic without doping which has a lot of pores in

cross-section, it is clear that and the density is greatly improved by CuO additives (0.5%-3.0%), the improved sinterability could be attributed to liquid phase with lower melting pointing.

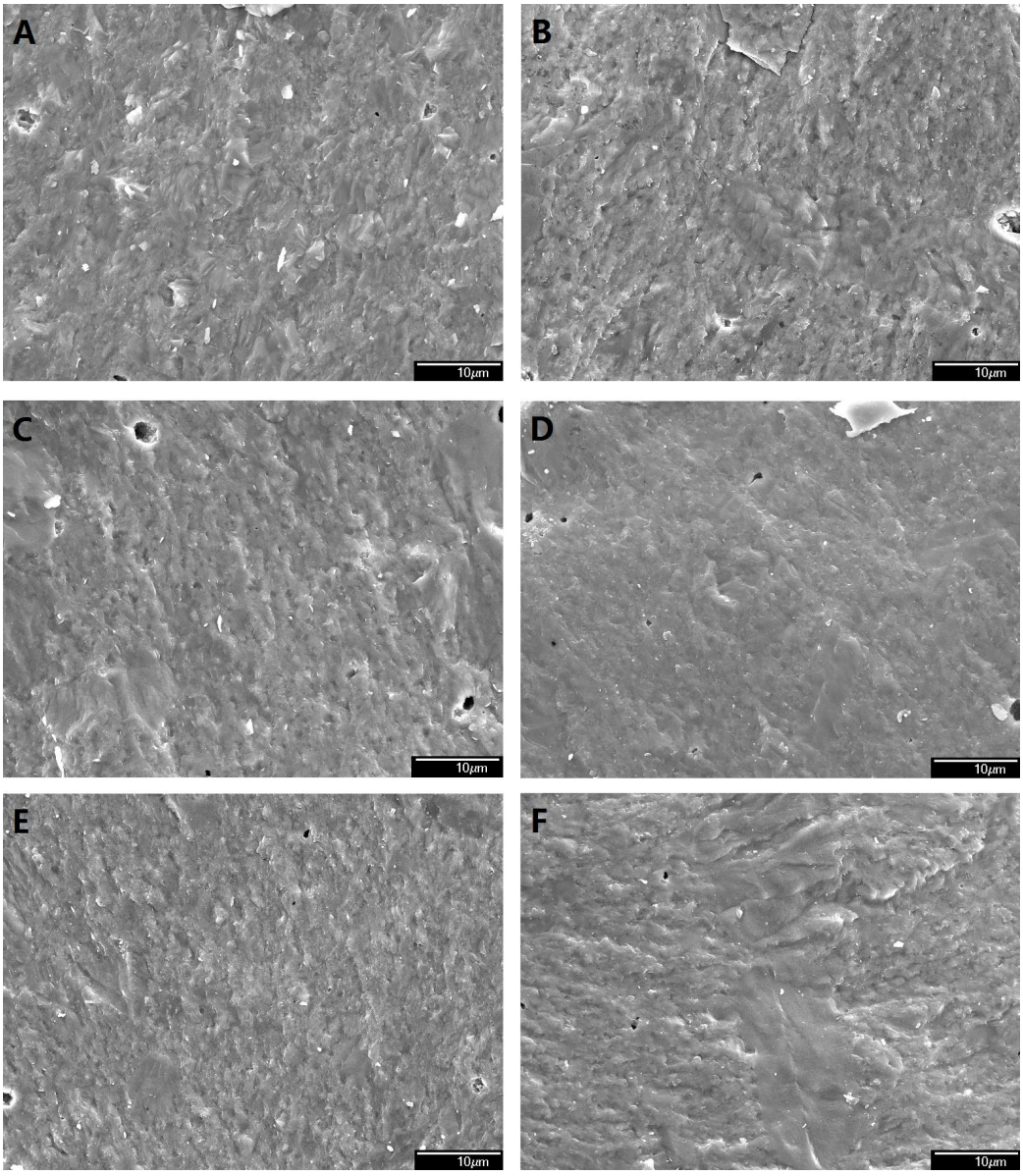

Figure 5-6 SEM pictures of 2.5 wt% SiO_2 coated $BaTiO_3$ glass-ceramics with different contents of CuO (a) 0, (b) 1.0, (c) 1.5, (d) 2.0, (e) 2.5, and (f) 3.0 mol%

5.3.2 Dielectric Properties

5.3.2.1 Frequency Dependency of Dielectric Properties at Room Temperature

Due to the largest increase on dielectric constant, the frequency dependence of dielectric properties of 950 °C hydrogen atmosphere pretreated composites are given in **Figure 5-7**, properties of 950 °C vacuum pretreated composites are given in **Figure 5-8**. As shown in **Figure 5-7 (a)**, an obvious decrease of dielectric constant was detected with the increasing of SiO_2 content, due to the addition of nonpolar composition and the consumption of ferroelectric composition. As the SiO_2 content increase from 0 to 20 wt%, the dielectric constant of the composite was reduced from 6049 to 35 (at 100Hz). The dielectric constant of 2.5 to 20 wt% composites shown a frequency dependence similar to the pure $BaTiO_3$ ceramics, which shows that the observed frequency dependence of the dielectric constant is mainly dominated by the behavior of the ferroelectric composition. However, for the pretreated ceramic without nonpolar SiO_2 shells, the dielectric behavior showed a stronger frequency dependence due to the conductivity increasing caused by vacancies introduction. From the dielectric loss of composites with various SiO_2 contents were shown in **Figure 5-7 (b)**, the first conclusion can be presented is that the losses of composites were effectively reduced by increasing the ratio of SiO_2 composition; It is also apparent that the huge difference on dielectric loss between 0 and 2.5 wt% SiO_2 composites (decreased from 0.32 to 0.05). This phenomenon suggested that the dielectric loss caused by vacancies can be partially eliminated by the formation of insulating layers, which was also confirmed as illustrated in **Figure 5-7 (c)**, the addition of SiO_2 composition decreases the conductivity of the composite resulting in an overall lower loss. By the changing of SiO_2 using amount, an adjustable conductivity range from 1.10×10^{-5} to 2.57×10^{-9} S/m (at 100Hz) of

the $BaTiO_3$-SiO_2 composites can be achieved. For the composites using 950 °C vacuum pretreated $BaTiO_3$, the ε_r are also increased compared with the composites using untreated $BaTiO_3$. For the composite with 2.5 wt.% SiO_2, ε_r is 3160 at 1k Hz. However, the high anδ of pretreated $BaTiO_3$ were reduced compared with hydrogen pretreated composites (decreased to 0.02 at 1k Hz). This phenomenon suggested that the dielectric loss caused by vacancies can be partially eliminated by the insulating layers, which was also confirmed by the largely decreased σ between the composites with 0 and 2.5 wt% SiO2 coating. Summarize the results discussed above, we can conclude that with pretreatment and SiO_2 coating, the composites have a high dielectric constant with a relatively low dielectric loss. Regarding the of dielectric properties with different testing frequencies, both of the composite using vacuum pretreated $BaTiO_3$ shown the weak frequency dependence, which is due to the modification of $BaTiO_3$ properties by vacancies introduction.

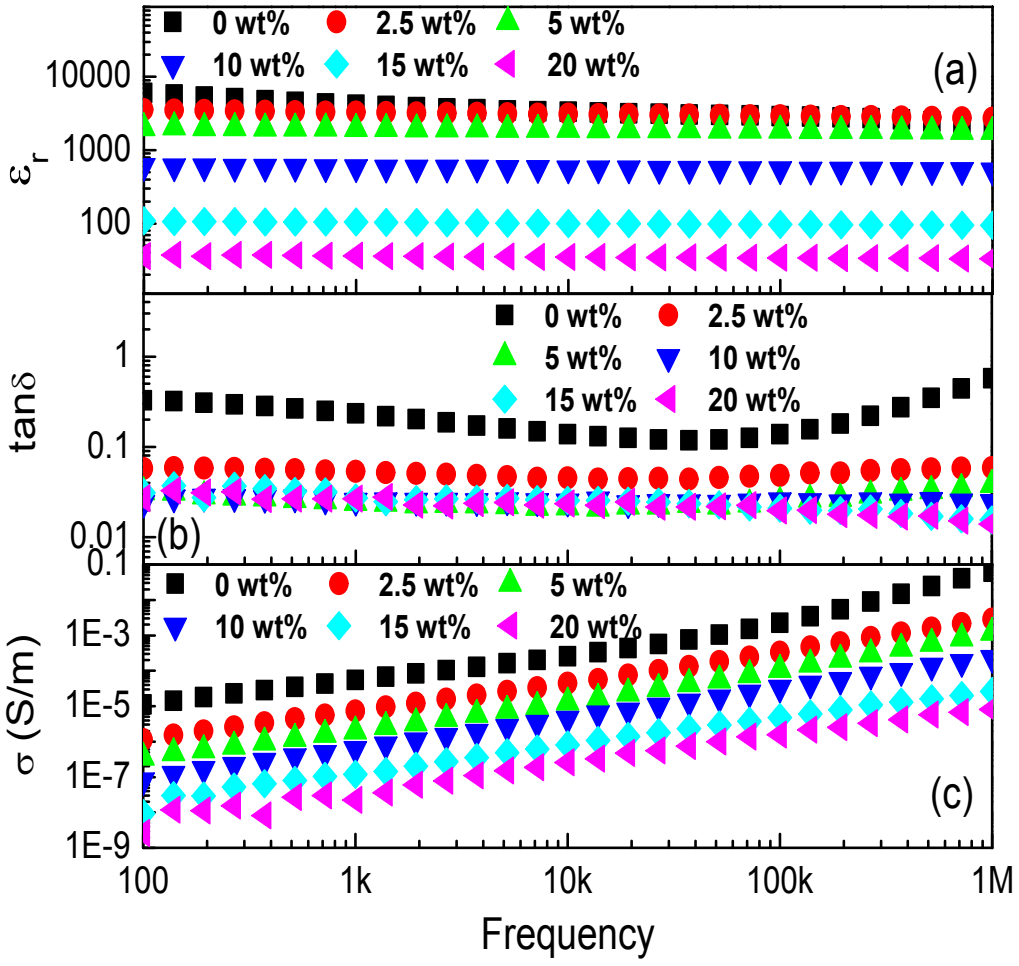

Figure 5-7 The (a) dielectric constant, (b) dielectric loss, and (c) conductivity against different of SiO_2 ratios with 950 °C hydrogen pretreatment

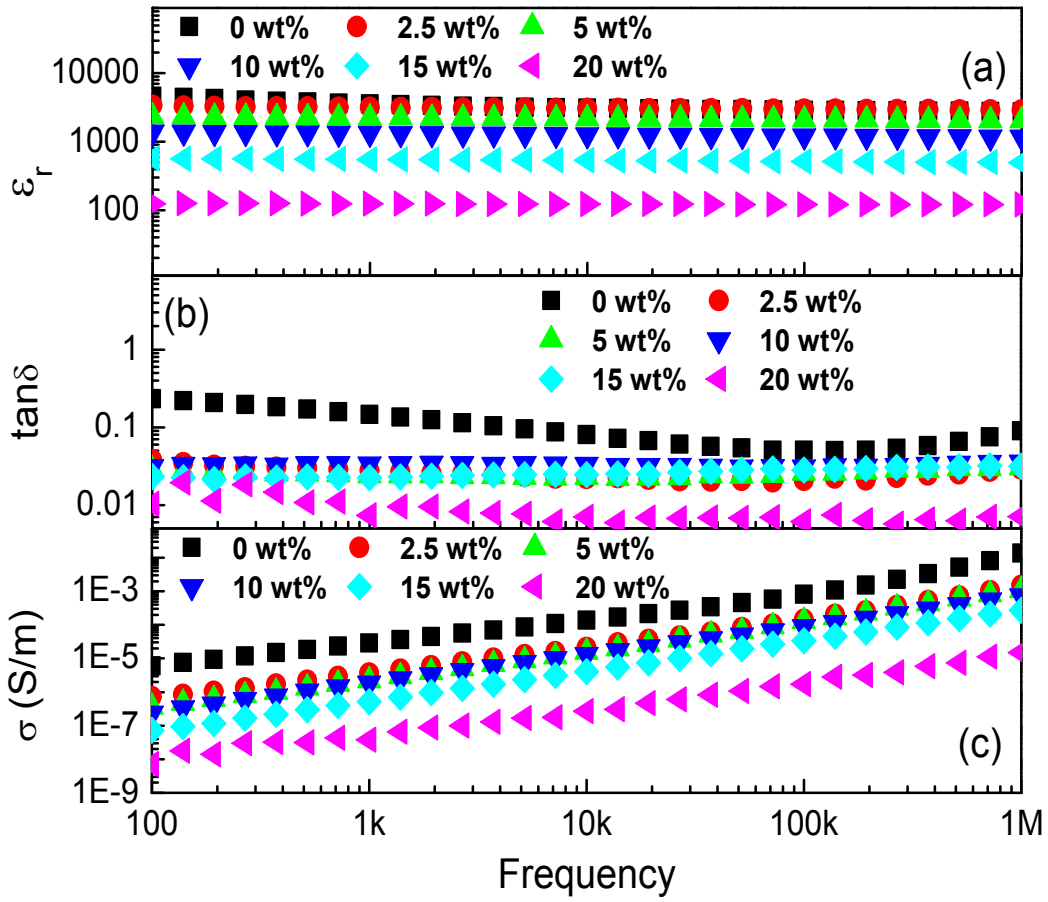

Figure 5-8 The (a) dielectric constant, (b) dielectric loss, and (c) conductivity against different of SiO_2 ratios with 950 °C vacuum pretreatment

5.3.2.2 Temperature Dependency of Dielectric Properties

The temperature dependence of the dielectric constant and loss of composites using 950 °C vacuum pretreated $BaTiO_3$ at 1 kHz, 10 kHz, 100 kHz, and 1 MHz are characterized in the range from -50 °C to 140 °C and the results were given in **Figure 5-9**. Obviously, the dielectric constant increase with the increasing filler concentration in the whole temperature range. A dielectric constant of more than 5700 was recorded at 100 Hz when the temperature

reaches 140 °C. Similar to the pure $BaTiO_3$ ceramics, there are two characteristic temperatures were found. Due to the increase of SiO_2 content, both of the phase transition temperatures are relocated at the higher temperature and the relaxation related peaks are the trend to become weaker and wider. Therefore, by adding the SiO_2 coating layer on $BaTiO_3$ ceramic cores, the dielectric stability with changing temperature can be improved. The temperature dependency of composites with 0, 0.5, 1.0, 1.5, 2.0, 2.5 and 3.0 wt% CuO were also shown in **Figure 5-10**. The phase transition temperatures of glass-ceramic are higher than pure $BaTiO_3$ ceramic and shift to a lower temperature with the increasing CuO content. A nearly 15 °C down shift appears with 3 mol% CuO additive. The broad of frequency dependent peaks in dielectric constant suggests that a diffuse phase transition was induced by CuO additives. And peaks of dielectric loss indicate that the glass-ceramics exhibit obvious relaxation when the content of CuO is lower than 2.0 mol%.

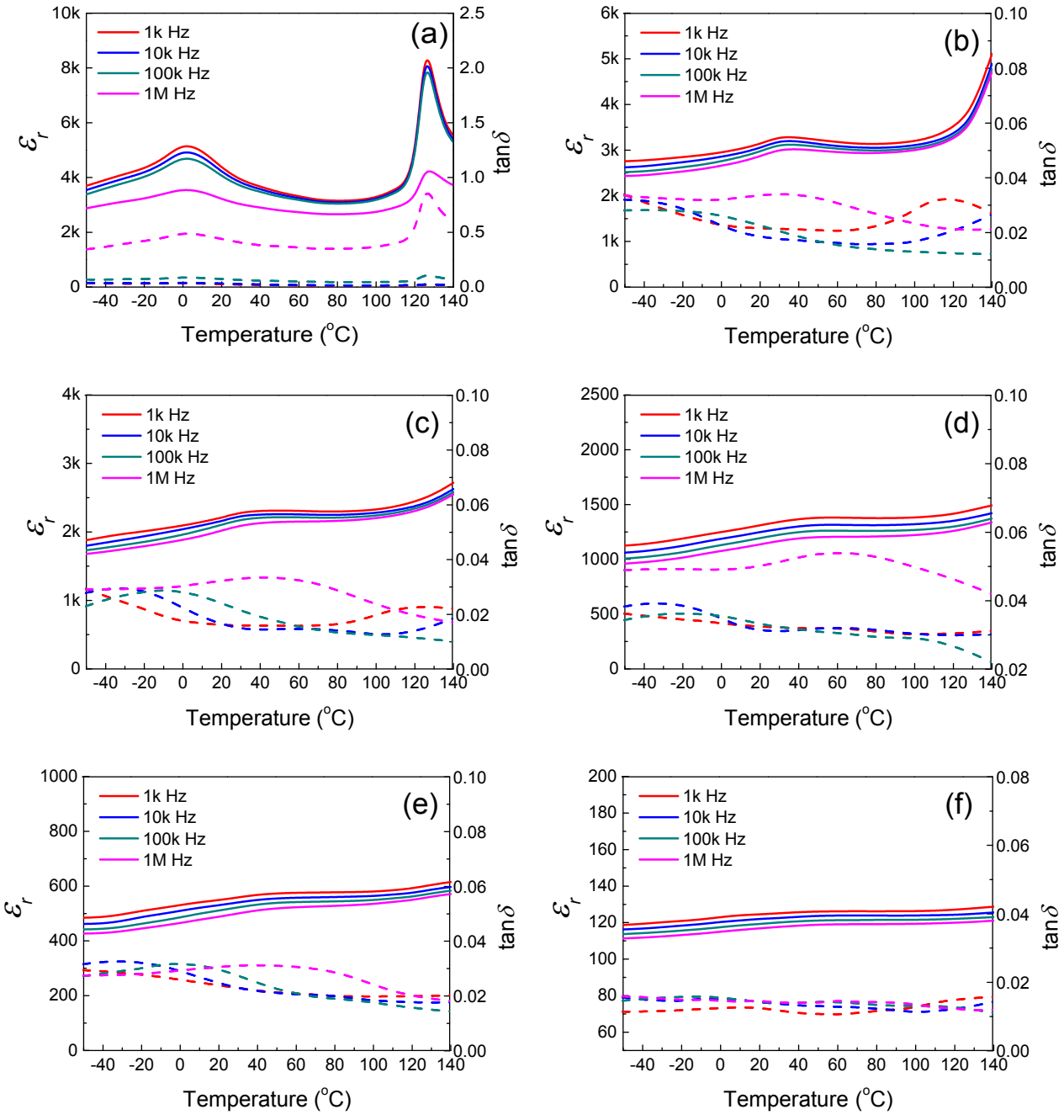

Figure 5-9 The temperature dependence of the dielectric constant and loss of composites: a), using $BaTiO_3$ without coating; b), c), d), e), f) using the 950 °C pretreated $BaTiO_3$ coated with 2.5, 5, 10, 15, 20 wt.% SiO_2.

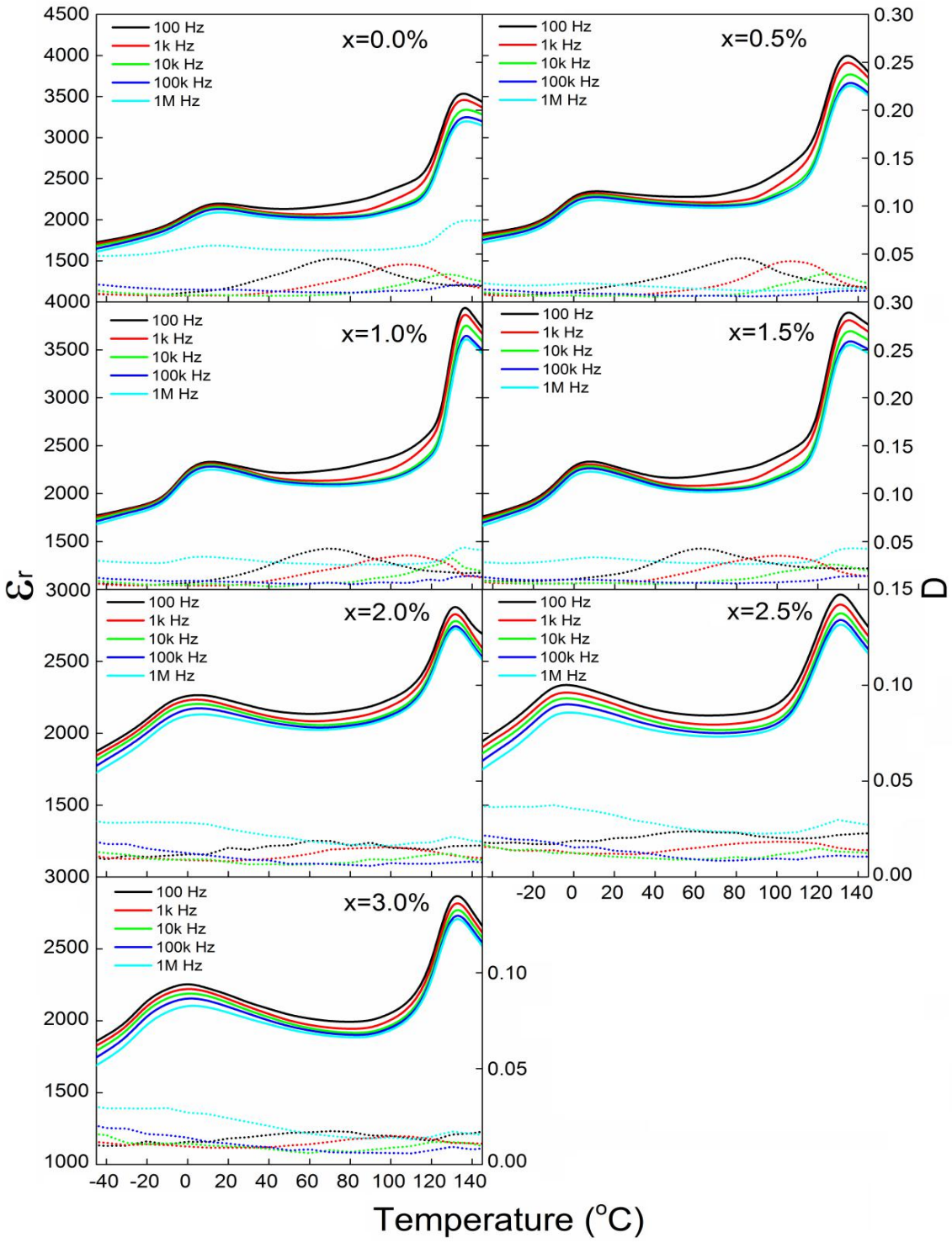

Figure 5-10 The temperature dependence of the dielectric constant and dielectric loss of sintered glass-ceramics with different content of CuO (X is the mol. Percentage of CuO)

5.3.2.3 P-E Loop and Energy Density

To further study the dielectric properties for the purpose of energy storage, the room temperature P-E hysteresis loops of SiO_2-$BaTiO_3$ composites were recorded under the electric fields prior to breakdown strength. Because of the largest increase in dielectric constant, the P-E loop of 950 °C hydrogen atmosphere pretreated composites was selected as representative and shown in **Figure 5-11 (a)**. Consistent with the change in dielectric constant, the saturated polarization of composites are obviously decreasing with the increase of SiO_2 content due to the consumption of ferroelectric composition. In contrast, the breakdown strength of $BaTiO_3$ sharply increased by the improving of coating layers which may be ascribed to the formation of high resistivity layer, high density, and small grain sizes during sintering (up to 45 MV/m for 20 wt% composites). The breakdown strength and saturated polarization with different pretreat temperatures were plotted and shown in **Figure 5-11 (b)**. From the summarized data, it can be found that the breakdown strength of composites is almost independent with pretreatment; However, there is a considerable increase in the saturated polarization after pretreatment especially for the hydrogen atmosphere pretreated composites (up to 35.05 μC/cm^2 for 950 °C composites). To evaluate the storage ability of composites, the energy density of each sample should be obtained:

$$W_E = \int_0^{P_{\max}} EdP = \int_0^{E_{\max}} PdE \tag{5-1}$$

where W_E are energy storage density (J/m^3), E and P are electric field and polarization, respectively. Based on Equation 5-1, the energy density of the composites can be calculated by integrating the area between the saturated polarization axis and discharge curve of the P-E loop.

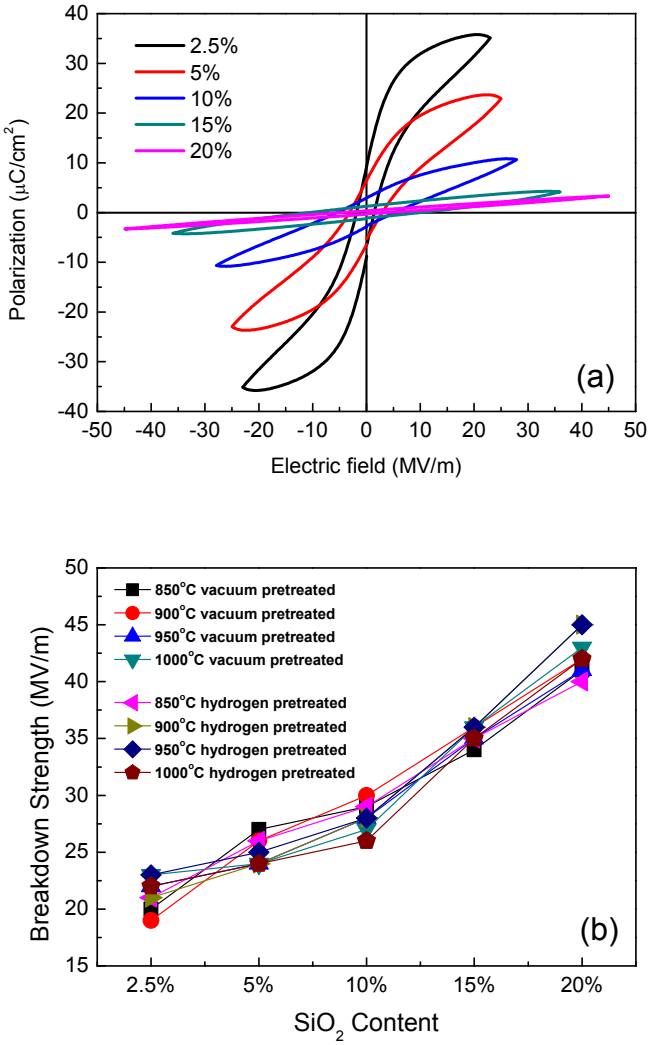

Figure 5-11 (a) The P-E loops of 950 °C hydrogen pretreated composites at room temperature and (b) the breakdown strength as the function of SiO_2 content with different pretreat methods and temperatures

5.3.3 Discussion

5.3.3.1 CuO Content Dependency of Properties

The dielectric properties and the P-E loop of $BaTiO_3$-SiO_2 composites with different SiO_2 content were recorded and shown as follows. The dielectric constant and loss of $BaTiO_3$-SiO_2 composites with different CuO contents as a function of testing frequency were shown in **Figure 5-12**. It is found that the dielectric constant and loss are significantly affected by the content of CuO. The dielectric constant is enhanced by 0.5 mol% CuO additive and then decreases when the content of CuO further increases. The dielectric loss decreases with CuO when the content is below 2.0 mol% and increases when CuO further increases to 3.0 mol%. At room temperature, the dielectric constants and loss of 2.5 wt% SiO_2 coated $BaTiO_3$-xCuO (x=0, 1.0, 1.5, 2.0, 2.5, 3.0) at 100 Hz were recorded as 2158, 2307, 2262, 2223, 2192, 2127 and 0.020, 0.019, 0.018, 0.019, 0.014, 0.021, 0.014, respectively.

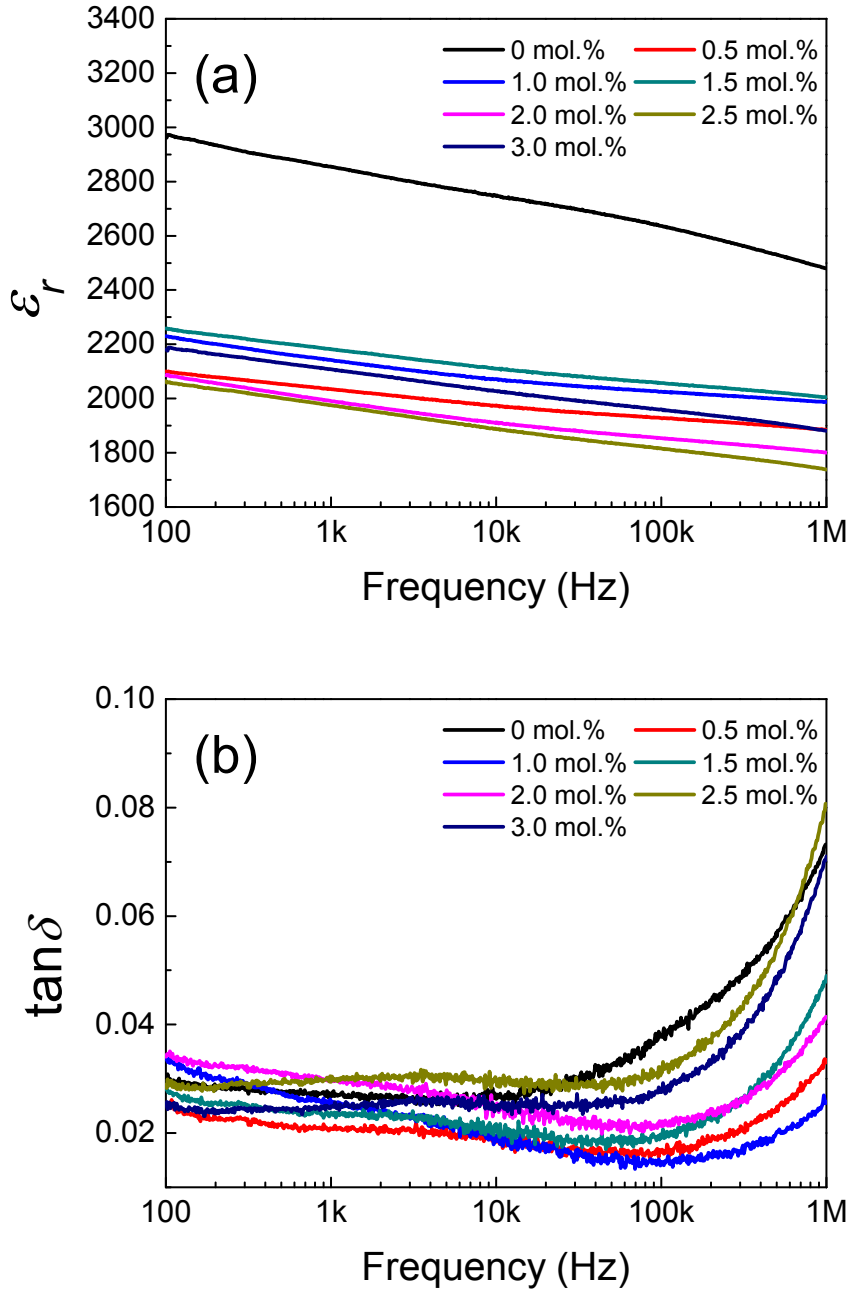

Figure 5-12 The (a) dielectric constant and (b) loss of SiO_2 coated $BaTiO_3$ glass-ceramics with different contents of CuO

The P-E hysteresis loops of sintered glass-ceramics with x mol% of CuO (x=0, 1.0, 1.5, 2.0, 2.5, 3.0) tested at room temperature under electric fields prior to breakdown strength are shown in **Figure 5-13**. From the P-E loops, the energy density of composites was increased by the adding of CuO. Compare with the sample without CuO, both of the satisfied polarization and breakdown strength were improved with CuO doping. The composite with 2.0 wt% CuO has shown the maximum value of energy density of 1.42 J/cm^3.

As discussed previously, the dielectric breakdown strength and polarization are responsible for the application of energy storage. The energy density of composites with different amount of CuO were calculated by integrating the areas between the polarization and charge curve or discharge curves in the P-E hysteresis loops from **Figure 5-13** and the efficiencies are calculated by the ratios of discharge energy density and charge energy density, the calculated results of properties are shown in **Table 5-2** and the trends of properties change with CuO content were shown in **Figure 5-14**.

Figure 5-13 P-E hysteresis loops of glass-ceramics with different content of CuO

Table 5-2 The properties of sintered glass-ceramics as a function of the content of CuO

CuO xmol%	E_b （kv/cm）	P_m ($\mu C/cm^2$)	P_r ($\mu C/cm^2$)	E_c （kv/cm）	Charge (J/cm^3)	Discharge (J/cm^3)	Efficiency (%)
0	140	18.51	7.56	15.47	1.06	0.37	0.35
0.5	200	25.16	8.15	13.53	1.66	0.72	0.43
1.0	200	25.45	8.41	12.25	1.70	0.79	0.45
1.5	220	26.58	9.40	13.48	1.89	0.87	0.46
2.0	290	28.32	6.95	14.92	2.70	1.42	0.53
2.5	240	27.58	6.20	9.45	2.08	1.10	0.52
3.0	220	27.02	6.18	9.31	1.84	0.96	0.52

Figure 5-14 Breakdown strength, polarizations, coercive field, charge energy density, discharge energy density, and energy storage efficiency of sintered glass-ceramics as a function of the content of CuO additives

5.3.3.2 Influence of Pretreatment

Recorded form the impedance analyzer, the dielectric constant of $BaTiO_3$ based composites with fixed SiO_2 content (2.5 wt%) as the function of vacuum pretreat temperatures at room temperature are shown in **Figure 5-15 (a)** and **(b)** respectively. In the whole range of tested frequencies (100 to 1M Hz), an obvious increase of dielectric constant was detected with the increasing of pretreat temperatures up to 950 °C, along with a low an δ; However, by further increase the temperature to 1000 °C, the dielectric constant drops down. After vacuum pretreatment, the dielectric constants of composites show a frequency dependence similar to the pure ceramic, which indicates that the observed frequency dependence of the dielectric constant is mainly dominated by the behavior of $BaTiO_3$. Interestingly, composites using pretreated $BaTiO_3$ with a high SiO_2 content shows the higher increasing ratio of ε_r compares with the composites using untreated $BaTiO_3$. For the composite using 950 °C pretreated $BaTiO_3$ with 20 wt.% SiO_2, ε_r increased to 120 at 1k Hz, which is about six times of the composite without pretreatment ($\varepsilon r = 20$).

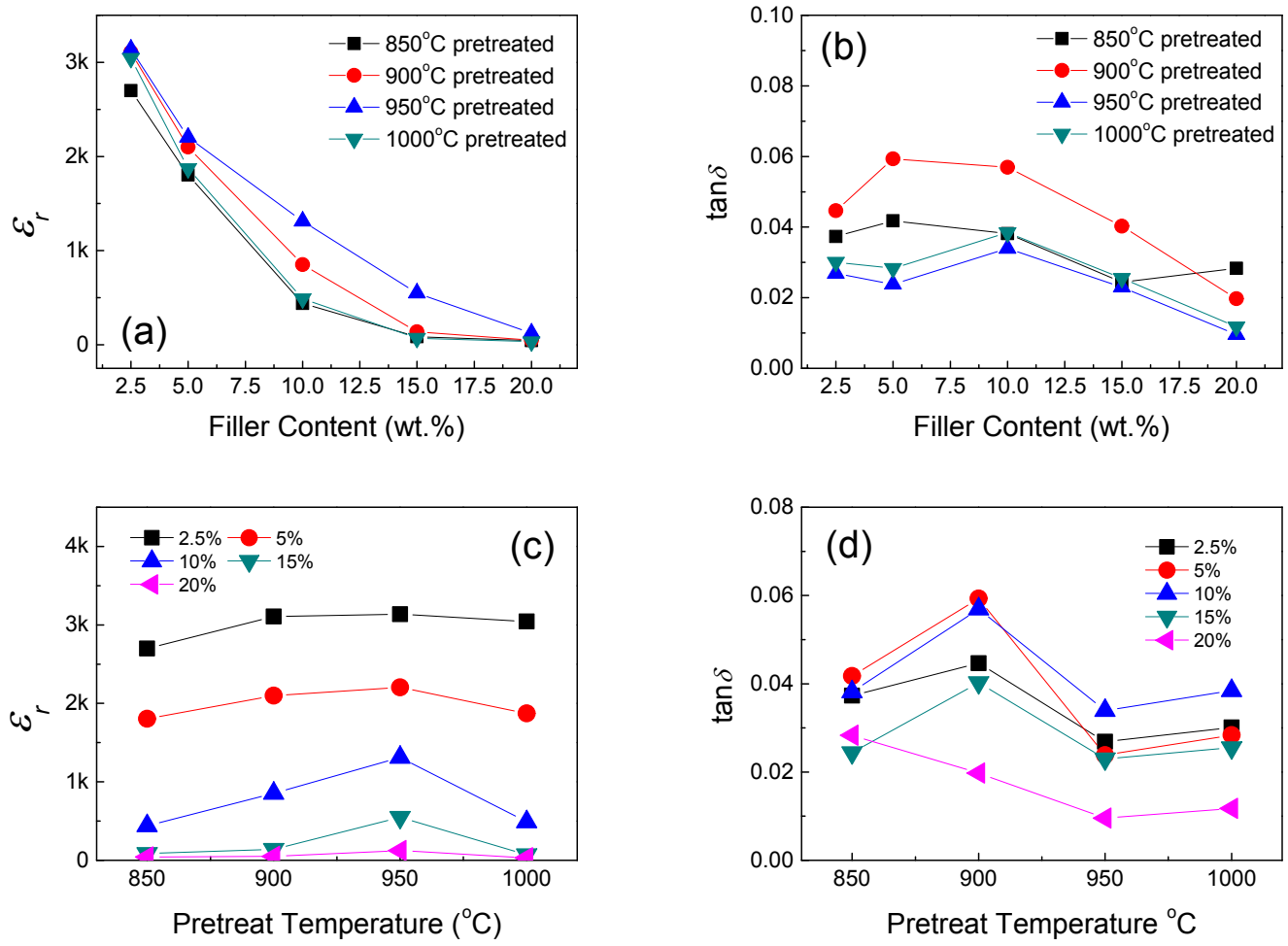

Figure 5-15 The properties of the composites at 1k Hz: a) dielectric constant and b) loss of composites as the functions of SiO_2 content; c) dielectric constant and d) loss of composites as the functions of vacuum pretreat temperatures

By summarizing the representative parameter of the conductivity for all samples with different prepare conditions, the processing effect and adjustment ranges of the electric property for SiO_2-$BaTiO_3$ composites were evaluated and shown in **Figure 5-16 (a)**. For all of the tested

samples, the logarithm of conductivity almost linearly decreased with the increasing SiO_2 content; Compare with vacuum pretreated samples, the composites with hydrogen atmosphere pretreatment behaved a better predictability and expanded the range of conductivity. Among the samples, 950 °C hydrogen atmosphere pretreated composites have shown the largest adjustability of conductivity. In other words, by using the method of hydrogen atmosphere pretreatment, the conductivity of composites can be adjusted in the range of 10^{-6} to 10^{-9} S/m; Considering the adjustable pretreatment conditions, this range may be further extended, to better meet the demand of a variety of applications. In addition, as an intuitive index of the capacitive ability, the trend of energy density as the functions of SiO_2 content with different pretreatment for all the composite was shown in **Figure 5-16 (b)**. From the summarized data, the energy density of composites are mainly dependent on the SiO_2 content and achieved the maximum with 2.5 wt% of SiO_2 coating. The vacancies introduced by pretreatment effectively improved the saturated polarization, simultaneously the high breakdown strengths obtained by SiO_2 addition were maintained; For the same pretreat temperature, hydrogen atmosphere pretreatment gives a larger energy density improvement compare with the vacuum pretreatment. With a 950 °C hydrogen atmosphere pretreatment, the 2.5 wt% SiO_2-$BaTiO_3$ composites achieved the maximum energy density (up to 1.82 J/cm^3), which make the composites potential in dielectric energy storage applications.

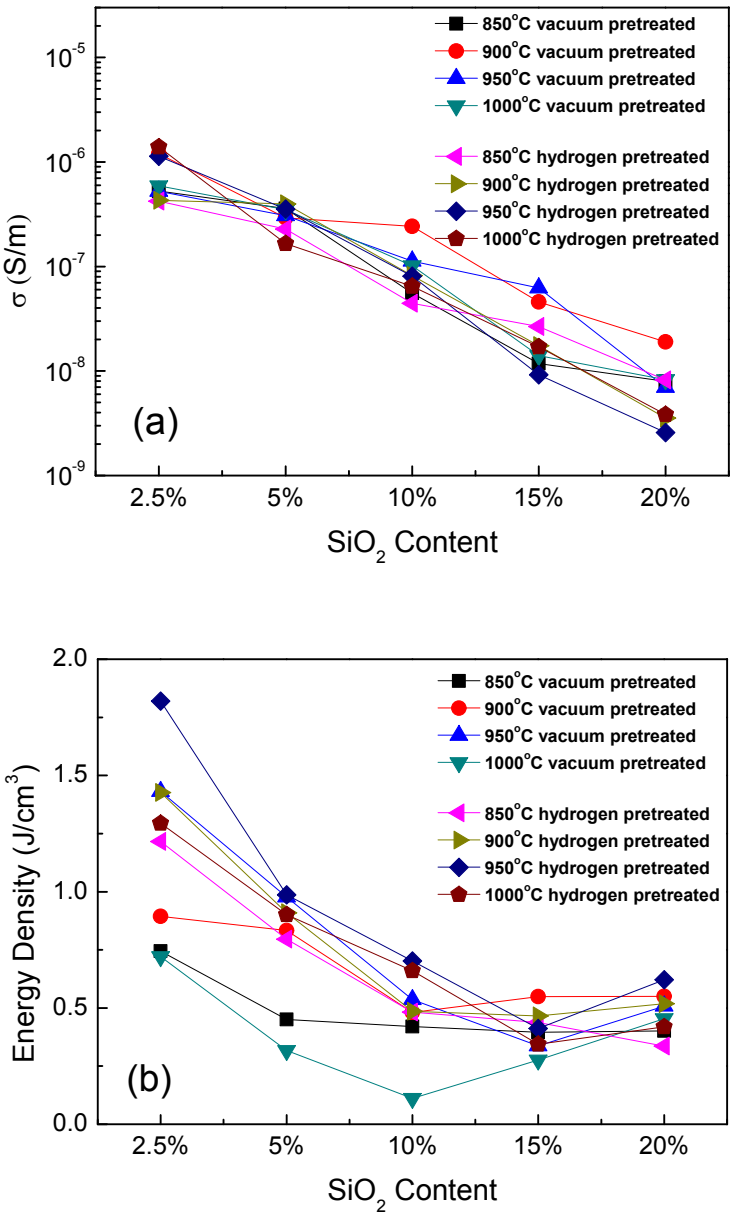

Figure 5-16 (a) The conductivity and (b) the energy density of samples with different pretreatment as the functions of SiO_2 content

5.3.3.3 Effect of Particle Size

The previously discussed 950 °C hydrogen atmosphere pretreated composites were prepared by using the 200 nm $BaTiO_3$ nanoparticles. For the purpose of finding the particle size effect on dielectric properties of composites, the room temperature P-E hysteresis loops of 100 nm SiO_2-$BaTiO_3$ composites were recorded from 950 °C pretreated composites and shown in **Figure 5-17**. Consistent with the change in dielectric constant, the polarization of composites are slightly smaller compared with the 200 nm composites. As an example, the saturated polarization of 950 °C pretreated 2.5 wt% 100 nm composites is 34.55 $\mu C/cm^2$, which is smaller than that of 200 nm sample (35.05 $\mu C/cm^2$). From P-E loops, the breakdown strength of 100 nm SiO^2-$BaTiO^3$ composites is also decreased. With the different SiO_2 content, the breakdown strength changing from 17 to 36 MV/m, which are much smaller than that of 200 nm sample when the content is fixed (from 23 to 45 MV/m). By calculation, the maximum energy density of 100 nm composites is decreased to 1.19 J/cm^3, due to the smaller polarization, smaller breakdown strength, and larger loop area.

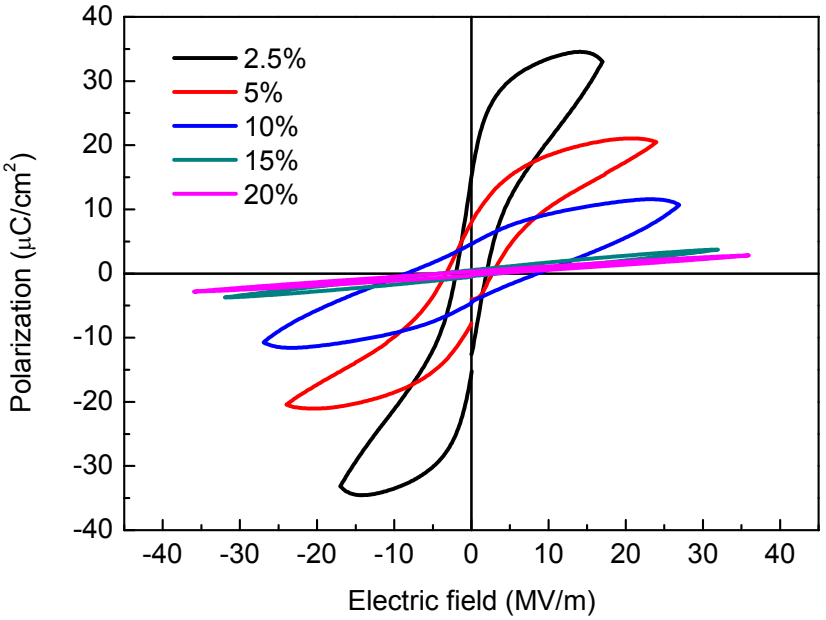

Figure 5-17 The P-E loops of 950 °C pretreated 100 nm composites at room temperature

5.4 $BaTiO_3$-SiO_2 Composites Prepared by Spark Plasma Sintering

5.4.1 Structure and Morphology Characterization

5.4.1.1 X-ray Diffraction

For the analysis of SPS ceramics, room temperature X-ray diffraction patterns were taken. The composite pellets created by using 2.5 wt.% SiO_2 coated 100 nm nanopowders provided by Auburn University were used as the representative samples in the study. The comparison of XRD patterns between conventional sintering and SPS were shown in **Figure 5-18 (a)**. From the figure, the second phase of $Ba_2TiSi_2O_8$ was found from both conventional sintering and SPS samples. However, there is difference between the two sintering methods. Compare with

conventional sintering, the SPS composites have shown an increased intensity on the peaks of $Ba_2TiSi_2O_8$; additionally, a much broader peak was found near the peaks of (100) form $BaTiO_3$, which might be an evidence of the appearance of amorphous. Although the samples showed the similar phases, the intensity ratio between the two phases are differed greatly between the composites by different methods, and this ratio was changed with the horizontal rotation of the composite piece in XRD testing. The XRD patterns of SPS composites with different scan angles were shown in **Figure 5-18 (b)**. The phenomenon suggested that the crystallinity of each phase in SPS composites maybe influenced by orientations.

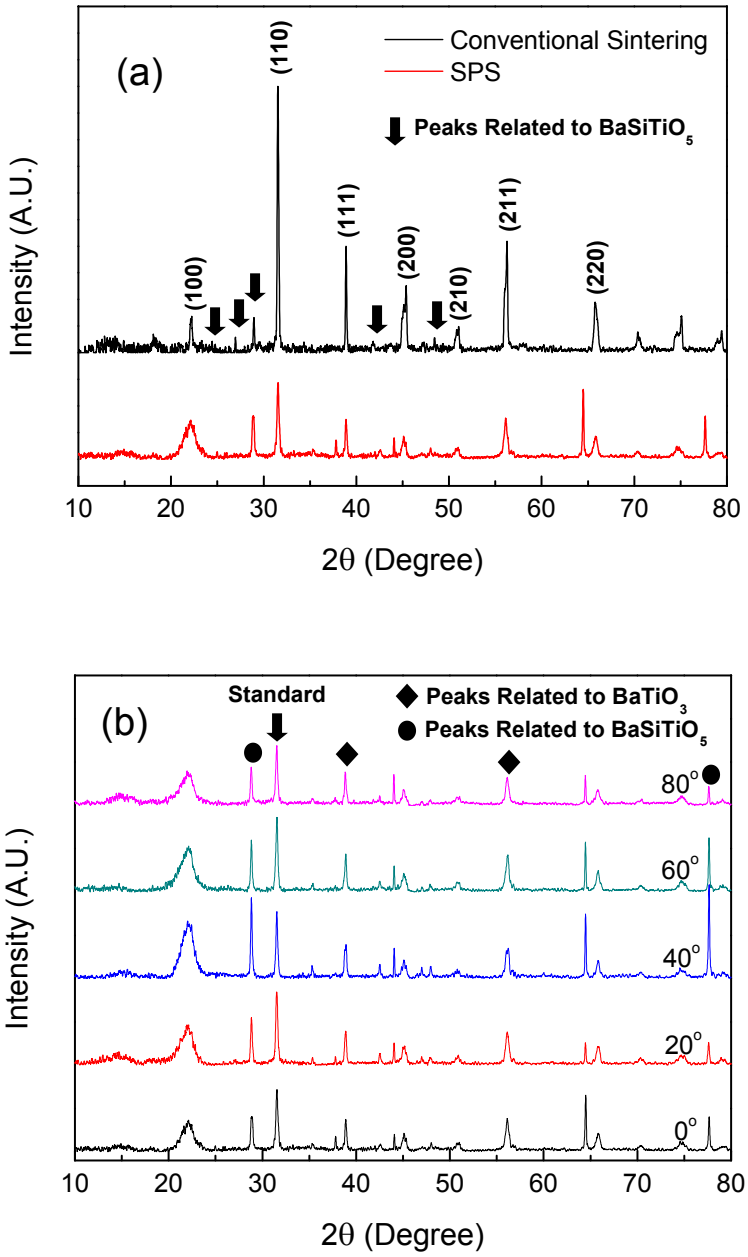

Figure 5-18 XRD patterns of (a) $BaTiO_3$-SiO_2 composites by conventional sintering and SPS, (b) SPS composites with different scan angles

For the research on the orientation dependency of microstructure, XRD was taken on the sample by different scan angles. The horizontally scanning of 0-90° were taken in the testing process as shown in **Figure 5-19**, where the angle from incident beam to the detector was defined as diffracted angle 2θ and the rotate angle of the sample was defined as plane rotation angle Φ. Information including intensity, peak height, and peak breadth was recorded; the peak area FWHM (Full width at half maximum) can be obtained by calculation. For the comparison between two phases, a sharp peak of $BaTiO_3$ from (110) at $2\theta = 31.5°$ was used as the standard for the calculation of the relative intensity of other peaks. In the comparison, the peaks at 39° and 56° were selected to represent $BaTiO_3$ phase; the peaks at 29° and 77.5° were selected to represent $Ba_2TiSi_2O_8$ phase. The peaks representing both $BaTiO_3$ and SiO_2 were marked in **Figure 5-18 (b)**. As the results, the trend of relative intensity, peak area and FWHM of both phases as the functions of scan angle were shown in **Figure 5-20**, **Figure 5-21** and **Figure 5-22**, respectively. From the figures, all of the factors for $BaTiO_3$ related peaks are keeping constant while scan angle changes; however, a clear maximum of intensity and peak area of $Ba_2TiSi_2O_8$ related peaks were detached at the scan angle of 40°, which is an evidence that the formation of $Ba_2TiSi_2O_8$ phase in SPS process is strongly influenced by the origination. The data of different factors at the maximum intensity angle was listed in **Table 5-3**.

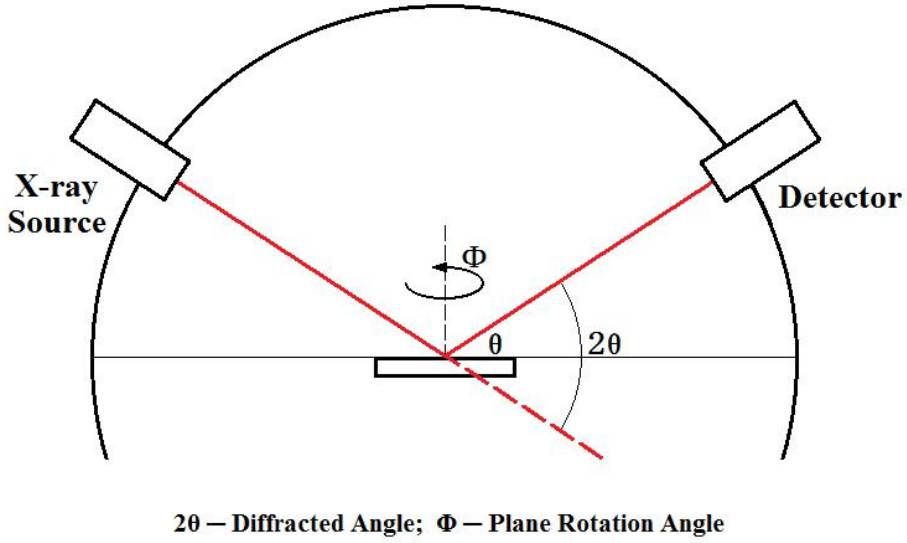

Figure 5-19 The schematic of horizontally scanning taken in the testing process

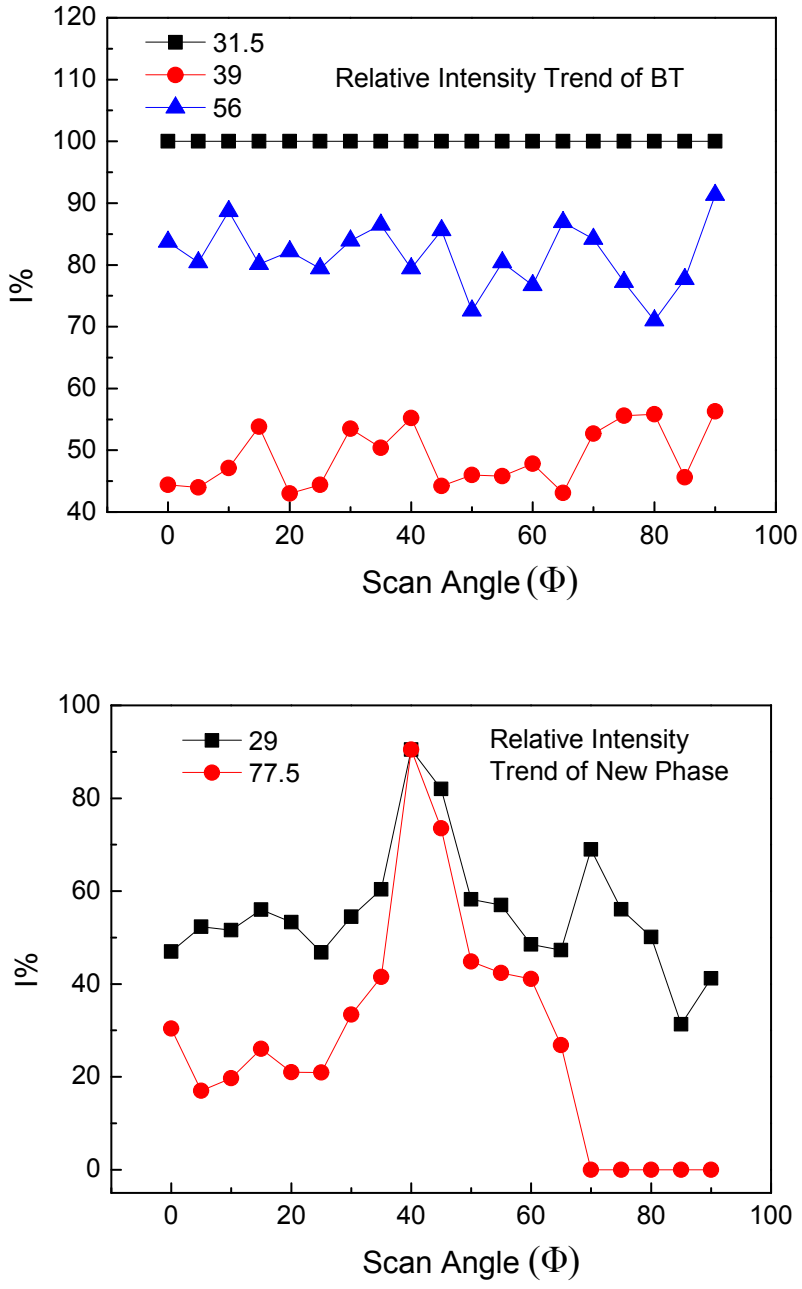

Figure 5-20 The trend of relative intensity for $BaTiO_3$ and $Ba_2TiSi_2O_8$ representative peaks

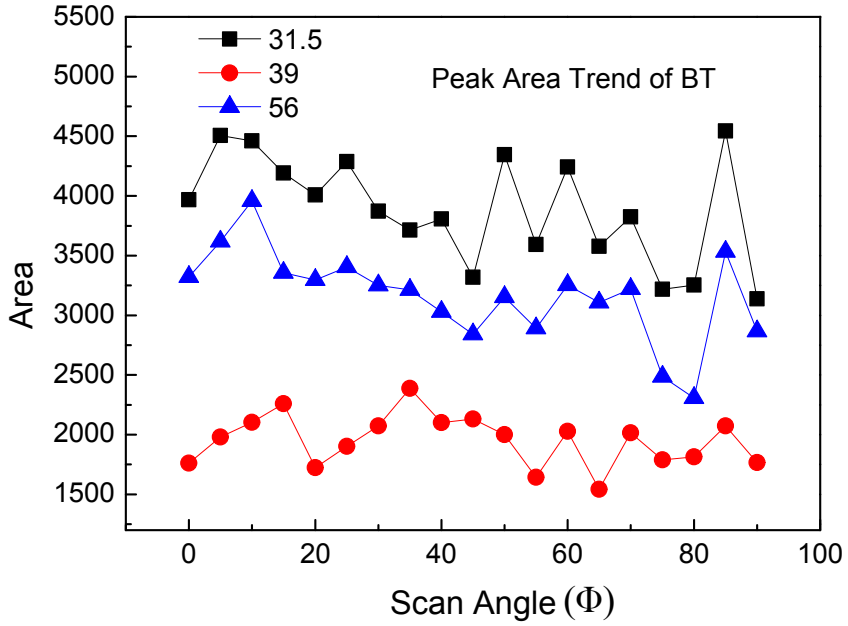

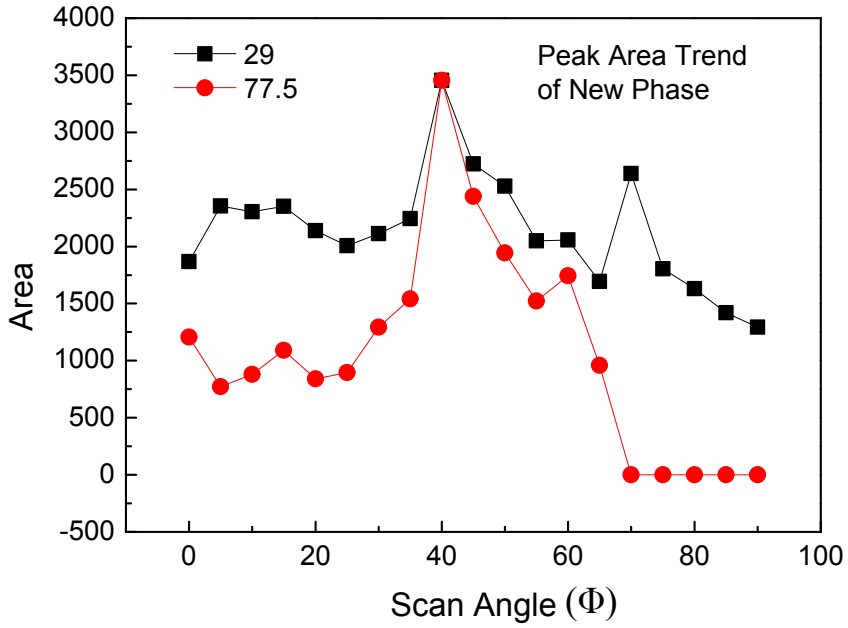

Figure 5-21 The trend of peak area for $BaTiO_3$ and $Ba_2TiSi_2O_8$ representative peaks

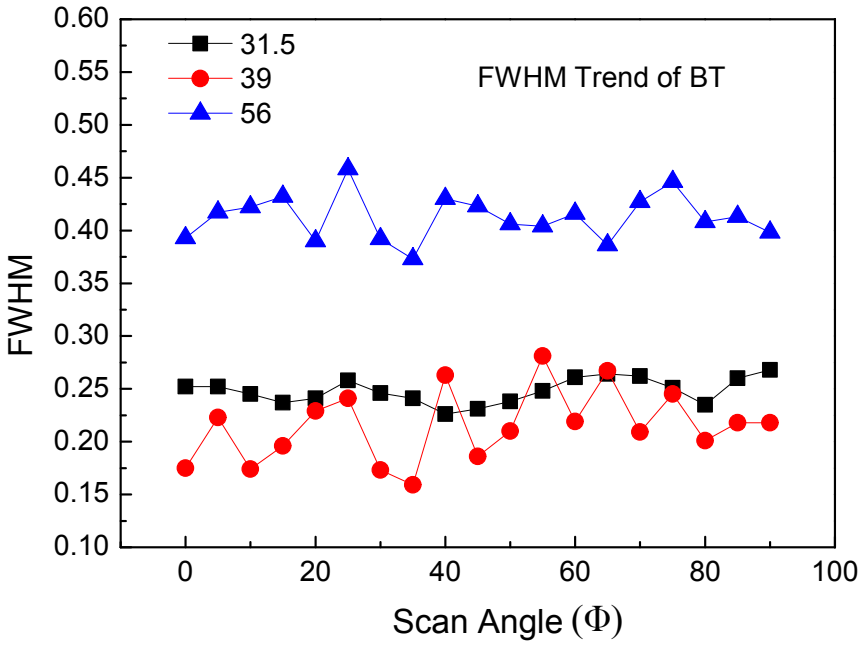

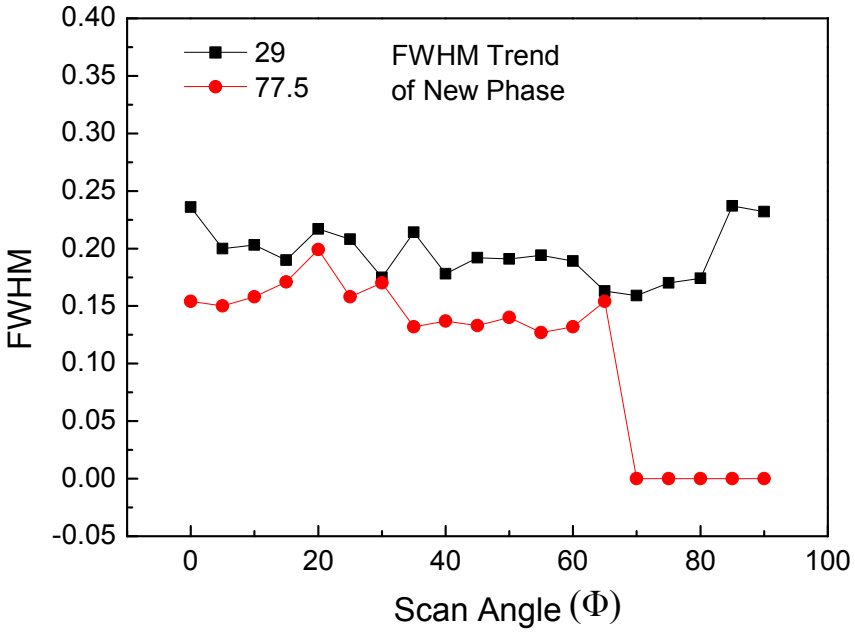

Figure 5-22 The trend of FWHM for $BaTiO_3$ and (b) $Ba_2TiSi_2O_8$ representative peaks

Table 5-3 The factors of all XRD peak at the scan angle of 40

2-Theta	d(A)	Centroid	Height	Area	I%	Skew	FWHM	Breadth
22.123	4.0148	22.077	109	15127	100	0.133	1.376	1.522
28.826	3.0946	28.83	180	3455	22.8	-0.095	0.178	0.211
31.542	2.8341	31.539	151	3807	25.2	0.054	0.226	0.277
38.897	2.3134	38.872	77	2100	13.9	0.369	0.263	0.299
44.063	2.0535	44.064	72	547	3.6	-0.065	0.076	0.083
56.108	1.6378	56.131	65	3028	20	-0.212	0.43	0.511
64.471	1.4441	64.474	170	2188	14.5	-0.112	0.105	0.141
65.831	1.4175	65.8	35	1579	10.4	0.271	0.445	0.495
77.658	1.2285	77.646	226	3454	22.8	0.33	0.137	0.168

According to the results, as shown previously, it can be found that the SPS ceramics are highly possible to be ordered partially. Therefore, a two-dimensional x-ray diffraction was conducted using Gaddis XRD system, then a fixed incident angle θ_1 and a fixed 2D detecting angle θ_2 were used. It is well known that for the polycrystal samples which are randomly orientated, the diffraction ring obtained from the 2D detector will have a uniform intensity; for the single crystal samples with high orderliness, the separated spots will be observed instead of a diffraction ring. For comparison, the results for the as-received surface and cutting cross section of SiO_2-BT recorded and shown in **Figure 5-23** and **Figure 5-24**, respectively; the results for the as-received surface and cutting cross section of ZrO_2-BT recorded and shown in **Figure 5-25** and **Figure 5-26**, respectively. From the 2D x-ray patterns of both SPS ceramics, the non-uniform diffraction rings with some spots were observed, which provides the evidence that the ceramic samples are partially oriented during the process of SPS.

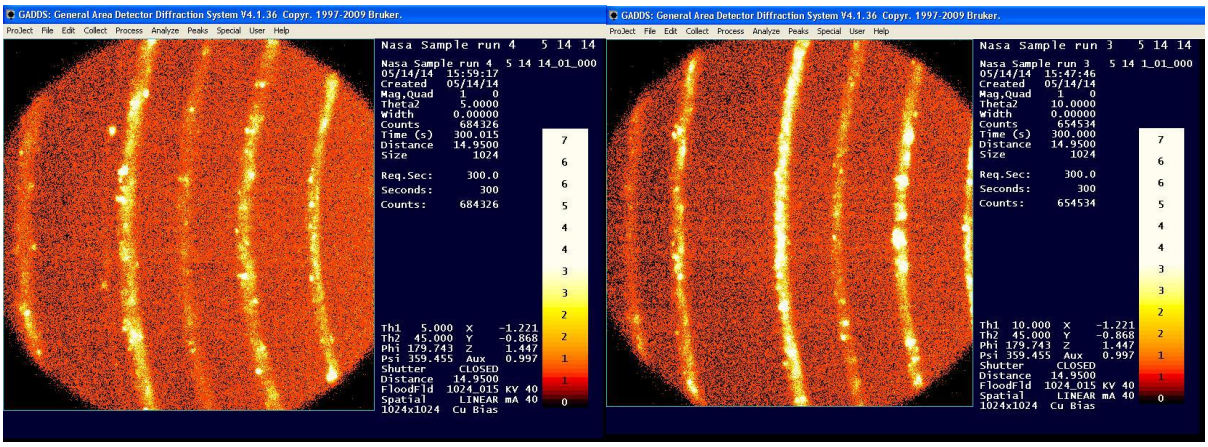

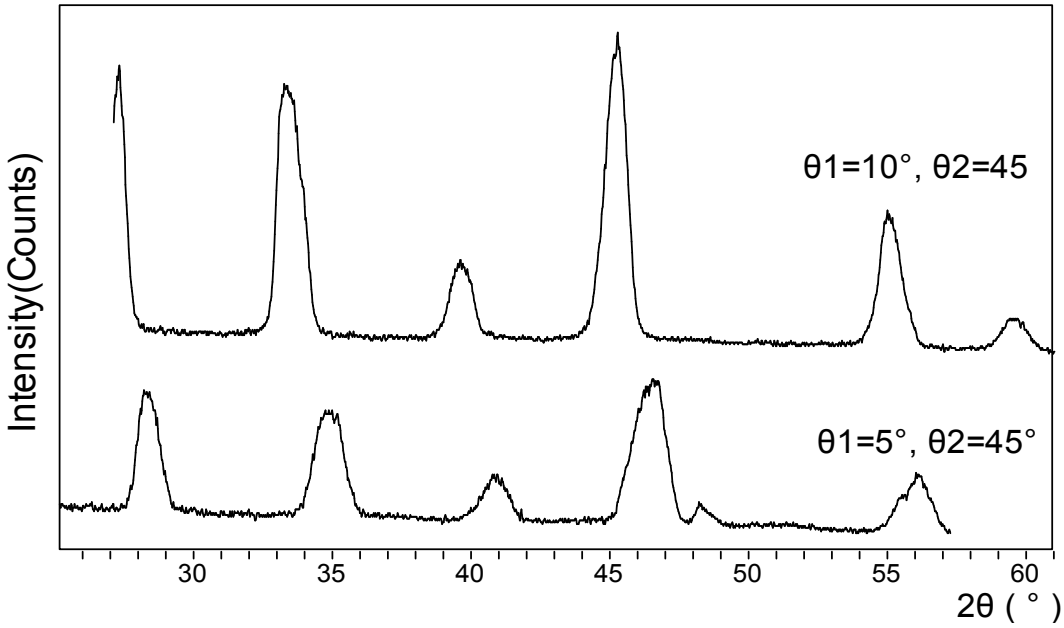

Figure 5-23 The 2D x-ray patterns of the surface of SiO_2-BT as received

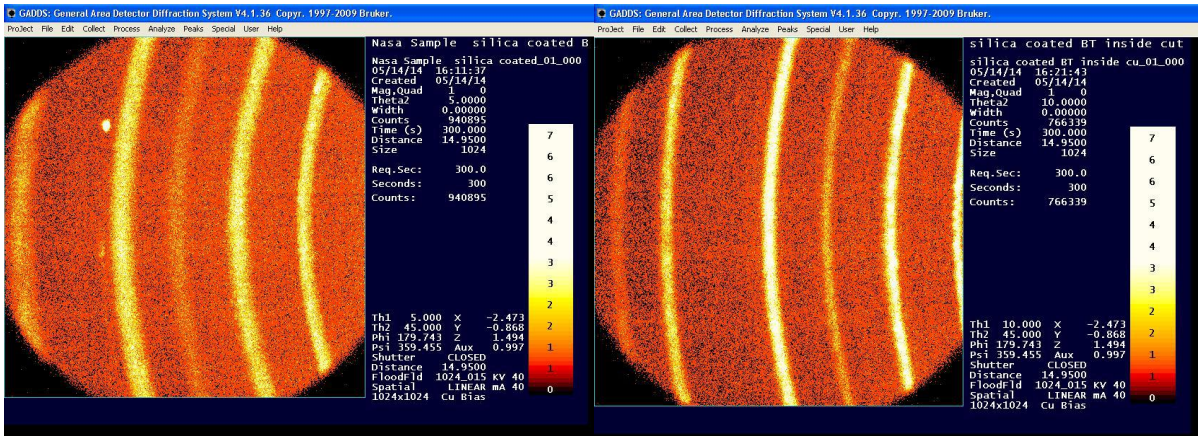

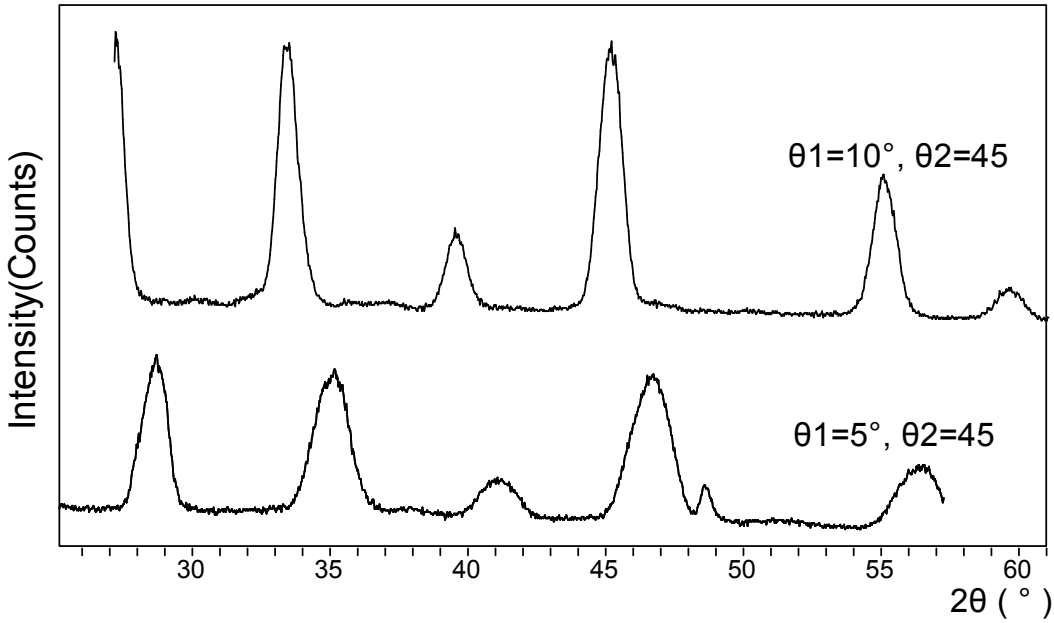

Figure 5-24 2D x-ray patterns patterns of the cross section of SiO_2-BT by cutting

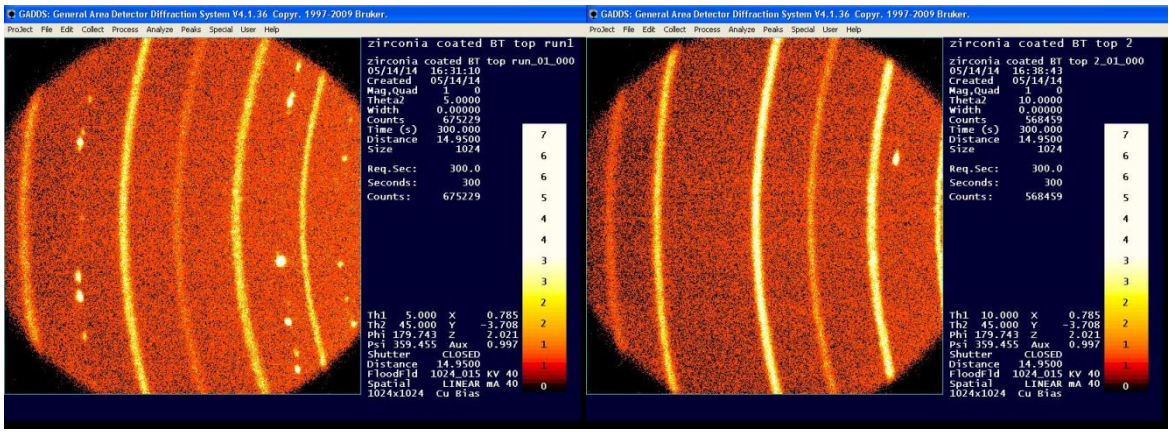

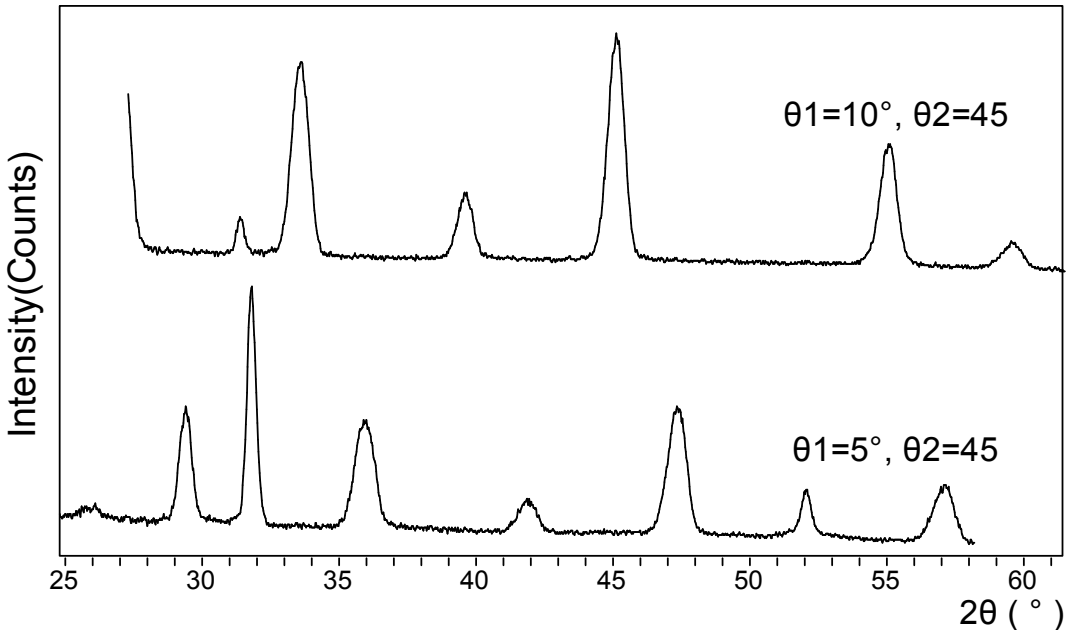

Figure 5-25 2D x-ray patterns patterns of the surface of ZrO_2-BT as received

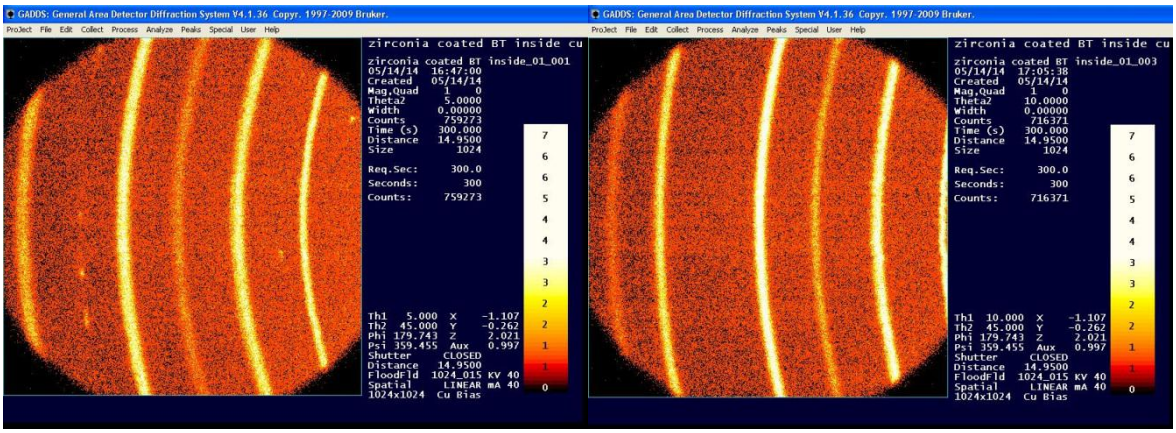

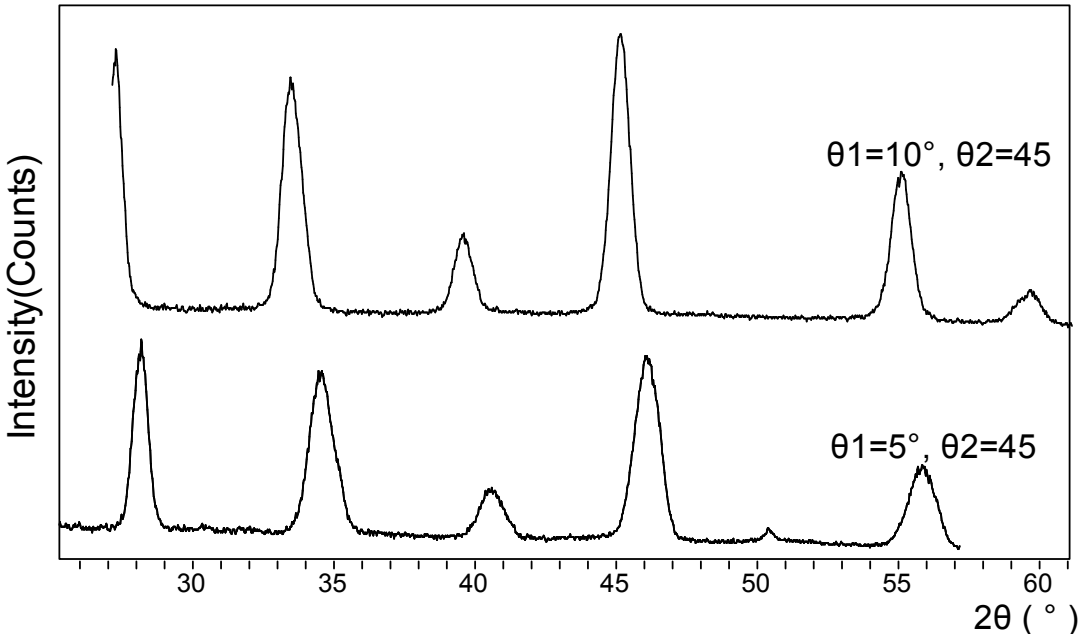

Figure 5-26 2D x-ray patterns patterns of the cross section of ZrO_2-BT by cutting

5.4.1.2 Scanning Electron Microscopy

For the confirmation of the SPS composite microstructure and uniformity, the SEM was used to characterize the morphology of ceramic pieces. In the beginning of the study, the composites provided by Auburn University were used as the sample to show the difference

between SPS and conventional sintering. The composite samples were coated with Au for conductivity in SEM observation, then the cross sections morphology were observed. Three BT/SiO_2 ceramics produced by 100 nm coated powders and the other three produced by 200 nm coated powders were observed in the experiments. All of the samples were cut from the cross sections to two different layers obtained and then polished, the information and dimension of the sample are listed in **Table 5-4**.

Table 5-4 The information and dimension of Auburn University BT/SiO_2 sample

Sample	Material	Area	Thickness
100-1-A	100 nm BT coated by 2.5 wt% SiO_2	86.0 mm2	0.434 mm
100-1-B		34.8 mm^2	0.343 mm
100-2-A		45.9 mm^2	0.391 mm
100-2-B		94.9 mm^2	0.443 mm
100-3-A		48.5 mm^2	0.383 mm
100-3-B		37.8 mm^2	0.402 mm
200-1-A	200 nm BT coated by 2.5 wt% SiO_2	56.8 mm^2	0.321 mm
200-1-B		27.4 mm^2	0.369 mm
200-2-A		85.5 mm^2	0.238 mm
200-2-B		86.2 mm^2	0.344 mm
200-3-A		94.2 mm^2	0.435 mm
200-3-B		78.4 mm^2	0.300 mm

By observing and comparing the cross section for both 100 nm and 200 nm ceramics under SEM, a conclusion can be found that the 100 nm ones have a better uniformity; the grains in 100 nm ceramics are in the nano level and uniform size. For 200 nm samples, obvious phase separation was found and the difference in grain distribution was determined to be the origin of

the separation. One of the phase (phase A) shown a uniform and dense structure, while a large number of pores was found in the other phase (phase B). As an example, the pictures on the cross-section of sample 100-1-A and sample 200-1-A were shown in **Figure 5-27** and **Figure 5-28**, which shows the clear difference on their structures. As shown in the pictures with different magnifications in **Figure 5-27**, a dense and uniform structure of 100 nm composites were confirmed; For the cross section of 200 nm composites as shown in **Figure 5-28**, two regions with different colors were found on the non-uniform cross-section. The high magnification pictures of the two regions were shown in **Figure 5-28 (c)** and **(d)**, respectively. From the cross-section pictures, it can be observed that the may differentiate between the two regions are density. The overview of the distribution for the two phases in 200 nm ceramics was also added to **Figure 5-28** in **(e)** and **(f)**, in which the outline of both phases can be clearly determined by the color change in the pictures.

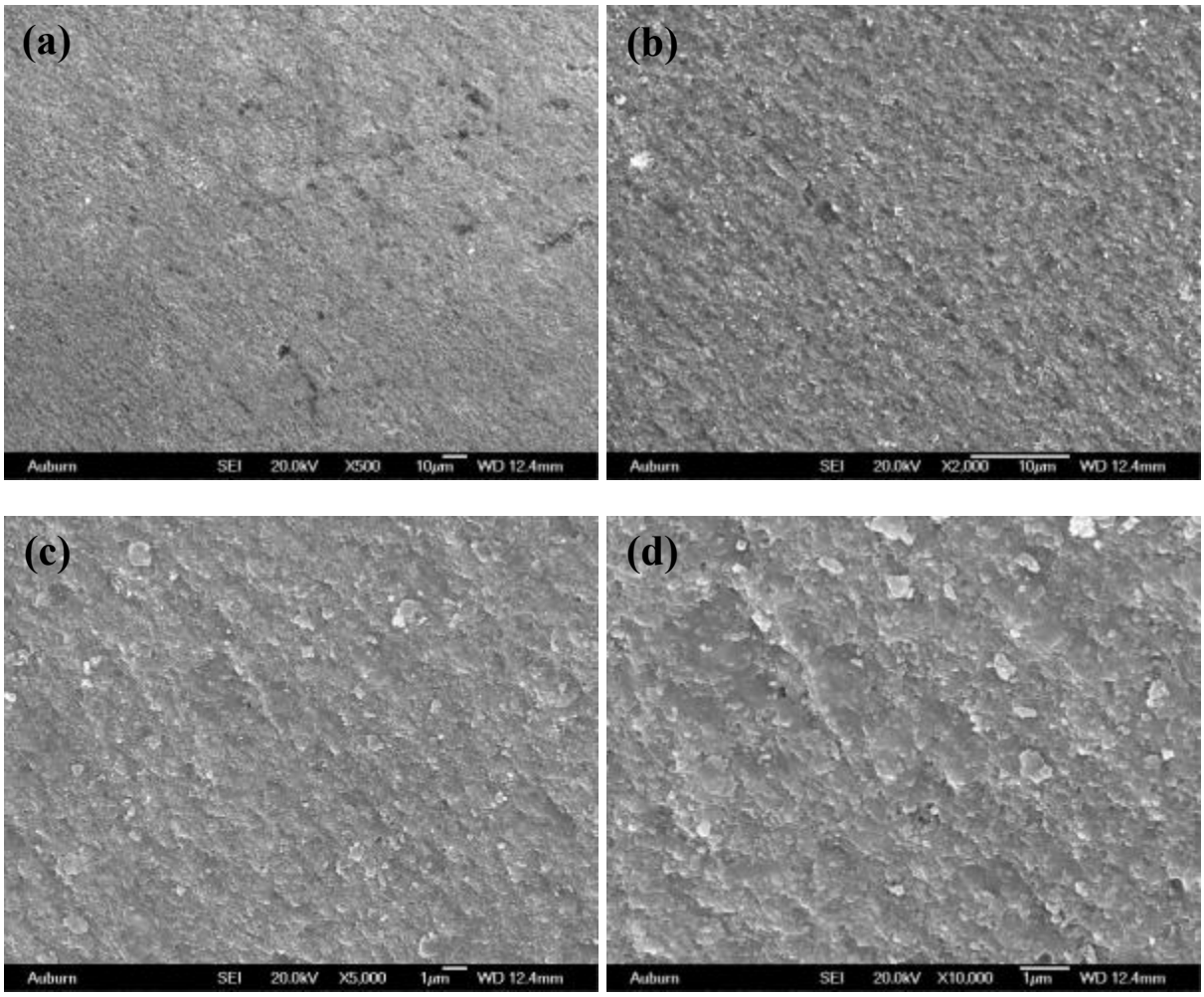

Figure 5-27 Different magnifications of SEM pictures for the cross section of 100-1-A

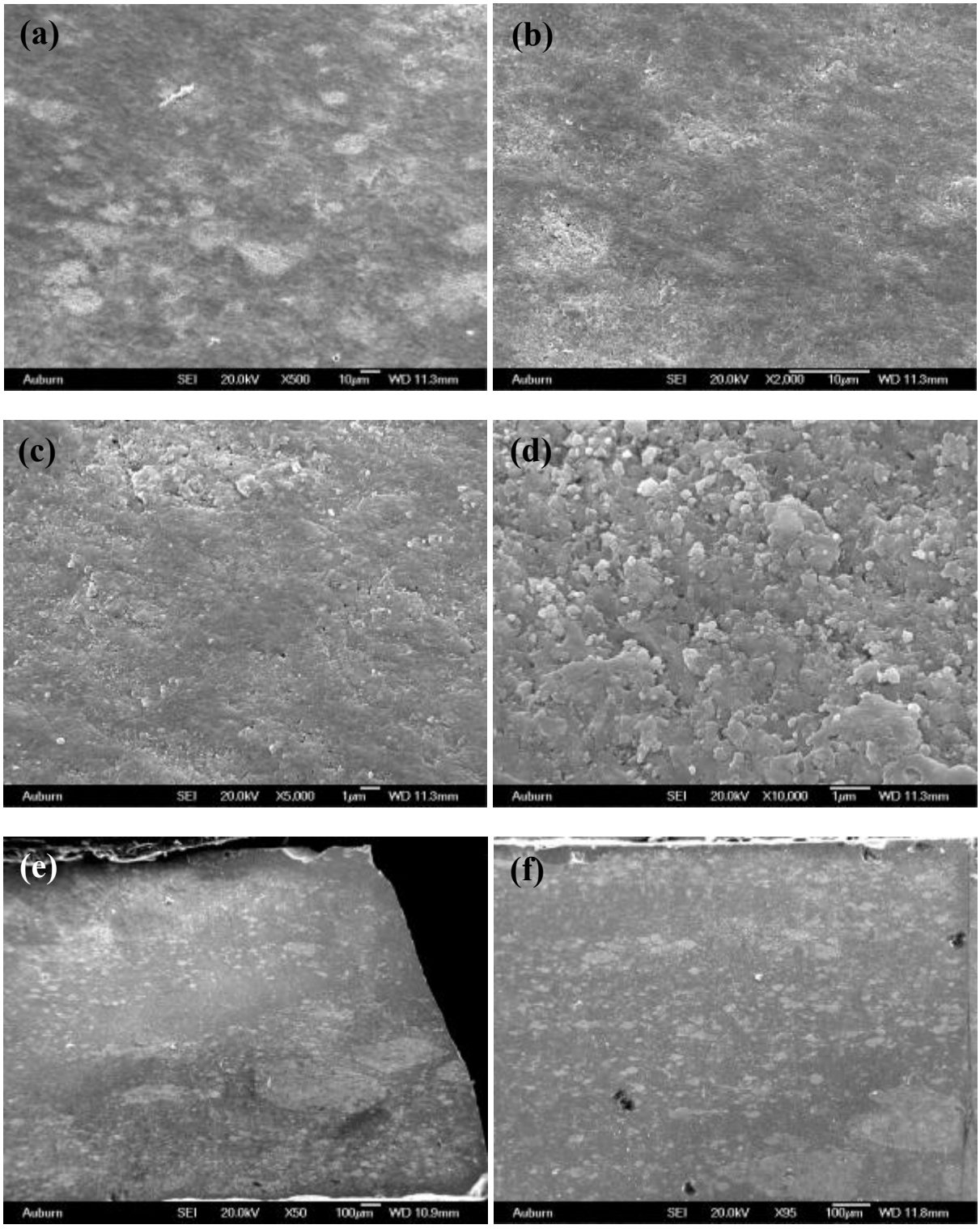

Figure 5-28 Different magnifications of SEM pictures for the cross section of 200-1-A

The morphology of SPS composites made by different nanopowders provided by other researchers was also studied by SEM. The observed samples include SiO_2/BT produced by stöber process from the researcher in French (marked as French-SiO_2); SiO_2/BT produced by vapor press deposition (marked as VP-SiO_2); SiO_2/BT produced by atomic layer deposition (marked as ALD-SiO_2) and Al_2O_3/BT produced by atomic layer deposition (marked as ALD-Al_2O_3). By looking the color distribution of the cross sections, two different layers has been observed on French-SiO_2 and VP-SiO_2; the other samples (ALD-SiO_2 and ALD-Al_2O_3) have shown an integrated cross section. According to the colors, the two layers cut from each one of the pellets were separated as the white and black regions; the SEM was used to characterize the morphology of both parts.

Firstly, by observing and comparing the cross-section of both regions of French-SiO_2, a conclusion can be found that the white part of the sample is relatively uniform but porous, a large number of cracks exists in its cross-section; the structure of the black part of the sample is close to white part but have fewer pores. In addition, the grains of both regions are in the nano level and uniform size. The pictures of the cross-section of both white part and black part of French-SiO_2 are shown in **Figure 5-29** and **Figure 5-30**. Although there is difference on the extent of porosity the two regions, the similar structure was found in both of them which is relatively uniform but porous and existing cracks. Next, the VP-SiO_2 are showing non-uniform structures under the SEM observation. As shown in **Figure 5-31** and **Figure 5-32**, the cross-section of VP-SiO_2 are not dense and the obvious phase separation was observed, the white and dark areas on its cross section are shown the significant difference. The white part of VP-SiO_2 are porous

therefore having a relatively low density; compare with it, the black part is much denser but still far from uniform. Both of the two regions have the relatively uniform grains in its whole cross section.

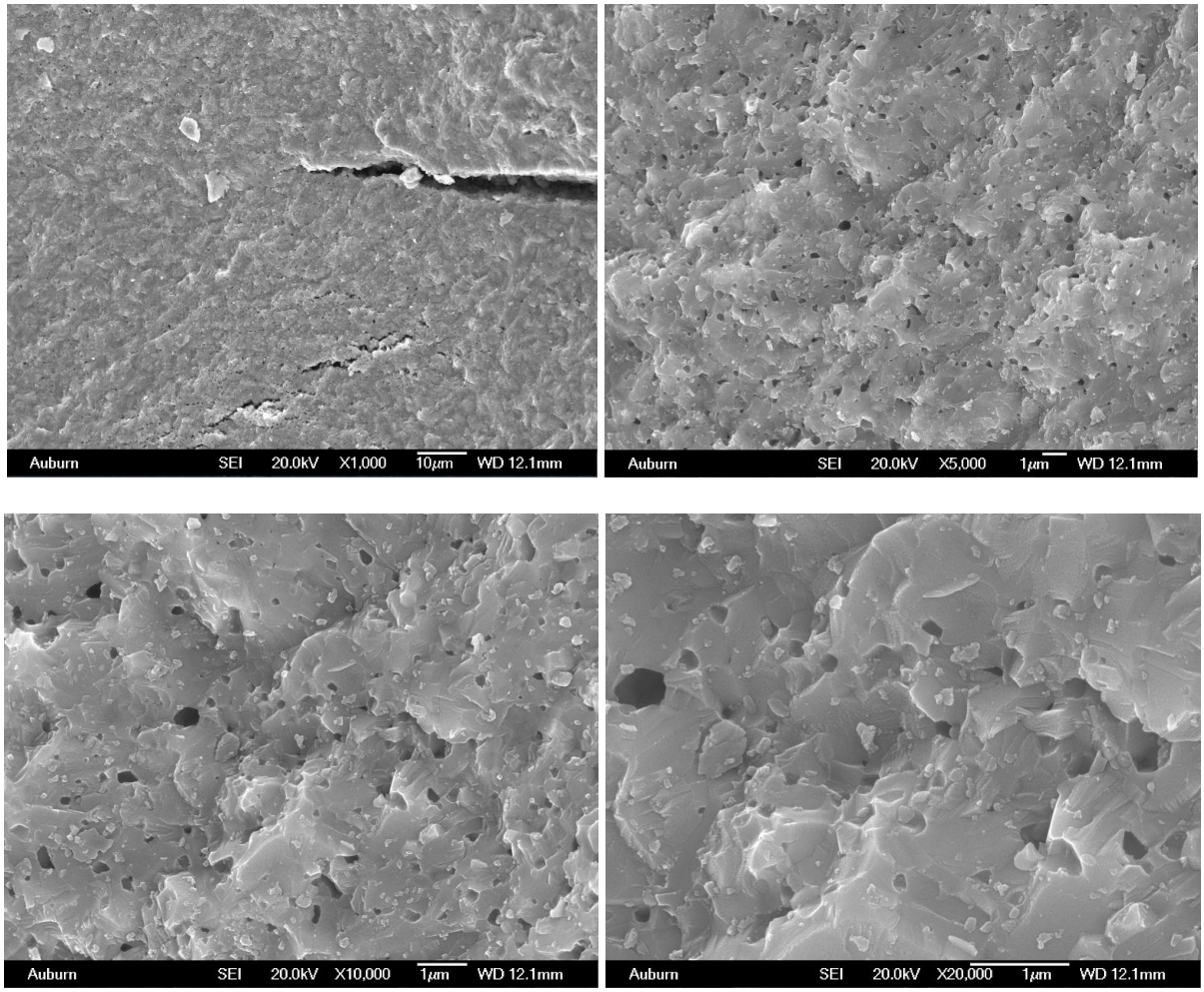

Figure 5-29 The cross section pictures of the white part of French-SiO_2

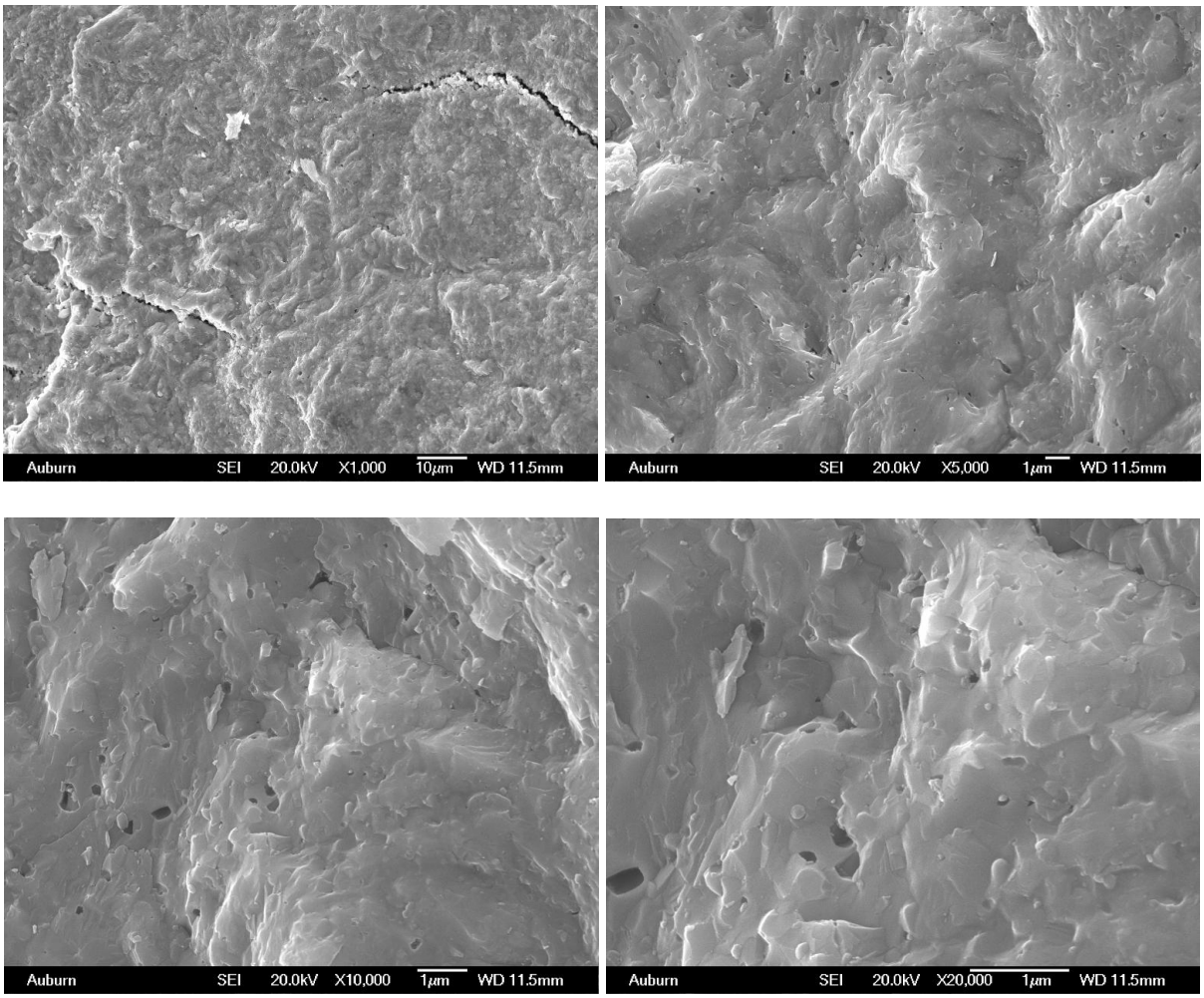

Figure 5-30 The cross section pictures of the black part of French-SiO_2

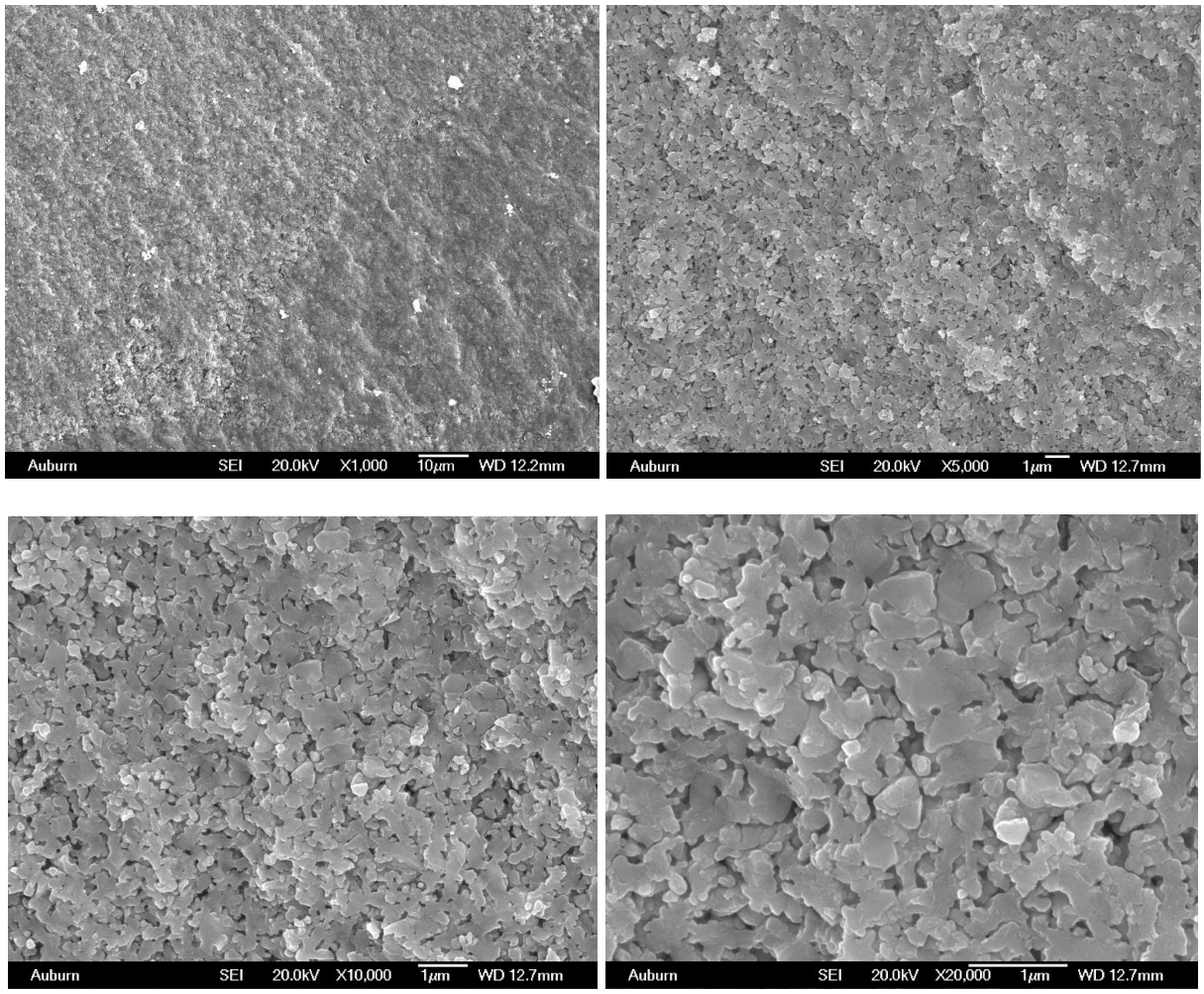

Figure 5-31 The cross section pictures of the white part of VP-SiO_2

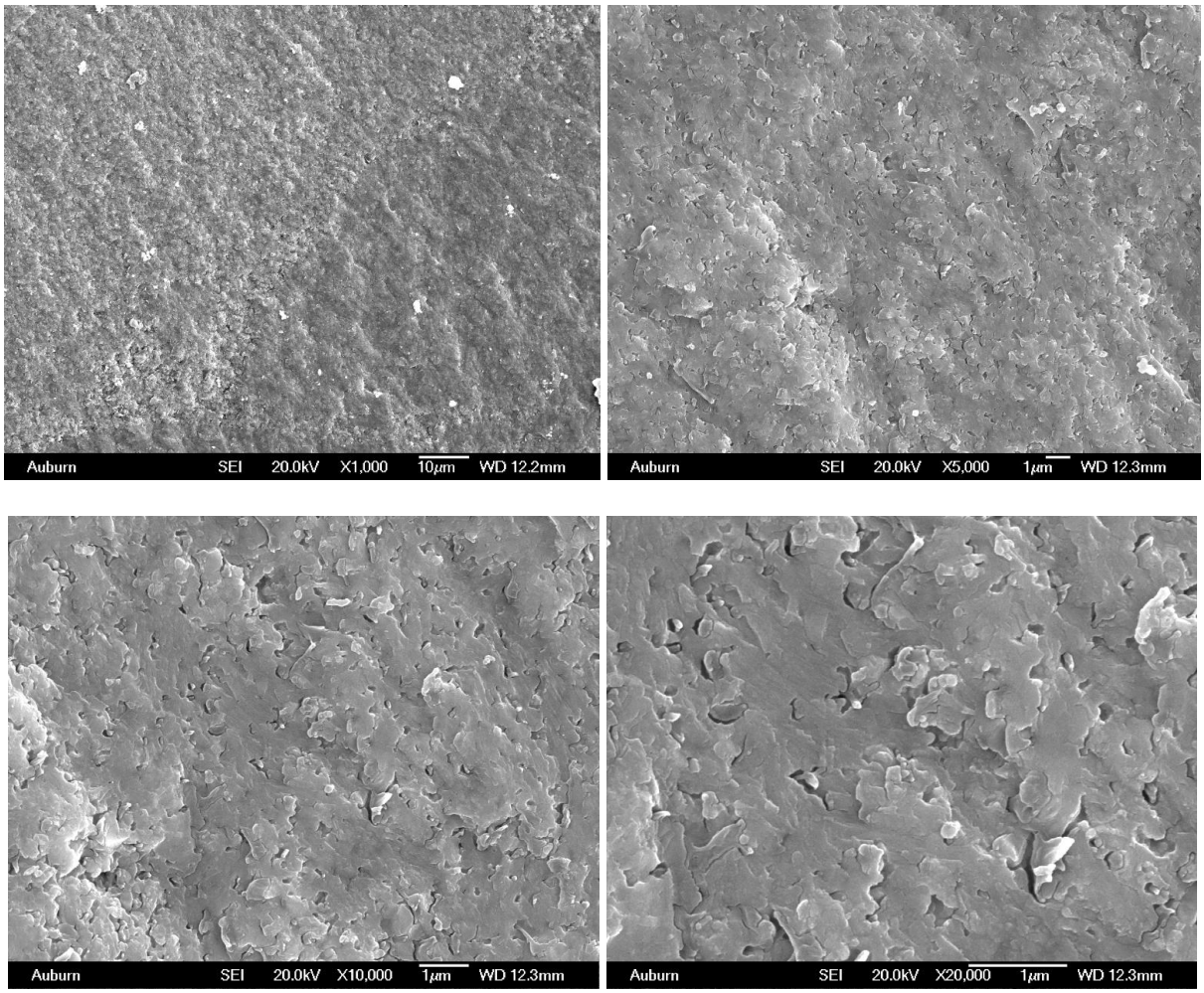

Figure 5-32 The cross section pictures of the black part of VP-SiO_2

In the observation of the cross-section of ALD-SiO_2, the composites made from 140 nm and 500 nm powders were studied respectively. The pictures of the cross-section of 140 nm ALD-SiO_2 was shown in **Figure 5-33**. From the figure, a conclusion can be made that the sample 140 nm ALD-SiO_2 are relatively uniform; the grains are at the nano level and uniform size. However, in spite of the consistent color on its cross-section, the uniformity of 500 nm ALD-SiO_2 are still not as good as 140 nm ALD-SiO_2. As shown in **Figure 5-34** and **Figure 5-35**, the

image from the different locations of the cross-section of 500 nm ALD-SiO_2 is showing different structures. Although the grains are partially covered by the amorphous silica, the composite is still showing low porosity and bad uniformity. As shown in **Figure 5-35**, a part the cross-section is relatively smooth and the clear edges of grains cannot be observed under SEM, which might indicate the better uniformity can be obtained with the higher silica content. Compare with ALD-SiO_2, the ALD-Al_2O_3 sample are showing a better consistency in large scale, but the density and uniformity are much poorer for its microstructure. As shown in **Figure 5-36** of the cross-section of ALD-Al_2O_3, they have the very large difference in grain sizes, some of the grains have the crystal-like shape and the others do not. The connection between large grains and small grains are not good, and a lot of pores were found which shows a relatively low density. The obvious cracks were also found.

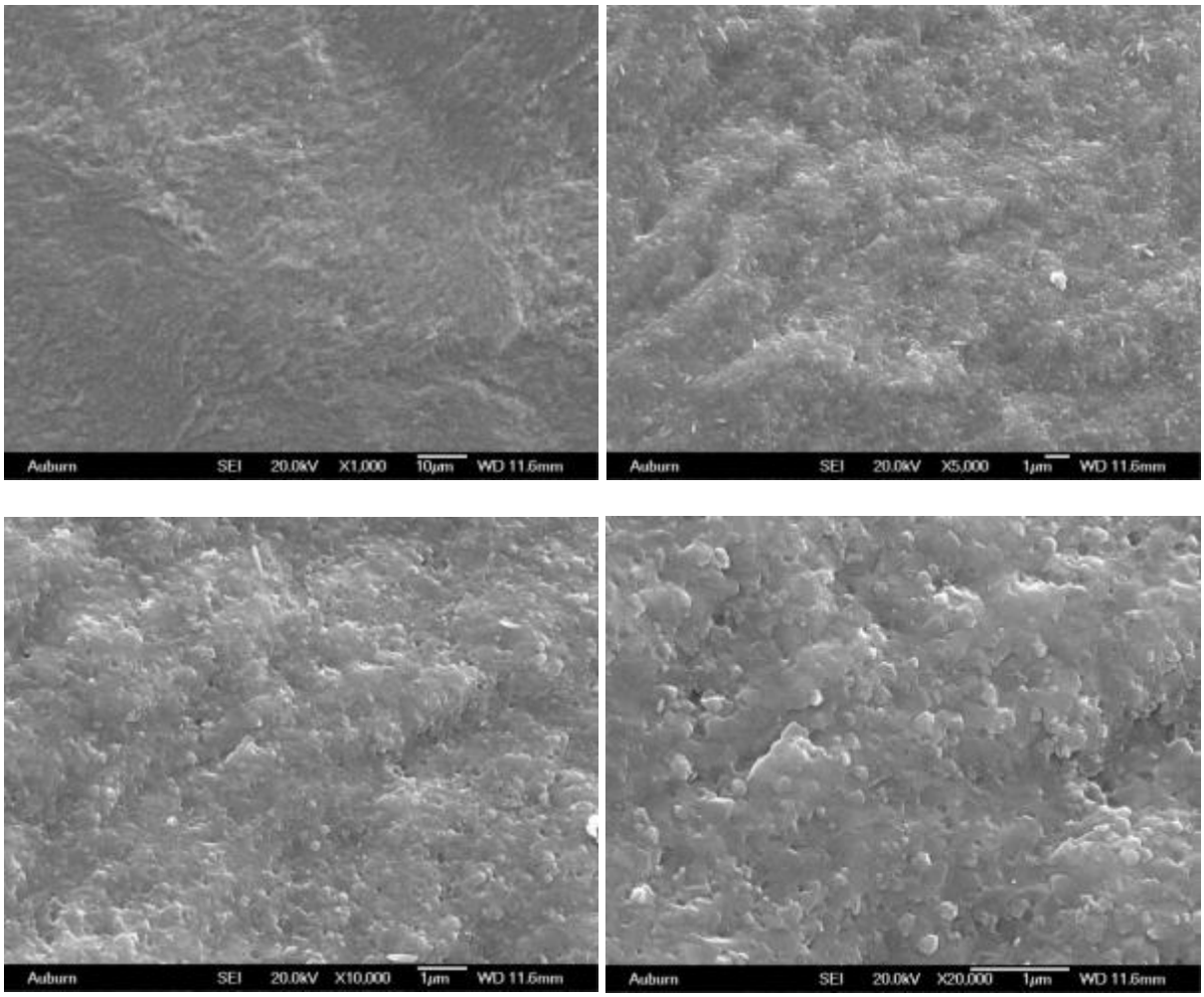

Figure 5-33 The cross section pictures of the 140 nm ALD-SiO_2

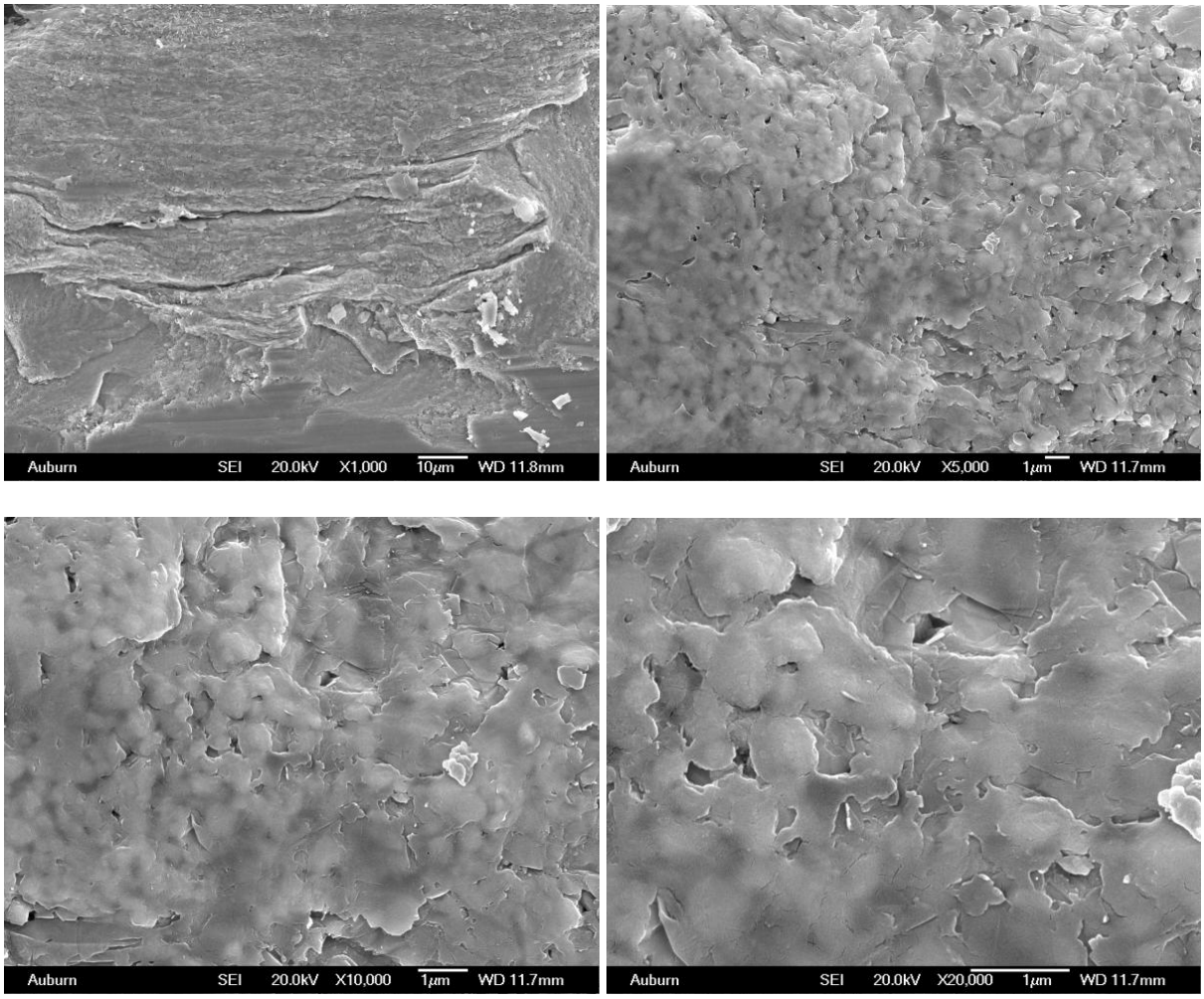

Figure 5-34 The porous part of cross section pictures of the 500 nm ALD-SiO_2

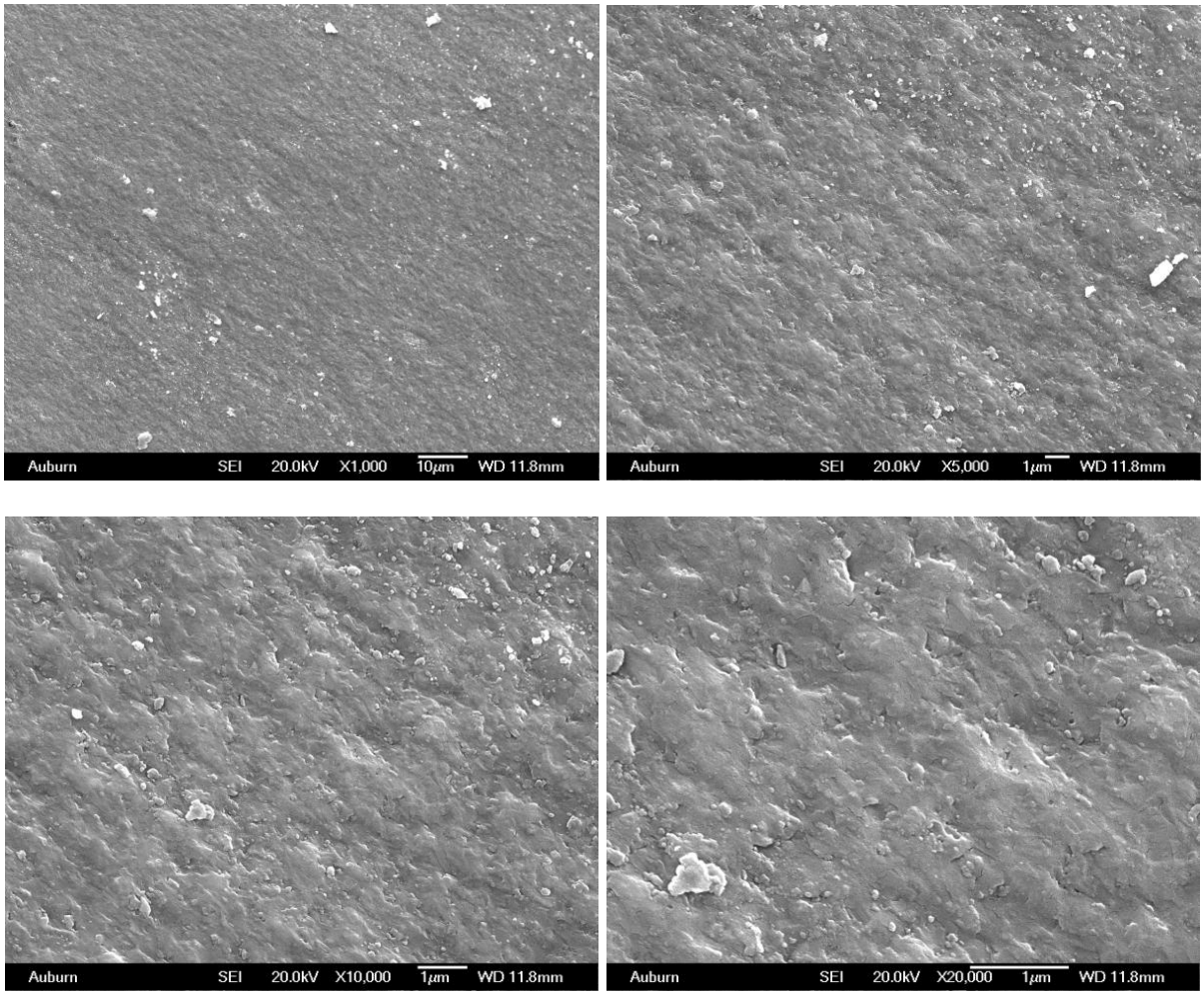

Figure 5-35 The dense part of cross section pictures of the 500 nm ALD-SiO_2

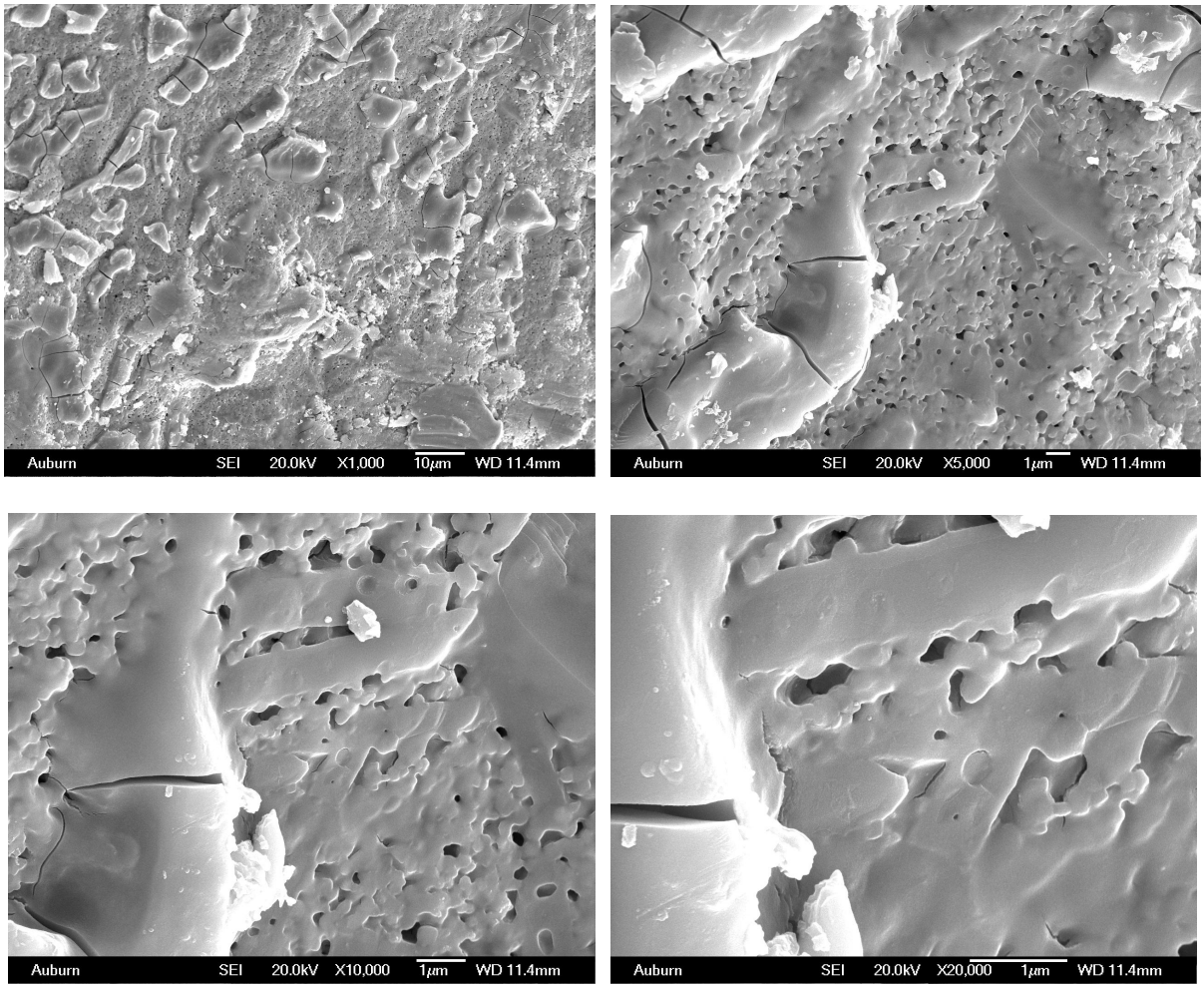

Figure 5-36 The cross section pictures of the 500 nm ALD-Al_2O_3

In summary, the morphology studied by SEM have confirmed the results of poor uniformity and low density of the SPS composites. Although a relatively good consistency in large scale were obtained by ALD, the resulting microstructures are still far from uniform and dense. For the samples made by other methods, their cross section are showing the obvious phase separation on the cross section, which may lead to the difference of the dielectric properties between the two layers obtained from the same sample. In order to reduce the impact of the non-

uniformity and obtain representative test results, the dielectric properties of samples with relatively good uniformity and high density which confirmed by SEM should be focused on in the testing, including the samples made from ALD-SiO_2 and the powders provided by Auburn University.

5.4.1.3 Element Mapping by High Resolution STEM

As discussed, the layered structure of SPS composites were found by using SEM. For the deeper study on the element distribution of each layers of samples, the STEM with high resolution were used to characterize the morphology. In the experiments, two SiO_2/BT samples received from NASA were examined using TEM. One of the sample have a good uniformity and the other one are showing the layered structures. One of the composite sample with a NASA number of "031815-01" is uniform are showing a black color, was prepared at 1100 °C under a pressure of 30 MPa for 30 s and annealed at 800 °C for 12 hr; The other composite sample with a NASA number of "012815-01" have two layers with different colors, was prepared at 1070 °C under a pressure of 50 MPa for 30s and annealed at 800 °C for 12hr. The color illustration of the cross section of both samples are illustrated in **Figure 5-37**.

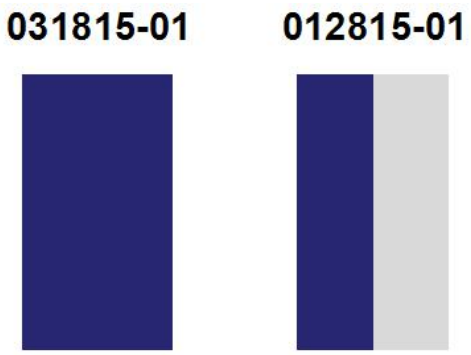

Figure 5-37 Color illustration of the cross section of 031815-01 and 012815-01

As mentioned above, two ceramics (031815-01 and 012815-01) are studied by TEM. For 012815-01 ceramic, two areas with different colors are selected for TEM study, while for 031815-01 ceramic only one area was selected for STEM study. For following discussion, the samples from the white region of 012815-01 ceramic is named as "W1"; the sample from black region of 012815-01 ceramic is named as "B1"; while the samples from 031815-01 ceramic is named as "U1". For all of the three prepared samples, following experiments were then carried out: 1) High resolution SEM observations were taken on nanoscale (~100nm) of "W1" and "U1" to get the information of grains; 2) The element maps were recorded to study the uniformity of sample "W1" and "U1" on the high resolution SEM observed areas; 3) TEM observation at higher magnification (~10nm) was carried out on sample "U1" to get the information of its grain boundary; 4) The large scale EDS mapping have made up on the cross section of 012815-01 ceramic including the "W1" and "B1" to intuitively understand the segregation of silicon.

The results shown in **Figure 5-38** are the high resolution SEM image of the sample "W1". Clearly, the ceramic is not density since the sintering temperature is not enough to form complete uniform structures, the grain size of "W1" is about 150nm~600nm. By compare the area of solid

and empty parts on the image, the porosity of “W1” can be calculate to 18.7%. This verified the porous structure observed from SEM are showing the representative mechanism at this preparing condition. As comparison, the high resolution pictures of “U1” cross section were shown in **Figure 5-39**. Opposite with the porous structure of “W1”, “U1” shown more dense structure between grains. The grain size of “U1” is about 200nm~800nm. As shown in figures, this sample has a dense polycrystalline form, different composition may changed between grains.

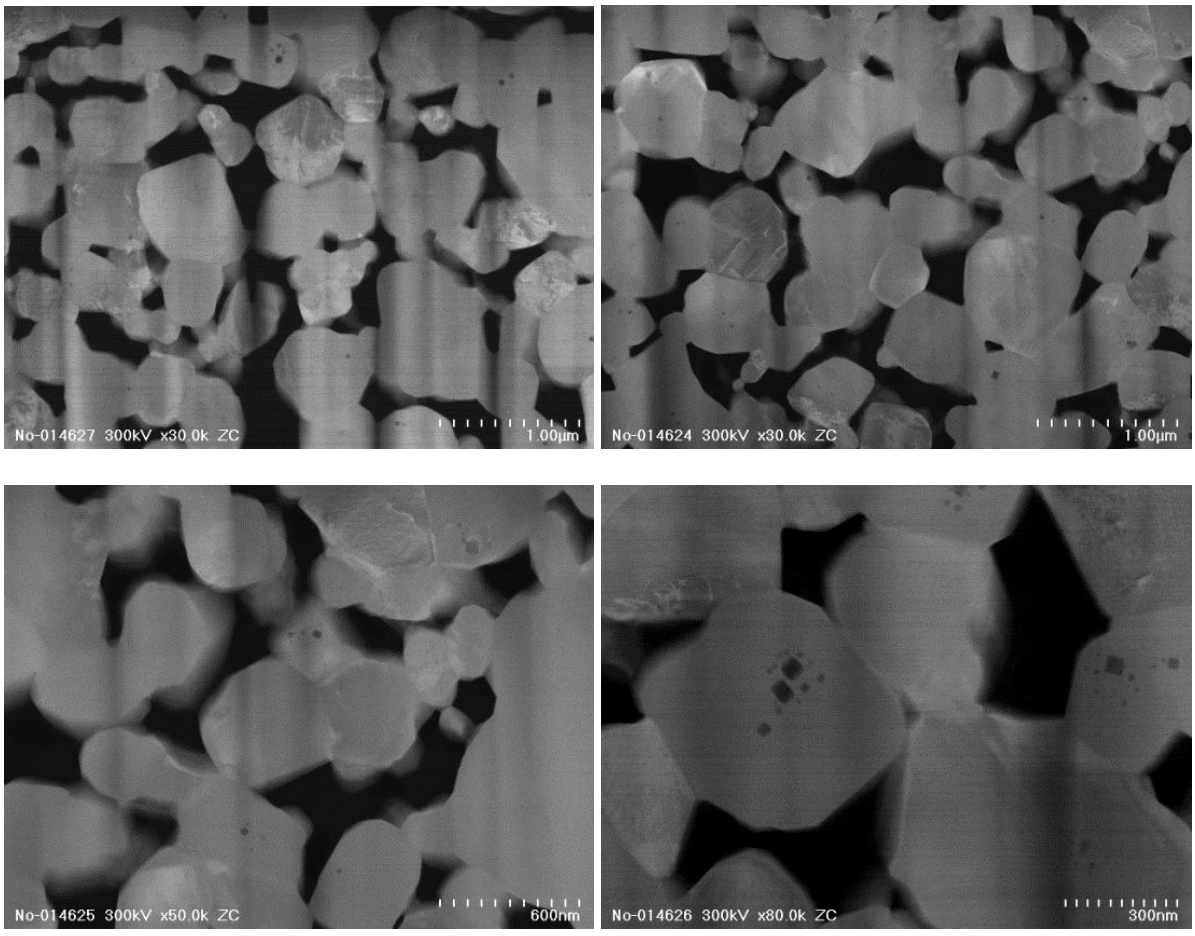

Figure 5-38 The high resolution STEM pictures of “W1” samples

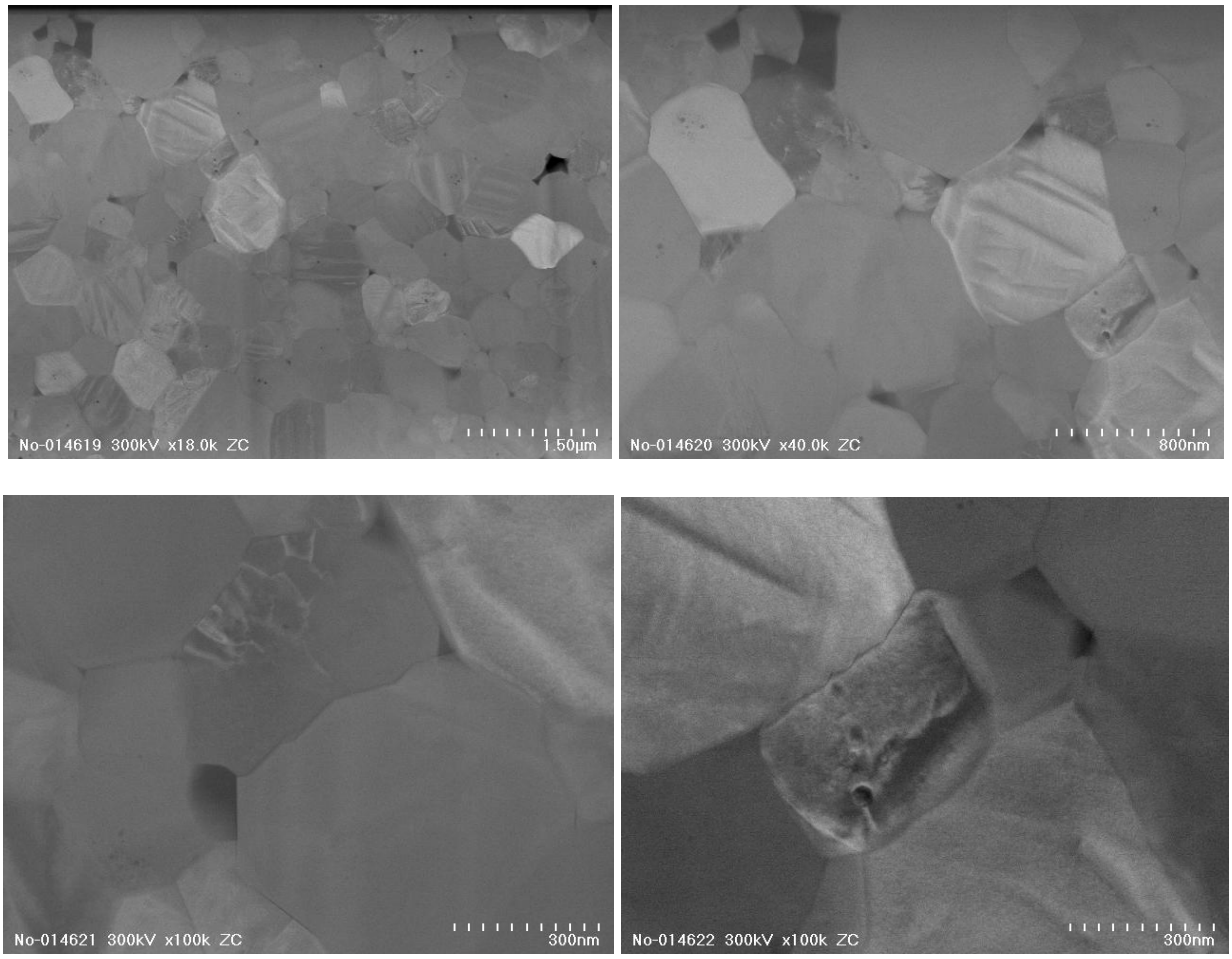

Figure 5-39 The high resolution STEM pictures of "U1" samples

For looking at the transition region of different composition, the high magnification TEM pictures of the cross section of "U1" on grain boundary were taken and shown in **Figure 5-40**. From the TEM observation, at grain boundary the crystalline were found on both side, which verified the polycrystalline observed from STEM are showing the representative mechanism at this preparing condition.

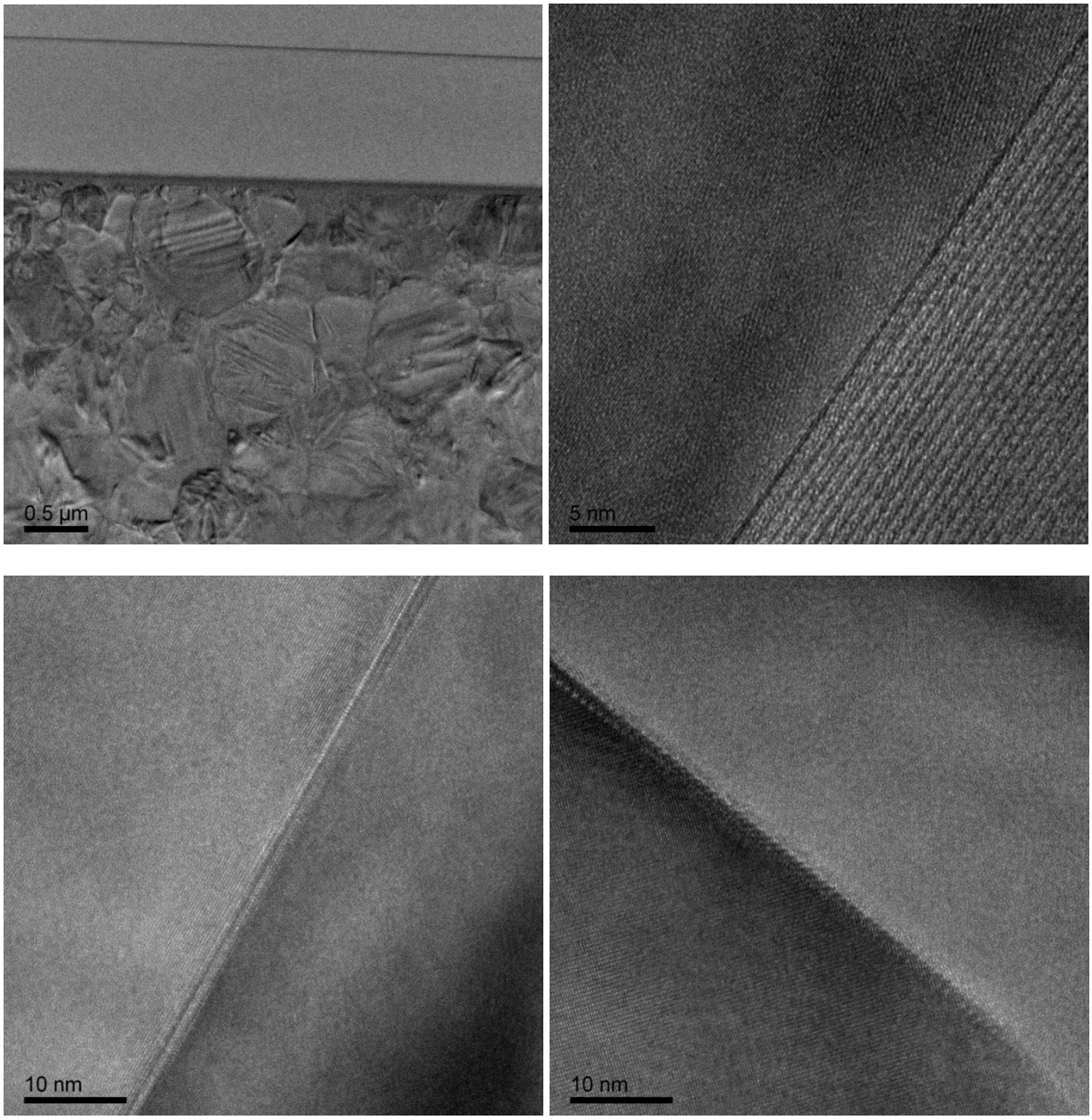

Figure 5-40 The high magnification TEM pictures of "U1" cross section

The EDS mapping were then taken on both large scale and nano scale for "W1" and "U1", to find the element origin of phase separation. The nano scale EDS mapping results of samples "W1" was shown in **Figure 5-41**, nano scale EDS mapping results of samples "U1" was shown

in **Figure 5-42**. The maps are showing silicon have a relative uniform composition in both of the samples. Compare with "W1", "U1" showing the barium concentration change between grains, this phenomenon also points out the BTO in ceramic may also have valence changes at high temperature, which may cause the conductivity change.

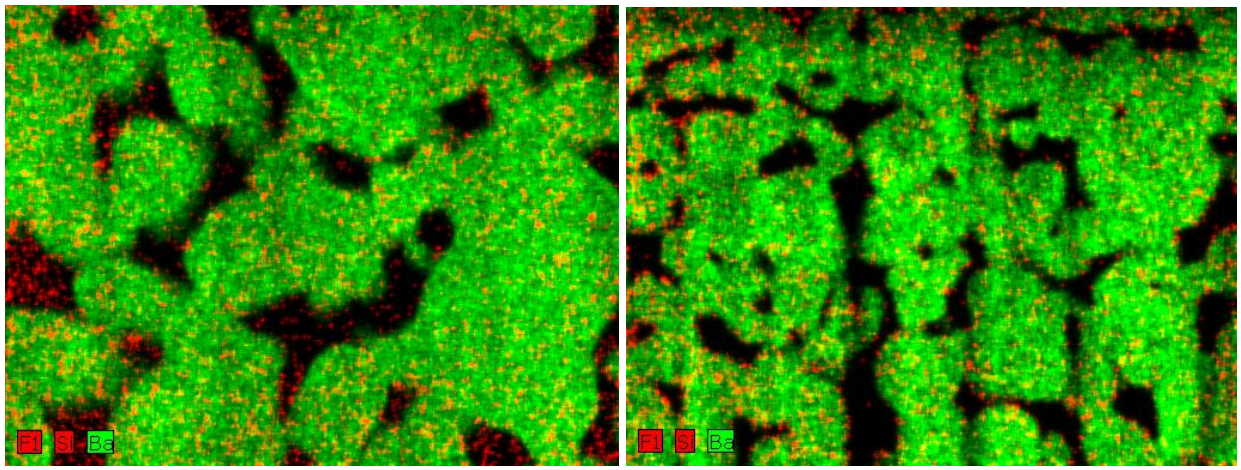

Figure 5-41 The EDS mapping of "W1" TEM observed area

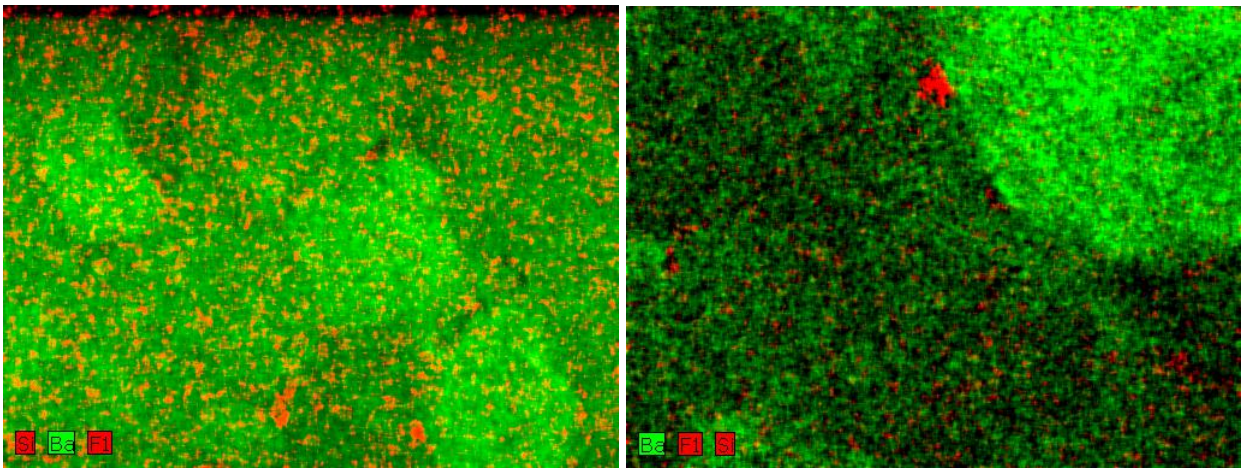

Figure 5-42 The EDS mapping of "U1" TEM observed area

The large scale EDS mappings were also made up and recorded for 012815-01, provides information of the Si-rich phase segregation. For the 012815-01 cross sections prepared for large scale mapping, SEM was used to observe the morphology, the images were shown in **Figure 5-43**. Among the pictures, (a) was recorded form the white and black changing areas (including the typical structure showing in "W1" and "B1"); (b) was focused on the black area, showing the gathering area of small grains; (c) and (d) are also taken from the black areas, in which (c) was helped in finding the element distribution in large grains, and (d) are good in showing the concentration change around one grain.

The EDS mapping of 012815-01 cross section on large scale SEM observed areas were shown in **Figure 5-44**, the four mapping results are correspondence in the SEM images in **Figure 5-43** one by one. In the mapping, from the white and black changing area (a), we can see the silicon mainly concentrated and inhomogeneous distributed in black areas, surrounded by the line which separate two parts of ceramic; The mapping focused on small grains of black area (b), indicates different silicon concentrations depending on the grain size in the same darkness region, which possibly due to the sintering temperature unevenness; The phenomenon that silicon gathering around large grain shown in (c) indicates SiO_2 are forming insulating layers, but these insulating layer can not be continuously formed, which causes the sample appears conductive path; from (d) we can see the SiO_2 layer around one large grain having good quality, but it can not play a good role in the dielectric properties because of the discontinuous. The structure of this ceramic shown that we are far from the relative uniform structure, which may due to the decrease temperature; it also suggested if the SiO_2 layer can be formed continuously, the loss may decrease.

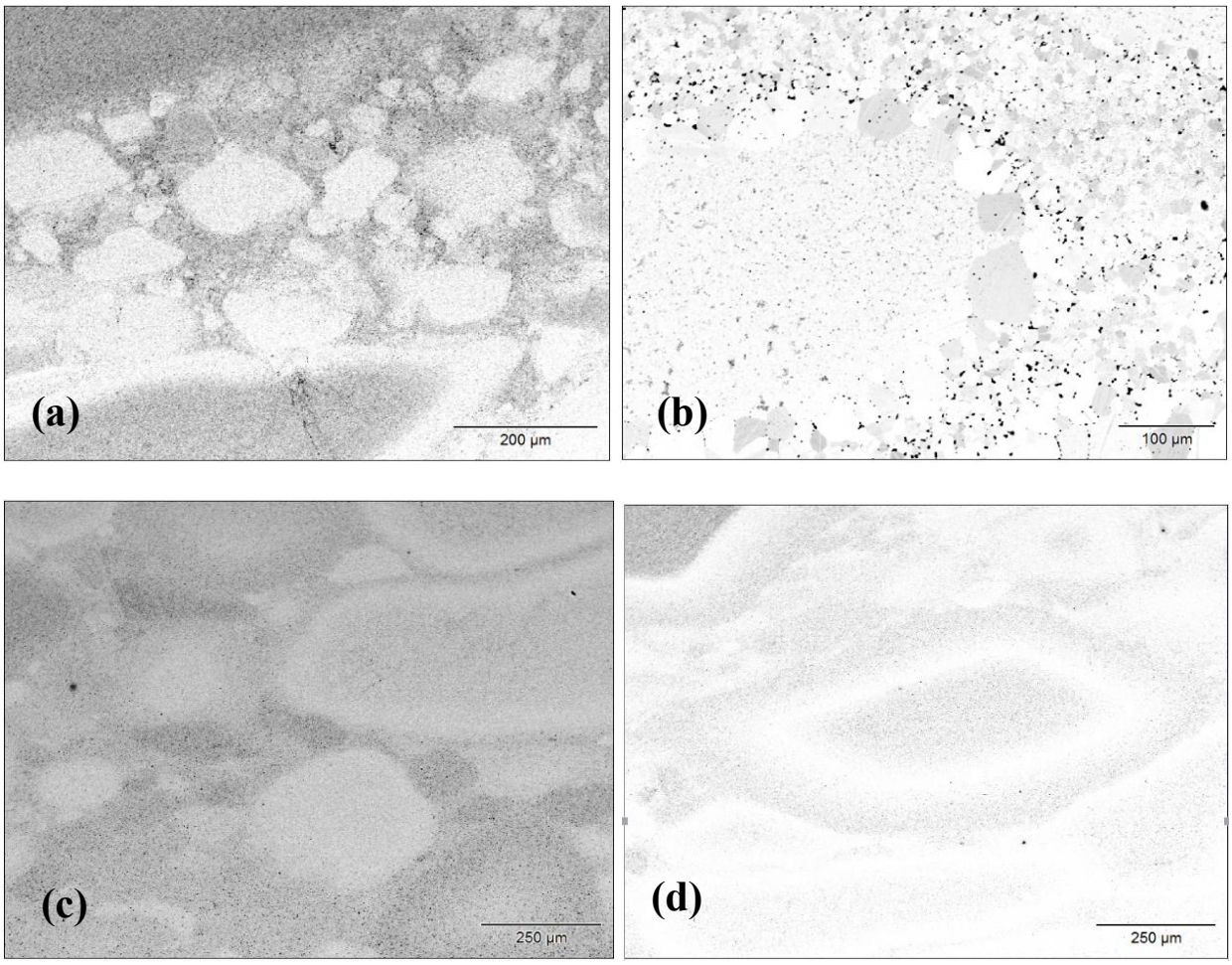

Figure 5-43 The EDS mapping of 012815-01 cross section TEM observed area

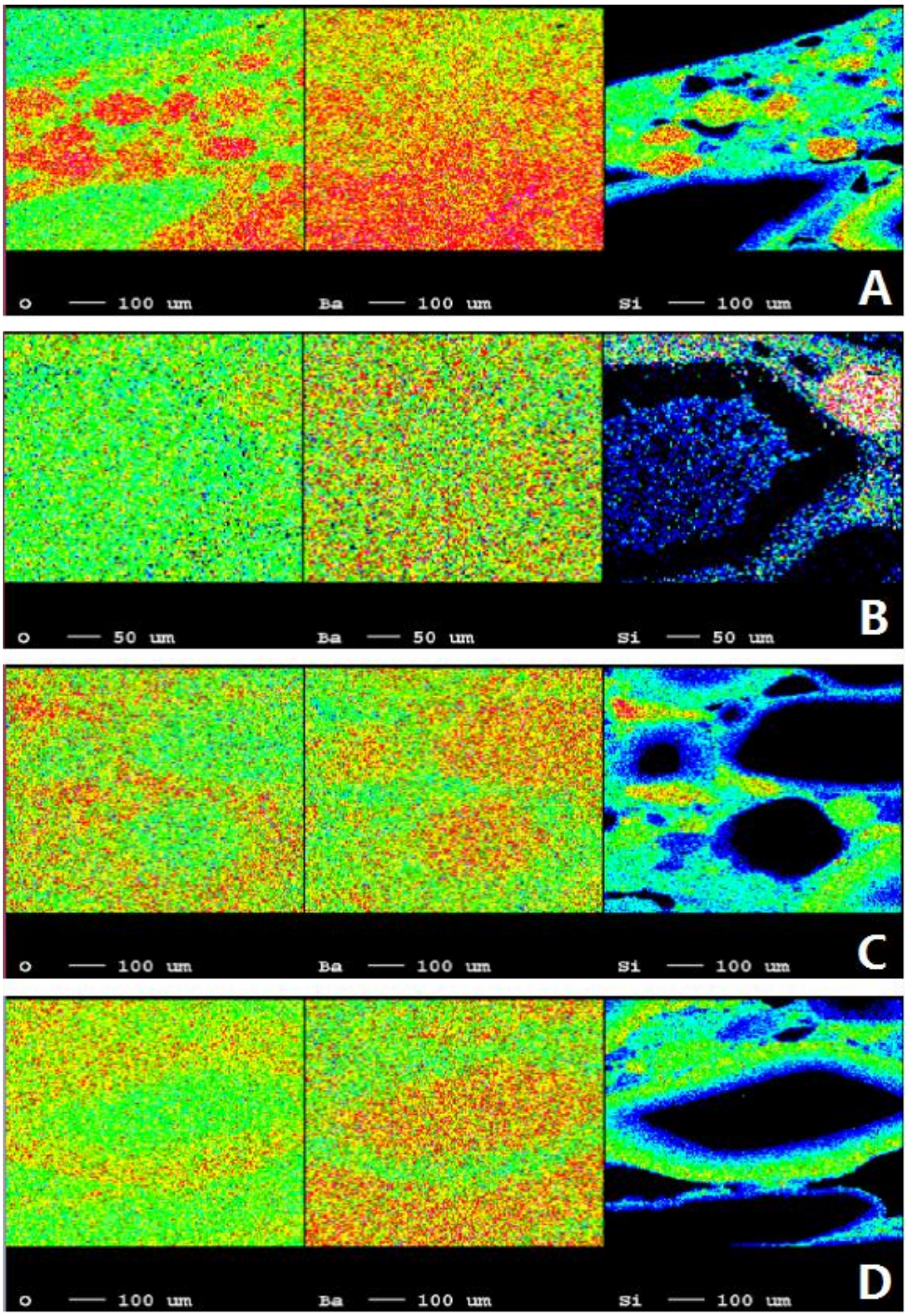

Figure 5-44 The EDS mapping of elements O, Ba and Si of 012815-01 cross section on large scale SEM observed areas

5.4.2 Dielectric Properties

5.4.2.1 Frequency Dependency of Dielectric Properties at Room Temperature

The study of the dielectric properties of SPS composites was started from the testing on the samples made by nanopowders provided by Auburn University. Three BT/SiO_2 ceramics made of both 100 nm and 200 nm BT powders coated with 2.5 wt.% SiO_2 were cut from the cross sections two two layers and polished for further processing as introduced in Chapter 2. The information and dimension of the sample are listed in **Table 5-5**.

Table 5-5 The information and dimension of ALD BT/SiO_2 sample

Sample	Material	Area	Thickness
100-1-A	100 nm BT coated by 2.5 wt% SiO_2	86.0 mm^2	0.434 mm
100-1-B		34.8 mm^2	0.343 mm
100-2-A		45.9 mm^2	0.391 mm
100-2-B		94.9 mm^2	0.443 mm
100-3-A		48.5 mm^2	0.383 mm
100-3-B		37.8 mm^2	0.402 mm
200-1-A	200 nm BT coated by 2.5 wt% SiO_2	56.8 mm^2	0.321 mm
200-1-B		27.4 mm^2	0.369 mm
200-2-A		85.5 mm^2	0.238 mm
200-2-B		86.2 mm^2	0.344 mm
200-3-A		94.2 mm^2	0.435 mm
200-3-B		78.4 mm^2	0.300 mm

Due to the layered structure of SPS ceramics, the frequency dependence of dielectric constant and loss of each pieces obtained by cutting were tested for comparison for the study of relation between the microstructure and properties. All of the samples obtained from 100 nm and 200 nm ceramics are showing the high permittivity and high loss; However, largely difference

were found in their dielectric properties. At 1kHz, the highest permittivity appears on one sample from the 100 nm ceramics sample 100-2-A (771,778), at same time relatively low loss (1.4280); one of the sample from 200 nm ceramics is sample 200-3-A also showing the high permittivity (611,184) but higher loss (7.4963). For 100 nm ceramics, the lowest loss at 1kHz 1s 0.7896, from the sample 100-1-B, while for 200nm ceramics is 0.9830 from 200-2-B; the lowest loss from all of the samples in the testing frequency range was also recorded from the sample 100-1-B, which exhibits a relatively lower permittivity (56,461) and low loss (0.3540) at 72,921Hz. The permittivity, loss and resisivity of all the pieces of samples were shown in **Table 5-6**, the frequency dependence of properties of all the samples were show in **Figure 5-45** to **Figure 5-50**. It can be found that the dielectric properties of two layers from one sample can be very different; Compare with the difference between two layers from one sample, the difference between samples made by 100 nm and 200 nm nanopowders are not large.

Table 5-6 Dielectric constant, loss and resisivity of Auburn University BT/SiO_2 samples

Samples	At 1 kHz			Minimum value of loss			
	ε_r	tanδ	ρ (Ω·m)	Freq. (Hz)	ε_r	tanδ	ρ (Ω·m)
100-1-A	520,946	2.0978	13.40	21,450	284,003	0.5358	1.22
100-1-B	156,129	0.7896	56.02	72,921	56,461	0.3540	1.37
100-2-A	771,778	1.4280	10.94	26,826	297,945	0.5982	0.99
100-2-B	319,891	0.6463	25.62	6,393	233,321	0.3764	3.97
100-3-A	277,388	4.7213	13.14	37,275	151,690	0.5985	1.40
100-3-B	224,597	5.5097	14.06	60,653	100,598	0.6132	1.31
200-1-A	271,962	4.0002	15.55	24,790	157,818	0.6635	2.11
200-1-B	227,185	1.5190	36.35	53,175	99,552	0.4154	1.20
200-2-A	333,588	14.6462	3.66	158,489	133,325	0.6252	0.38
200-2-B	563,821	0.9830	15.94	11,557	281,092	0.5961	2.43
200-3-A	611,184	7.4963	3.85	118,654	204,765	0.6189	0.33
200-3-B	330,785	1.0620	27.13	15,437	169,485	0.5292	2.84

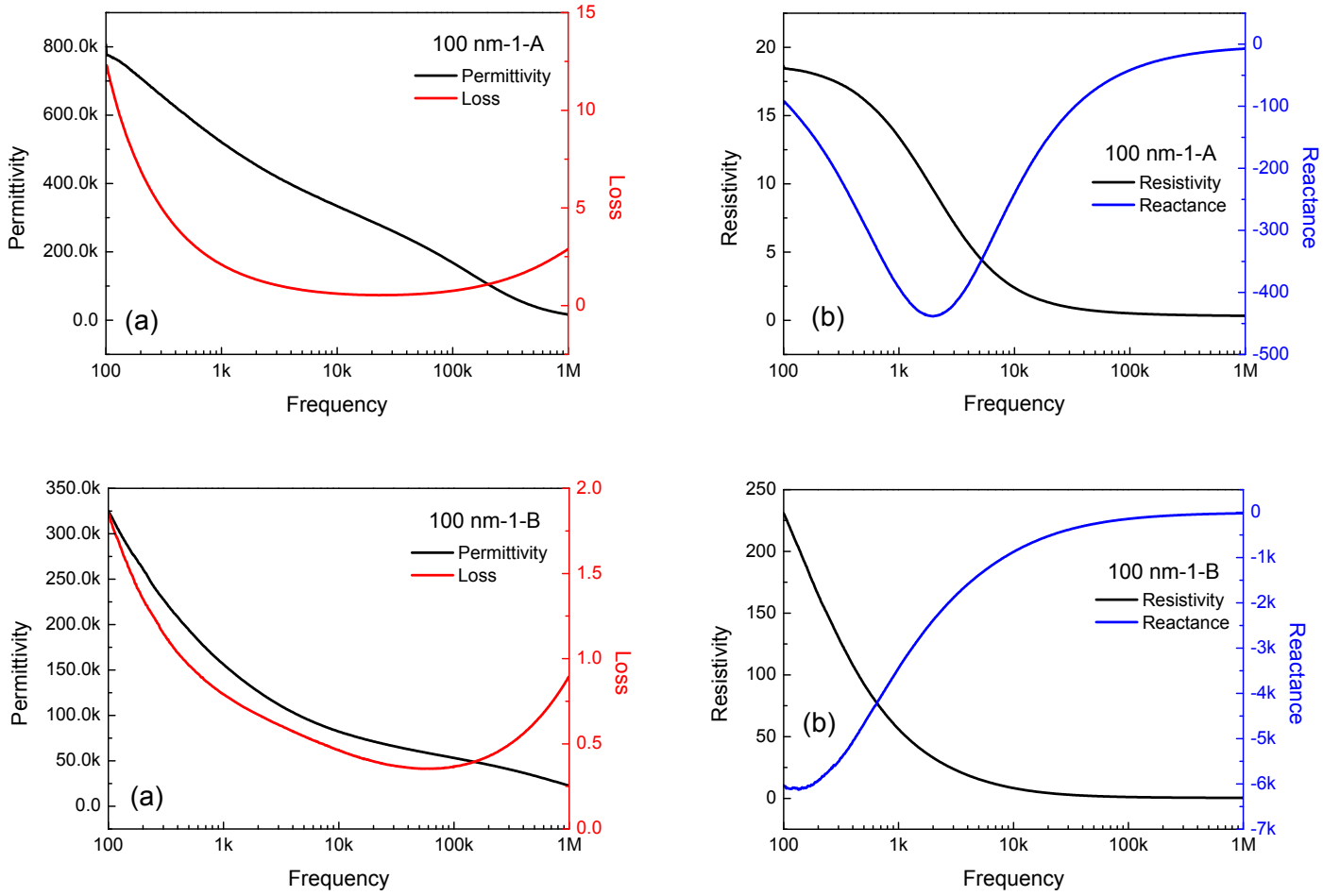

Figure 5-45 Frequency dependence of (a) Permittivity ~ Loss, and (b) Resisivity ~ Reactance of two layers from 100nm-1 ceramic

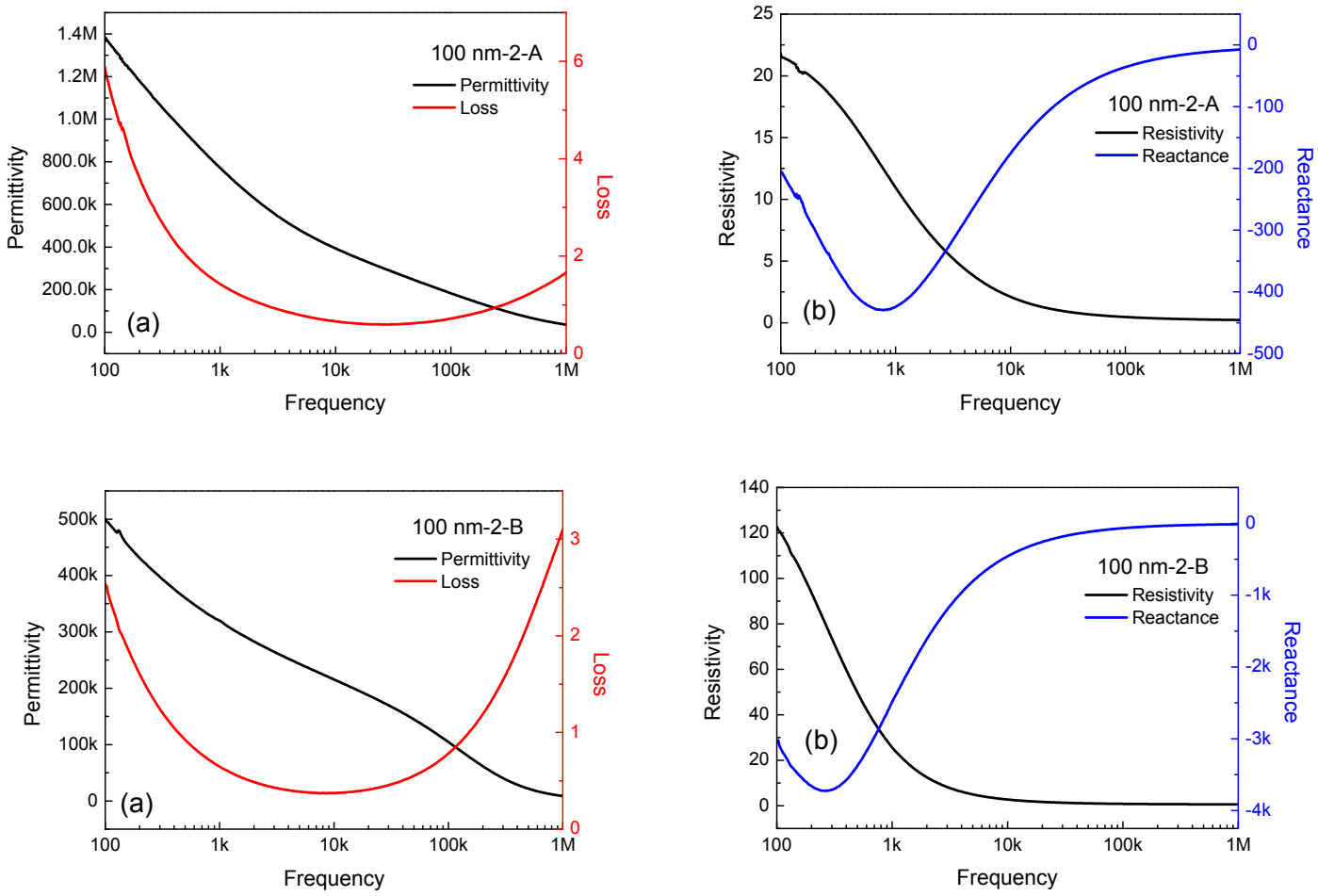

Figure 5-46 Frequency dependence of (a) Permittivity ~ Loss, and (b) Resisivity ~ Reactance of two layers from 100nm-2 ceramic

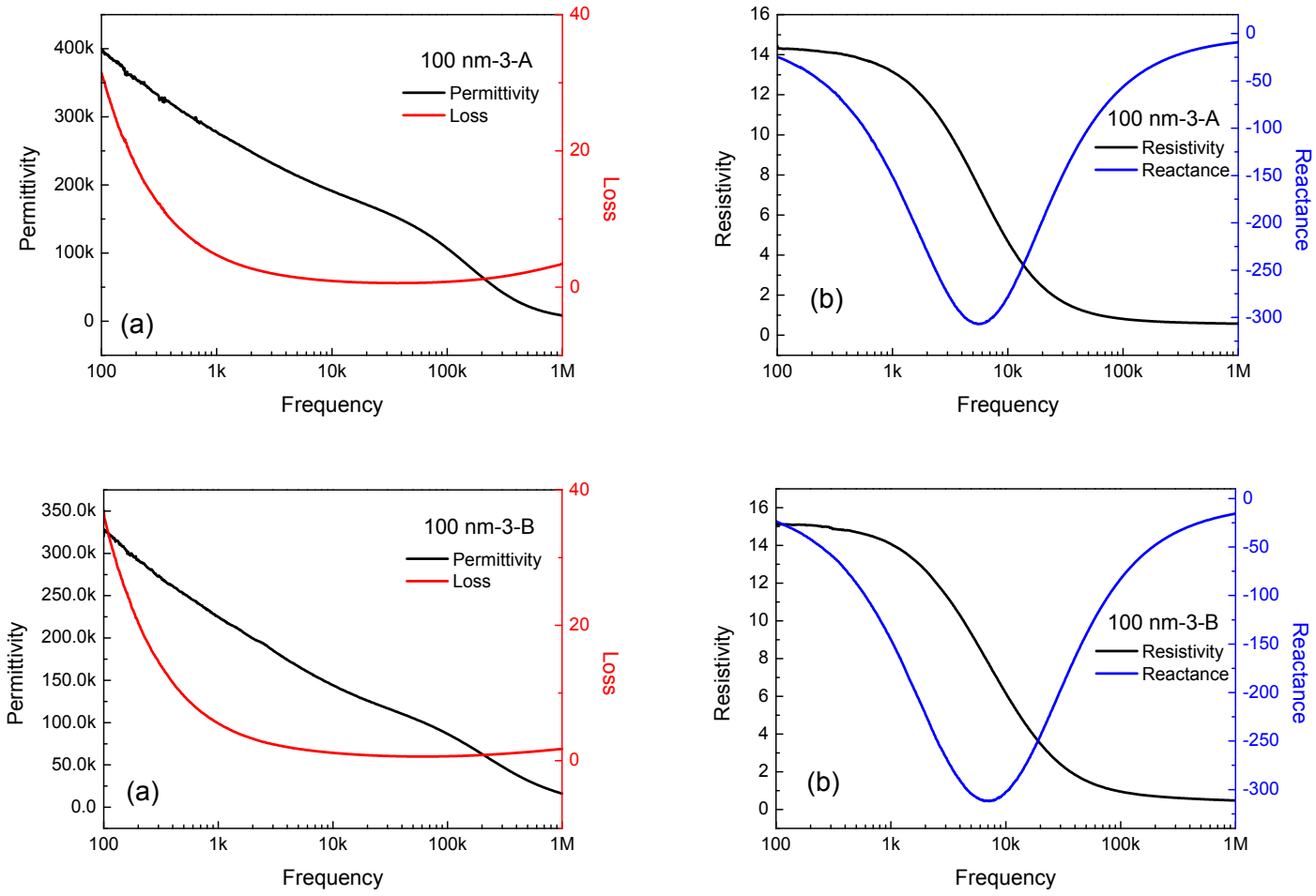

Figure 5-47 Frequency dependence of (a) Permittivity ~ Loss, and (b) Resisivity ~ Reactance of two layers from 100nm-3 ceramic

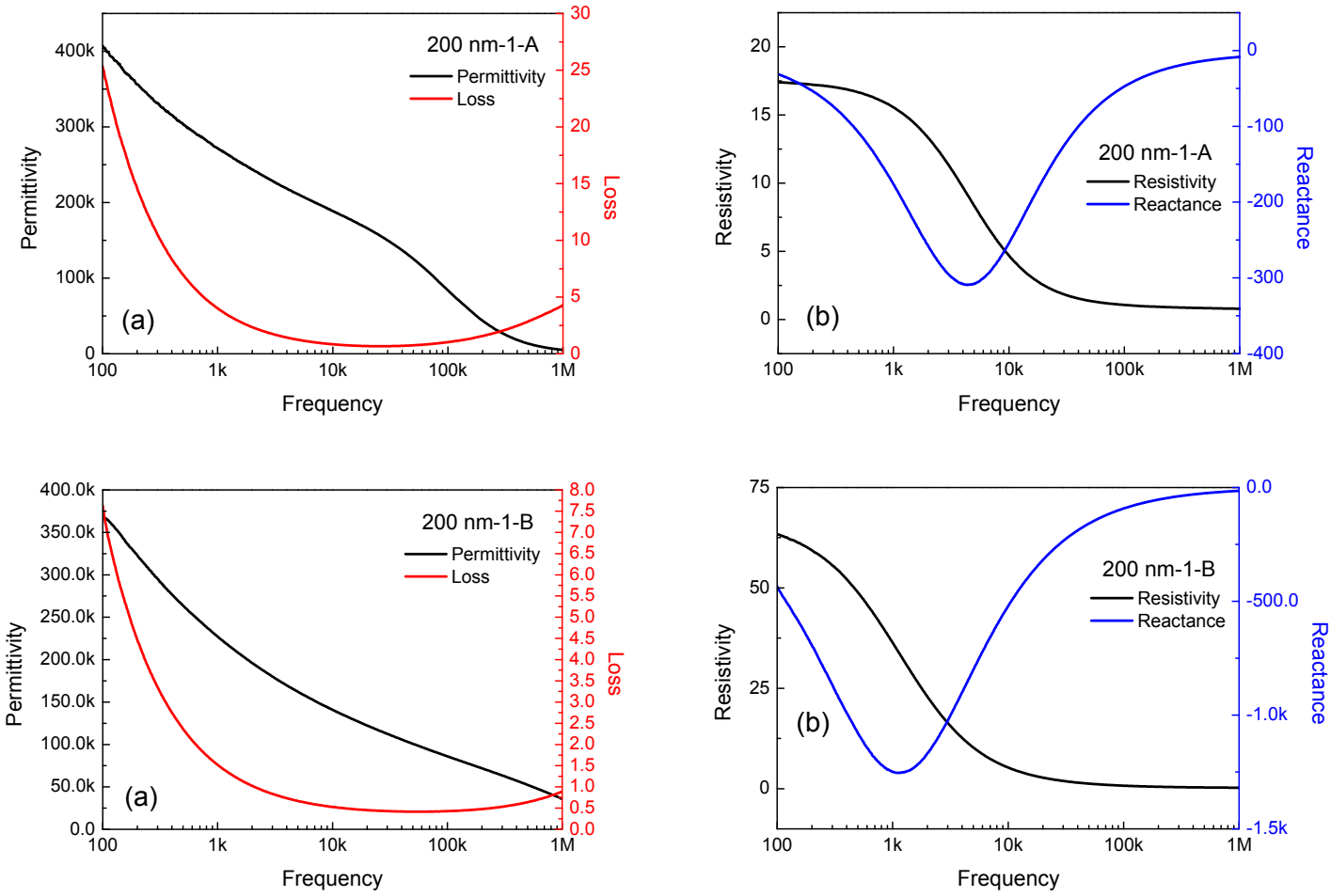

Figure 5-48 Frequency dependence of (a) Permittivity ~ Loss, and (b) Resisivity ~ Reactance of two layers from 200nm-1 ceramic

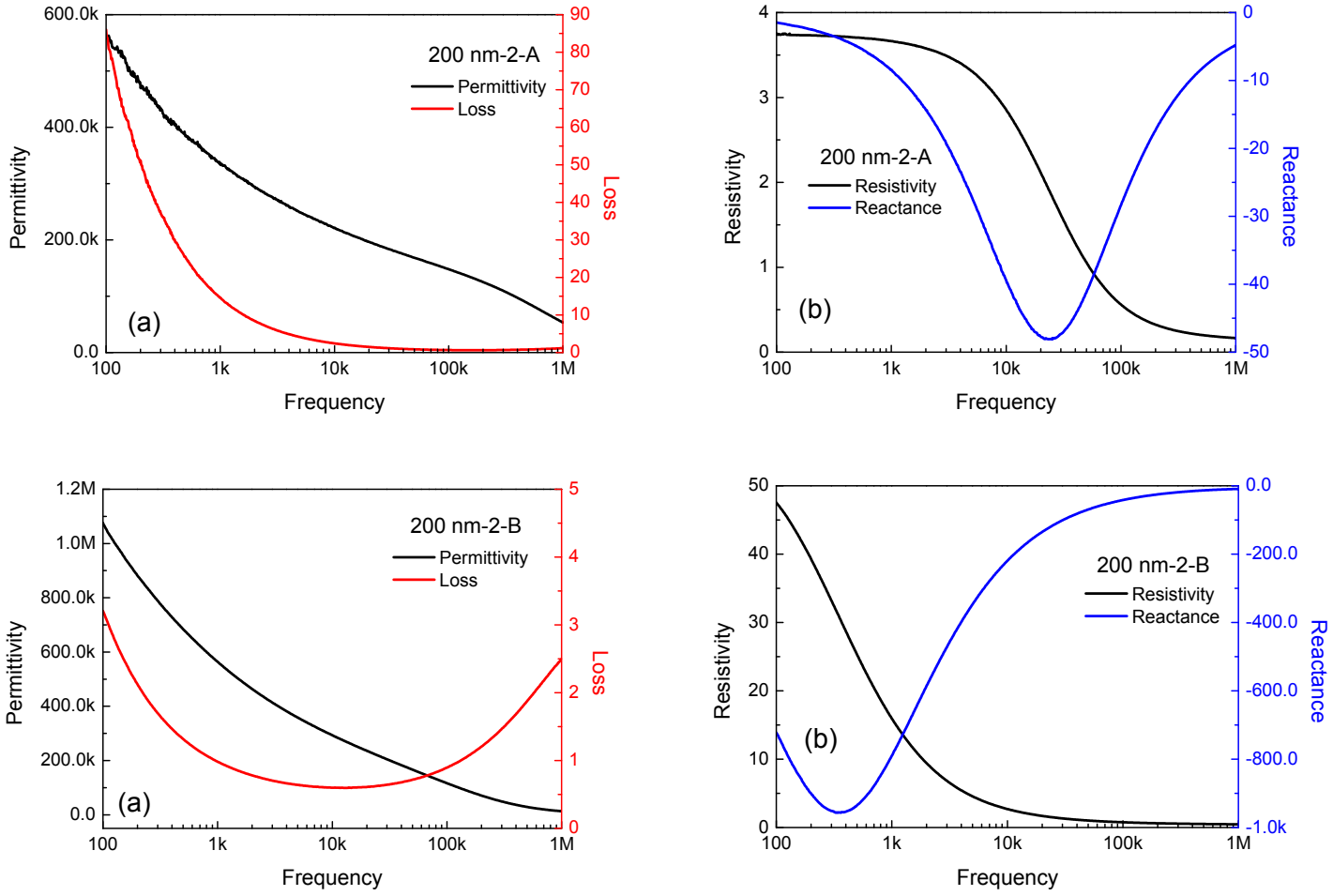

Figure 5-49 Frequency dependence of (a) Permittivity ~ Loss, and (b) Resisivity ~ Reactance of two layers from 200nm-2 ceramic

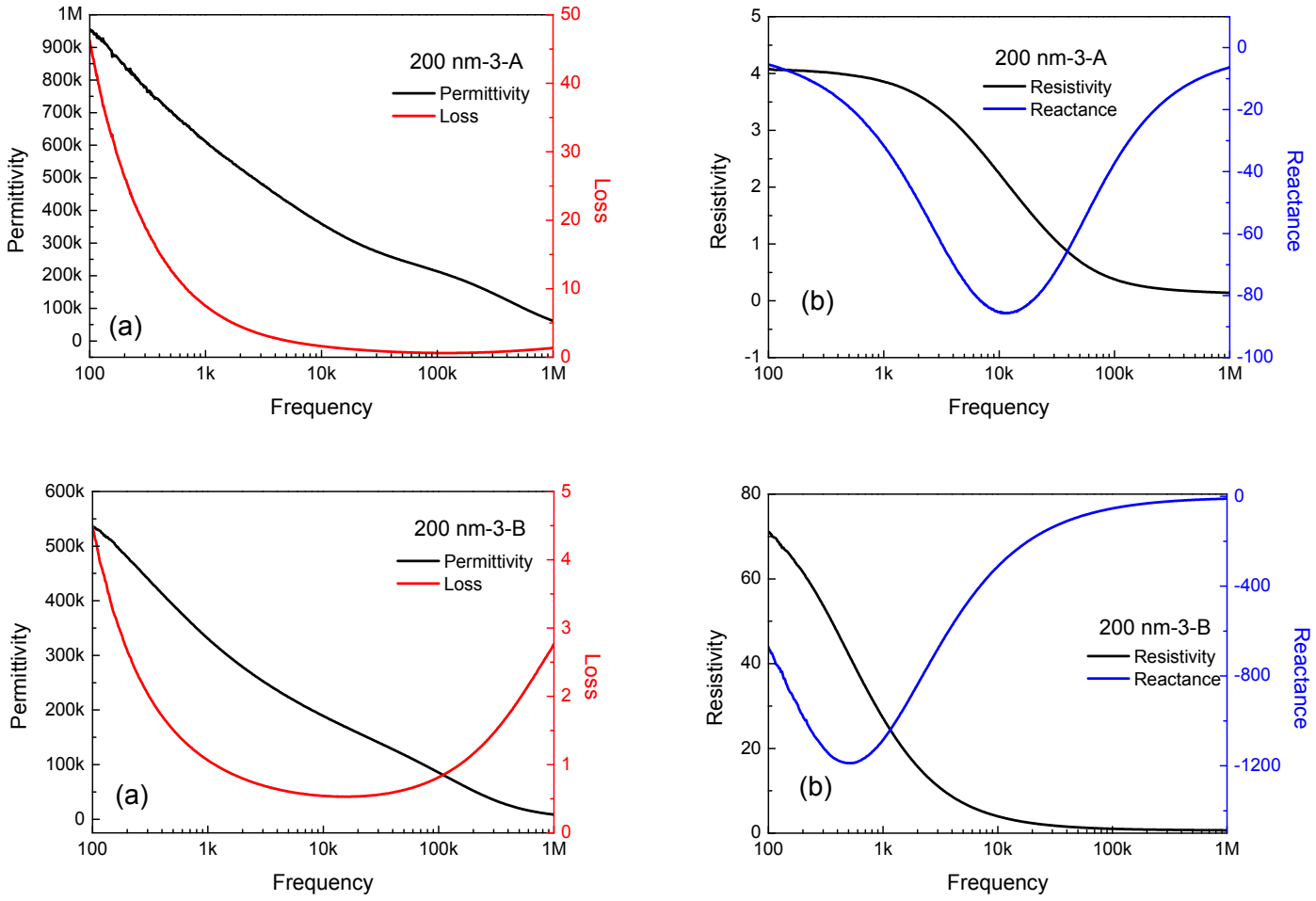

Figure 5-50 Frequency dependence of (a) Permittivity ~ Loss, and (b) Resisivity ~ Reactance of two layers from 200nm-3 ceramic

5.4.2.2 Breakdown Strength and P-E Loop

To further study the properties related to energy storage of SPS composites, the breakdown strength at room temperature of all samples received from NASA used in impedance testing were recorded. Due to the conductor-like properties of the tested SPS composites, most of

the samples are showing high dielectric constants and high loss, but very low breakdown strengths. For some of the samples with insulator-like properties with relative high breakdown strengths, the P-E loops were tried to collect under different electric fields prior to breakdown strength. Consistent with the grouping in the previous testing, the breakdown strengths of the samples with different coating methods, glass compositions and processing conditions were separately shown in **Table 5-7**, **Table 5-8** and **Table 5-9**. Due to the available voltage of the instrument are limited by a minimum value, the breakdown strength of the samples broken with a initial testing at 10 V are not able to be obtained.

Table 5-7 The breakdown strengths of BT/SiO_2 samples with different coating methods

Sample	Material	Thickness	Breakdown Voltage (V)	Breakdown Strength (MV/m)
French-SiO_2-A	SiO_2/BT produced by stöber process	1.302 mm	80	0.061
French-SiO_2-B		0.762 mm	45	0.059
VP-SiO_2-A	SiO_2/BT produced by vapor press deposition	0.754 mm	15	0.020
VP-SiO_2-B		1.332 mm	25	0.019
ALD-SiO_2-140-A	140 nm BT/SiO_2 produced by atomic layer deposition	1.159 mm	<10	--
ALD-SiO_2-140-B		1.062 mm	<10	--
ALD-SiO_2-500-A	500 nm BT/SiO_2 produced by atomic layer deposition	1.014 mm	<10	--
ALD-SiO_2-500-B		0.897 mm	<10	--

Table 5-8 The breakdown strengths of BT based samples with different glass compositions

Sample	Material	Thickness	Breakdown Voltage (V)	Breakdown Strength (MV/m)
ALD-Al_2O_3-A	BT/Al_2O_3 produced by atomic layer deposition	0.637 mm	<10	--
ALD-Al_2O_3-B		0.733 mm	15	0.020
ALD-ZrO_2-A	BT/ZrO_2 produced by atomic layer deposition	0.37 mm	600	1.622
ALD-ZrO_2-B		0.74 mm	<10	--
ALD-ZrO_2-C		0.68 mm	<10	--

Table 5-9 The breakdown strengths of BT/SiO_2 samples with different processing conditions

Sample No.	Preparation Condition	Thickness	Breakdown Voltage (V)	Breakdown Strength (MV/m)
SiO_2/BT 012815-01-A	1070 ºC/50MPa/30s/annealed 800ºC/12hr D=5.725g/cm^3	0.42 mm	<10	--
SiO_2/BT 012815-01-B		0.97 mm	<10	--
SiO_2/BT 012815-01-C		0.53 mm	<10	--
SiO_2/BT 012815-01-D		0.90 mm	<10	--
SiO_2/BT 012815-01-E		0.35 mm	<10	--
SiO_2/BT 020715-01-A	1100 ºC/50MPa/30s/annealed 800ºC/12hr D=5.902g/cm^3	0.40 mm	<10	--
SiO_2/BT 020715-01-B		0.73 mm	<10	--
SiO_2/BT 031715-02-A	1100 ºC/50MPa/2min/annealed 800ºC/16hr D=5.835g/cm^3	0.97 mm	<10	--
SiO_2/BT 031715-02-B		0.53 mm	<10	--
SiO_2/BT 031815-02-A	1100 ºC/25MPa/30s/annealed 800ºC/12hr D=5.783g/cm^3	0.73 mm	<10	--
SiO_2/BT 031815-02-B		1.12 mm	<10	--

From the results of breakdown testing, It can be found that most of the SPS composites are so close to conductive materials therefore the breakdown strength are not exist for those samples. For other samples which have shown insulator-like properties, a low but clear breakdown strength can be found. However, in the P-E testing, some of the samples with insulator-like properties still can not show the loops even below the breakdown strength. Here, the P-E loops for three of the samples (French-SiO_2-A, French-SiO_2-B and ALD-ZrO_2-A) were recorded and shown in the following figures. As shown in **Figure 5-51**, the two pieces French-SiO_2-A and French-SiO_2-B from the same original pellet are showing very close properties, the polarization of both samples are beyond 100 $\mu C/cm^2$ under an external electric field of 0.06 MV/m. The loops of both samples are having very large areas, which means the huge losses therefore no energy were stored in material. Compare with other samples, ALD-ZrO_2-A shows relatively good dielectric properties. As discussed previously, it has a dielectric constant of 4732 and a dielectric loss 0.063 at 1 kHz. From its P-E loop under different voltages as shown in **Figure 5-52**, the breakdown field of ALD-ZrO_2-A reaches 1.622 MV/m and the polarization is around 19 $\mu C/cm^2$.

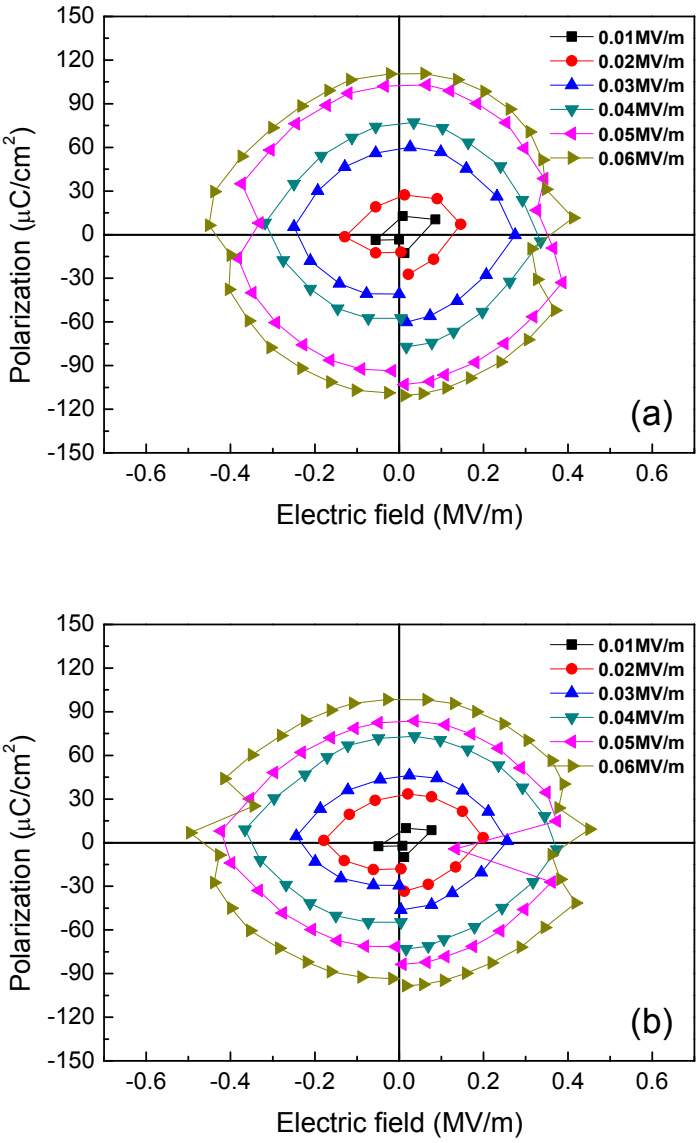

Figure 5-51 The P-E loop of (a) French-SiO_2-A, and (b) French-SiO_2-B

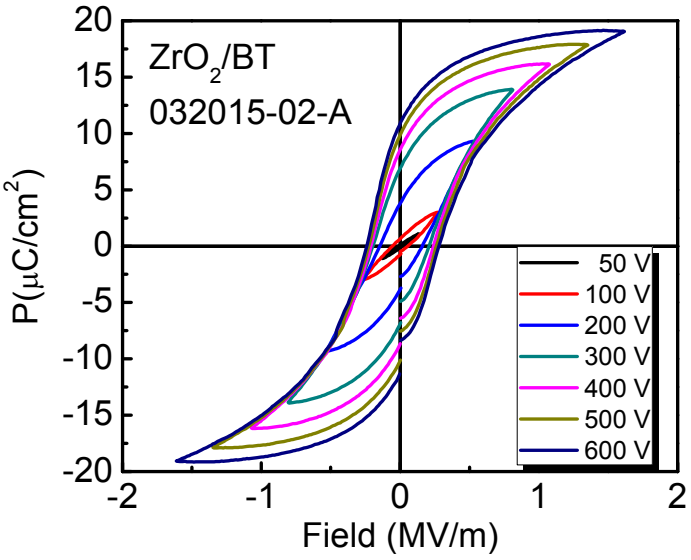

Figure 5-52 The P-E loop of sample ALD-ZrO_2-A under different voltages

5.4.3 Discussion

5.4.3.1 Influence of Coating Methods

For the purpose of obtain the dielectric testing resulting from different particles, the properties of SPS composites prepared by the SiO_2/BT nanopowders provided by other researches were also recorded. All of the samples used in microstructure studies by SEM were used in the testing. As discussed previously, the French-SiO_2 and VP-SiO_2 samples are showing the layered structures; the ALD-SiO_2 samples have shown an integrated cross section. The results of poor uniformity and low density of all composites were confirmed. Based on these facts, all of the composites were cut into two layers and tested as the same as the experiment previously. The information and dimension of the samples tested are listed in **Table 5-10**.

Table 5-10 The information and dimension of BT/SiO_2 samples made by different powders

Sample	Material	Area	Thickness
French-SiO_2-A	SiO_2/BT produced by stöber process	19.3 mm^2	1.302 mm
French-SiO_2-B		14.0 mm^2	0.762 mm
VP-SiO_2-A	SiO_2/BT produced by vapor press deposition	15.5 mm^2	0.754 mm
VP-SiO_2-B		35.9 mm^2	1.332 mm
ALD-SiO_2-140-A	140 nm BT/SiO_2 produced by atomic layer deposition	94.0 mm^2	1.159 mm
ALD-SiO_2-140-B		86.2 mm^2	1.062 mm
ALD-SiO_2-500-A	500 nm BT/SiO_2 produced by atomic layer deposition	34.2 mm^2	1.014 mm
ALD-SiO_2-500-B		28.9 mm^2	0.897 mm

The frequency dependence of dielectric constant and loss of each pieces obtained by cutting were tested. All of the samples are showing the relatively high permittivity; However, largely difference were found in their dielectric properties. First of all, sample French-SiO_2-A and French-SiO_2-B are shown the similar dielectric properties with a slightly higher dielectric constant (4,989 and 6,158) and high loss in same level (10.594 and 13.987) at 1 kHz. The similar properties indicates that even stratification happened, the samples still behave a good uniformity at current processing conditions; compare with the Auburn University samples test previously, the relatively high resistivity (337.23 and 207.73 Ω·m) illustrated that the SiO_2 coating on received powders obtained by stöber process are much stronger to form the barrier in the SPS composites. Compare with the French-SiO_2 samples, VP-SiO_2-A and VP-SiO_2-B, are showing the much higher dielectric constant (411,886 and 388,498) and lower loss (1.223 and 0.421) at 1kHz. Particularly, VP-SiO_2-A shown the most predominant dielectric constant (1,465,280) and

simultaneously low loss (0.898) at 100Hz. The properties of the two samples are close but still have some difference, which indicates that the uniformity of sample produced by vapor press deposition are relatively good but not excellence. For the composites made by atomic layer deposition, two layers of the samples ALD-SiO_2-140-A and ALD-SiO_2-140-B made by 140 nm nanopowders shows the extremely high dielectric constant (811,895 and 304,997) and low loss (0.457 and 0.435) at 1kHz; compare with them, the samples ALD-SiO_2-500-A and ALD-SiO_2-500-B, two layers made by 500 nm nanopowders, are showing a slightly lower dielectric constant (415,959 and 323,189) and higher loss (1.275 and 0.963) at 1kHz. The dielectric behaviors of the pieces obtained from one ceramic are very close, but the values of dielectric constant still have difference, which indicates that the uniformity of sample are relatively good but layered element distribution still occurs. The permittivity, loss and resisivity of all the pieces of samples were shown in **Table 5-11**, the frequency dependency of properties for the composites were shown from **Figure 5-53** to **Figure 5-56**. It can be found that the dielectric properties the sample with different prepare methods can be very different; by the optimization of SiO_2 coating quality, the results of a increased dielectric constant and a reduced loss can be achieved simultaneously.

Table 5-11 Dielectric constant, loss and resisivity of BT/SiO_2 samples made by different powders

Samples	At 1 kHz			Minimum value of loss			
	ε_r	tanδ	ρ (Ω·m)	freq.	ε_r	tanδ	ρ (Ω·m)
French-SiO_2-A	4,989	10.594	337.23	1,000,000	184	0.854	48.09
French-SiO_2-B	6,158	13.987	207.73	1,000,000	278	0.843	31.78
VP-SiO_2-A	411,886	1.223	21.39	100	1,465,280	0.898	61.01
VP-SiO_2-B	388,498	0.421	16.54	1,035	385,689	0.42	16.08
ALD-SiO_2-140-A	811,895	0.457	8.46	2,344	680,270	0.42	4.03
ALD-SiO_2-140-B	304,997	0.435	21.81	3,055	241,988	0.395	8.32
ALD-SiO_2-500-A	415,959	1.275	21.23	3,673	279,115	0.923	8.74
ALD-SiO_2-500-B	323,189	0.963	28.12	4,466	232,695	0.629	7.8

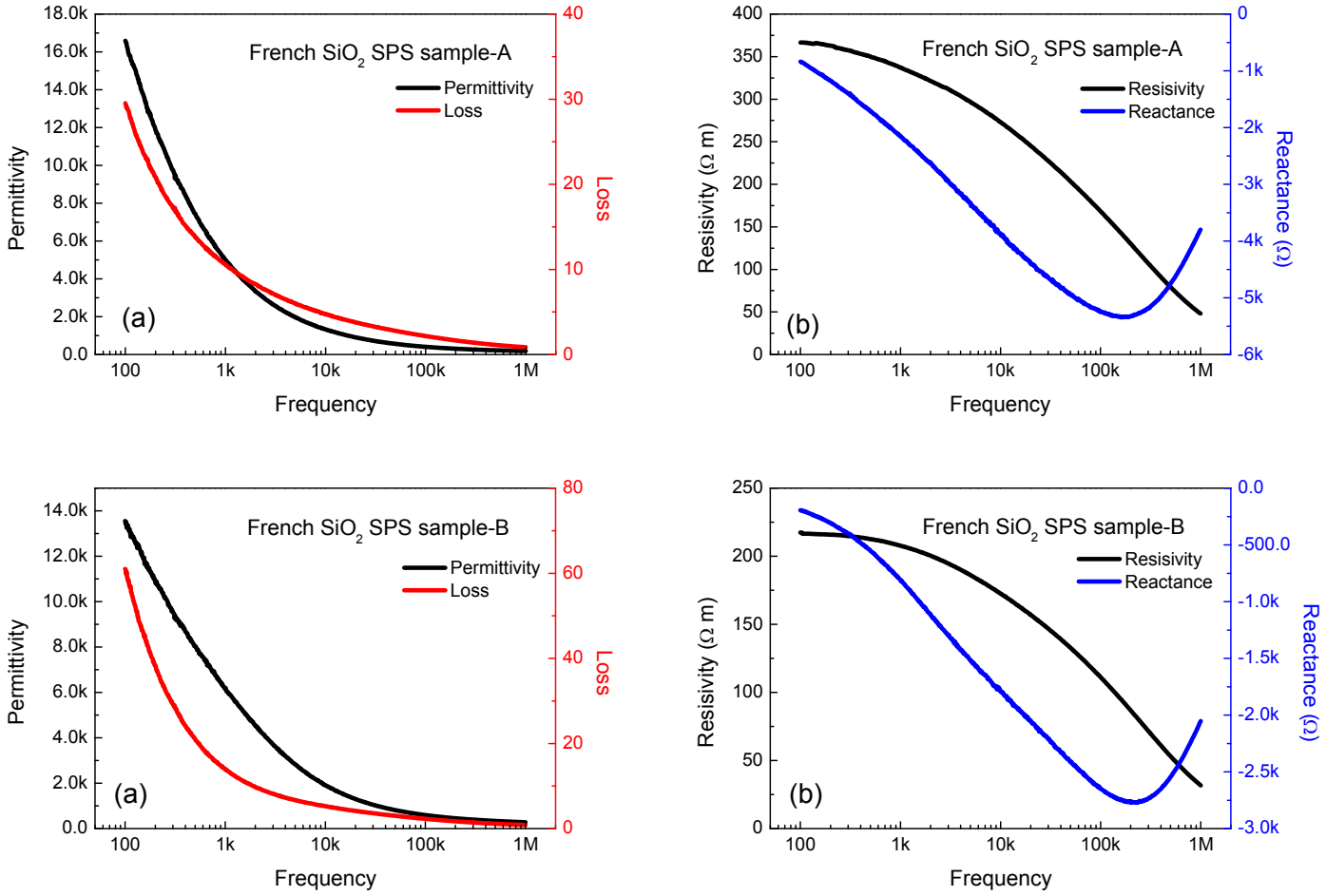

Figure 5-53 Frequency dependency of (a) Permittivity ~ Loss, and (b) R~X of French-SiO_2-A and French-SiO_2-B

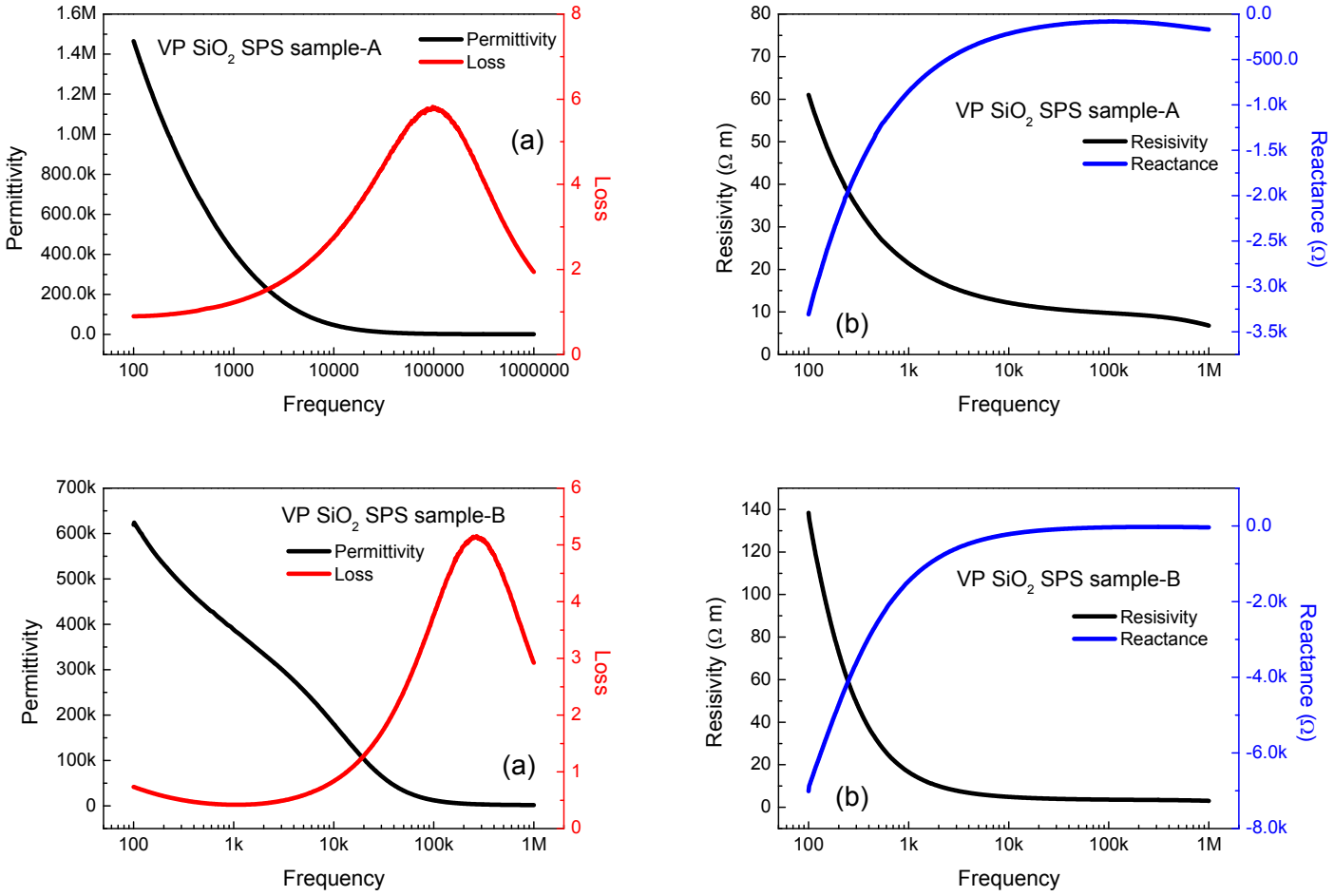

Figure 5-54 Frequency dependency of (a) Permittivity ~ Loss, and (b) R~X of VP-SiO_2-A and VP-SiO_2-B

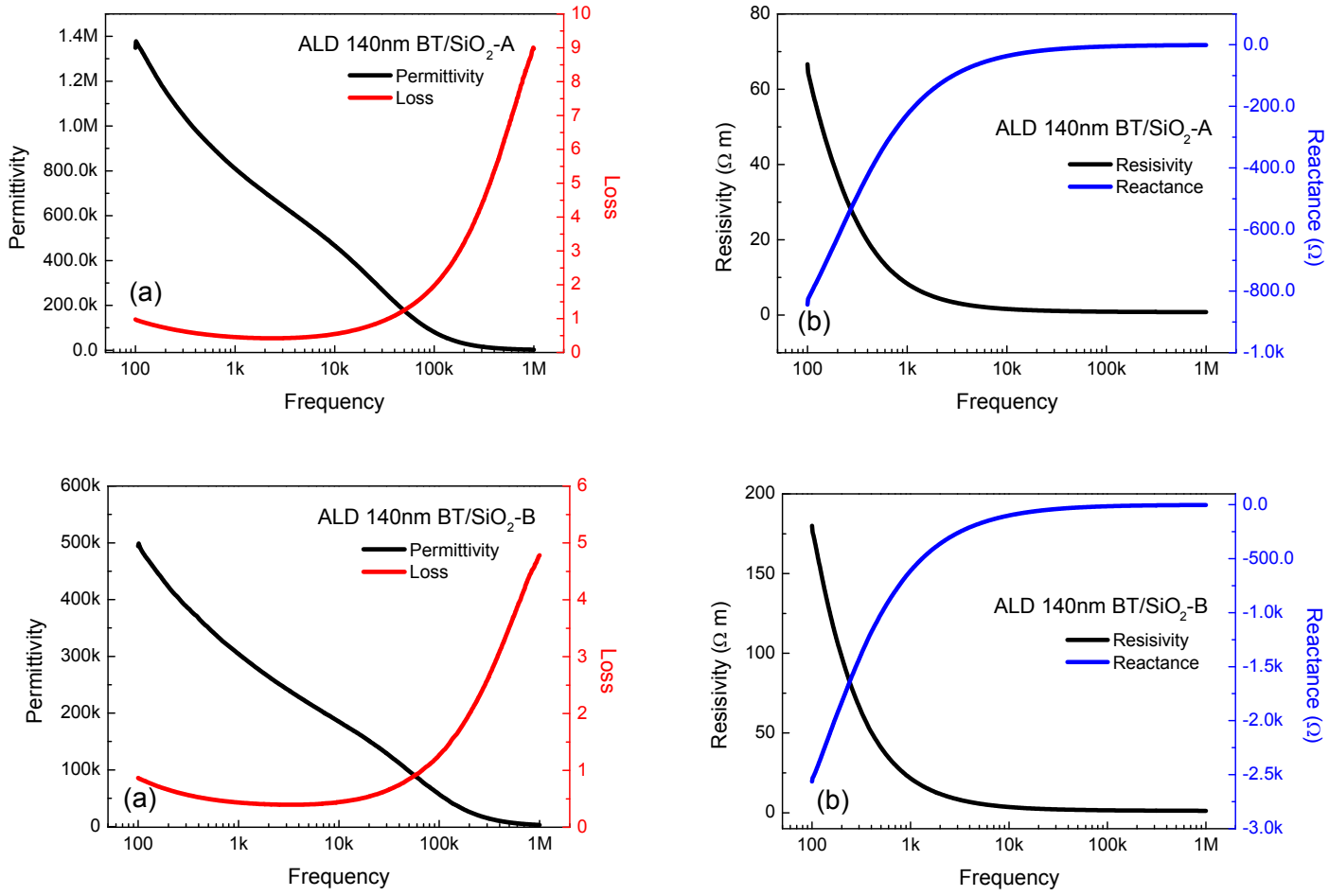

Figure 5-55 Frequency dependence of (a) Permittivity ~ Loss, and (b) Resisivity~Reactance of ALD-SiO_2-140-A and ALD-SiO_2-140-B

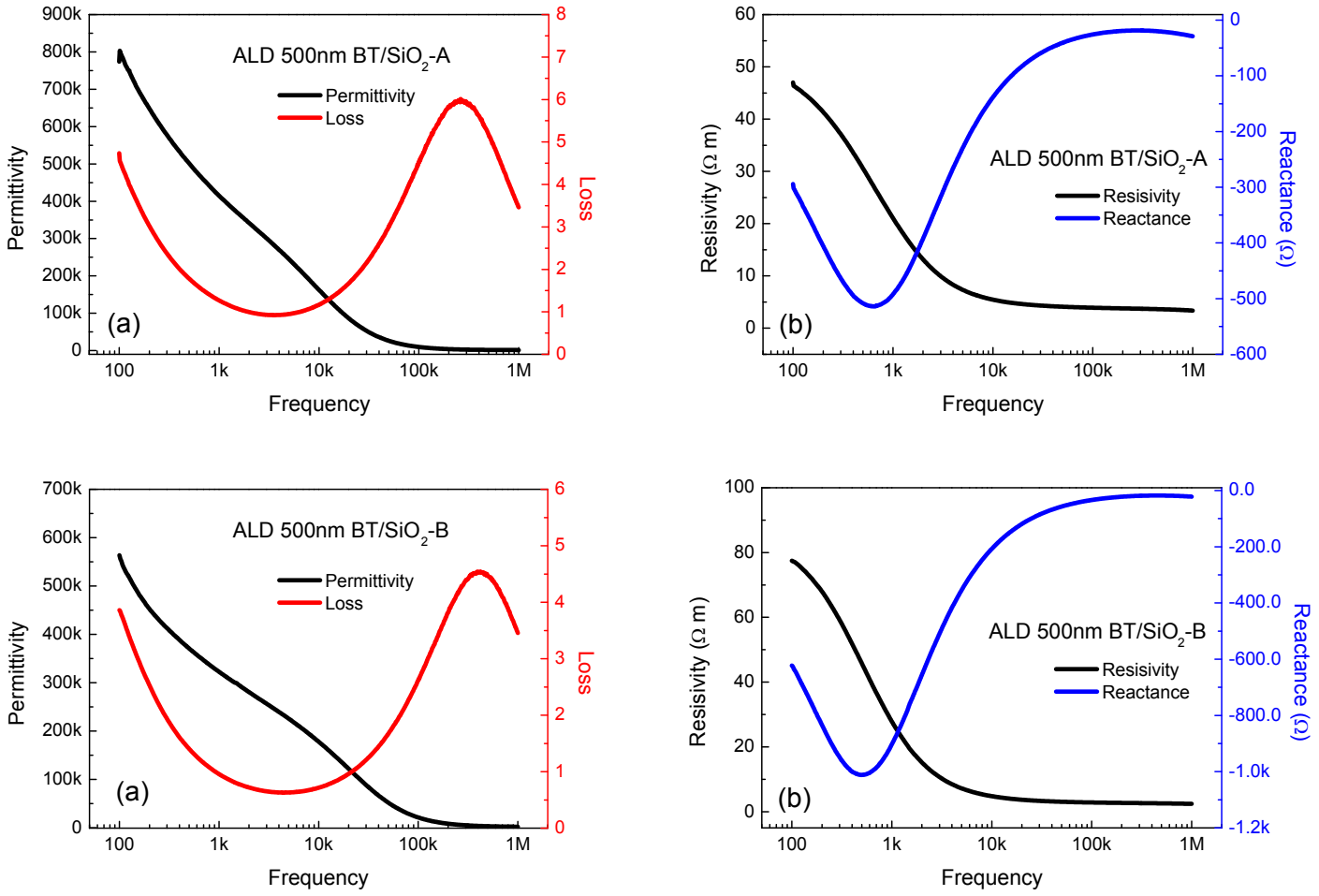

Figure 5-56 Frequency dependence of (a) Permittivity ~ Loss, and (b) Resisivity~Reactance of ALD-SiO_2-500-A and ALD-SiO_2-500-B

5.4.3.2 Influence of Glass Compositions

For the SPS composites produced by $BaTiO_3$ nanoparticles coated with different glass, the properties of ZrO_2/BT and Al_2O_3/BT pellets received from NASA were recorded. As the same as previously, the ALD-Al_2O_3 and ALD-ZrO_2 samples were cut from the cross section. Differently, the ALD-Al_2O_3 sample were into two layers and the ALD-ZrO_2 sample were cut into

three layers due to the larger thickness. The information and dimension of the samples tested are listed in **Table 5-12**.

Table 5-12 The information and dimension of BT based samples made by different powders

Sample	Material	Area	Thickness
ALD-Al_2O_3-A	BT/Al_2O_3 produced by atomic layer deposition	11.3 mm^2	0.637 mm
ALD-Al_2O_3-B		11.2 mm^2	0.733 mm
ALD-ZrO_2-A	BT/ZrO_2 produced by atomic layer deposition	27.3 mm^2	0.37 mm
ALD-ZrO_2-B		16.6 mm^2	0.74 mm
ALD-ZrO_2-C		22.0 mm^2	0.68 mm

The frequency dependence of dielectric constant and loss of each pieces obtained by cutting were tested. Among them, the sample ALD-Al_2O_3-B and ALD-ZrO_2-A, with white color part in original SPS samples, show insulator like properties; The other samples are in the color of dark blue, and show a very high dielectric constant but a high loss at low frequency which means a high electrical conductivity. For the samples close to insulators, the sample ALD-Al_2O_3-B obtained from the original sample ALD-Al_2O_3 shows a dielectric constant close to general ceramics (4,137) and low loss (0.162) at 1 kHz; the sample ALD-ZrO_2-A obtained from the original sample ALD-ZrO_2 also shows the dielectric constant (4,732) and low loss (0.063) in the same level at 1 kHz. For the other samples, the dark part of ALD-Al_2O_3 shown relatively high dielectric constant (313,808) and extremely high loss (115.023) at 1 kHz, which is close to the conductive materials; the ones from ALD-ZrO_2 shown a relatively high dielectric constant (13,379 for ALD-ZrO_2-B and 11,540 for ALD-ZrO_2-C) and loss (0.212 for ALD-ZrO_2-B and 0.409 for ALD-ZrO_2-C) at 1 kHz. The difference between each layers from one pellet shown that

all of those samples have a poor uniformity. The dielectric constant, loss and resisivity of all samples were shown in **Table 5-13**, the frequency dependence of properties of all the samples were show in **Figure 5-57** to **Figure 5-58**.

Table 5-13 Dielectric constant, loss and resisivity of samples with different glass compositions

Samples	At 1 kHz			Minimum value of loss			
	ε_r	tanδ	ρ (Ω·m)	freq.	ε_r	tanδ	ρ (Ω·m)
ALD-Al_2O_3-A	313,808	115.023	0.50	372,759	112,842	1.541	0.28
ALD-Al_2O_3-B	4,137	0.162	26833.44	93,633	3,041	0.093	679.12
ALD-ZrO_2-A	4,732	0.063	60324.20	2,928	4,570	0.058	23171.90
ALD-ZrO_2-B	13,379	0.212	6340.41	13,593	11,002	0.123	977.65
ALD-ZrO_2-C	11,540	0.409	3810.20	10,000	7,757	0.304	762.62

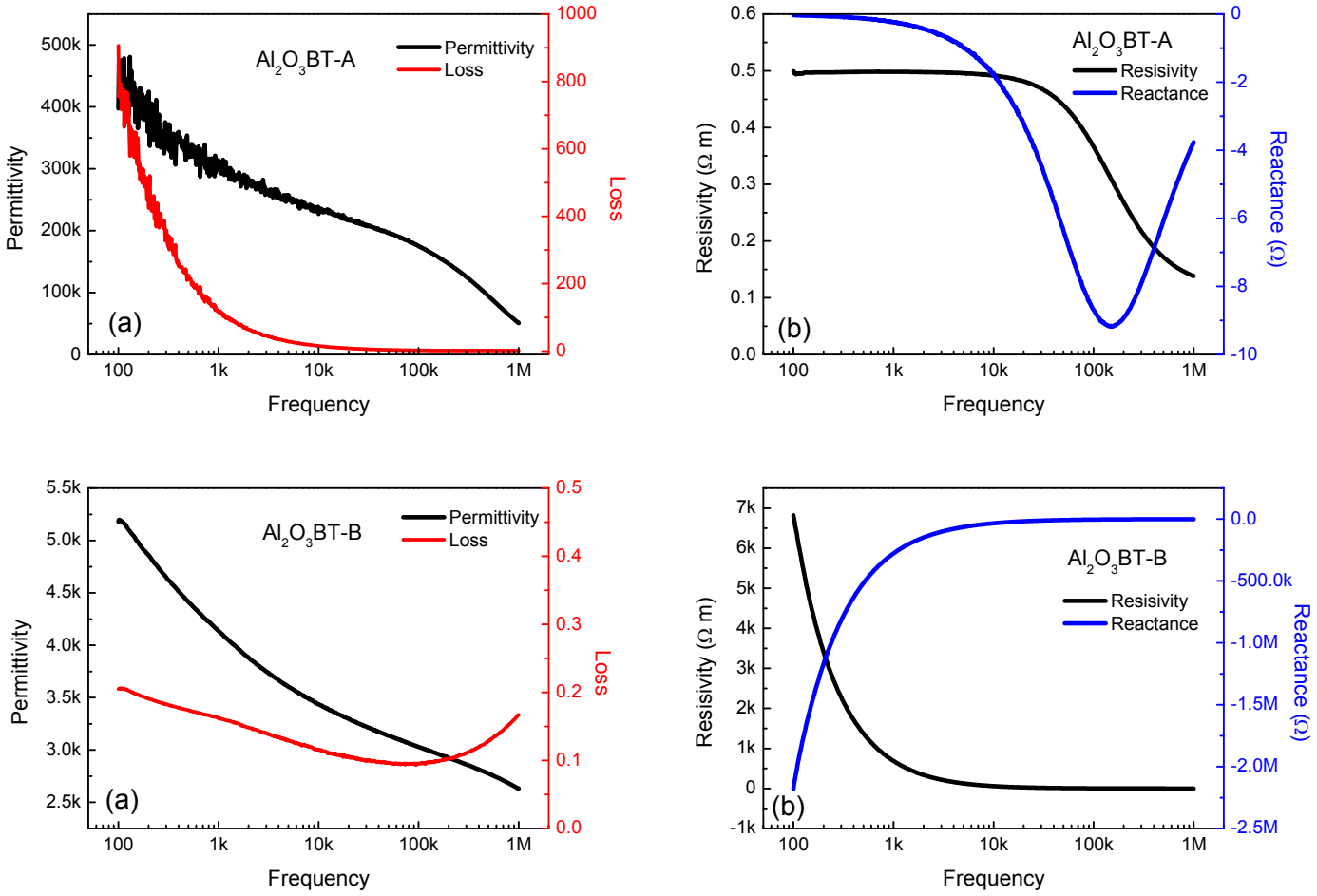

Figure 5-57 Frequency dependence of (a) Permittivity ~ Loss, and (b) R~X of sample ALD-Al_2O_3-A and ALD-Al_2O_3-B

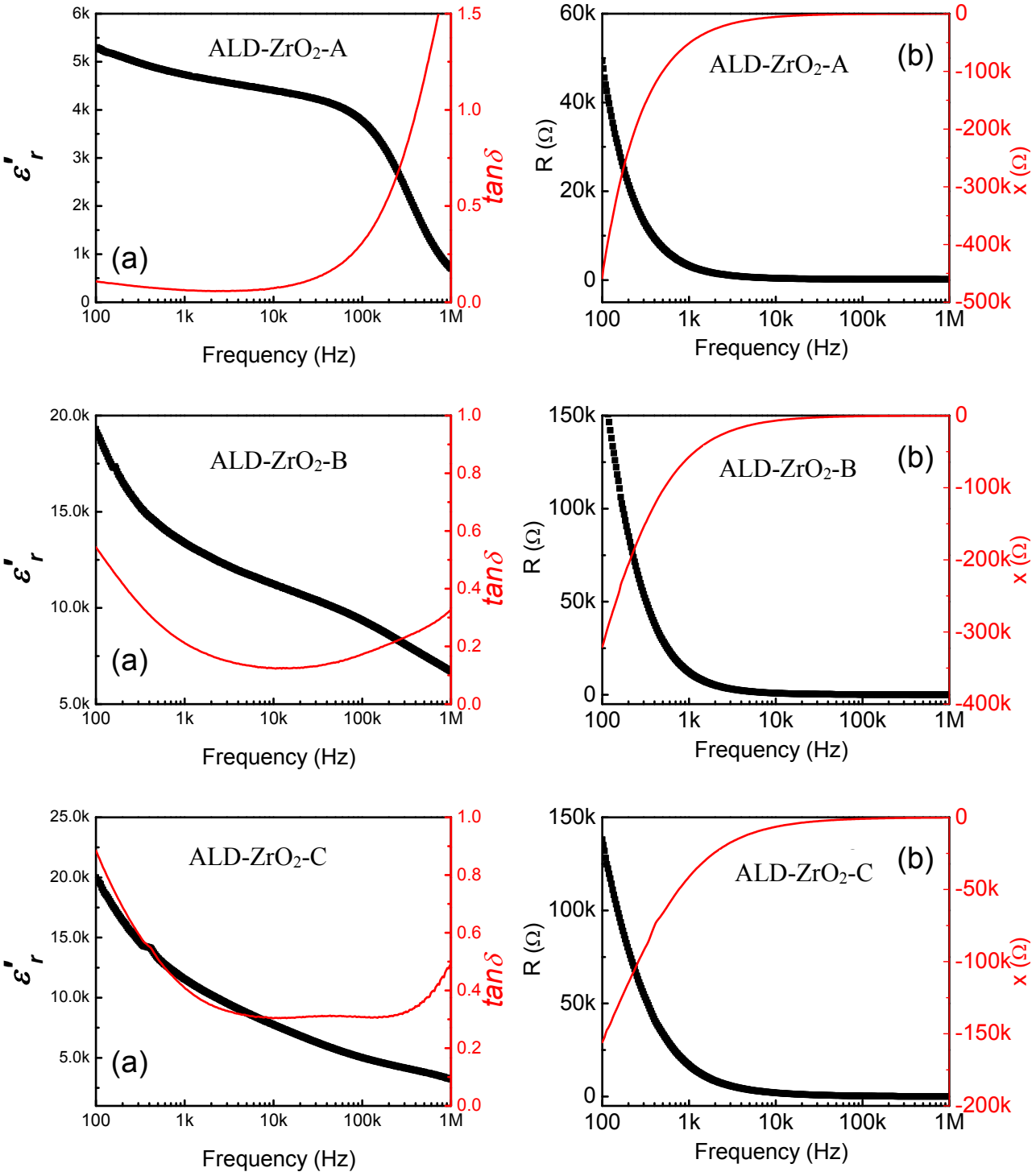

Figure 5-58 Frequency dependence of (a) Permittivity ~ Loss, and (b) R~X of sample ALD-ZrO_2-A, ALD-ZrO_2-B and ALD-ZrO_2-C

5.4.3.3 Influence of Processing Conditions

The different samples prepared by different coating methods and glass compositions have been discussed previously. To study the influence of processing in SPS, the dielectric properties of SiO_2/BT pellets received from NASA produced with different conditions were recorded. As the same as previously, the composite samples were cut from the cross section; according to the different thickness of samples, different number of layers from each samples were obtained. In the testing, the frequency dependences of ε_r-tanδ (the dielectric constant and loss) and R-X (the real and imaginary part of resistivity) for different samples at room temperature and at frequencies ranging from 100 Hz to 1 MHz were characterized. The results are summarized in **Table 5-14**. As can be seen from the results, according to the difference in dielectric properties, these ceramics can be classified into two types: 1. the composites with a high dielectric constant and also a high loss, and 2. the composites with a small dielectric constant and a low loss.

Firstly, the difference between samples sintered with different temperatures were identified. The ceramic 012815-01 with a sinter temperature of 1070 °C have shown an low density of 5.725g/cm^3 and an obviously layered structure, which resulting a greatly different dielectric constant between layers obtained by cutting. The high dielectric constant of 313,623 at 1kHz was found from the piece of 012815-01-B, while a significantly lower value of 1,944 was found from the piece of 012815-01-C which is the part right next to 012815-01-B in the original pellet. By increasing the sinter temperature to 1100 °C without any change in other conditions, the density of sample 020715-01 weas increased to 5.902g/cm^3; in addition, the dielectric constant between layers are much smaller (132,315 for 020715-01-A and 95,121 for 020715-01-B). This suggested that the sintering at high temperature will result in a dense and uniform

structure. For the next sample 031715-02, the time of sintering and annealing were increased from 12 to 16 hr. However, the difference between the two layers are still large (28,718 for 031715-02-A and 420,987 for 031715-02-B) and the density was not increased (5.835g/cm^3), therefore the sintering and annealing in SPS are not required a long time. Finally, by reducing the value from 50 to 25 MPa with the fixed sinter temperature of 1100 °C, the pressure was found to be another important factor to improve the uniformity. The dielectric constant between the layers of sample 031815-02 are much closer (273,680 for 031815-02-A and 385,856 for 031815-02-B). Simultaneously, the density of 031815-02 were decreased to 5.783g/cm^3 due to the low pressure. Overall, after optimizing the processing conditions, the SPS composites are still far from uniform. The frequency dependence of properties of all the samples were show in **Figure 5-59** to **Figure 5-62**. In some of the following figures, two curves constituted by different symbols were shown due to the different analyzers used in testing. The solid symbols are representing the results from Agilent 4294A Impedance Analyzer, the hollow symbols are representing the results from Solartron 1260A Impedance Analyzer. Due to the higher accuracy in the frequency range, the results from Agilent 4294A Impedance Analyzer were used in the **Table 5-14**.

Table 5-14 Dielectric constant and loss of samples with different processing conditions

NASA No.	Preparation	At 1 kHz		Minimum loss		
		ε_r	$tan\delta$	*freq.*	ε_r	$tan\delta$
SiO_2/BT 012815-01-A	1070 ºC/50MPa/30s/annealed 800ºC/12hr D=5.725g/cm^3	163,815	1.413	39,810	109,068	0.208
SiO_2/BT 012815-01-B		313,623	0.991	64,565	105,488	0.288
SiO_2/BT 012815-01-C		1,944	0.072	45,708	1,804	0.023
SiO_2/BT 012815-01-D		1,779	0.102	136,458	1,578	0.024
SiO_2/BT 012815-01-E		2,195	0.115	197,242	1,895	0.025
SiO_2/BT 020715-01-A	1100 ºC/50MPa/30s/annealed 800ºC/12hr D=5.902g/cm^3	132,315	3.799	104,713	63,959	0.362
SiO_2/BT 020715-01-B		95,121	0.324	35,481	66,355	0.147
SiO_2/BT 031715-02-A	1100 ºC/50MPa/2min/annealed 800ºC/16hr D=5.835g/cm^3	28,718	110.25	1,000,000	2,235	2.702
SiO_2/BT 031715-02-B		420,987	0.738	1,634	356,130	0.723
SiO_2/BT 031815-02-A	1100 ºC/25MPa/30s/annealed 800ºC/12hr D=5.783g/cm^3	273,680	10.17	45,012	81,237	1.484
SiO_2/BT 031815-02-B		385,856	3.916	14,017	243,955	0.922

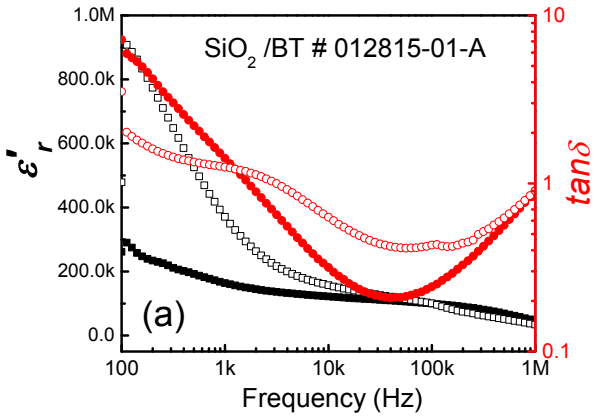
SiO2 /BT # 012815-01-A
(a)
ε'r
tanδ
Frequency (Hz)

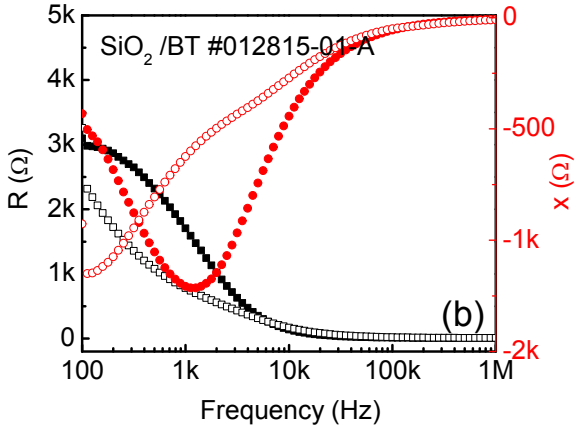
SiO2 /BT #012815-01-A
(b)
R (Ω)
x (Ω)
Frequency (Hz)

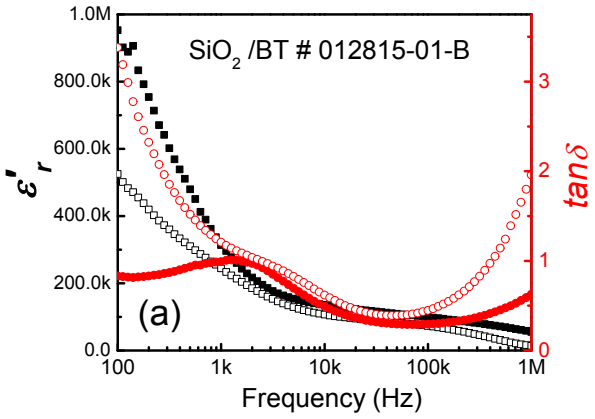
SiO2 /BT # 012815-01-B
(a)
ε'r
tanδ
Frequency (Hz)

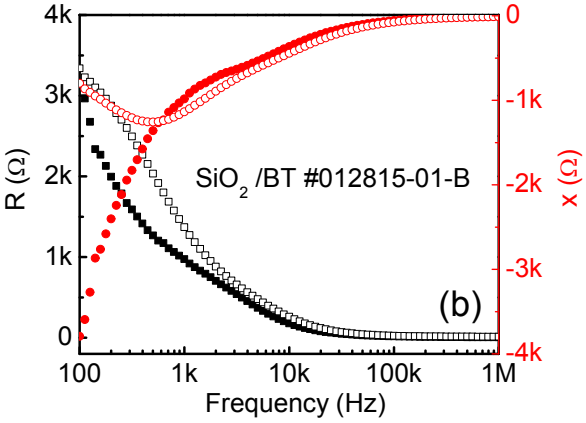
SiO2 /BT #012815-01-B
(b)
R (Ω)
x (Ω)
Frequency (Hz)

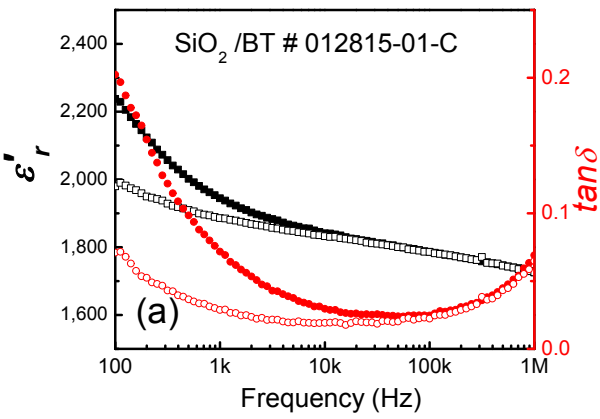
SiO2 /BT # 012815-01-C
(a)
ε'r
tanδ
Frequency (Hz)

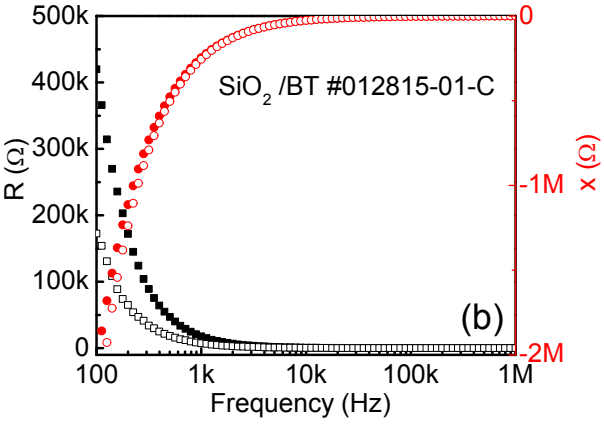
SiO2 /BT #012815-01-C
(b)
R (Ω)
x (Ω)
Frequency (Hz)

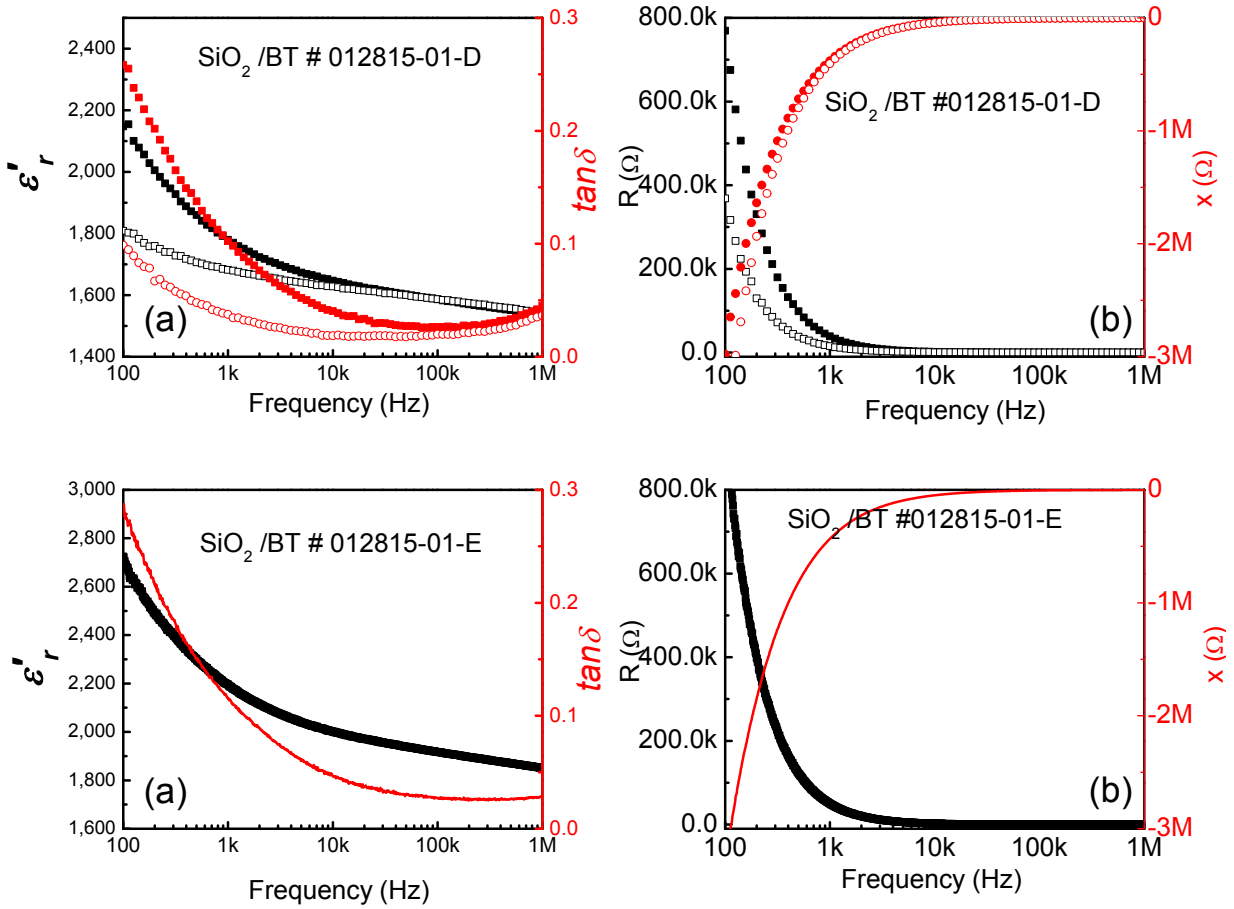

Figure 5-59 Frequency dependence of (a) Permittivity ~ Loss, and (b) R~X of sample 012815-01-A, 012815-01-B, 012815-01-C, 012815-01-D and 012815-01-E

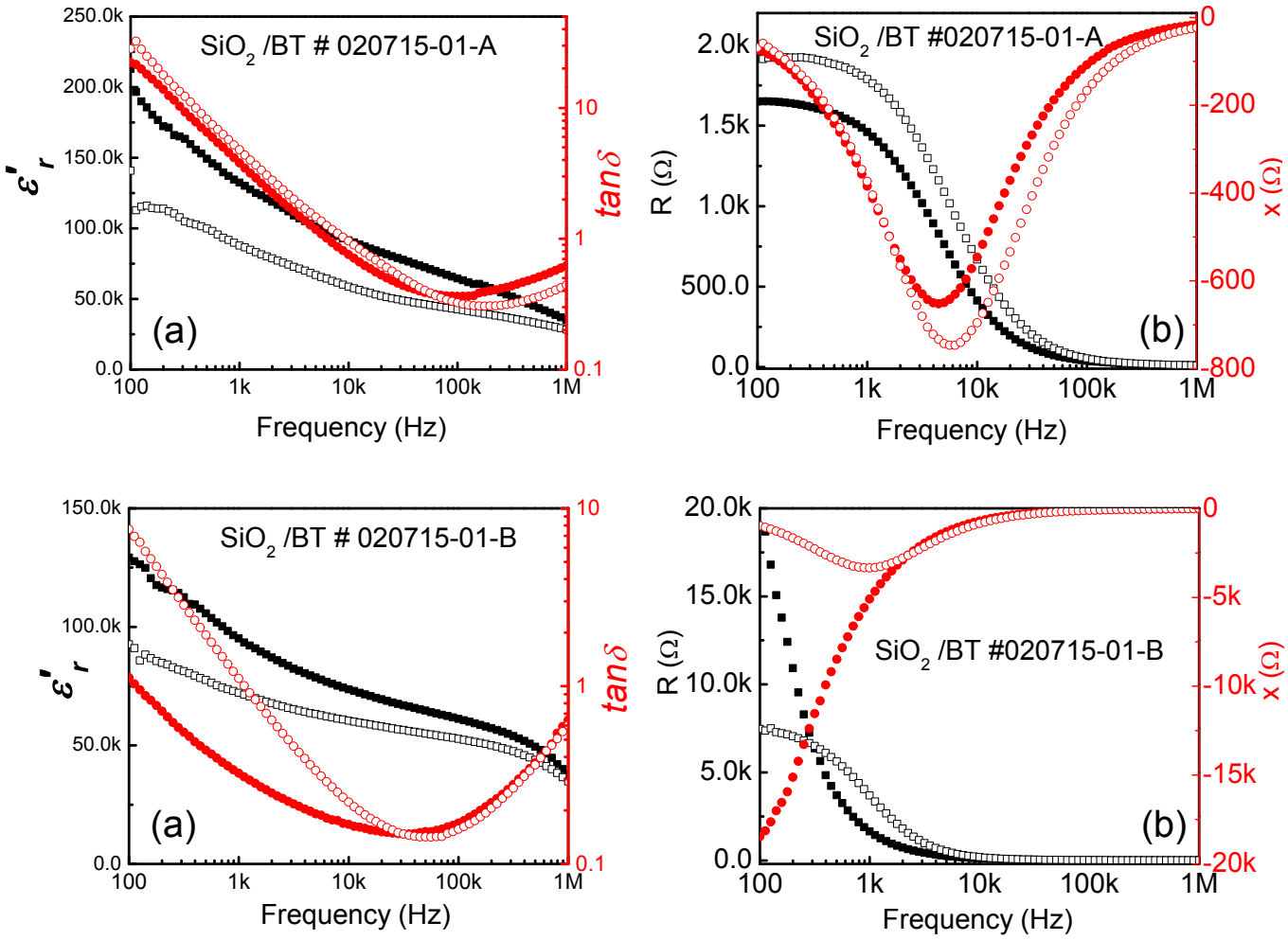

Figure 5-60 Frequency dependence of (a) Permittivity ~ Loss, and (b) R~X of sample 020715-01-A and 020715-01-B

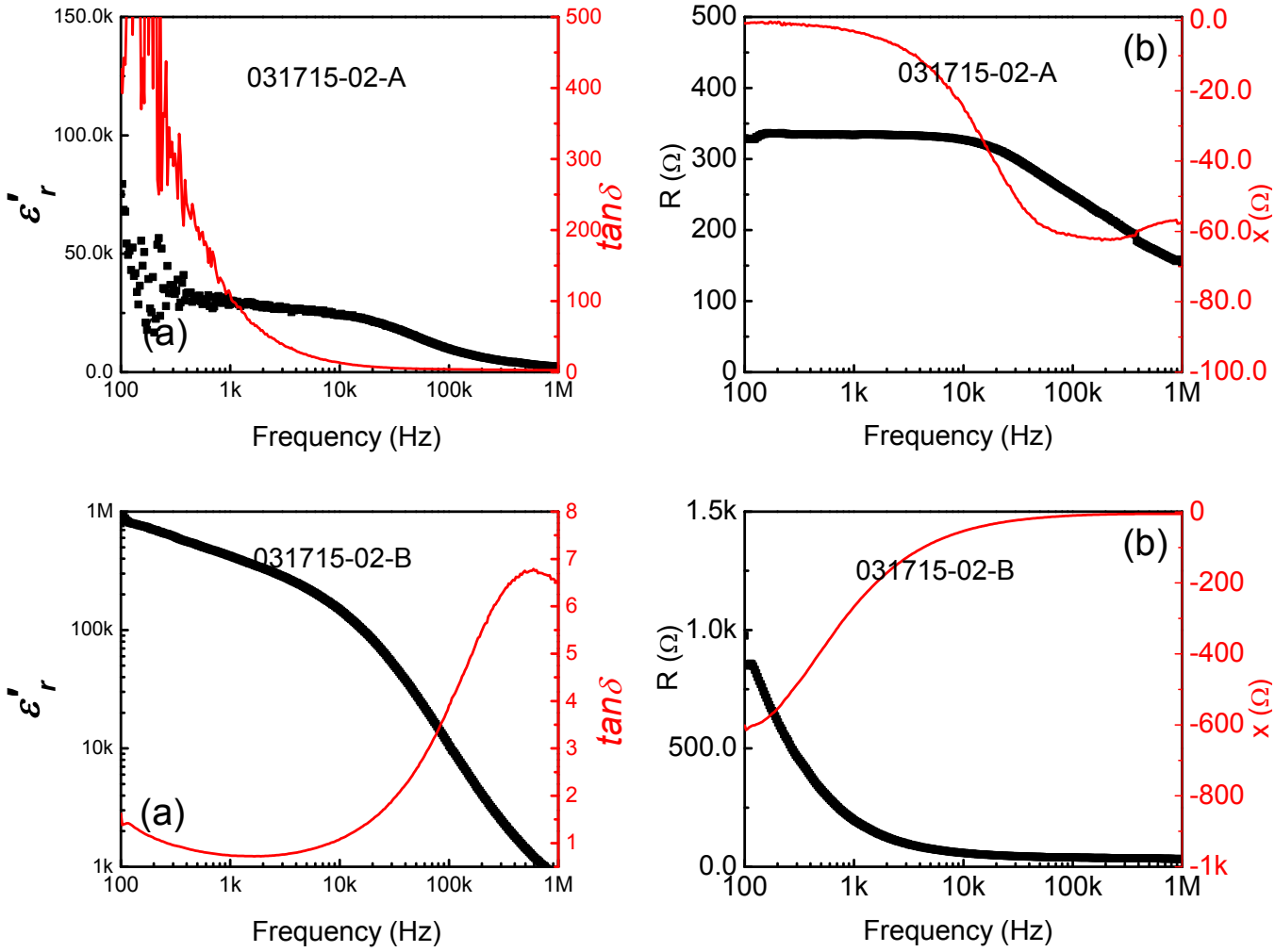

Figure 5-61 Frequency dependence of (a) Permittivity ~ Loss, and (b) R~X of sample 031715-02-A and 031715-02-B

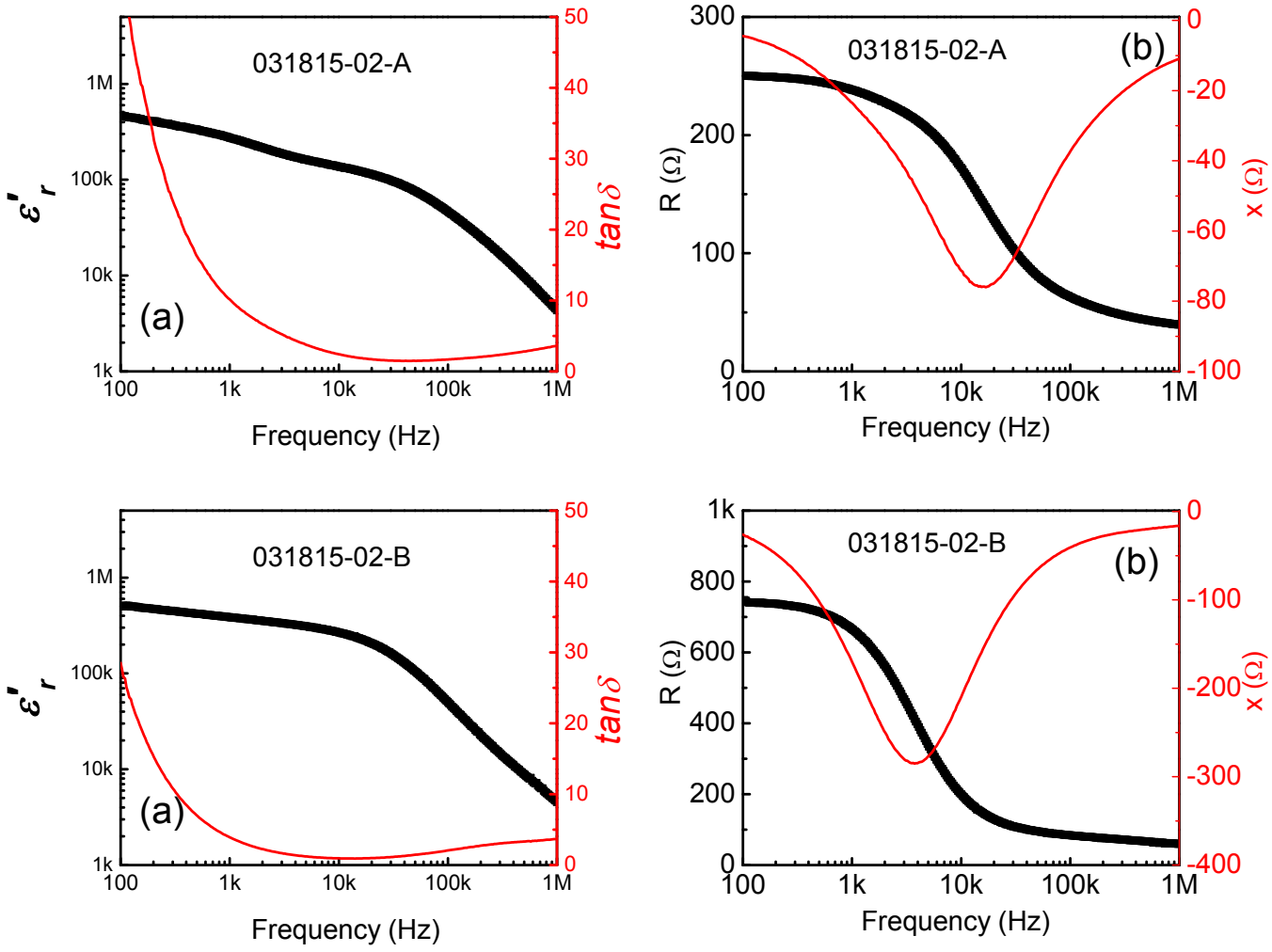

Figure 5-62 Frequency dependence of (a) Permittivity ~ Loss, and (b) R~X of sample 031815-02-A and 031815-02-B

5.5 $Ba_{0.5}Sr_{0.5}TiO_3$-SiO_2 Composites Prepared by Conventional Sintering

5.5.1 Structure of Composites

5.5.1.1 X-ray Diffraction

For the confirmation of the phase composition with different processing conditions, the XRD patterns of $Ba_{0.5}Sr_{0.5}TiO_3$-SiO_2 composite were taken and shown as follows. The XRD patterns of $Ba_{0.5}Sr_{0.5}TiO_3$-SiO_2 composites with different SiO_2 contents (0, 1, 2, 3, 4, and 5 wt%) were shown in **Figure 5-63**. All of the recorded XRD patterns indicate that the composites exhibit a mainly topical cubic perovskite phase at room temperature, which is higher than the tetragonal-cubic phase transition temperature of $Ba_{0.5}Sr_{0.5}TiO_3$. Amorphous phase along with perovskite phase were observed for all the composites, which caused by the glass matrix in composites; in addition, a secondary phase of $BaTiSiO_5$ is detected when the composites have a noticeable content of SiO_2 (>4 wt%). Although the SiO_2 contents lower than 4% does not result in noticeable peaks of impure phase in the glass ceramic composites, the shifts to higher angle of peak positions could be noticed in all samples, which means that the lattice parameters would be effected by SiO_2 addition. The impure phase $BaTiSiO_5$ was crystallized in the sintering process and was considered could reduce the ratio of Ba/Sr in BST. Since Ba^{2+} (1.35 Å) is larger than Sr^{2+} (1.18 Å), peaks in XRD pattern shifts to higher angle caused by compressed lattice by smaller Ba/Sr ratio.

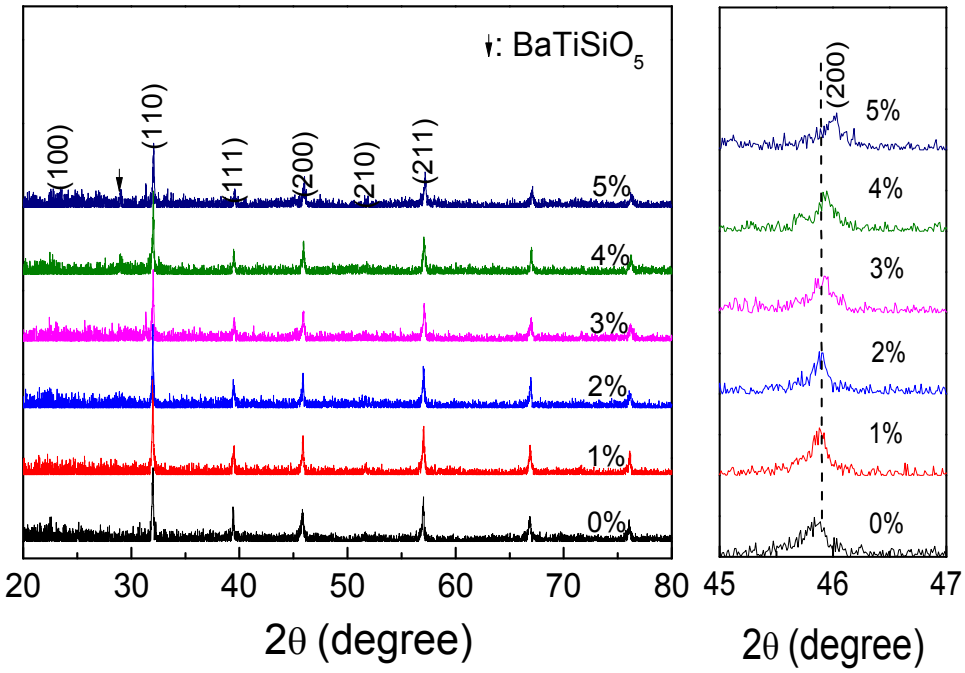

Figure 5-63 XRD patterns of 2.5 wt% SiO_2 coated $Ba_{0.5}Sr_{0.5}TiO_3$ glass-ceramics with different contents of CuO

5.5.1.2 Scanning Electron Microscopy

For the confirmation of the composite microstructure with different SiO_2 content, the SEM picture of cross section of composite films were taken and shown as follows. The pictures of composites with different SiO_2 contents (0, 1, 2, 3, 4, and 5 wt%) were shown in **Figure 5-64**. It can be found that there are a lot of large particles and holes are existed in the pure BST ceramic, which could be attributed to the grains are not uniform and the low density. Though there is still some nonuniformity in the glass ceramic composites, the microstructures of the composites get denser with increase of glass content due to the effect of SiO_2 in the sintering

process. Composites with high content of SiO_2 show glass like morphology, which could be attributed to higher volume of glass phase in composites.

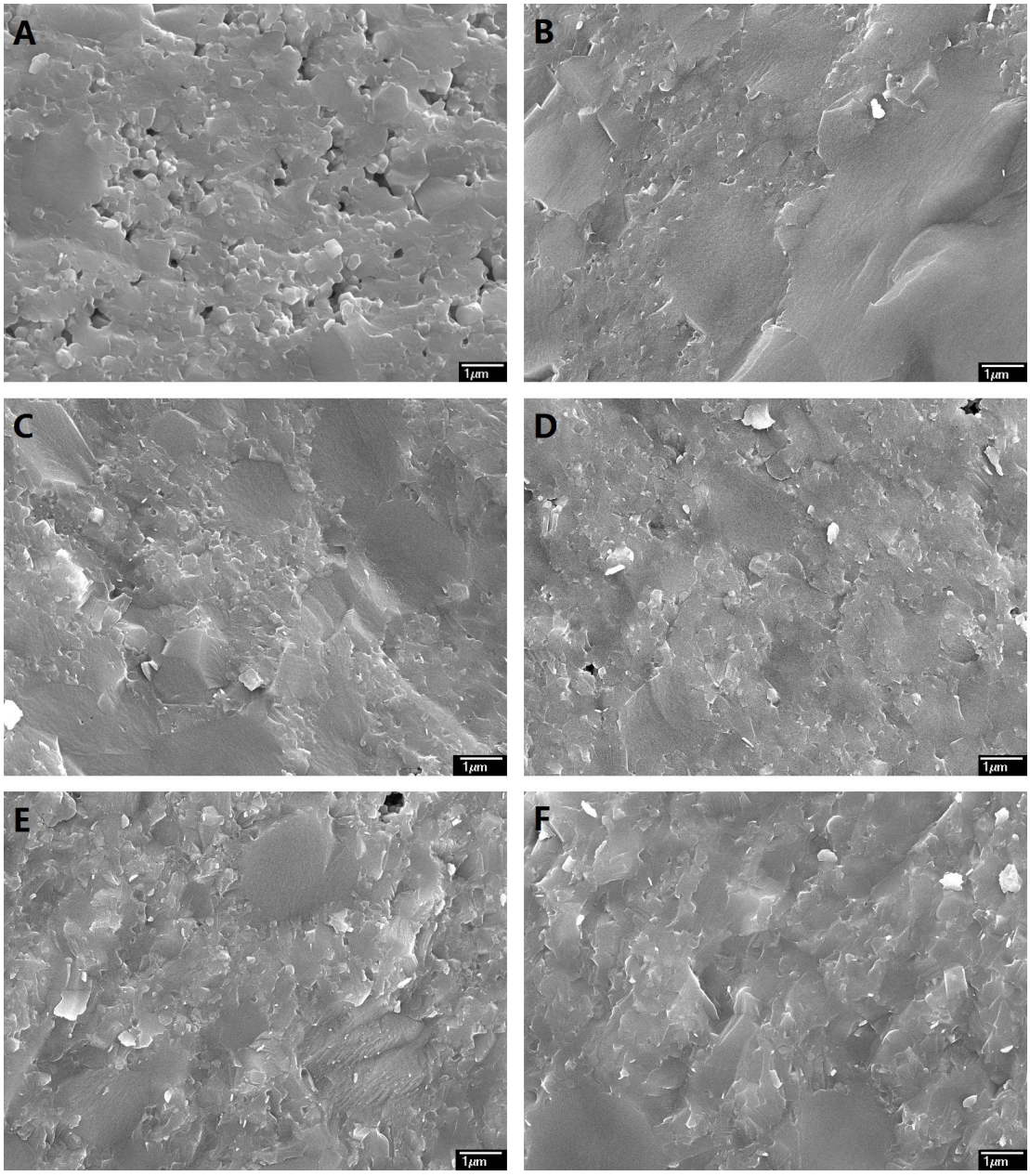

Figure 5-64 SEM pictures of $Ba_{0.5}Sr_{0.5}TiO_3$-SiO_2 glass ceramics composites with (a) 0, (b) 1, (c) 2, (d) 3, (e) 4, and (f) 5 wt% of SiO_2

5.5.2 Dielectric Properties

5.5.2.1 Frequency Dependency of Dielectric Properties at Room Temperature

The dielectric properties and P-E loops of composites with different SiO_2 content were recorded and shown as follows. The frequency dependences of dielectric constant and loss of $Ba_{0.5}Sr_{0.5}TiO_3$-SiO_2 composites at room temperature were shown in **Figure 5-65**. From the figure, it can be seen that dielectric content were dramatically reduced by the SiO_2, which could be attributed to the addition of low dielectric constant phase in composites. However, the loss of composites still sustain in a low level (<0.01). In addition, the frequency stability of dielectric constant of all composites is good with small decreases in the frequency range from 100 Hz to 1 MHz. Moreover, frequency stability could be remarkably improved with increasing content of SiO_2 additive.

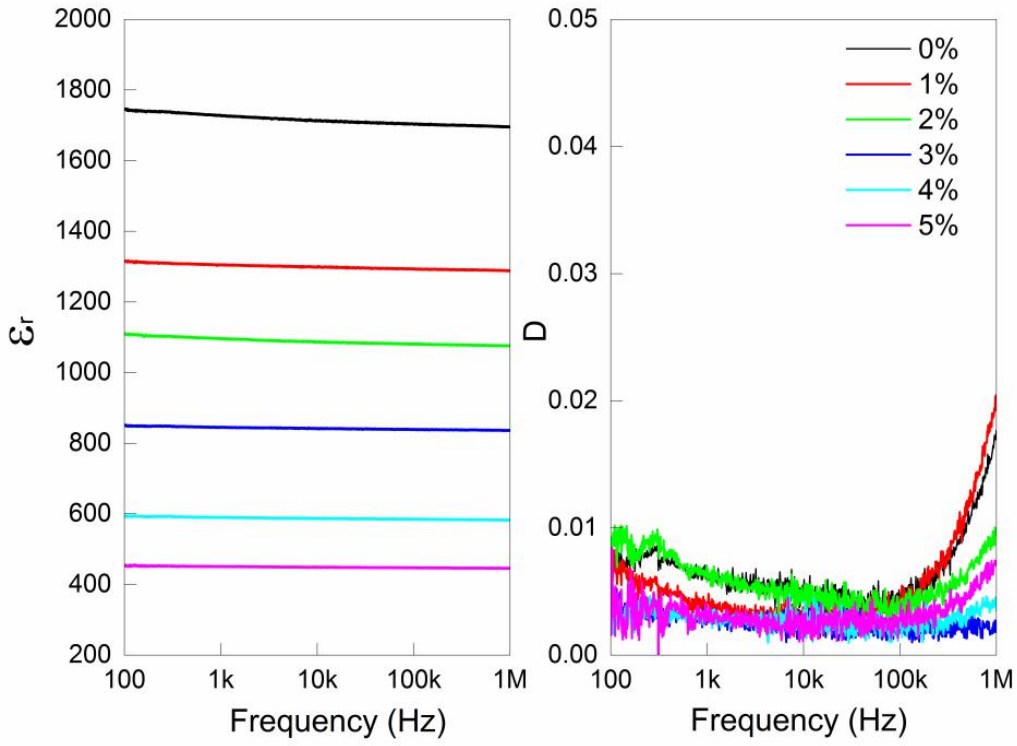

Figure 5-65 The frequency dependence of dielectric constant and loss of $Ba_{0.5}Sr_{0.5}TiO_3$-SiO_2 composites with different SiO_2 contents

5.5.2.2 Energy Storage Properties

The P-E loops of 100 nm composites as a function of testing frequency were shown in **Figure 5-66**. It can be seen that the breakdown strength could be dramatically improved from 120 kV/cm to 290 kV/cm by 1 wt.% SiO_2 additive and could be improved indistinctively with increasing content of SiO_2. It is well known that one of the main reasons of ceramic breakdown could be attributed to local charge breakdown related to the defects in ceramics. As discussed previously, SiO_2 plays a critical role as sintering agent and could relatively improve the density

of composites, so the breakdown strength is enhanced accordingly. Additionally, the amorphous glass matrix with high breakdown strength plays an important role to in the enhancement.

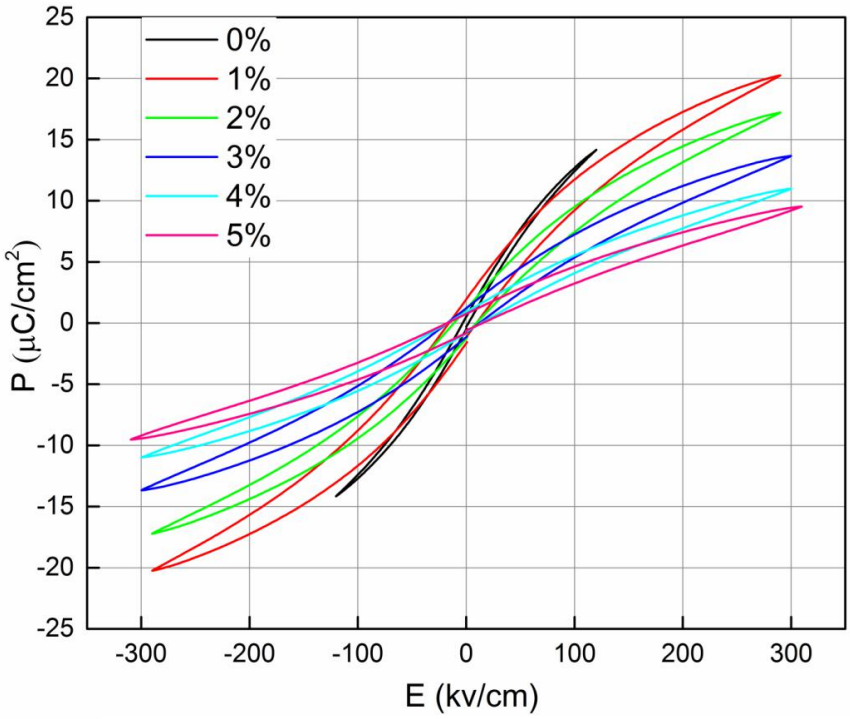

Figure 5-66 P-E loops of of $Ba_{0.5}Sr_{0.5}TiO_3$-SiO_2 glass-ceramic composites with different SiO_2 content up to the electric breakdown strength

5.5.2.3 Temperature Dependency of Properties

The temperature dependency of dielectric constant and loss of composites were recorded and shown as follows. The temperature dependence of dielectric constant and dielectric loss of $Ba_{0.5}Sr_{0.5}TiO_3$-SiO_2 composites with different SiO_2 contents (0, 0.5, 1.0, 1.5, 2.0, 2.5, and 3.0 wt%) were measured at selected frequencies as 100 Hz, 1 kHz, 10 kHz, 100 kHz and 1 MHz in

the temperature range from -70 °C to 70 °C, as shown in **Figure 5-67**, the temperature dependence of dielectric constant and loss of composites measured at 1 kHz are shown in **Figure 5-68**. It can be seen that the dispersion of dielectric constant decreases with increasing temperature above T_c and all the samples have a very low dielectric loss (< 0.01), and the Curie temperature T_c of glass ceramic composites shifts to lower temperature with increasing SiO_2 content. Here, the T_c of those composites could be identified by the dielectric constant peak in **Figure 5-67**. As shown, the T_c of all samples is far below room temperature, which indicates the temperature stability of the composites are reliable around room temperature; the decrease of Curie temperature and suppression of the dielectric peak are obvious with increasing SiO_2 content. It is well known that the relationship of dielectric constant and temperature above Curie point of a normal ferroelectric material follows the Curie-Weiss law[15]:

$$\frac{1}{\varepsilon_r} = \frac{T - T_C}{C} \quad (T > T_C) \tag{5-5}$$

where ε_r is the relative dielectric constant, T_c is Curie temperature, T is the operating temperature, and C is a constant. It can be seen that relationship is quite linear above Tc. A small deviation from the Curie-Weiss relation can be clearly seen in the right range nearby Curie point, which could be attributed to the existence of polar clusters in relaxor ferroelectrics[16]. The obvious deviation from Curie-Weiss relation at high temperature might be related to the effect of SiO_2 on the electrical properties of grain boundary[17]. Based on the Devonshire's theory, dielectric constant of polycrystal ceramics under DC field could be expressed as[15]:

$$\varepsilon_r(T,E) = \frac{\varepsilon_r(T,0)}{(1+\alpha[\varepsilon_0\varepsilon_r(T,0)]^3 E^2)^{\frac{1-\beta}{3}}} \tag{5-6}$$

where the $\varepsilon_r(T,E)$ is the relative dielectric constant at temperature T and DC field E, $\varepsilon_r(T,0)$ is the relative dielectric constant at temperature T without DC field, ε_0 is vacuum dielectric constant, and E is the external DC electric field; the bias exponent β ($0<\beta<1$) represents the order of suppression of the DC electric field effect, and α is the anharmonic coefficient to quantify the efficiency of bias electric field in reducing dielectric constant, which could be considered as constant with temperature. As described in Equation (5-6), above Curie temperature, the tunability is related to the dielectric constant at the operating temperature, which indicates that most of the tunable materials were designed and used nearby the Curie temperature. However, the loss is also much higher near by the Curie temperature.

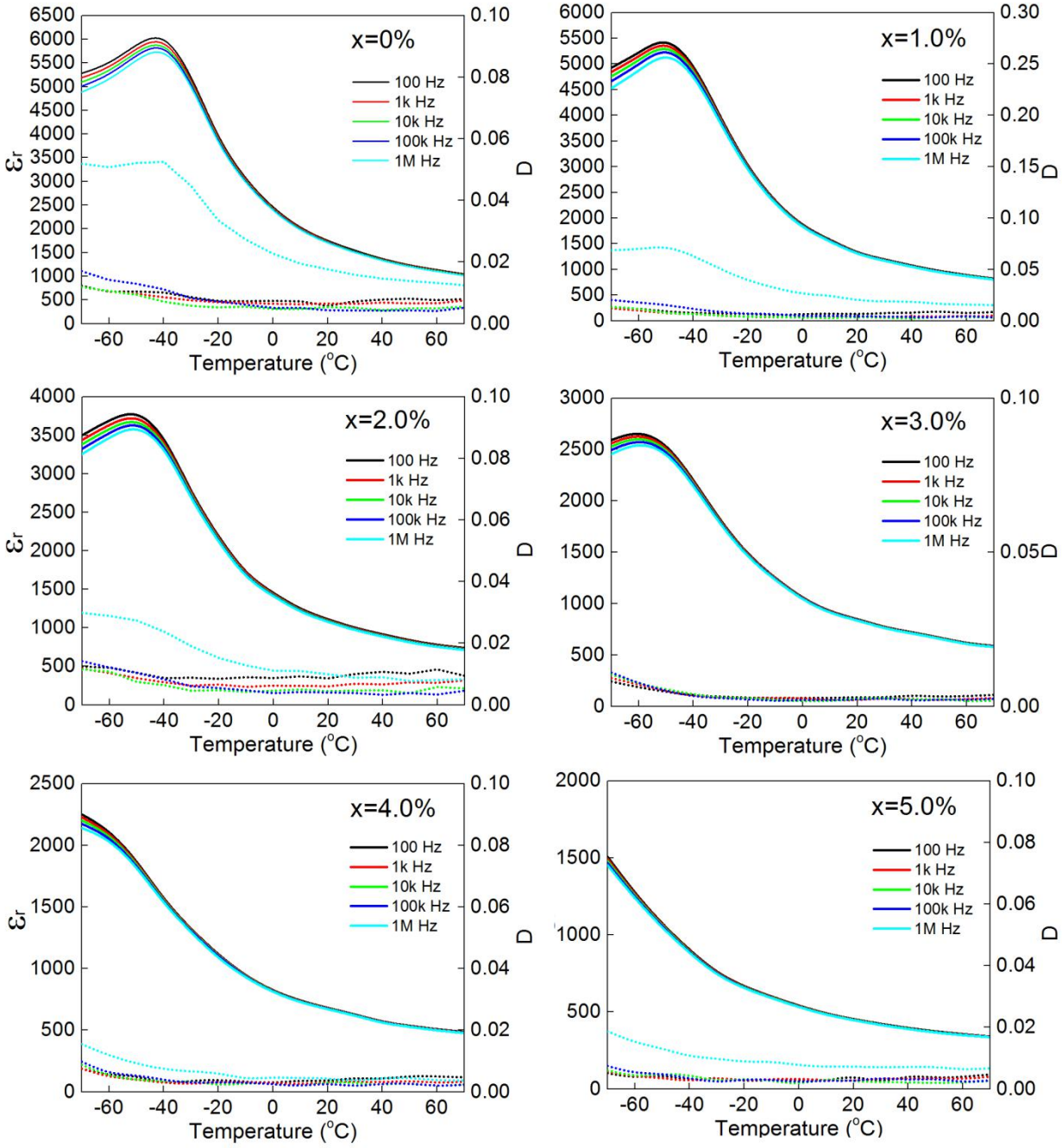

Figure 5-67 Temperature dependence of dielectric constant and dielectric loss of $Ba_{0.5}Sr_{0.5}TiO_3$-SiO_2 glass ceramics composites with different SiO_2 contents

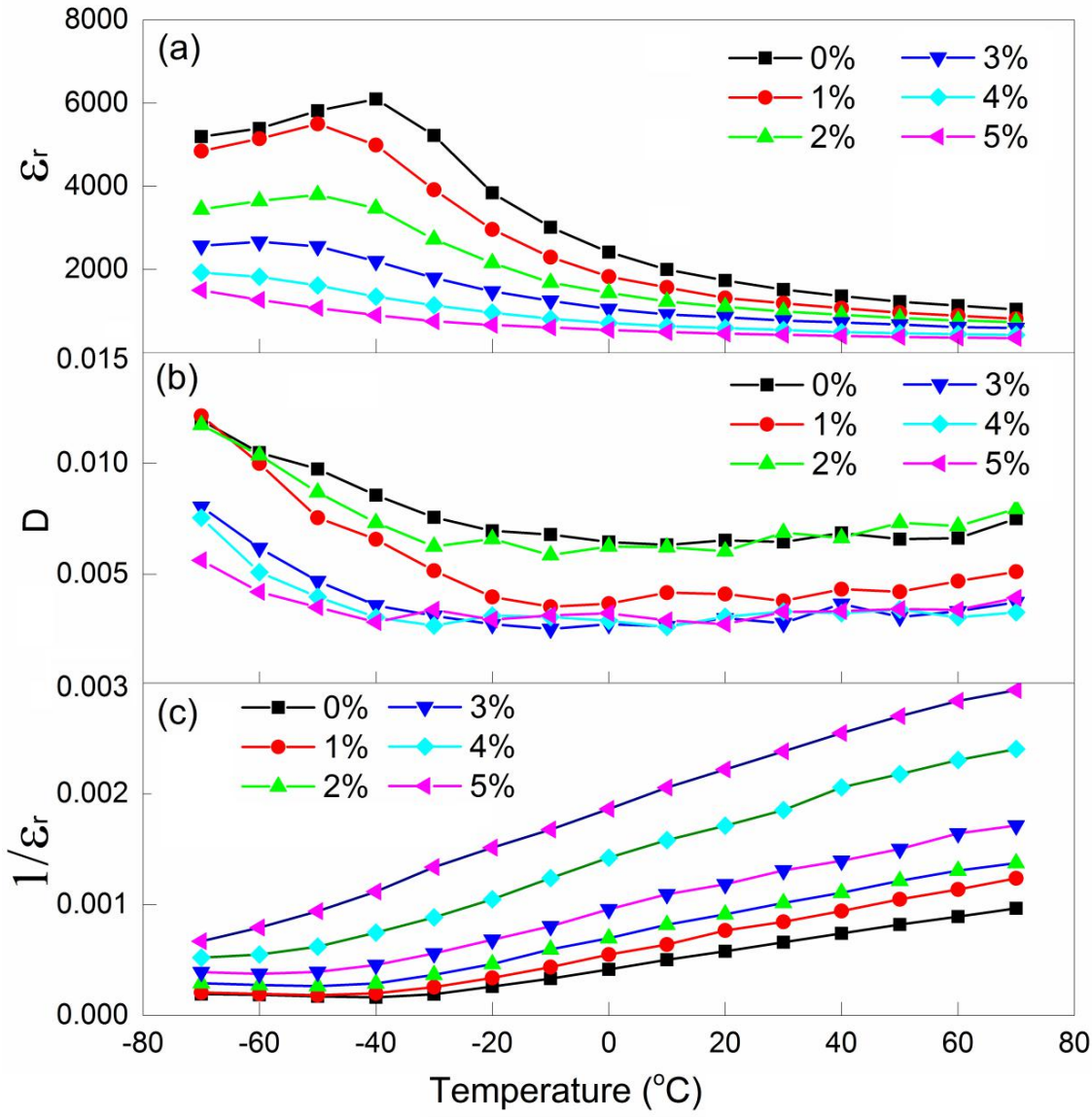

Figure 5-68 The temperature dependence of dielectric constant and loss of Ba0.5Sr0.5TiO3-SiO_2 composites with different SiO_2 content at 1 kHz

5.5.3 Discussion

5.5.3.1 Trend of Dielectric Properties as the Functions of Glass Contents

All of the properties of prepared composites with different preparing conditions were summarized and shown as follows. The dielectric constant and Curie temperature vs SiO_2 content (0, 1, 2, 3, 4, and 5 wt%) of $Ba_{0.5}Sr_{0.5}TiO_3$-SiO_2 glass ceramics were shown in **Figure 5-69**, the maximum polarizations, charge energy densities, discharge energy densities and energy storage efficiency of $Ba_{0.5}Sr_{0.5}TiO_3$-SiO_2 glass ceramics with different SiO_2 contents and under different electric fields were shown in **Figure 5-70**, the breakdown strength, polarizations, charge energy density, discharge energy density and energy storage efficiency of $Ba_{0.5}Sr_{0.5}TiO_3$-SiO_2 composites with different SiO_2 content were shown in **Table 5-15**.

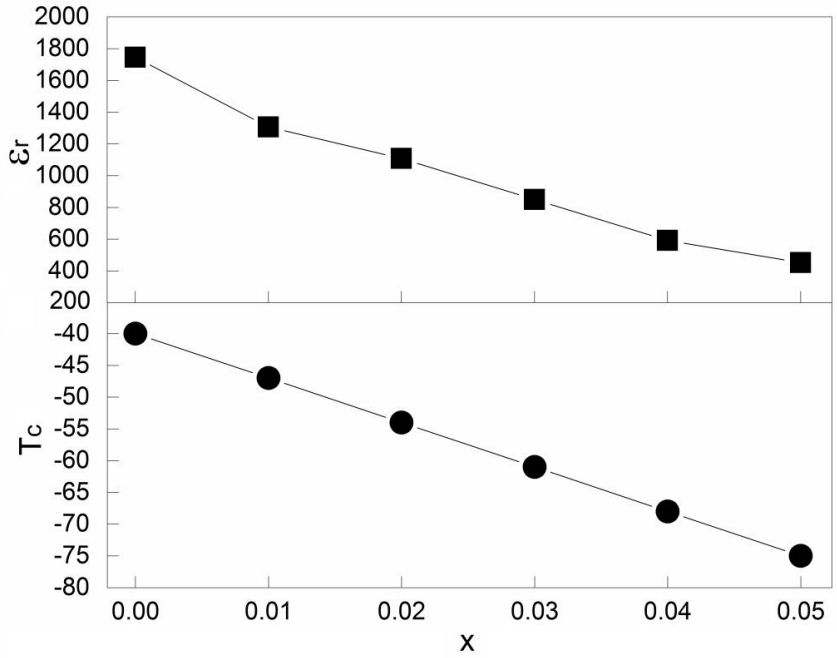

Figure 5-69 The dielectric constant and T_c vs SiO_2 content of $Ba_{0.5}Sr_{0.5}TiO_3$-SiO_2 glass ceramics with different SiO_2 contents

Table 5-15 The breakdown Strength, maximum polarizations, charge energy density, discharge energy density and energy storage efficiency of $Ba_{0.5}Sr_{0.5}TiO_3$-SiO_2 composites with different SiO_2 contents up to the electric breakdown strength

SiO_2 (mol%)	E_b (kv/cm)	P_m ($\mu C/cm^2$)	Charge (J/cm^3)	Discharge (J/cm^3)	Efficiency (%)
0	120	14.19	0.78	0.72	92
1	290	20.28	2.56	2.01	79
2	290	17.20	2.25	1.78	79
3	300	14.26	1.95	1.52	78
4	300	10.96	1.60	1.25	78
5	310	9.50	1.57	1.23	78

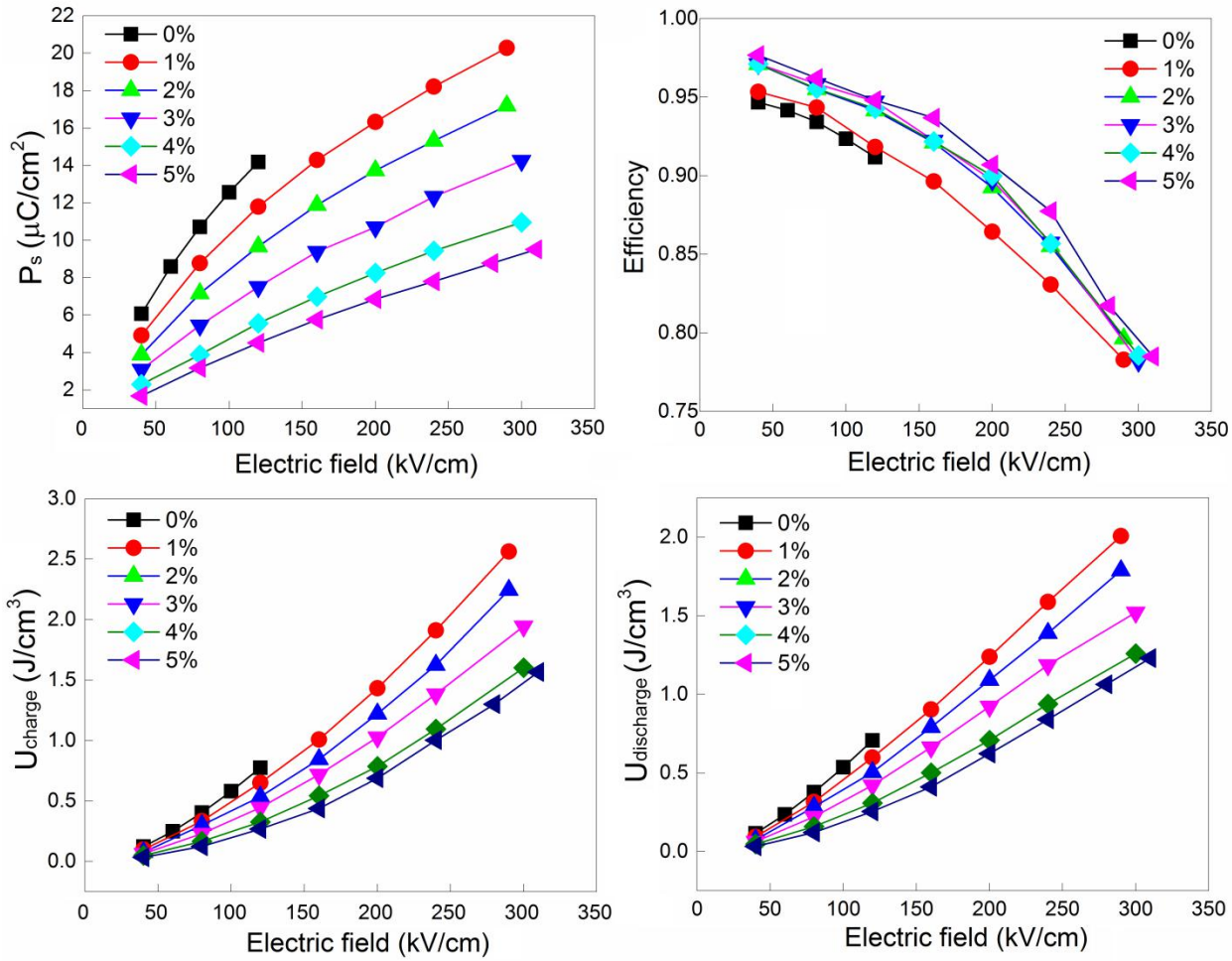

Figure 5-70 The maximum polarizations, charge energy density, discharge energy density and energy storage efficiency of $Ba_{0.5}Sr_{0.5}TiO_3$-SiO_2 glass ceramics composites with different SiO_2 contents and under different electric fields

5.5.3.2 Tunability of $Ba_{0.5}Sr_{0.5}TiO_3$-SiO_2 composites

Above Curie temperature, the material's tunability is related to the dielectric constant at the operating temperature, which indicates that most of the tunable materials were designed and used nearby the Curie temperature. The tunability of $Ba_{0.5}Sr_{0.5}TiO_3$-SiO_2 composites were recorded and shown as follows. The temperature dependence of tunability of $Ba_{0.5}Sr_{0.5}TiO_3$-SiO_2

composites with different SiO_2 contents at electric field of 20 MV/m was shown in **Figure 5-71**. It can be seen that the tunability of BSTS composites is greatly affected by temperature. BSTS exhibits a smaller tunability when the operating temperature gets far away from Curie point. Tunability of all composites is above 40% at room temperature. Although tunability of all composites decreases with the content of SiO_2 at same temperature, the breakdown strength could be enhanced at the same time.

The electric field dependence of dielectric constant and tunability of composites was shown in **Figure 5-72**. From the figure, it is clear that the dielectric constants decrease with increasing electric fields which induce higher tenability under higher electric field. It can be seen that, tunability decreases with content of SiO_2 under the same electric field, which can be attributed to the decreasing of dielectric constant and the lower Curie temperature. However, tunability of BSTS composites under maximum electric field is about 71%, which is higher than 51% of pure ceramic. As discussed previously, it is easily understood that dielectric tunability of a given material is correlative with strength of the external field and the higher the external field is applied, the higher the tunability will be.

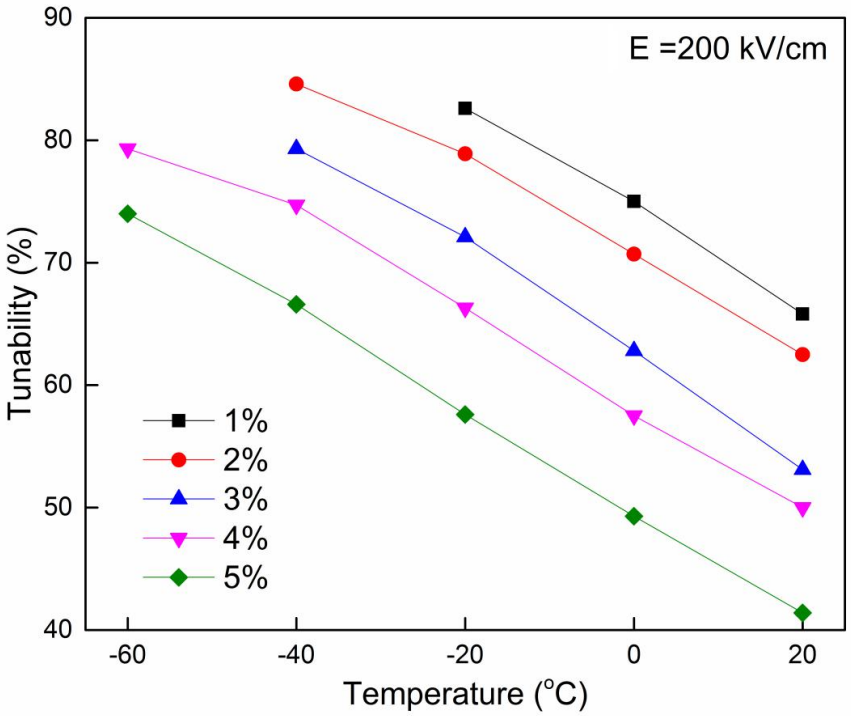

Figure 5-71 The temperature dependence of tunability of $Ba_{0.5}Sr_{0.5}TiO_3$-SiO_2 composites with different SiO_2 contents at electric field of 20 MV/m

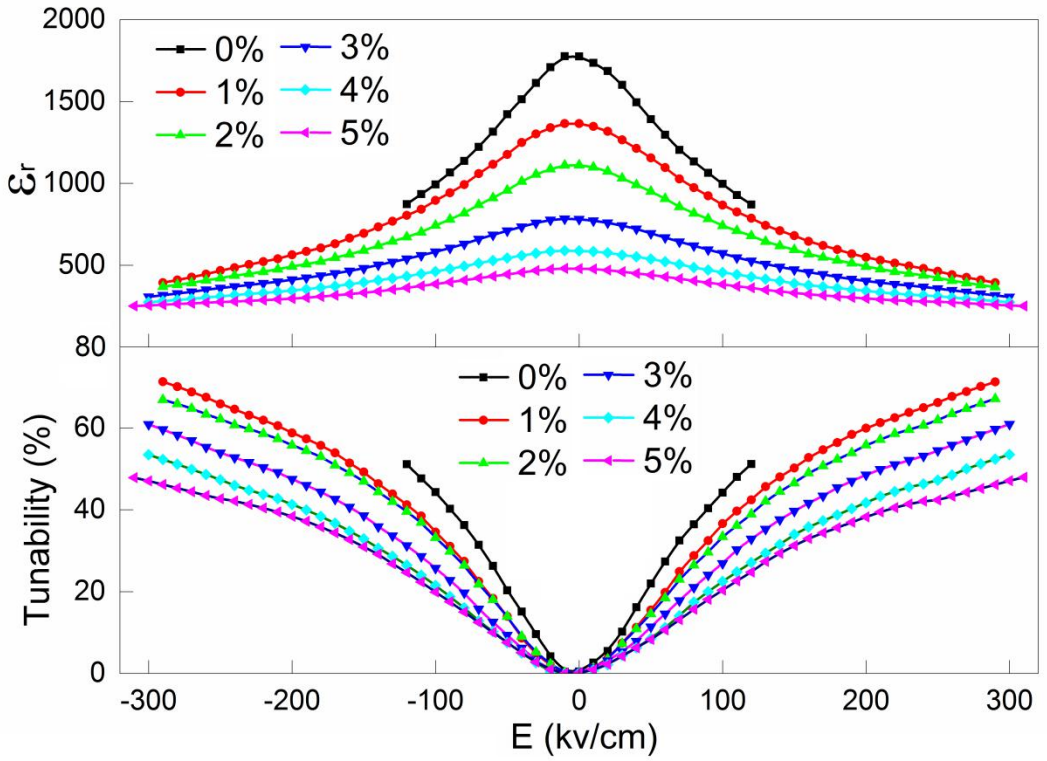

Figure 5-72 The electric field dependence of dielectric constant and tunability of $Ba_{0.5}Sr_{0.5}TiO_3$-SiO_2 composites with different SiO_2 contents at 1 kHz

5.6 Summary

In summary, the ceramic-glass composites were created with the different featured properties. Firstly, a composite with high dielectric constant, adjustable conductivity and high energy density was developed by the combination of vacancies introduced $BaTiO_3$ and SiO_2 coating layers. The composites shown uniform microstructure due to the liquid phase sintering and new phase formation. The maximum energy density obtained is about 1.82 J/cm^3, which is more than four times compare with the pure $BaTiO_3$ ceramics. At room temperature, the 950 °C hydrogen atmosphere pretreated 2.5 wt% composite exhibits a high dielectric constant of 3540 at

100 Hz; Simultaneously, the dielectric loss of this composite is 0.05 at 100 Hz which is much smaller then the pretreated ceramics without SiO_2 coating. It indicates that the insulating layer are formed by the sintering with coating layers, which also increased the breakdown strength of composites. An expanded adjustable conductivity range of 10^{-6} to 10^{-9} S/m were achieve by changing the SiO_2 content; In addition, a better dielectric stability with changing temperature were obtained due to the relocation of the phase transformation temperature and weakened peaks. Therefore, the $BaTiO_3$-SiO_2 composites created by coating SiO_2 shells on the $BaTiO_3$ cores were confirmed to be a potential dielectric for a variety of applications. By adding the CuO additives into 2.5% SiO_2 coated $BaTiO_3$ glass-ceramics without pretreatment, new composites with the modified properties were then prepared after solid state sintering. The effects of CuO content on the phase compositions, microstructures, dielectric properties and energy storage performances were intensively investigated. The density of the glass-ceramics was greatly enhanced by adding CuO; the crystal structure is also found to be tetragonal with trace of a second phase of $BaTiSiO_5$ based on the XRD analysis. The maximum polarization, remnant polarization, coercive field and dielectric breakdown strength were strongly dependent on the amount of CuO additives. For energy storage application, the best performances appear in glass-ceramic with 2 mol% of CuO additive and the results indicated CuO is effective to improve the energy storage performances of the SiO_2 coated $BaTiO_3$ ceramic-glass. An energy storage density of 1.42 J/cm^3 with a energy storage efficiency of 53% was achieved, which is about 3.8 times higher than those of pure ceramics.

Secondly, $Ba_{0.5}Sr_{0.5}TiO_3$-$xSiO_2$ (x=0, 1, 2, 3, 4, 5 wt%) glass ceramic composites were fabricated by the same process with SiO_2 coating layers obtained from Stöber method and

conventional ceramic sintering to investigate the influences of glass additive on the dielectric properties and energy storage performance of the BST based ceramic-glass composites. The SiO_2 additive was confirmed to be effective to reduce the sintering temperature of $Ba_{0.5}Sr_{0.5}TiO_3$ ceramics to about 1230 °C. Impure $BaTiSiO_5$ phase formatted from the reaction of SiO_2 additive and BST are mainly amorphous in the composites and would change the Ba/Sr ratio in the ceramic phase, which would lead to right shift in XRD patterns, decrease of T_c and lower dielectric constant of the composites. It was observed that the SiO_2 additive could significantly optimize the microstructure of the bulk material and remarkably improve the breakdown strength. With 1 wt% SiO_2 additive, the maximum polarization, breakdown strength are about 20.28 $\mu C/cm^2$ and 260 kV/cm, which suggests an energy storage density about 2.56 J/cm^3 with a efficiency as high as 79%. The tunablity of produced composites was found to be a function of the zero-DC dielectric constant, which could be explained by a modified Devonshire's theory. Tunability of the BSTS composites was reduced by introduction of SiO_2, whereas the breakdown strength of the composites was improved remarkably, which is much advantageous for high power tunable applications. Consequently, the results suggests that the SiO_2 added BST glass ceramic composites are the promising candidates for high energy density capacitors; due to the suitable dielectric constant, low dielectric loss and acceptable tunability, the composites can also meet the requirements of tunable device applications.

Finally, the glass coated $BaTiO_3$ nanopowders were used in spark plasma sintering to create the composites with high dielectric constant. For most of the SPS composites, the layered structures have been confirmed, therefore the different layers from each pieces from one original SPS ceramic pellet are showing largely different dielectric properties. A maximum dielectric

constant of 811,895 at 1k Hz were detected from the composites made by SiO_2 atomic layer deposited 140 nm $BaTiO_3$ nanopowders, which is about 200 times compare with the pure $BaTiO_3$ ceramics; simultaneously, a high dielectric loss of the composite was detected to be 0.457. Except the composites showing high dielectric constants and high loss which is close to the properties of conductors, there are some samples are showing ordinary dielectric constants and low loss which is close to the properties of insulators. For example, a dielectric constant of 4,137 and a loss of 0.162 at 1 kHz were obtained from a sample made by Al_2O_3 atomic layer deposited 140 nm $BaTiO_3$ nanopowders. For some of the composites, the properties of different layers are largely different, this phenomenon indicates that the non-uniform structures were formed by SPS. The properties which are close to conductors also lead to the decrease of breakdown strength. By the coating of ZrO_2, the breakdown field of composites were increased to 1.622 MV/m, along with a polarization of 19 $\mu C/cm^2$ under the external voltage of 600V. Consider the extremely high dielectric constant, relative high loss and low breakdown strength, the $BaTiO_3$-SiO_2 composites created by SPS provides a candidate dielectric for high permittivity applications.

Chapter 6

Conclusions and Future Works

6.1 Conclusions

Base on the experiments, the feature of different dielectric composites was studied in detail. As the result, a series of excellent candidates for high permittivity and energy storage applications were found. For the convenience of compare, the overview of results for ceramic-polymer, conductor-polymer, and ceramic-glass composites was listed; from the listed results, some conclusions were made and shown as follows.

1. For the conductor-polymer composites $Ti_3C_2T_X$-P(VDF-TrFE), a uniform microstructure was observed by SEM by the two steps process consisted of solution casting and hot pressing. The percolation threshold is dependent on the testing frequency and is about 11.96 wt% at 100Hz, which is smaller than the composites using spherical conductive particle fillers. At room temperature, the 12 wt% composite exhibits a high dielectric constant higher than 2100 at 100 Hz; In addition, the 10 wt% composite exhibit the high dielectric constant of more than 1500 associated with a loss of 0.8 at 100 Hz which is much smaller then other reported high-dielectric constant 2-D filler based composites. It indicates that the new relaxation processes are induced in composites due to the adding of 2-D shape fillers, which is the dominating mechanism of stability improvement in changing temperatures. Due to the flexibility and excellent dielectric properties of the new composite material created, a bright future have been shown that the material may become a strong candidate of applications such as soft/wearable electrics, high permittivity capacitors, sensors and energy storage devices. *From this work, a*

conclusion can be obtained that by just a small amount of 2-D conductive material the conductor-polymer composite can sharply improve the dielectric constant compared with polymer matrix to form the flexible dielectrics which are suitable for the application of wearable electronics; however it also results in a high dielectric loss and a low dielectric strength that is limited in energy storage applications.

2. For the ceramic-polymer such as CCTO-P(VDF-CTFE), the dielectric constant of composites are increased compare with the pure polymer but are still limited; However, due to the sharp increase of dielectric strength, the relative high energy density can be obtained by the adding of coupling agents. For the fixed CCTO percentage samples, the permittivity decreases as the frequency increases. In the whole frequency range, the permittivity obtained are higher than that of P(VDF-CTFE), but much lower than that of pure CCTO; The dielectric constant and breakdown field of composites films strongly dependent on the annealing process, 160°C annealing shows the best result. The dielectric permittivity and loss for all samples increase with increasing temperature, a sudden increase in dielectric permittivity was found at high temperature are due to the space charge or interfacial polarization effects. *The results from this work displayed the representative features of ceramic-polymer composite that are effective in improve the energy density by increasing dielectric strength but are limited in obtaining high dielectric constant.*

3. For the ceramic-glass composites including $BaTiO_3$-SiO_2, a conclusion can be made based on the results recorded and discussed that the glass-ceramic composite with relatively good energy storage properties can be achieved by sintering the vacuum pretreated $BaTiO_3$ nanopowders coated with uniform SiO_2 shells. During sintering, the silica coating layer can

modify the grain boundary between $BaTiO_3$ cores, which lead to the effectively suppress of the grain growth of composites. The modification can be partially ascribed to the secondary phases formation due to the reaction between SiO_2 shell and $BaTiO_3$ core. Among the samples with different concentrations, the 2.5wt% SiO_2-$BaTiO_3$ shows the highest energy storage density. Due to the high breakdown strength of homogeneous SiO_2 shells, smaller grains size and better $BaTiO_3$ particles distribution, the breakdown strength of glass-ceramic composite was greatly improved. The oxygen vacancies induced by vacuum pretreatment can significantly increase the permittivity and polarization of the $BaTiO_3$. Although the dielectric loss of the pure $BaTiO_3$ increased significantly by this method, the high-quality silica coating layer makes the $BaTiO_3$-based composites keep increasing permittivity while maintaining a low loss. Combining all the suitable conditions discussed, the most optimized composite was made by using the 950 °C pretreated 200nm $BaTiO_3$ powders with 2.5 wt.% SiO_2 layer sintered at 1230 °C showed the maximum energy storage density of 1.66 J/cm^3 with energy storage efficiency of 45.08%, and the dielectric constant up to more than 3100 simultaneously keep a low loss of 0.023 which makes them attractive for high energy density capacitors and electric energy storage devices. *Overall, the ceramic-glass composites shown the best ability in keeping the balance in obtaining high dielectric constant and energy density. In addition, the high dielectric constant obtained even may be adjusted by changing the condition of pretreatment that are favorable in variety of applications related to pulse generation and energy storage.*

4. For the $BaTiO_3$-SiO_2 composites made by SPS, a conclusion can be made based on the results that the composite with extremely high dielectric constant can be achieved by the spark plasma sintering of glass coated $BaTiO_3$. In this process, a layered structure of composite can be

obtained which lead to largely different dielectric properties between different pieces from the sample obtained by cutting. Among the samples with different preparations, a maximum dielectric constant of 811,895 and a loss of 0.457 at 1 kHz were detected from the composites made by SiO_2 atomic layer deposited 140 nm $BaTiO_3$ nanopowders. In addition, all of the samples with high dielectric constant have shown a high loss and low breakdown strength; some samples with ordinary dielectric constants and low loss were also produced simultaneously with the same condition due to the layered structure. *Overall, a larger part of the $BaTiO_3$-SiO_2 composites produced by SPS shown the extremely high dielectric constant and high loss. The low breakdown strength limited the application of the composites. If the breakdown strength can be improved, SPS can be expected as a effective method for the production of a variety of applications related to pulse generation and energy storage.*

5. From the X-ray Diffraction (XRD) study of polymer-based nanocomposites, the structure of polymer matrix was found to be modified due to the adding of nano-sized fillers. In spite of the position of prominent peak in XRD pattern do not shown much differences with different filler contents, it was observed that with the increasing filler content, this peaks are becoming significantly sharper and stronger at first and then decreases. In contrast, the 2θ of prominent peak are firstly decreases and then increases. The estimated crystallinity were then found to behave a clear increase from 50.3 to 87.7 % was observed with the addition of small amount nano-sized fillers; with the increase of amount adding to polymer matrix, the drop of crystallinity suggesting that the crystallization process will be hindered by too much doping. *Therefore, it can be concluded that the nano-sized fillers, especially 2-D nano-sheets, provides*

an objective contribution on the crystallinity in composite formation, which may also modify the dielectric properties of the fabricated samples.

6.2 Future Works

1. For the study on conductor-dielectric composites, it can be found the composites exhibited a high dielectric constant when the filler concentration was close to the percolation threshold, which results in a high dielectric loss and a low breakdown strength. Therefore, it is important to find the ways in increasing the breakdown strength and reducing the dielectric loss. In addition, the crystallinity of polymer-based composites with different shape and size should be studied.

2. For the study of ceramic-polymer composites, the effect of silane coupling agent was confirmed. An increased breakdown strength was obtained by coupling agent addition. However, the detailed studies of coupling agent amount on the dielectric properties of polymer matrix should be confirmed; also, the different temperatures of coupling agent adding should be studied.

3. For the study of ceramic-glass composites, the increased breakdown strength and better temperature stability were achieved by adding of the glass composition. By using different ceramics, the dielectric property of final products varying a lot. Therefore, more compositions of ceramics and glasses should be tried to further increase the dielectric constant and breakdown field. In addition, more efforts should be spent on the SPS process to obtain the composites with uniform structures.

References

References of Chapter 1

1. K. C. Kao, Dielectric Phenomena in Solids, Elsevier Academic Press, San Diego, CA 2004.

2. A. V. Hippel, Dielectric Materials and Applications, Technology Press of MIT, Cambridge, Boston 1954.

3. Rao, Y.; Ogitani, S.; Kohl, P.; Wong, C. P. J. Appl. Poly. Sci 2002, 83, 1084-1090.

4. Rao, Y.; Wong, C. P. J.Appl. Poly. Sci 2004, 92, 2228-2231.

5. Zhang, Q. M.; Li, H.; Poh, M.; Xia, F.; Cheng, Z.-Y.; Xu, H.; Huang, C. Nature 2002, 419, (19), 284-287.

6. Newnham, R. E. Ann. Rev. Mat. Sci 1986, 16, 47-68.

7. Dias, C. J.; Das-Gupta, D. K., Ferroelectric Polymer and Ceramic-Polymer Composites. Trans Tech Publications Ltd., Switzerland: 1994.

8. Gregorio, R.; Jr., M. C.; Bernardino, F. E. J. Mater. Sci. 1996, 31, 2925-2930.

9. Barsoum, M. W., Fundamentals of Ceramics. Institute of Physics Publishing: Bristol and Philadephia, 1997.

10. VonHippel, A. R., Dielectric Materials and Applications. Cambridge: Technology Press of MIT: Boston, 1954.

11. VonHippel, A. R., Dielectrics and Waves. Wiley: New York, 1954.

12. Xie, H. K.; Kao, K. C. IEEE Trans Electr Insul 1985, EI-20, 293-294.

13. M. W. Barsoum, Fundamentals of Ceramics, Institute of Physics Publishing, Bristol and Philadelphia, 1997.

14. R. F. Cava, W. F. Peck, and J. J. Krajewski, Nature 377, 215(1995).

15. Newnham, R. E., Properties of Materials. Oxford University Press: New York, 2005.

16. Kittel, C., Introduction to Solid State Physics. Wiley: New York, 1988.

17. Mitsui, T., An introduction to the Physics of Ferroelectrics. Gordon and Breach Science Publishers: New York-London-Paris, 1976.

18. Phelan D, Stock C, Rodriguez-Rivera J A, et al. Proceedings of the National Academy of Sciences, 2014, 111(5).

19. Alam M A, Azarian M H, Osterman M, et al. Circuit World, 2010, 36(1): 22-30.

20. Baojin Chu; Xin Zhou; Kailiang Ren; Bret Neese; Minren Lin; Qing Wang; F.Bauer; Q.M.Zhang. Science 2006, 313, (21), 334-336.

21. Arbatti, M. Development of High-Dielectric-Constant Polymer-Ceramic Composites Based on Calcium Copper Titanate. Auburn University, Alabama, 2004.

22. Branwood, A.; Hurd, J. D.; Tredgold, R. H. Br.J.Appl.Phys. 1962, 13, 528.

23. X, Shan. High dielectric constant 0-3 ceramic-polymer composites[J]. 2009.

24. Miller, Charles. Illustrated Guide to the National Electrical Code, p. 445, Cengage Learning 2011.

25. Downie N, Pradier M. Method and apparatus for monitoring fluid pressure: U.S. Patent 7,526,961[P]. 2009-5-5.

26. R. E. Newnham, D. P. Skinner and L. E. Cross, Mater. Res. Bull. 13, 525 (1978).

27. D. P. Skinner, R. E. Newnham and L. E. Cross, Mater. Res. Bull. 13, 599 (1978).

28. N. Jayasundere, B. V. Smith and J. R. Dunn, J. Appl. Phys. 76, 2993 (1994).

29. C. K. Wong, Y. M. Poon and F. G. Shin, J. Appl. Phys. 90, 4690 (2001).

30. S. M. Pilgrim and R. E. Newnham, Mater. Res.Bull. 21, 1447 (1986).

31. M. T. Sebastian and H. Jantunen, Int. J. Appl. Ceram. Technol. 7, 415 (2010).

32. A. K. Jonscher, J. Phys. D: Appl. Phys. 32, R57 (1999).

33. C. W. Nan, Y. Shen and J. Ma, Annu. Rev. Mater. Res. 40, 131 (2010).

34. L. Zhang and Z.-Y. Cheng, J. Adv. Dielect. 1, 389 (2011).

35. L. Zhang, Fundamental Study and Development of 0-3 Dielectric Composites with High Dielectric Constant[D]. Auburn University, 2013.

36. E. Reichmanis, H. Katz, C. Kloc, and A. Maliakal, Bell Labs Tech. J. 10, 87 (2005).

37. Q. M. Zhang, V. Bharti and X. Zhao, Science 280, 2101 (1998).

38. Z. M. Li, S. Q. Li and Z.-Y. Cheng, J. Appl. Phys. 97, 014102 (2005).

39. X. Zhou, X. H. Zhao, Z. G. Suo, C. Zou, J. Runt, S. Liu, S. H. Zhang and Q. M. Zhang, Appl. Phys. Lett. 94, 162901 (2009).

40. M. Wegener and K. Arlt, J. Phys. D: Appl. Phys. 41, 165409 (2008).

41. Z. M. Li, Y. H. Wang and Z.-Y. Cheng, Appl. Phys. Lett. 88, 062904 (2006).

42. Z. M. Dang, C. W. Nan, D. Xie, Y. H. Zhang and S. C. Tjong, Appl. Phys. Lett. 85, 97 (2004).

43. D. N. Fang, A. K. Soh, C. Q. Li and B. Jiang, J. Mater. Sci. 36, 5281 (2001).

44. S. Komarneni, J. Mater. Chem. 2, 1219 (1992).

45. Z.-Y. Cheng, A.Q. Guo, and X. Yao, Ferroelectrics 190, 167 (1997).

46. Z.-Y. Cheng, L. Y. Zhang and X. Yao, J. Appl. Phys. 79, 8615 (1996).

47. M. E. Lines and A. M. Class, Principles and Applications of Ferroelectrics and Related Materials, Clarendon Press, Oxford, 1977.

48. A. N. Vasil'ev and O. S. Volkova, Low Temp. Phys. 33, 895 (2007).

49. I. P. Raevski, S. A. Prosandeev, A. S. Bogatin, M. A. Malitskaya and L. Jastrabik, J. Appl. Phys. 93, 4130 (2003).

50. M. D. Arbatti, X. B. Shan and Z.-Y. Cheng, Adv. Mater. 19, 1369 (2007).

51. P. Kim, S.C. Jones, P.J. Hotchkiss, J.N. Haddock, B. Kippelen, S.R. Marder, and J.W. Perry, Adv. Mater. 19, 1001-1005 (2007).

52. J.J. Li, J. Claude, L.E. Norena-Franco, S.I. Seok, and Q. Wang, Chem. Mater. 20, 6304–6306 (2008).

53. P. Kim, N.M. Doss, J.P. Tillotson, P.J. Hotchkiss, M.J. Pan, S.R. Marder, J.Y. Li, J.P. Calame, and J.W. Perry, ACS Nano 3(9), 2581–2592 (2009).

54. M.N. Almadhoun, U.S. Bhansali and H.N. Alshareef, J. Mater. Chem. 22, 11196 (2012).

55. K. Yu, H. Wang, Y.G. Zhou, Y.Y. Bai, and Y.J. Niu, J. Appl. Phys. 113, 034105 (2013).

56. S. Siddabattuni, T.P. Schuman, F.D., Materials Science and Engineering B176, 1422– 1429 (2011).

57. H.M. Jung, J.H. Kang, S.Y. Yang, J.C. Won, and Y.S. Kim, Chem. Mater. 22, 450–456 (2010).

58. H.X. Tang, Y.R. Lin, and H.A. Sodano, Adv. Energy Mater. 2013 DOI: 10.1002/aenm.201200808

59. X.L. Dou, X.L. Liu, Y. Zhang, H. Feng, J.F. Chen, and S. Du, Appl. Phys. Lett. 95, 132904 (2009).

60. W.M. Xia, Z. Xu, F. Wen, Z.C. Zhang, Ceramics International 38. 1071–1075 (2012).

61. Y. Song, Y. Shen, P.H. Hu, Y.H. Lin, M. Li, and C. W. Nan, Appl. Phys. Lett. 101, 152904 (2012).

62. H.X. Tang, Y.R. Lin, Clark Andrews and Henry A Sodano, Nanotechnology 22, 015702 (2011).

63. V. Tomer, E. Manias, and C. A. Randall, J. Appl. Phys. 110, 044107 (2011).

64. Y. Bai, Z.-Y. Cheng, V. Bharti, H. S. Xu, and Q. M. Zhang, Appl. Phys. Lett. 76, No. 25 (2000).

65. Dang, Z.-M.; Wang, L.; Wang, H. Appl. Phys. Lett 2005, 86, 172905-3.

66. Dang, Z.-M.; Wang, L.; Yin, Y.; Zhang, Q.; Lei, Q.-Q. Adv. Mater 2007, 19, (6), 852-857.

67. Wang, L.; Dang, Z.-M. Appl. Phys. Lett 2005, 87, 042903--3.

68. Yao, S.; Dang, Z.-M.; Xu, H.; Jiang, M.; Bai, J. Appl. Phys. Lett 2008, 92, 082902-3.

69. Deepa, K. S.; Nisha, S. K.; P.Parameswaran; Sebastian, M. T.; James, J. Appl. Phys. Lett 2009, 94, 142902-3.

70. C. W. Nan, Prog. Mater. Sci. 37, 1 (1993).

71. R. Zallen, The Physics of Amorphous Solids, New York, Wiley, 1983.

72. J. Y. Yi and G. M. Choi, J. Electroceram. 3:361(1999).

73. D. J. Bergman and Y. Imry, Phys. Rev. Lett. 39, 1222 (1977).

74. I. Webman, J. Jortner and M. H. Cohen, Phys. Rev. B 15, 5712 (1977).

75. M. Panda, V. Srinivas, and A. K. Thakur, Appl. Phys.Lett. 92, 132905 (2008).

76. L. Qi, B. I. Lee, S. H. Chen, W. D. Samuels and G. J. Exarhos, Adv. Mater. 17, 1777 (2005).

77. Z. M. Dang, B. Peng, D. Xie, S. H. Yao, M. J. Jiang, and J. B. Bai, Appl. Phys. Lett. 92, 112910 (2008).

78. Y. J. Li, X. Man, J. Q. Feng and Z. M. Dang, Appl. Phys. Lett. 89, 072902 (2006).

79. Z. M. Dang, Y. Shen, L. Z. Fan, N. Cai and C. W. Nan, J. Appl. Phys. 93, 5543 (2003).

80. Z. M. Dang, J. P. Wu, H. P. Xu, S. H. Yao, M. J. Jiang and J. B. Bai, Appl. Phys. Lett. 91, 072912 (2007).

81. J. Macutkevic, D. Seliuta, G. Valušis, J. Banys, V. Kuznetsov, S. Moseenkov and O. Shenderova, Appl. Phys. Lett. 95, 112901 (2009).

82. L. Wang and Z. M. Dang, Appl. Phys. Lett. 87, 042903 (2005).

83. Q. Li, Q. Z. Xue, L. Z. Hao, X. L. Gao and Q. B. Zheng, Compos. Sci. Technol. 68, 2290 (2008).

84. Z. M. Dang, L. Wang, Y. Yin, Q. Zhang and Q. Q. Lei, Adv. Mater. 19, 852 (2007).

85. J. K. Yuan, S. H. Yao, Z. M. Dang, A. Sylvestre, M. Genestoux and J. B. Bai, J. Phys. Chem. C 115, 5515 (2011).

86. F. He, S. Lau, H. L. Chan and J. T. Fan, Adv. Mater. 21, 710 (2009).

87. V. Panwar, R. M. Mehra, J. O. Park and S. H. Park, J. Appl. Polym. Sci. 125, E610 (2012).

88. J. K. Yuan, Z. M. Dang, S. H. Yao, J. W. Zha, T. Zhou, S. T. Li and J. B. Bai, J. Mater. Chem. 20, 2441(2010).

89. L. Zhang, Z. Cheng, J. Adv. Dielectr, 01, (2011) 389-406.

90. V. Panwar, R. Mehra, J. Park, S. Park, J. Appl. Polym. Sci. 125, (2012) E610-E619.

91. Q. Li, Q. Xue, L. Hao, X. Gao, Q. Zheng, Compos. Sci. Technol. 68, (2008) 2290-2296.

92. J. Yuan, S. Yao, Z. Dang, A. Sylvestre, M. Genestoux, J. Bai, J. Phys. Chem. C115, (2011) 5515-5521.

93. F. He, S. Lau, H. Chan, J. Fan, Adv. Mater. 21, (2009) 710-715.

94. L. Zhang, Z. Liu, X. Lu, G. Yang, X. Zhang, Z. Cheng, Nano Energy. 26, (2016) 550-557.

95. W. Zheng, X. Lu, W. Wang, Z. Wang, M. Song, Y. Wang, C. Wang, Phys. Status Solidi A. 207, (2010) 1870-1873.

96. Y. Li, X. Man, J. Feng, Z. Dang, Appl. Phys. Lett. 89, (2006) 072902.

97. Wang Y, Cui J, Wang L, et al, Journal of Materials Chemistry A, 2017, 5(9): 4710-4718.

98. F. He, S. Lau, H. Chan and J. Fan, Adv. Mater. 21, (2009) 710.

99. J. Yuan, S. Yao, Z. Dang, A. Sylvestre, M. Genestoux, J. Bai, J. Phys. Chem. C 115, (2011) 5515.

100. Wang T, Wang Z, Wang C, et al, Ceramics International, 2017.

101. C. Wu, X. Huang, L. Xie, X. Wu, J. Yu, P, Jiang, J. Mater. Chem. 21, (2011) 17729-17736.

102. Z. Dang, L.Wang, Y. Yin, Q. Zhang, Q. Lei, Adv. Mater. 19, (2007) 852-857.

103. M. Naguib, M. Kurtoglu, V. Presser, J. Lu, J. Niu, M. Heon, L. Hultman, Y. Gogotsi, M. Barsoum, Adv. Mater. 23, (2011) 4248.

104. J. Come, M. Naguib, P. Rozier, M. Barsoum, Y. Gogotsi, P. Taberna, M. Morcrette, P. Simon, J. Electrochem. Soc. 159, (2012) A1368.

105. J. Hu, B. Xu, C. Ouyang, S. Yang, Y. Yao, J. Phys. Chem. C. 118, (2014) 24274.

106. Guo D, Cai K, Wang Y, Journal of Materials Chemistry C, 2017, 5(10): 2531-2541.

107. C. Mao, X. Sun, J. Du, Q. Tang, Journal of Physics: Conference Series 152, 012061 (2009).

108. E. P. Gorzkowski, M. J. Pan, B. Bender, C. C. M. Wu, Journal of Electroceramics 18, 269 (2007).

109. Q. Zhang, L. Wang, J. Luo, Q. Tang, J. Du, J. Am. Ceram. Soc. 92, 1871 (2009).

110. X. Wang, Y. Zhang, X. Song, Z. Yuan, T. Ma, Q. Zhang, C. Deng, T. Liang, J. Eur. Ceram. Soc. 32 (2012).

111. Z. Wu, H. Liu, M. Cao, Z. Shen, Z. Yao, D. Hao, H. Luo, J. Ceram. Soc. Jpn. 116 (2008).

112.Y. Zhang, M. Cao, Z. Yao, Z. Wang, Z. Song, A. Ullah, H. Hao, H. Liu, Materials Research Bulletin 67 (2015).

113. Liu J, Zhang J, Wei M, et al, Journal of Materials Science: Materials in Electronics, 2016, 27(7): 7680-7684.

114. Wang J, Tang L, Shen B, et al, Ceramics International, 2014, 40(1): 2261-2266.

115. Xiao S, Xiu S, Zhang W, et al, Journal of Alloys and Compounds, 2016, 675: 15-21.

116. Xiao S, Xiu S, Xue S, et al, Journal of materials science, 2016, 51(12): 5880-5888.

117. Todd, M. G.; Shi, F. G. J.Appl. Phys 2003, 94, (7), 4551-4557.

118. Lewis, T. J, J. Phys. D: Appl. Phys. 2005, 38, 202-212.

119. Schadler, L. Nature Mater 2007, 6, 257-258.

References of Chapter 2

1. M. Naguib, M. Kurtoglu, V. Presser, J. Lu, J. Niu, M. Heon, L. Hultman, Y. Gogotsi, M. Barsoum, Adv. Mater. 23, (2011) 4248.

2. J. Come, M. Naguib, P. Rozier, M. Barsoum, Y. Gogotsi, P. Taberna, M. Morcrette, P. Simon, J. Electrochem. Soc. 159, (2012) A1368.

3. J. Hu, B. Xu, C. Ouyang, S. Yang, Y. Yao, J. Phys. Chem. C. 118, (2014) 24274.

4. Lei J C, Zhang X, Zhou Z. Frontiers of Physics, 2015, 10: 276-286.

5. M. Kurtoglu, M. Naguib, Y. Gogotsi, and M. W. Barsoum, MRS Commun. 2(04), 133 (2012).

6. M. Khazaei, M. Arai, T. Sasaki, C. Y. Chung, N. S. Venkataramanan, M. Estili, Y. Sakka, and Y. Kawazoe, Adv. Funct. Mater. 23(17), 2185 (2013).

7. M. Naguib, O. Mashtalir, J. Carle, V. Presser, J. Lu, L. Hultman, Y. Gogotsi, and M. W. Barsoum, ACS Nano 6(2), 1322 (2012).

8. J. Come, M. Naguib, P. Rozier, M. W. Barsoum, Y. Gogotsi, P. L. Taberna, M. Morcrette, and P. Simon, J. Electrochem. Soc. 159(8), A1368 (2012).

9. J. Hu, B. Xu, C. Ouyang, S. A. Yang, and Y. Yao, J. Phys. Chem. C 118(42), 24274 (2014).

10. X. Xie, S. Chen, W. Ding, Y. Nie, and Z. Wei, Chem. Commun. 49(86), 10112 (2013).

11. Subramanian, M. A.; Li, D.; Duan, N.; B. A. Reisner; Sleight, A. W. J Solid State Chem 2000, 151, 323-325.

12. Subramanian, M. A.; A.W.Sleight. Solid State Sciences 2002, 4, 347-351.

13. Adams, T. B.; Sinclair, D. C.; R.West, A. Adv.Mater. 2002, 14, (18), 1321-1323.

14. Homes, C. C.; Vogt, T.; Shapiro, S. M.; Wakimoto, S.; Ramirez, A. P. Science 2001, 293, (27), 673-676.

15. Almeida, A. F. L.; P.B.A.Fechine; Góes, J. C.; Valente, M. A.; Miranda, M. A. R.; A.S.B.Sombra. Mat.Sci.Eng B 2004, 111, 113-123.

16. Kretly, L. C.; Almeida, A. F. L.; R.S de Oliveira; J.M Sasaki; Sombra, A. S. B. Microwave and Optical Tech Lett 2003, 39, 145-150.

17. Sinclair, D. C.; Adams, T. B.; Morrison, F. D.; West, A. R. Appl. Phys.Lett 2002, 80, 2153-2155.

18. Wu, L.; Y. Zhu; S. Park; S. Shapiro; Shirane, G. Phys.Rev.B 2005, 71, 014118.

19. Varshney D, Kumar A. Optik-International Journal for Light and Electron Optics, 2015, 126(22): 3437-3441.

20. Shan X. High dielectric constant 0-3 ceramic-polymer composites[J]. 2009.

21. A. Young, G. Hilmas, R.W. Zhang, S.C. Schwartz, J. Am. Ceram. Soc. 90, (2007).

22. P. Kim, S. C. Jones, P. J. Hotchkiss, J. N. Haddock, B. Kippelen, S. R. Marder, and J.W. Perry, Adv. Mater. 19, 1001 (2007).

23. T. R. Armstrong, K. A. Young, and R. C. Buchanan, J. Am. Ceram. Soc. 73, 700 (1990).

24. D. M. Ginsberg, World Scientific, Singapore, 1989.

25. Jaffe B, Cook W R, Jaffe H. Piezoelectric Ceramics Academic[J]. New York, 1971.

25. K. Yao, S. Chen, M. Rahimabady, M. S. Mirshekarloo, S. Yu, F. E. H. Tay, T. Sritharan and L. Lu, Ultrason., Ferroelectr. and Freq. Control 58, 19568 (2011).

26. Müller K A, Burkard H. Physical Review B, 1979, 19(7): 3593.

27. Ichinose N, Ogiwara T. Japanese journal of applied physics, 1993, 32(9S): 4115.

28. X.H. Zhu, D.N. Zheng, W. Peng, J. Li, Y.F. Chen, Materials Letters 60 (2006) 1224–1228.

29. S.Y. Wang, B.L. Cheng, Can Wang, H.B. Lu, Y.L. Zhou, Z.H. Chen, G.Z. Yang, Journal of Crystal Growth 259 (2003) 137–143.

30. S.B. Herner, F.A. Selmi, V.V. Varadan, V.K. Varadan, Materials Letter, 15 (1993) 317–324.

31. Yih-Chien Chen, Long Wu, Yi-Ping Chou, Yuan-Tu Tsai, Materials Science and Engineering B, 76 (2000) 95–100.

32. Mingwei Zhang, Jiwei Zhai, Jingji Zhang, Haitao Jiang, Xi Yao, Materials Research Bulletin 46 (2011) 1102–1106.

33. Mingwei Zhang, Jiwei Zhai, Bo Shen, Xi Yao, Materials Research Bulletin 46 (2011) 1045–1050.

34. Nowotny J, Rekas M. Defect chemistry of BaTiO3[J]. Solid State Ionics, 1991, 49: 135-154.

35. Kessel M, De Souza R A, Martin M. Oxygen diffusion in single crystal barium titanate[J]. Physical Chemistry Chemical Physics, 2015, 17(19): 12587-12597.

36. Guillon O, Gonzalez-Julian J, Dargatz B, et al. Field-assisted sintering technology/spark plasma sintering: mechanisms, materials, and technology developments[J]. Advanced Engineering Materials, 2014, 16(7): 830-849.

37. Sairam K, Sonber J K, Murthy T S R C, et al. Influence of spark plasma sintering parameters on densification and mechanical properties of boron carbide[J]. International Journal of Refractory Metals and Hard Materials, 2014, 42: 185-192.

References of Chapter 3

1. L. Zhang, Z. Cheng, J. Adv. Dielectr, 01, (2011) 389-406.

2. C. W. Nan, Y.Shen, J. Ma, Annu. Rev. Mater. Res. 40, (2010) 131-151.

3. M. T. Sebastian, H. Jantunen, Int. J. Appl. Ceram. Technol. 7, (2010) 415-434.

4. L. Zhang, Z. Liu, X. Lu, G. Yang, X. Zhang, Z. Cheng, Nano Energy. 26, (2016) 550-557.

5. M. Naguib, M. Kurtoglu, V. Presser, J. Lu, J. Niu, M. Heon, L. Hultman, Y. Gogotsi, M. Barsoum, Adv. Mater. 23, (2011) 4248.

6. J. Come, M. Naguib, P. Rozier, M. Barsoum, Y. Gogotsi, P. Taberna, M. Morcrette, P. Simon, J. Electrochem. Soc. 159, (2012) A1368.

7. J. Hu, B. Xu, C. Ouyang, S. Yang, Y. Yao, J. Phys. Chem. C. 118, (2014) 24274.

8. Zhang L, Shan X, Bass P, et al. Scientific Reports, 2016, 6.

9. W. Li, L. Yu, Y. Zhu, et al, Journal of applied polymer science. 116, (2010) 663-667.

10. Z. Pi, J. Zhang, C. Wen, et al, Nano Energy. 7, (2014) 33-41

11. M. Boota, M. Pasini, F. Galeotti, et al, Chemistry of Materials. 29, (2017) 7: 2731-2738

12. Z. Cheng, Q. Zhang, F. Bateman, J. Appl. Phys. 92, (2002)6749-6755.

13. D. J. Bergman and Y. Imry, Phys. Rev. Lett. 39, 1222 (1977).

References of Chapter 4

1. Y. Cao, P.C. Irwin and K. Younsi, IEEE Trans. Dielectr. Electr. Insul. 11, 797 (2004).

2. G. R. Love, J. American Ceram. Soc. 73, 323 (1990).

3. K. Yao, S. Chen, M. Rahimabady, M. S. Mirshekarloo, S. Yu, F. E. H. Tay, T. Sritharan and L. Lu, IEEE Trans. Ultrason., Ferroelectr. and Freq. Control 58, 19568 (2011).

4. Q. M. Zhang, Hengfeng Li, Martin Poh, Feng Xia, Z.-Y. Cheng, Haisheng Xu, Cheng Huang, Nature, 419, 19 (2002).

5. B.J. Chu, X, Zhou, K.L. Ren, B. Neese1, M.R. Lin, Q. Wang, F. Bauer and Q. M. Zhang, Science 313, 334 (2006).

6. Z. M. Dang, J. K. Yuan, J. W. Zha, T. Zhou, S. T. Li, and G. H. Hu, Progress in Materials Science 57, 660 (2012).

7. Q. Wang and L. Zhu, Macromolecules 45, 2937 (2012).

8. X. H. Hao, Journal of Advanced Dielectrics, 3, 1330001 (2013).

9. Q. Wang and L. Zhu, J. Polym. Sci., Part B: Polym. Phys. 49, 1421 (2011).

10. L. Zhang and Z.-Y. Cheng, Journal of Advanced Dielectrics 1, 389 (2011).

11. M.D. Arbatti, X.B. Shan, Z.-Y. Cheng, Adv. Mater. 19, 1369 (2007).

12. Z. M. Dang, T. Zhou, S. H. Yao, J. K. Yuan, J. W. Zha, H. T. Song, J. Y. Li, Q. Chen, W. T. Yang and J. B. Bai, Adv. Mater. 21, 2077 (2009).

13. L. Zhang, X. B. Shan, P. X. Wu, and Z.-Y Cheng, Ferroelectrics 405, 92 (2010).

14. L. Zhang, X. B. Shan, P. X. Wu and Z.-Y. Cheng, J. Appl. Phys. A 107, 597 (2012).

15. C. Ehrhardt, C. Fettkenhauer, J. Glenneberg, W. Münchgesang, H.S. Leipner, M. Diestelhorst, S. Lemm, H. Beige, and S. G. Ebbinghaus, J. Mater. Chem. A 2, 2266 (2014).

References of Chapter 5

1. Mao C, Sun X, Du J, et al. Preparation and dielectric properties of Nb2O5-BaO-Na2O-SiO2 glass-ceramic for energy storage capacitors[C]. Journal of Physics: Conference Series. IOP Publishing, 2009, 152(1): 012061.

2. Gorzkowski E P, Pan M J, Bender B, et al. Glass-ceramics of barium strontium titanate for high energy density capacitors[J]. Journal of electroceramics, 2007, 18(3-4): 269-276.

3. Zhang Q, Wang L, Luo J, et al. Improved energy storage density in barium strontium titanate by addition of BaO-SiO_2-B_2O_3 glass[J]. Journal of the American Ceramic Society, 2009, 92(8): 1871-1873.

4. Li Z, Fredin L A, Tewari P, et al. In situ catalytic encapsulation of core-shell nanoparticles having variable shell thickness: dielectric and energy storage properties of high-permittivity metal oxide nanocomposites[J]. Chemistry of Materials, 2010, 22(18): 5154-5164.

5. Wang X, Zhang Y, Song X, et al. Glass additive in barium titanate ceramics and its influence on electrical breakdown strength in relation with energy storage properties[J]. Journal of the European Ceramic Society, 2012, 32(3): 559-567.

6. Wu Z H, Liu H X, Cao M H, et al. Effect of BaO-Al2O3-B2O3-SiO2 glass additive on densification and dielectric properties of Ba0.3Sr0.7TiO3 ceramics[J]. Journal of the Ceramic Society of Japan, 2008, 116(1350): 345-349.

7. Wang X, Zhang Y, Baturin I, et al. Blocking effect of crystal–glass interface in lanthanum doped barium strontium titanate glass-ceramics[J]. Materials Research Bulletin, 2013, 48(10): 3817-3821.

8. Li Y Q, Liu H X, Yao Z H, et al. Characterization and Energy Storage Density of BaTiO3-Ba(Mg1/3Nb2/3)O3 Ceramics[C]. Materials Science Forum. Trans Tech Publications, 2010, 654: 2045-2048.

9. Zhang Y, Cao M, Yao Z, et al. Effects of silica coating on the microstructures and energy storage properties of BaTiO3 ceramics[J]. Materials Research Bulletin, 2015, 67: 70-76.

10. Stöber W, Fink A, Bohn E. Controlled growth of monodisperse silica spheres in the micron size range[J]. Journal of colloid and interface science, 1968, 26(1): 62-69.

11. Tadanaga K, Morita K, Mori K, et al. Synthesis of monodispersed silica nanoparticles with high concentration by the Stöber process[J]. Journal of sol-gel science and technology, 2013, 68(2): 341-345.

12. Tao Li, Kun Yang, Journal of Materials Science: Materials in Electronics, 22 (2011) 838-842.

13. Ying-Chieh Lee, Chia-Wei Lin, and Wei-Hua Lu, Journal of Applied Ceramic Technology, 6 (2009) 692-701.

14. Tae-Jin Park, Mark J. Davis, Paula Vullo, Tina M. Nenoff, James L. Krumhansl and Alexandra Navrotskyw, Journal of American Ceramic Society, 92 (2009) 2053-2058.

15. Wei Chen, Xi Yao, Xiaoyong Wei, Applied Physics Letters, 90 (2007) 182902.

16. Huichun, Yu, Zuo-Guang Ye, Journal of Applied Physics, 103 (2008) 034114.

17. Chunli Diao, HanxingLiu, HuaHao, MingheCao, ZhonghuaYao, Ceramics International, 42(2016)12639–12643.